Elevation changes of mountain glaciers in the Antarctic Peninsula using ASTER-controlled archival aerial photography

a thesis submitted by

Matthias Kunz

for the degree of

Doctor of Philosophy

Newcastle University

School of Civil Engineering and Geosciences

November 2013

For Stefan Schönwitz

Abstract

Over the last 50 years a significant increase in the atmospheric and upper ocean temperatures in the Antarctic Peninsula (AP) region has been observed. As a result major ice-shelves have retreated during the 20^{th} century. In connection, glaciers have accelerated and an increased dynamic ice mass loss is observed, especially over the last decade. Despite these major changes, an exact quantification of ice mass changes of the AP, with its roughly 1000 glaciers, is not available.

Almost no long-term (multi-decadal) glacier mass balance records for the AP exist and in-situ measurements are rare. On the other hand, the United States Geological Survey (USGS) and British Antarctic Survey (BAS) archives hold a large number of historic aerial stereo-photographs of the AP, dating back to the early 1940s. These images contain a valuable source of information and have been used to demonstrate widespread retreat of glaciers in this region. Less effort has been made so far to use this stereo-photography for the extraction of elevation data to compare it with recent elevation information to determine glacier volume change from which mass changes may be estimated. This dissertation seeks to close this research gap and to extend the number of mass balance records for the AP, by investigating, measuring, and analysing historical glacier elevation change in the AP using digital elevation models (DEMs) derived from USGS and BAS airborne (1948-2005) and ASTER spaceborne (2001-2010) stereo imagery.

To ensure reliable and accurate measurements of surface elevation change, extracted DEMs need to be registered in a precise manner. The lack of ground control information in the AP is a major obstacle for this and can result in inaccurate absolute orientations of DEMs. If uncorrected, possible offsets between DEMs introduce significant error and

can lead to an over- or underestimation of glacier change. Thus, in order to precisely co-register corresponding historic and modern DEMs an iterative robust least squares surface matching algorithm was applied. The underlying surface matching approach was previously developed for small-scale coastal erosion studies at Newcastle University. Within the context of this work it has been successfully modified and improved to enable large scale glacier change assessment in areas of steep topography which is typical for the AP.

For a total of 12 glaciers in the AP, located along the western coast between 64° and 71° S, DEMs from the historic archive stereo-imagery were successfully extracted and combined with DEMs derived from modern aerial and ASTER satellite imagery. The improved surface matching approach allowed precise co-registration of these DEMs and enabled the accurate measurement of glacier surface mass balance at the lower portion of the glaciers. Widespread frontal glacier surface lowering, of up to 50 m, has been observed on 12 glaciers with a mean lowering rate of 0.28 ± 0.03 m/yr over a period of 37 years (1970-2007). Higher rates, of up to 0.6 m/yr, were observed in the north-western Peninsula. Two glaciers which have multi-epoch coverage show a significantly larger-than-average lowering since about 1990. These results are in close correspondence with an increase in positive degree days over the last four decades and suggest that much of this lowering can be attributed to atmospheric forcing. However, the observed spatial and temporal variations in the lowering rates suggests that the pattern of surface change is not a simple one and that a regional upscaling is not straight forward. The glaciers represent only 1.2 % of all estimated glaciers in the AP and only the glacier fronts (~20 % of each glacier) were studied. Observations also show an elevation increase at some higher altitude locations within a few km of the glacier fronts, raising the potential that the lowering may have been at least partially compensated for by increased high-altitude accumulation.

Publications related to this thesis

[1] Paul, F. and 24 others (2013): The Glaciers Climate Change Initiative: Methods for creating glacier area, elevation change and velocity products. *Remote Sensing of Environment*. Climate Change Initiative Special Issue. http://dx.doi.org/10.1016/j.rse.2013.07.043.

[2] **Kunz, M.**, King, M. A., Mills, J. P., Miller, P.E., Fox, A. J., Vaughan, D. G., and Marsh, S. (2012). Multi-decadal glacier surface lowering in the Antarctic Peninsula. *Geophys. Res. Lett.*, 39:L052823. doi:10.1029/2012GL052823.

[3] **Kunz, M.**, Mills, J. P., Miller, P. E., King, M. A., Fox, A. J., and Marsh, S. (2012). Application of surface matching for improved measurements of historic glacier volume change in the Antarctic Peninsula. *International Archives of the Photogrammetry, Remote Sensing and Spatial Information Sciences*, 39(B8): 579–584.

[4] Miller, P.E., Mills, J. P., and **Kunz, M.** (2012). Improving the Accuracy of ASTER Elevation Data for Glacial Change Assessment in Antarctica. *RICS Research Report* , March 2012. *RICS, London*. 36 pages.

[5] **Kunz, M.** (2010). Measuring land surface change using ASTER DEMs. *Sensed, The RSPSoc Newsletter*, 37.

[6] Miller, P. E., **Kunz, M.**, Mills, J. P., King, M. A., Murray, T., James, T. D., and Marsh, S. (2009). Assessment of Glacier Volume Change using ASTER-based Surface Matching of historical photography. *IEEE Transactions on Geosciences and Remote Sensing*, 47(7): 1971-1979. doi:10.1109/ TGRS.2009.2012702.

Acknowledgements

First and foremost, I want to thank my supervisors Jon Mills, Matt King and Pauline Miller for giving me the opportunity and encouragement for doing a PhD. Your support and advice has been invaluable and your companionship has always been enjoyable - professionally and beyond work.

During the PhD I had the possibility to meet and work with great people and scientists from around the world. I want to acknowledge the British Geological Survey BUFI and NERC for funding this research, especially Stuart Marsh for his support. Acknowledgment to the British Antarctic Survey and the United States Geological Survey for contributing data and valuable comments towards this research, especially Adrian Fox and David Vaughan. I want to thank the glacier groups at the UAF in Fairbanks and UNIS in Svalbard for making their summer schools very enjoyable and memorable events. I also want to thank the entire team of the School of Civil Engineering & Geosciences and all the other people and friends at Newcastle University that have made my time in the Toon an unforgettable and fun experience. It's been an amazing time.

Finally, I want to thank my family and friends, especially Mutti and Vati. Thanks to my grandparents and Micha. Very special thanks go to my brother Michael (aka. Miczta) for the countless swim sessions in Freevalley :) This thesis would have not been possible without your unlimited support and motivation. You always believed in me and my dreams. Thank you all and keep smiling!

Contents

List of Figures

List of Tables

List of Abbreviations

AABB	Axis-Aligned Bounding Boxes
AP	Antarctic Peninsula
ASTER	Advanced Spaceborne Thermal Emission Radiometer
BAS	British Antarctic Survey
DEM	Digital Elevation Model
DPW	Digital Photogrammetric Workstation
ELA	Equilibrium-Line Altitude
ERS	European Remote-Sensing Satellite
GCM	Global Climate Model
GCP	Ground Control Point
GIA	Glacial Isostatic Adjustment
GMBB	Glacier Mass Balance Bulletin
GNSS	Global Navigation Satellite Systems
GPS	Global Positioning System
GRACE	Gravity Recovery and Climate Experiment
Gt	Gigatonne
ICESat	Ice, Cloud,and land Elevation Satellite
IPCC	Intergovernmental Panel on Climate Change
IRLS	Iterative Robust Least Squares
LVIS	Land, Vegetation, and Ice Sensor
m w.e.	Meter water equivalent
MOA	Mosaic of Antarctica
NASA	National Aeronautics and Space Administration

PDD	Positive Degree Days
SAM	Southern Hemisphere Annular Mode
SAR	Synthetic Aperture Radar
SLE	Sea-Level Equivalent
SMT	Surface Matching Tool
SVD	Singular Value Decomposition
TIN	Triangulated Irregular Network
TMA	TriMetrogon Aerial photography
USGS	United States Geological Survey
WAP	Western Antarctic Peninsula

Chapter 1. Introduction

The Earth's surface air temperature has increased significantly over recent decades (~0.74 °C in the last century) and a further increase of ~2 °C by 2100 is predicted (IPCC, 2007). When discussing global warming two keywords are often mentioned in the same context, sea-level rise and glacier change. That is, when the temperature of glaciers and ice sheets is increased larger volumes of water will be released into the ocean and raise sea-levels. It is important to explain and understand the complex links between climate, sea-level and glaciers in detail but also to understand each component in itself. In view of the global importance of this subject science needs to deliver clear results and statements to decision makers and the public.

1.1 Background

Glaciers and ice sheets have undergone impressive changes over time. Two million years ago, in the Quaternary period, glaciers and ice sheets covered almost one third of the Earth's surface, while today this has reduced to approximately 10 % (Benn and Evans, 1998). It is estimated that the current amount of fresh water held in the form of ice and snow in Antarctica alone can rise the global sea-level by roughly 57 m (Lythe and Vaughan, 2001). This number is impressive given that half the Earth's population lives within 200 km proximity to a coastline (Small and Cohen, 2004).

Changes in the ice caps and ice shelves over the past 50 years have been dramatic. A famous example is the breakup of the Larsen B ice shelf in Antarctica in 2002 which was already anticipated by scientists in 1978 (Mercer, 1978). In the late 1970s scientists began to understand the link between changes in the Earth's climate system from external forces and the direct and indirect responses of glaciers and ice sheets to it. Since

then glaciers have been used as climate indicators with high confidence (Dyurgerov and Meier, 2000; Oerlemans, 2005). Figure 1.1 shows a clear correlation between global surface temperature rise and glacier mass loss. The mass balance of a glacier is a direct response to the climate while fluctuations in glacier length are indirect or delayed responses (Benn and Evans, 1998). Climate and glaciers are coupled in both directions. That is, the climate has an influence on glacier growth but so does glacier growth influence the climate. The so called feedback[1] between glaciers and climate has various timeframes and spatial levels.

Numerical models can help to resolve this problem. The modelling of dynamic processes is one of the most complex subjects in science. Large computer clusters are calculating different global climate models (GCMs) to predict the weather or future climate. In the media and public, those models are often criticized as being too uncertain or they are misused to forecast unobjective climate scenarios. Any model is dependent on reference data (observations) in two directions. First of all as starting values for the model calibration and secondly for validation. To improve such models, whether they are climate or glacier related, more real-world observations of model parameters such as ice mass, temperature or precipitation are needed. Regarding glaciers, several papers (e.g. Cogley, 2009b) find that the lack of quantity and existence of historical data is a problem. The study of Oerlemans et al. (1998) showed that exact glacier volume measurements are needed to calibrate global models for glacier change and stressed the need for further monitoring of glaciers. It is obvious that a better understanding of glacier change will lead to a better understanding of the global climate and vice versa. Equally important is the prediction of sea-level rise.

After the last ice age, approximately 21,000 years ago, global sea-level rose by about 130 m and stabilized around 6000 years ago. Until the end of the 19th century global sea-level remained relatively unchanged. After that time it started to rise significantly (Woodworth et al., 2011). The main causes of the observed sea-level rise are the thermal expansion of the oceans and the loss of land-based ice due to increased melting

[1] Feedback = Process in which the effect or output of an action is 'returned' (fed-back) to modify the next action. It is distinguished between positive (amplifies the direction of change of the output) and negative (reverses the direction of change of the output) feedback

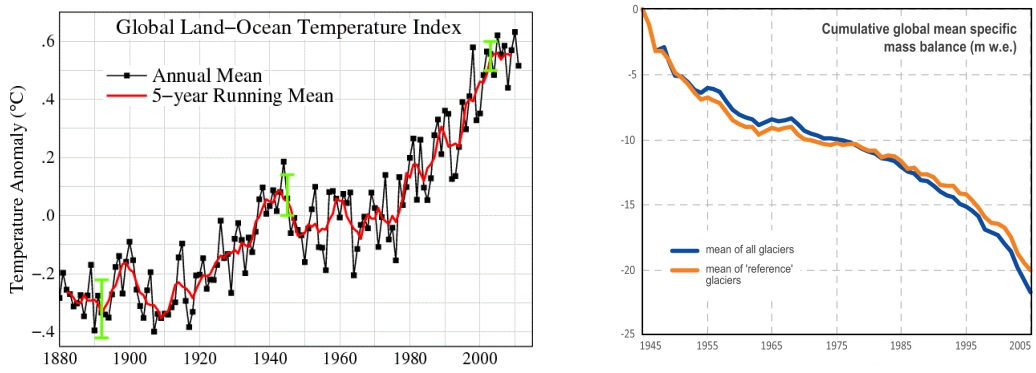

Figure 1.1: Global temperature change (left, Hansen et al., 2006) and global glacier mass balance (right, UNEP-WGMS, 2008)

(Bindhoff et al., 2007). Thermal expansion is caused by density changes in the upper ocean layers due to increased ocean surface temperature. For the period 1961-2003 thermal expansion contributed about 25 % to sea-level rise and melting ice-sheets and glaciers somewhat under 50 %, meaning that about one quarter of the rise could not be explained. One explanation could be an error in the ice loss estimates from glaciers (Rahmstorf, 2007). Explaining and eliminating these uncertainties is very important. The study of Gardner et al. (2011) found that between 2007 to 2009 the largest contributor to eustatic sea-level rise outside Antarctica and Greenland was the Canadian Arctic Archipelago, a region whose contribution was largely unknown until then. Glaciers and ice-sheets contributed over 30 mm between 1951-2008, with a particular increased contribution during the 1990s (Church et al., 2011). However, from roughly 160,000 glaciers worldwide only about 350 glaciers had long-term mass balance records (Figure 1.2) at the beginning of the 21st century. Before the 1960s, less than 20 glaciers had a mass balance record. Moreover, most glaciers with long-term records are located in the northern hemisphere and in regions that are relatively easy to access (Dyurgerov, 2003). In the last decade numerous glacier change studies have been published (Dyurgerov and Meier, 2000; Braithwaite, 2002; Oerlemans, 2005; Cook et al., 2005; Dyurgerov, 2011) and more glacier mass balance records are available every year but there is still a clear lack of records, especially for the southern hemisphere.

It is important to understand that there are regional variations in climate change and its impacts. Although globally most glaciers are retreating, some regions are affected more than others. One region that has warmed rather rapidly is the Antarctic Peninsula (AP),

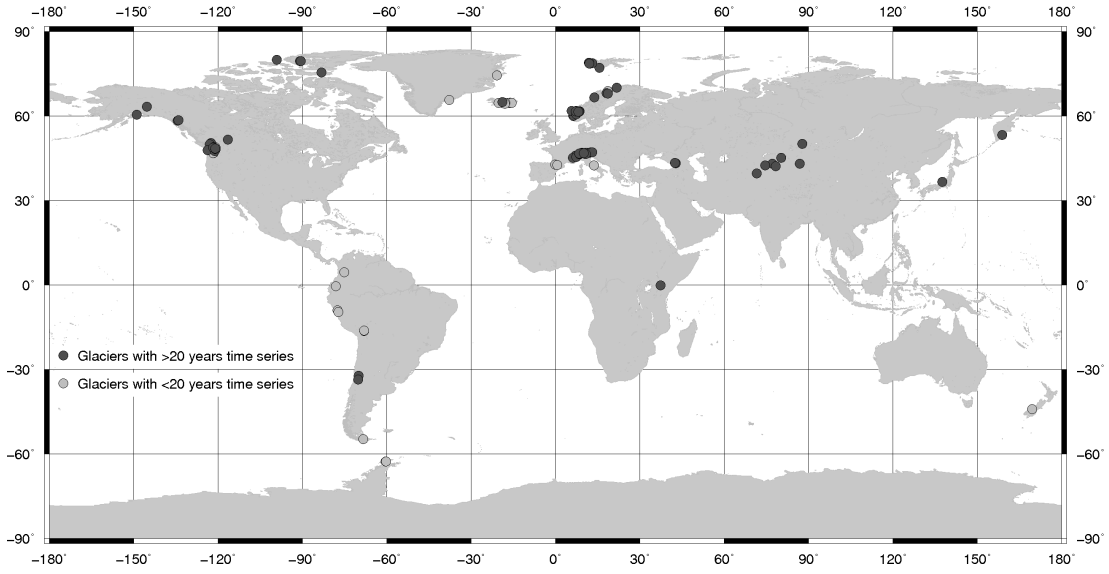

Figure 1.2: Existing long-term glacier mass balance records (WGMS, 2011). Note the lack of observation in the southern hemisphere.

the most northern part of Antarctica. In fact, it is one of the fastest warming regions in the context of global climate change with station records showing a warming equivalent to more than +3.5 °C per century (Vaughan et al., 2003; Turner et al., 2005). Compared to the global mean of +0.74 °C per century this region is particularly subject to climate change. If all ice (95,200 km^3 in volume) on the AP would melt global sea-level would rise by a approximately 25 cm (Pritchard and Vaughan, 2007). In recent decades widespread glacier retreat and acceleration has been observed in the AP and ice shelves in the region have lost more than 28,000 km^2 in area over the last 60 years (Scambos et al., 2004; Cook et al., 2005; Pritchard and Vaughan, 2007; Cook and Vaughan, 2010). Cook et al. (2005) observed 87 % of 244 glaciers studied in the AP retreated over the period 1953-2004. Given the rapid warming and increased melting potential, mass balance observations are particularly needed for the AP to estimate the past, current and future sea-level contribution.

However, as already noted, almost no mass balance records for the AP exist, especially long-term records. As a result, the AP glaciers have not been included in most mountain glacier inventories (Dyurgerov, 2002), and are generally overlooked in global projections of sea-level rise (Lemke et al., 2007). The missing Antarctic contribution equates to nearly 40 % of the total uninventoried glacier area globally (Radić and Hock, 2010). Recent glacier mass balance compilations have resorted to inferring AP mass balance

from global averages (Leclercq et al., 2011) or from estimates of the Canadian High Arctic (Dyurgerov and Meier, 2005). This is unsatisfactory and almost certainly produces biased estimates (Kaser et al., 2006). It is therefore essential to fill existing inventory gaps for the AP region.

Repeated direct glaciological measurements are difficult given the polar proximity and climate. The mountainous terrain and challenging environment make the area difficult to access and in-situ measurements are rare (Smith et al., 1998). A suitable solution is remote sensing which offers a tool for the mapping of inaccessible areas. The areal extent of glaciers and ice-shelves is now mapped relatively well but of primary interest here is the volumetric change. Sensors like GRACE (Gravity Recovery And Climate Experiment) can directly assess changes in the Earth's mass and produce estimates of ice mass or volume changes for the present-day, but they are unable to look back in time.

1.1.1 Use of elevation models for glacier change assessment

An alternative approach to glacier change assessment is to derive volume change estimates through the comparison of surface elevations changes over a glacier. Often this is done by differencing digital elevation models (DEMs). When integrated over the whole glacier area together with a known density, the glacier mass balance can be calculated. This technique is also known as geodetic mass balance calculation and can be applied repeatedly over large areas. Altimetry sensors such as ERS-1, ERS-2, CryoSat-2, or ICESat can provide such elevation information but often lack spatial resolution or have difficulties in steep terrain. Oerlemans et al. (1998) noted that "combining high-resolution satellite imagery with digital terrain information and automated analyses [...] seems most promising" for the monitoring of glaciers. To observe long-term trends a combination of DEMs derived from historical and modern stereo-imagery is ideal.

British Antarctic Survey (BAS) and United States Geological Survey (USGS) hold large archives of historical aerial stereo-photography of Antarctica, collected since the 1920s, including the AP. The full potential of these historical datasets, spanning several decades, is not yet explored despite the need for observations. In combination with modern stereo-imagery this data can be used to close the inventory gaps discussed so far.

Fox and Czifersky (2008) used BAS archive data in combination with modern GPS (Global Positioning System) controlled aerial photography to successfully measure volume change for one glacier in the AP. The availability of ground control is, however, limited and overlapping modern aerial imagery is uncommon. One modern satellite sensor with high resolution stereo-imaging capability of the entire AP is the Advanced Spaceborne Thermal Emission Radiometer (ASTER). The sensor has been frequently used to map glacier change since 1999 (e.g. Bolch and Kamp, 2006; Kääb, 2007; Miller et al., 2009) and offers a spatial resolution of up to 15 m. ASTER data can be used for DEM generation and for comparison with the aforementioned historical data. Additional data from the IceBridge LVIS altimeter, the SPOT SPIRIT DEM or the recently released TanDEM-X can add further data.

However, the comparison of these datasets is not free of error. When combining data from different sensors the challenge is to deal with these multi-source, multi-temporal and multi-resolution datasets in a way that ensures reliable measurements. A specific problem are the historical aerial photographs of the AP. They were mainly flown for rapid mapping purposes and calibration or ground control point (GCP) information is often unavailable. Over several decades the paper prints have changed ownership and potentially degraded. Hence, the photogrammetric processing of this data is non-trivial. Uncertainties in elevation measurements will lead to decreased accuracy in the assessment of elevation change. The absolute accuracy of an ASTER DEM, without the use GCPs, is known to be around 20 m to 50 m, and deteriorating further over steep terrain (Fujisada et al., 2005), which will introduce further uncertainties to any comparison with historical datasets. The accuracy of topographic datasets is essential and existing offsets between DEMs need to be analyzed and removed before any change calculation is made. If not corrected this leads to biases in estimates of mass balance and its sea-level-equivalent (SLE).

Correction of these biases can be achieved by DEM co-registration. Conventional techniques utilize common GCPs to register one surface to another with acceptable results. Without the availability of ground control this traditional approach may be inapplicable and unconventional methods need to be applied. In particular in areas where

GCPs cannot be measured easily. One of these methods is called surface matching. The underlying idea is to register an uncontrolled surface to a reference surface, in this case a DEM, in a way that differences between them are minimized without the need for GCPs. Instead all points of the surface are used to achieve co-registration. Such an algorithm has been developed at Newcastle University by Buckley (2003) and Miller (2007). Although developed for coastal erosion studies, the algorithm has been shown to work in the context of glacier change estimation for a Svalbard test glacier (Miller et al., 2009). The scale-stability of ASTER DEMs appears to offer a solution for the registration of DEMs extracted from aerial imagery without the use of ground control and, at the same time, allow for historic ice volume change to be determined for the first time within that context (Miller et al., 2009). In the absence of ground control the registration is reliant on stable features which often coincide with the mountainous terrain. Thus, to enable the full potential of the technique and to make measurements over large areas, further development and analysis is needed, particularly on the DEM co-registration in areas with steep topography.

This brief overview has highlighted the existing research gap. Firstly, there is a lack of long-term glacier mass balance records for Antarctica. The AP is of particular interest due to high melting rates and rapid warming. A combination of historical and recent stereo-imagery can help to fill this lack of data. Secondly, there is a need to improve the accuracy of glacier mass balance estimates derived from an integration of multi-source, multi-temporal and multi-scale datasets. Answers to these problems are of interest to the communities within the field of glaciology, climate science, photogrammetry and remote sensing.

1.2 Aims and Objectives

The overall aim of this research is to *enable multi-decadal glacier volume change assessment in the Antarctic Peninsula from aerial archive stereo-imagery and modern satellite stereo-imagery*. This will go some way to closing the gap of long-term mass balance observations for the AP region. The main objectives are:

1. to provide an improved surface matching algorithm that is able to handle large datasets efficiently.
2. to investigate the accuracy and reliability of surface matching for glacier volume change studies in areas with steep topography.
3. to investigate the useability of DEMs derived from archive stereo-imagery and modern ASTER data for glacier change studies.
4. to apply the developed approach to study multi-decadal glacier mass change in the Antarctic Peninsula and to extend the number of records for the region.
5. to analyse past and predict future changes of glaciers in the Antarctic Peninsula with respect to climate and glaciology data.

From these formulated objectives further research questions arise which are related to the datasets that are used to achieve these objectives. Especially the accuracy, precision, reliability and combination of archive imagery and modern reference data is of interest here. They will be addressed in detail in Chapter 2, Section 2.3.

1.3 Thesis outline

In the following the chapters of this thesis are outlined briefly.

Chapter 1 has set the wider research context and identified research gaps. Aims and objectives of this work were defined here.

Chapter 2 explains the regional setting of this work in Antarctica and gives a general overview of glacier mass balance and existing measurement techniques. Previous work on AP glacier change assessment is summarised and discussed and a possible monitoring strategy for long-term glacier mass balance is outlined. This chapter provides the context needed to support objective five.

Chapter 3 describes the datasets that are used in this study and the data processing. The main focus is on DEM extraction from ASTER and USGS/BAS archive stereo-imagery. Methods and validation techniques that are used to achieve long-term glacier mass balance records for the AP are explained. Furthermore, the implementation and further

development of an existing surface matching software is explained in detail (objective one). The validation and evaluation of the surface matching algorithm is also described here (objective two).

Chapter 4 investigates the useability of DEMs derived from USGS/BAS archive stereo-imagery and modern ASTER data for glacier changes studies in areas with steep topography (objective two and three). The accuracy and reliability of surface matching for this application is discussed in here.

Chapter 5 contains the results from the measurement of glacier change and glacier mass balance for a total of 12 glaciers in the AP (objective four). A potential projection of the results to the whole AP region is shown.

Chapter 6 analyses the results from Chapter 5. Long-term glacier change in the AP is discussed together with a comparison to sea and air surface temperatures. Potential implications and future predictions are discussed (objective five).

Chapter 7 revisits the aims and objectives from chapter 1. A summary of major results and outcomes of the work is presented. Future research questions and are discussed here. Additionally, the wider use of the applied technique is discussed for other applications.

Chapter 2. Monitoring of Antarctic Peninsula Glacier Mass Balance

The previous chapter established the need and importance of long-term glacier mass balance observations. The World Glacier Monitoring Service (WGMS, 2013) was founded in 1986 to maintain and coordinate the systematic observation of glacier variations worldwide in a standardized way (UNEP-WGMS, 2008). All mass balance results for glaciers worldwide should be submitted online to the WGMS. A summary of these results is released every two years in the Glacier Mass Balance Bulletin (GMBB). The current GMBB (WGMS, 2011) reports data for only three glaciers in the AP. There have been various efforts over the last decade to extend these records, one of which is presented within this thesis. In the following a review of the literature on glacier mass balance measurements with focus on the Antarctic Peninsula is presented.

2.1 The Antarctic Peninsula

The Antarctic Peninsula is the most northerly part of Antarctica, located approximately between 55° to 76° west and 61° to 75° south. An overview map is given in Figure 2.1. It stretches approximately 1500 km from Ellsworth Land in the south towards the Drake passage in the north. The Weddell Sea lies to the east of the Peninsula, the Bellinghausen Sea to the west. Its geological formation is closely related to the Andes, both were formed in the Mesozoic period (Harrison et al., 1979). The terrain is highly mountainous with steep relief gradients (Figure 2.2). Elevations range from sea-level up to 2800 m for the highest peaks. For much of its length, elevations are above 2000 m but drop relatively quickly along the coastal fringes. The main land mass of the peninsula is

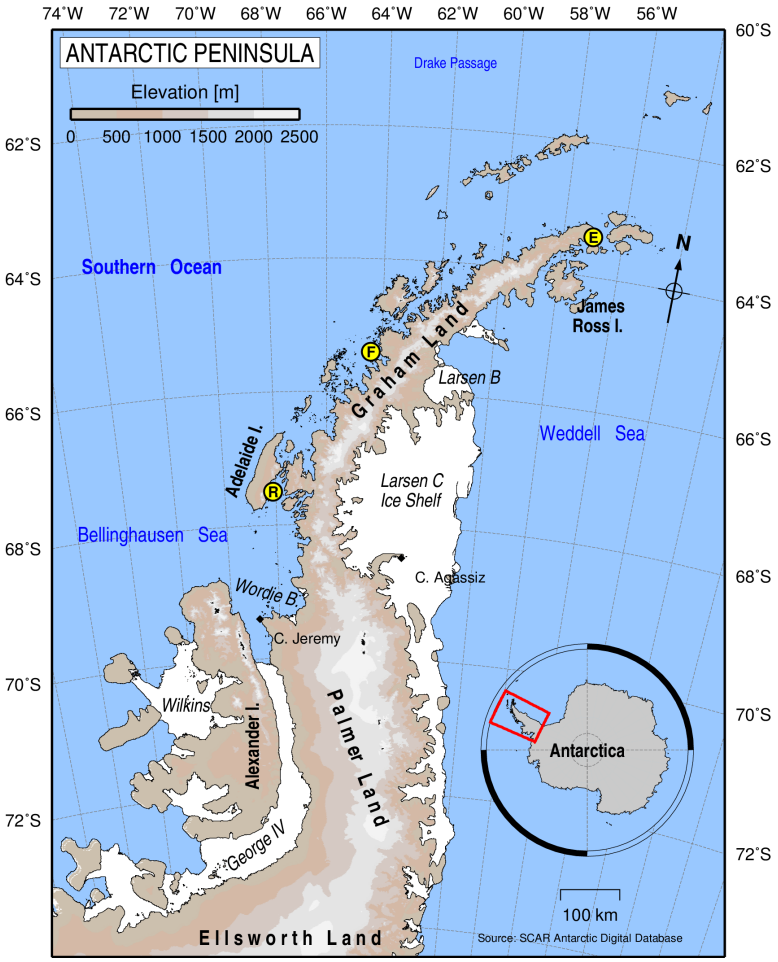

Figure 2.1: Overview map Antarctic Peninsula with long-term meteorological stations (R=Rothera, F=Faraday, E=Esperanza). Data source: SCAR (2013a).

surrounded by islands that are often connected via pack ice. The northern portion of the AP, called Graham Land, is more narrow (about half the width) than the southern portion, called Palmer Land. The line joining Cape Jeremy and Cape Agassiz is the notational division of the two regions. Major islands are Alexander Island in the south-western part of the Peninsula and James Ross Island in the north-western part.

Large ice-shelves (see Figure 2.1) are connected to the Peninsula. Major ice shelves are the Larsen Ice Shelf (an ice shelf that has undergone a considerable breakup in 2002), Wordie Ice Shelf (which broke up from the 1970s to 1990s), George IV Ice Shelf (connecting Alexander Island and Palmer Land) and the Wilkins Ice Shelf. The latter broke up in 2008. The peninsula is mostly covered by large ice caps and glaciers that flow from the mountains into the ice-shelves or the open ocean. According to the World Glacier Inventory (WGI) roughly 1000 glaciers are located on the AP (WGMS and NSDIC, 2012). Others sources (Vaughan, 2012, oral communication) state a number of

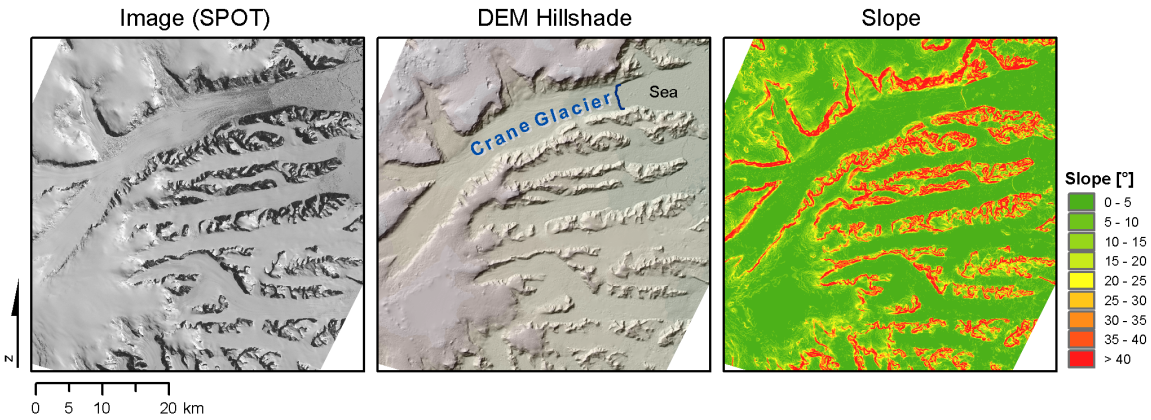

Figure 2.2: Typical mountainous terrain of the AP with marine-terminating glaciers. Data source: SPOT SPIRIT.

around 400 glaciers. One explanation for this rather large difference are challenges in the individual glacier delineation in the AP (Section 5.1.1). The majority of glaciers are fast-flowing mountain glaciers that are highly crevassed, especially in the western and northern AP. The total area of grounded ice is estimated at 120,000 km² of which 45,000 km² lie below 200 m a.s.l. (Vaughan, 2006). In the Antarctic winter (June to August) most of the land surface is covered by snow and the ocean is covered by sea ice. In the Antarctic summer (December to February) the ocean is usually free of thick sea ice making the area easier to access. The snow cover is reduced in the summer months.

Several research stations, i.e. Rothera (Britain), Palmer (USA), and O'Higgins (Chile), are located on the main part of the Peninsula and on smaller islands nearby. They are hubs for polar research and exploration of the Peninsula and the rest of Antarctica. Vegetation is sparse, and mostly occurs as mosses or grass. The AP is subject to glacial-isostatic adjustment (GIA) and therefore crustal uplift (Ivins et al., 2000). In recent years increased uplift rates have been observed, with some scientists (Thomas et al., 2011) suggesting this may be due to an increased surface mass loss of ice. However, recent findings (Nield et al., 2012) also show increased accumulation at higher elevations, which underpins the need for more complete mass balance records.

2.1.1 Climate

The AP has a moderate polar climate which is mainly influenced by the Southern Hemisphere westerlies and the Antarctic Circumpolar Current (ACC). The climate on

the western side is more maritime than on the eastern side. The mean surface air temperatures vary over the region with a north-easterly gradient. The most northern parts show annual mean temperatures between -2° to -5°C while the most southern parts exhibit mean temperatures below -15°C. In the summer months temperatures climb just above zero degrees, in rare cases up to +5°C, enabling the melting of snow and ice. This summer melt season is different to the rest of Antarctica. The AP is the wettest region of Antarctica with precipitation values ranging from 200 up to 2000 mm w.e./yr. Precipitation mostly occurs as snow. Highest values are found on the north-western slopes of the AP. The mean surface mass balance is estimated to be around +1.04 m w.e./yr, which corresponds to a net mass input of 280 Gt/yr over the AP (Turner et al., 2002; van Lipzig et al., 2004). Although the AP represents only 7 % of Antarctica's area, the AP receives about 25 % of the accumulation of the whole of Antarctica (Rignot and Thomas, 2002). About 80 % of the AP area north of 70° S is classified as a percolation zone[1] (Rau and Braun, 2002). The meltwater volume is around 59 Gt/yr and the number of melt days follows a north-easterly gradient. Average melt rates can reach up to 1000 mm w.e./yr in the most northern parts (Kuipers-Munneke et al., 2012). The spatial distribution of precipitation, temperatures and the wind field is influenced by the local topography and the mountain chain that divides the Peninsula into a western and eastern portion. The surface mass balance is locally influenced by snow drift. Often snow is removed at the peaks and transported to lower elevations or areas with diverging wind fields (van Lipzig et al., 2004).

Although long-term land surface temperature records[2] are rare, it has been shown that the climate in the Antarctic Peninsula has warmed significantly over the last 50 years (Morris and Vaughan, 2003; Vaughan et al., 2003) (see Figure 2.3 (a)), and to the greatest extent during winter periods. The region has warmed at a rate that is several times higher than the mean of global warming. Vaughan et al. (2003) observed a warming equivalent to +3.7 $\pm$ 1.6 ° C per century. In comparison, the global linear trend was +0.74 °C per century (1906-2005) according to the last IPCC report in 2007. The recent rapid regional warming of the AP region is believed to be driven by a combination

[1] Areas that are effected by melt events.
[2] Data available online (SCAR, 2013b)

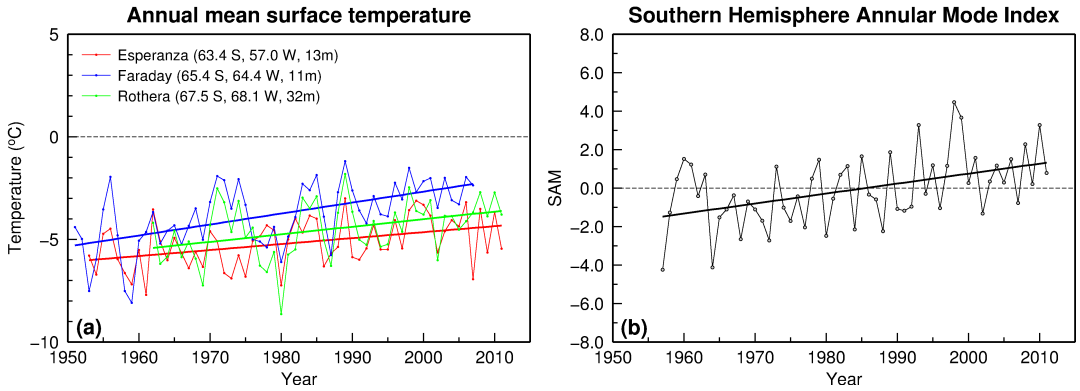

Figure 2.3: AP temperature trend (a) and SAM trend (b) (MET READER)

of changes in oceanic and atmospheric circulation as well as local greenhouse warming that is amplified by sea ice processes (Vaughan et al., 2003).

Causes and impacts of AP regional warming

Several studies have examined the effects of climate change on the AP, with particular focus on the western Antarctic Peninsula (WAP). For the WAP a climate transition from a cold-dry polar-type to a warm-humid sub-Antarctic type climate is observed (Smith et al., 1999; Montes-Hugo et al., 2009). There is evidence for a connection between the western AP and the tropical Pacific Ocean. Deep ocean water and surface temperatures in WAP have changed over recent decades, especially due to an increase in Circumpolar Deep Water temperature (CDW) and increased upwelling that leads to a reduction in sea ice extent (Martinson et al., 2008). A warming of more than 1 °C of the sea surface temperature was observed since 1955, especially in the upper 20 m of the ocean (Meredith and King, 2005). Temperature changes at depths of 100 m or more were found not to be significant (Meredith and King, 2005). Over recent decades the Southern Hemisphere Annular Mode (SAM)[3] index has increased (see Figure 2.3 (b)), leading to stronger westerly winds over the AP (Marshall, 2003; Marshall et al., 2006). As a result, the blocking effect of the AP is reduced and more air masses are transported eastwards over the mountains leading to Föhn[4] winds on the eastern side (Marshall et al., 2006). Furthermore, the increase in summer temperatures in the northern parts is related to a

[3]The SAM is commonly defined as the normalized difference in the zonal mean sea-level pressure between 40° S and 65° S

[4]A warm dry downslope wind which is produced by adiabatic warming (originally moist) air that is flowing over a mountain ridge.

positive SAM change (Marshall et al., 2006). A strong response exists between the El Niño / Southern Oscillation (ENSO) and the WAP oceanic and atmospheric temperatures (Tedesco and Monaghan, 2009; Shevenell et al., 2011). Lubin et al. (2008) also showed that surface air temperature anomalies are correlated with the occurrence of mesoscale cyclons and the SAM in a high index state.

These patterns of climate variability, such as ENSO or SAM, play an important role in the understanding of candidate mechanisms for the warming of the Peninsula. The SAM especially influences the local pressure/wind pattern and therefore the length of the sea-ice season and the transport of ocean heat towards the land. Despite the climatic change, no significant change in melt volume is observable, using regional climate models and satellite validation, for Antarctica since 1979, including the AP (Kuipers-Munneke et al., 2012). This could be explained by a relatively small increase in the summer temperatures during the melting season. As already noted, the recent warming is mostly attributed to an increase in the winter temperatures. However, the stations Esperanza and Faraday in the north-eastern AP show significant summer warming trends between 1965 to 2004, which would suggest increased melting. This discrepancy is explained by Kuipers-Munneke et al. (2012) as an underestimation of melt days from satellite-detected melt over mountainous terrain. In fact, the number of positive degree days (see Section 2.3.2) has significantly increased for the AP over the last decades. Thus, smaller mountain glaciers are likely to have increased melting potential.

It was shown that the sea-ice extent is negatively correlated with the temperatures in the WAP (Smith and Stammerjohn, 2001). The length of the sea-ice season has shortened over the continental shelf regions. With reduced sea-ice cover more heat transport from the open water is possible which influences the local air temperatures (Parkinson, 2002; Turner et al., 2005; Stammerjohn et al., 2008). The reduced sea-ice season also explains observations of higher summer surface salinity in the WAP region. During the sea-ice formation in the winter months fresh water is ‘removed’ from the ocean making it more saline. The rejected brine is equally mixed into the water layers during the winter. In the summer months, when the sea ice is melting, a stabilizing (less mixing) layer of fresh

water is added to the ocean surface. Reduced sea ice production during the winter will make the stable fresh water layer in the summer less effective and causes higher salinity (Meredith and King, 2005).

Along with the climatic change a shift in the ecosystems can be observed. Sea-ice dependent species are especially sensitive to a warming climate. With decreased sea-ice extents and warmer temperatures in the north those species are displaced farther south and eventually replaced by other species which are generally avoiding ice. The observation of penguin populations is a good indicator for such a transition and some species are already moving polewards (Smith et al., 1999). A decrease in chlorophyll content is observed in the north of WAP with an increase towards the pole. This has an impact on the distribution of krill from which larger animals such as fish, penguins or seals feed (Montes-Hugo et al., 2009). The availability of habitats for species that live in cold-dry climates will decrease further under the current conditions.

The loss of ice-shelves and shrinkage of ice-sheets and glaciers is the most noticeable impact of global and regional warming on the AP. Almost all major ice-shelves around the AP have lost substantial parts (Cook and Vaughan, 2010). The vast majority of glaciers have retreated and a speedup of glaciers is observed (Cook et al., 2005; Pritchard and Vaughan, 2007). As a result, ice mass loss contributes to a rising sea-level. Section 2.4 reviews the current knowledge of glacier, ice-sheet and ice-shelf mass changes in the AP in more detail. Before that glacier morphology and glacier mass balance are reviewed in a more general sense.

2.2 Glaciers

Glaciers are formed when snow accumulation exceeds ablation over the course of a year (Pellikka and Rees, 2010). Glaciers usually form in higher elevations which experience net accumulation (input or gains) and then flow towards lower areas with net ablation (output or losses). Accumulation and ablation can, however, take place over the whole length of a glacier. Given net accumulation at the end of a summer season, the snow will eventually densify into ice, depending on the temperature and density. If enough ice is

built up it will start to flow under its own weight due to increased gravitational stress[5] which causes a change in the shape of the ice, the so called strain[6]. The size and location of glaciers vary due to the processes of accumulation, ablation and ice flow and are highly dependent on the local climate and surrounding topography of each glacier (Benn and Evans, 1998). The topographic characteristics of a glacier change on very long time scales and are more important for glacier formation, while climatic changes occur in shorter time frames (months to years) and often have a higher influence on the dynamics of a glacier. The predominant climatic factors of glacier growth are snowfall and temperature. From a topographic perspective slope, aspect and elevation have greatest influence.

In general glaciers are broadly classified into (Benn and Evans, 1998):

- *Ice sheets and ice caps*: Unconstrained by the topography these are the largest glacier formations that submerge the landscape. Examples are the Antarctic and Greenland ice sheets or the ice caps of Svalbard. Also outlet glaciers fall into this category.
- *Glaciers constrained by topography*: The size of these glaciers is diverse but they have in common that their flow is dictated by topographic constraints. Examples are valley glaciers and ice fields.
- *Marine glaciers*: These are floating glaciers. Depending on the formation they are classified into glacier ice-shelves (free flotation of a glacier tongue) and sea-ice shelves (formed from frozen surface sea-water).

An exact differentiation of individual glaciers is difficult and the boundaries are often indistinct. This also explains why no exact number of glaciers worldwide actually exists. Although, it should be noted that, existing glacier inventories are becoming more complete due to international collaboration and combination of information from different sources (Cogley, 2009b). The Global Land Ice Measurement from Space (GLIMS, 2013) project provides a global dataset of glacier outlines (Arendt, 2012) and

[5]Measure of the internal force onto a deformable body as the result of external forces
[6]Measure of the amount of deformation that occurs as the result of stress

guidelines on how to derive glacier outlines from satellite imagery (Raup et al., 2007; Raup and Khalsa, 2010).

In the AP glaciers are mostly constrained by the steep topography and usually classified as mountain glaciers (Figure 2.2). From the ice cap along the central ridge of the AP, glaciers flow into the open ocean or surrounding ice shelves. The length of glaciers varies from a few kilometers up to tens of kilometers. Most glaciers, especially in the western AP, are not longer than 20 km. Larger glaciers with lengths of several tens of kilometer are found in the eastern side of the Peninsula, for example, Crane Glacier, Flask Glacier or Leppard Glacier. The ice shelves surrounding in the AP provide back stress and stabilize the glaciers (Angelis and Skvarca, 2003). Glaciers that extend into deep water are referred to as marine-terminating glaciers. Marine-terminating glaciers are very common in the AP. They can be differentiated into *tidewater glacier*, which are glaciers that terminate in the ocean but do not float, and *floating termini glaciers*, which are glaciers that have a floating extension. Tidewater glaciers are less sensitive to short-term climatic changes and often retreat and advance differently compared to land-terminating glaciers. Their behaviour is generally more complex because of the additional oceanographic forces (Pfeffer, 2003; Post et al., 2011).

The line at which a glacier leaves its bed and begins to float is the grounding line (GL). There are different GL definitions in the literature (Bindschadler et al., 2011) and its position can change over time. Mapping the GL is important for glacier mass balance calculations and for the understanding of ice-ocean interactions (e.g. Barrand et al., 2013). Assuming an average ice column density of 0.9, approximately 10 % of floating ice lies above the sea surface and 90 % beneath, when not constrained by sides and grounded ice upstream. Thus, the contribution of ice-shelves and free-floating glaciers to sea-level is only small. The loss of grounded ice that is more noticeable (Shepherd and Wingham, 2007). Without knowledge of the grounding line or the glacier bed, measurement of glacier-wide mass changes can be biased. The Antarctic ice grounding line was mapped by Scambos et al. (2007) using a MODIS-based mosaic of Antarctica (MOA), by Rignot et al. (2011a) using satellite radar interferometry and by Bindschadler et al. (2011) using satellite imagery and laser altimetry.

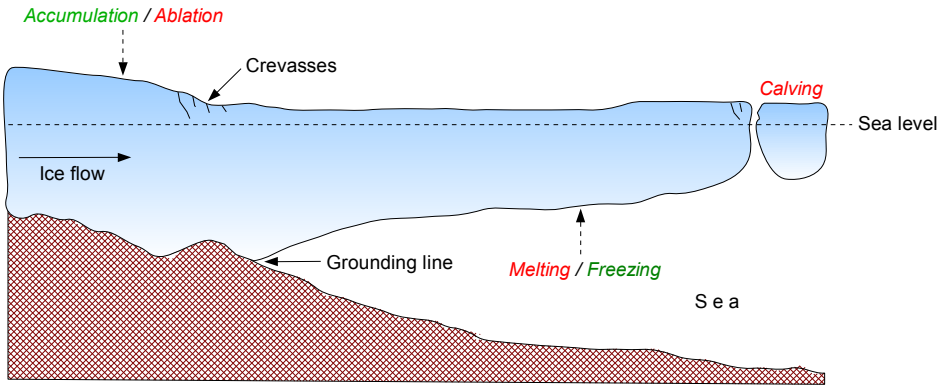

Figure 2.4: Schematic profile of a marine-terminating glacier front (system inputs shown in green, outputs shown in red). The grounding line is generally defined to where the glaciers begins to float and leaves its bed.

2.2.1 Glacier mass balance

A glacier system is in balance, or dynamic equilibrium, when the input rates equal the output rates. The location at which the accumulation zone and ablation zone can be separated is the equilibrium line altitude (ELA), that is, where annual accumulation and ablation are equal. The position of the ELA is not always uniform over a glacier due to topographic and climatic variations, especially with respect to the precipitation of snow. The ELA on the western side of the AP is often stated to be below 100 m or close to sea level (Ingolfsson et al., 1992; Hjort et al., 1997). On this side higher precipitation values are found and thus more accumulation of snow. For the nothern and western parts of James Ross Island, which lie in the precipitation shadow of the AP mountain rage, the ELA mostly lies above 400 m (Hjort et al., 1997), while the southern and eastern parts of James Ross Island actually exhibit a lower ELA due to increased snow input from the south (Smellie et al., 2008).

The difference between the gains and losses of mass of a glacier, or part of a glacier, over a given period of time is called the mass balance (MB). This time period is normally one year, though the definition of a year can vary depending on the method of measurement (Cogley et al., 2011). This so called annual mass balance is always related to a defined volume but specification is needed whether this volume refers to the whole glacier system (*glacier-wide mass balance*) or glacier part (*specific mass balance*). The mass balance itself can be quantified in different units. The common unit is the meter water

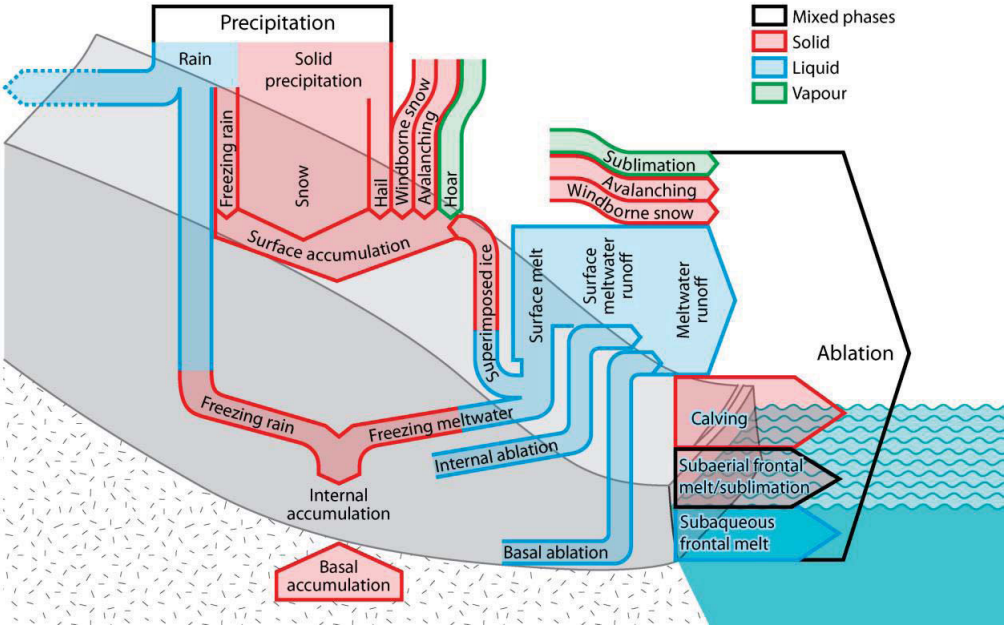

Figure 2.5: Glacier mass balance components (Figure 2 from Cogley et al., 2011)

equivalent (m w.e.) which is defined as:

$$1 \text{ m w.e.} = 1000 \text{ kg m}^{-2}/\rho_w \tag{2.1}$$

where ρ_w is the density of water with 1000 kg/m^3 . When the change is measured over ice or firn, different densities apply. Here an ice density ρ_{ice} of 917 kg/m^3 is assumed. Another MB unit is the gigatonne (Gt; 1 Gt = 10^{12} kg). There are different mass balance terms found in the literature and care needs to be taken when describing glacier mass balance changes. A useful summary and overview is given by Cogley et al. (2011). The mass balance can be converted into a sea-level-equivalent by multiplying the mass balance (kg/m^2) with the observed area of a glacier (m^2) and then dividing it by the product of density ρ_w and the area of the global ocean (362.5 x 10^{12} m^2). The unit is m but usually the SLE is stated in mm. An eustatic sea-level rise of 1 mm is equivalent to 360 Gt of ice (Shepherd and Wingham, 2007).

Figure 2.5 shows the various components of glacier mass balance. Some components are more relevant, i.e. snow fall or surface meltwater runoff, than others, i.e. hoar. It is beyond the scope of this thesis to explain all elements of glacier mass balance in detail. The gains or losses of glacier mass may balance out over the several years and no long-term mass balance change would be observed although inter-annual changes may

have been significant. However, with changing climate conditions this becomes unlikely. Because of the strong glacier-climate response the mass balance will not stay in an equilibrium state.

2.3 Mass balance monitoring techniques

The mass balance determination for a whole glacier is not trivial. Often measurements for parts of a glacier are interpolated or extrapolated to get a result for the entire glacier but this can introduce errors, especially when the glacier characteristics change with distance from each measurement (Berthier et al., 2010). To measure the glacier-wide mass balance everything that goes into the system and that goes out of the system needs to be accounted. In practice this is often impossible due to an inaccessibility for direct measurements or other unknown variables of a glacier i.e. the glacier bed topography, ice density or accumulation and ablation rates. In general the following techniques of mass balance determination can be differentiated (Benn and Evans, 1998; Kaser et al., 2003; Pellikka and Rees, 2010).

2.3.1 Direct methods

The direct method, also called the glaciological method, uses ground-based measurements. Usually measurements are collected for a large number of sample spots over a glacier to get a large sampling number and to account for variations in snowfall or the influence of varying topography. The measurement of accumulation or ablation is often done using stakes that are fixed into the ice. Additionally pits can be excavated to extract snow and ice cores. Such cores allow the determination of changes in density for different snow layers and can give an indication of the snowfall at the location. Because measurements are point-based it is important to obtain a large number of measurements. This can be difficult because glaciers are often located in extreme and dangerous environments. Worldwide only a few glaciers have long-term (more than 30 years) mass balance records from direct measurements. Examples can be found for Storglaciären in Sweden (Holmlund, 1987) and Storbreen in Norway (Ohmura et al., 2007).

2.3.2 Hydrological methods and climatic calculations

The hydrological method measures the water balance of a glacier catchment by determing the net balance (B_n) of precipitation (P), run-off (R) and evaporation (E). This can be expressed as:

$$B_n = P - R - E \tag{2.2}$$

Occasionally an additional positive term of horizontal advection, e.g. from snow drift, is added. The equation above presumes no calving, which would be an additional negative term. An advantage of this technique is that it delivers information about the glacier hydrology, e.g. how much water has gone into the system and how much went out of it. A problem of this method is the exact quantification and measurement of each component. If one wants to calculate the annual balance the components must be measured for the entire basin and many meteorological stations are needed. Undersampling is a problem and interpolation is needed to integrate for an entire glacier.

If enough meteorological data, e.g. precipitation, radiation fluxes, temperatures, etc., are available the energy balance[7] might be calculated or estimated. In cases where only data for the air temperature is available, which is relatively often the case, the annual mean temperature might be used to make assumptions about the available energy and conditions for melting or freezing (Hock, 2005). However, the annual mean temperature is not a direct indicator for the degree of glaciation as it does not give information about snowfall or precipitation. More advanced is the *positive degree-days* (PDD) method, that derives the sum of all positive temperatures at the same place over a given number of days (Braithwaite, 1984). Using PDD, melting rates for these days can be approximated and applied to other locations. Glaciers at maritime locations generally have a higher melt rate per PDD because of the higher humidity and wind speeds that enables more transfer of latent and sensible heat (Benn and Evans, 1998; DeWoul and Hock, 2005). In general ice and snow melt at 0°C, but this does not necessarily mean that melting will occur with an air temperature ≥ 0°C. Glacier melting is determined by the energy

[7] Change of amount of energy that is stored within a defined volume caused by fluxes of energy across the volume boundaries.

balance at the glacier surface, where air temperature is only one factor among many (Hock, 2005).

2.3.3 Dynamic (velocity, flux) method

Here the mass balance is approximated from a cross section of a glacier at the ELA together with an average velocity over that cross section. This approach is relatively simplistic but can be applied to estimate the mass balance of large glaciers. The difficulty is to measure the actual cross section, i.e. glacier depth, and to find the mean velocity. Cross sections can be measured with ground penetrating radar. The velocity is more difficult to measure and is different for each section of a glacier. The flow speed is highest at the surface and central line of flow. It decreases, both laterally and vertically, towards the bed. Feature tracking from remote sensing imagery is often used to calculate the flow speed at the glacier surface.

2.3.4 Geodetic methods

Using geodetic methods, changes of glacier volumes are commonly measured from maps or elevation models. By differencing two elevation models from different time steps together with a known density the mass balance can be calculated. Remote sensing offers a variety of techniques (explained below) that allow the extraction of such elevation profiles or models. Gravimetric measurements are different to that but can be equally counted as geodetic techniques. The photogrammetric method is decribed in more detail because DEMs in this work will be mainly derived from stereo-photogrammetry. The advantage of remote sensing methods is that the measurements can be made over a large area and therefore less interpolation is needed. Also repeated measurements are easier to make and have fewer problems due to inaccessibility. Furthermore, objects can be mapped in different wavelengths of the electromagnetic spectrum, thus allowing for the penetration of ice or snow to measure the surface beneath the ice. The determination of exact elevation values and densities are limiting factors for this technique. A combination of remote sensing with ground-based measurements is ideal.

Airborne and satellite stereo-photogrammetry

For many years stereo-photogrammetry was the main source for the production of surface elevation information from either analogue or digital instruments (McGlone et al., 2004; Kraus, 2007). Here the stereo-imaging case is described. The core principle is *triangulation*, the process of determining the location of a point by measuring angles between two known points at either end of a fixed baseline and an unknown point at which the line between the points intersect (Figure 2.7a). Knowing the baseline length B and the two angles, the distance H to the observed point P can be calculated. These measurements can be made with total stations, aerial photography, satellite imagery or other sensors. The mathematical concept is based on collinearity, that is, the image point P', the camera center O and the point of interest P form a straight line (see Figure 2.6; Kraus, 2007). The information is then extracted by the mathematical reconstruction of photogrammetric situation at the moment of image acquisition. An image represents the three-dimensional real world in two dimensions and at a different scale. Therefore different sets of coordinates need to be adopted and solved. This involves several variables that are either known or unknown (meaning they need to be determined).

Often some quantity of parameters from interior, relative or absolute orientation are unknown. The unknown quantities that are generally of greatest interest are the object coordinates. The reconstruction involves generally two steps, *interior orientation*, and *exterior orientation*. The exterior orientation can be further split into two steps, *relative orientation* and *absolute orientation*. Each orientation step requires homologue points. To solve the collinearity equation in the absence of parameter information and to model eventual deviations from it, it is important to achieve redundant measurements. In digital photogrammetric workstations (DPWs) image matching techniques are used to find corresponding points that are needed for the interior, relative and absolute orientation (Heipke, 1997) and subsequent outputs such as DEMs.

At first the interior orientation of each image is solved. It describes the orientation of the image plane to the centre of projection. The image coordinates are transformed into a

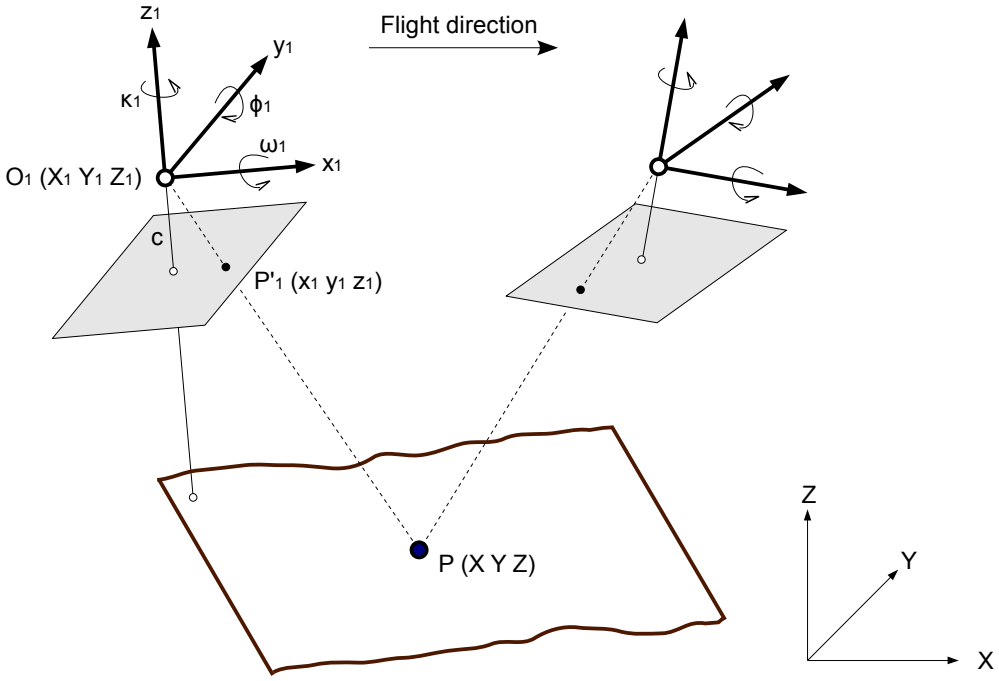

Figure 2.6: Principle of stereo-photogrammetry DEM generation. The core principle is triangulation between three points of which two have known coordinates.

local instrument system (with known geometry) by using fiducial marks[8] and an affine[9] transformation. The instrument system originates at the centre of the lens and the image is assumed to be perpendicular to the lens axis. The distance between the image centre and the lens centre is the focal length, c. The point at which the lens axis and the image intersect is the so called principle point. Usually this point is very close to the actual image centre. Knowing the principle point and focal length is crucial to solve the interior orientation. In most cases camera calibration protocols provide this information about fiducial marks, the camera focal length, lens distortion and other parameters depending on the camera type. When analogue images are processed, film distortions can emerge from degradation or incorrect storage. These need to be considered and corrected in the interior orientation, where possible. If uncorrected they introduce further errors that will lead to inaccurate measurements.

The next step is the relative orientation that reconstructs the position of two (or more) images relative to each other so the instrument system and object coordinate system can be related. It is based on the coplanarity condition, that is, the object point, projection

[8] points of reference with known instrument coordinates
[9] A transformation that preserves straight lines and ratios between points lying on a straight line

centre and image points need to form a plane. In the *normal case* of photogrammetry the base length is known and the camera axes are perpendicular to the base and parallel to one another, meaning the instrument system is parallel to the object coordinate system (Kraus, 2007). However, in reality there are slight deviations from that case. To solve for relative orientation the position of the projection centre and the rotation of the instrument need to be known . On modern sensors a GPS and an IMU (inertial measurement unit) are installed to allow the direct measurement of the relative orientation parameters at the moment of image acquisition. If not available it can be reconstructed using tie points between corresponding images. A successful relative orientation allows the intersection and resection of object points and therefore 3-dimensional measurements, in an local coordinate system.

The final step is the absolute orientation which transfers the local coordinate system into a global coordinate system. This is usually done using an 3-dimensional conformal[10] transformation (see Section 3.4.2). Often the relative and absolute orientation are solved simultaneously using bundle block adjustment (Kraus, 2007). For the orientation parameters only a few, usually well defined, points are needed. Once an image block is adjusted and the orientation parameters are known, surface elevations can be computed for each corresponding point in the overlapping images. In airborne photogrammetry images are usually taken with 60 % horizontal and 20 % lateral overlap, to ensure redundant measurements of points. When points can be measured in more than two images the solutions becomes more robust. Theoretically for each pixel an accurate position and elevation can be computed. In practice, however, this is not always possible. A perfect image orientation or bundle block adjustment does not automatically guarantee a complete and accurate DEM. For example, the image matching may fail or be false when searching for corresponding points in image parts with low contrast, e.g. clouds, water, or ice. This explains why raster based DEMs often contain blunders. Another explanation for erroneous point measurements is that the orientation was false or did not account for systematic effects, i.e. in the interior orientation. Most DPWs allow to store

[10] A transformation that preserves angles.

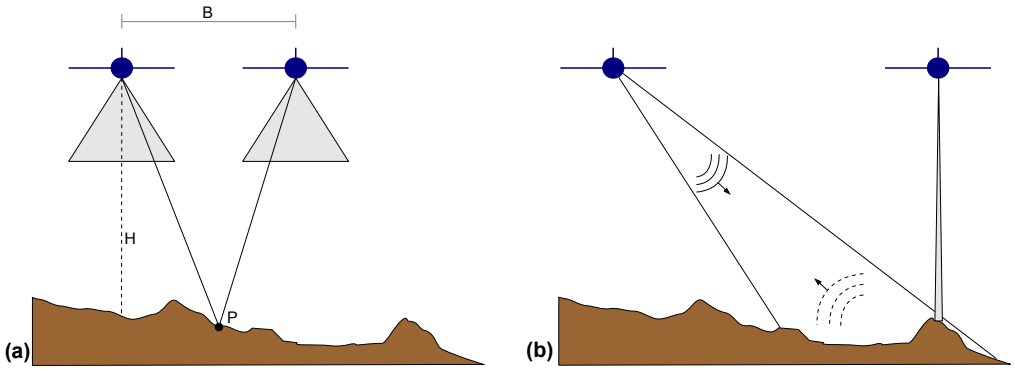

Figure 2.7: Viewing geometry of stereo-photogrammetry (a) and side-looking radar and altimetry (b)

DEMs as Triangulated Irregular Network (TIN[11]) so that only points with high confidence are kept. Grid sampling over textureless areas is not recommended because it often results in oversampling and erroneous height information (Fox and Nuttall, 1997). For a more complete introduction to stereo-photogrammetry and DEM generation the reader may refer to McGlone et al. (2004), Kraus (2007), Fryer et al. (2007) or Wolf and DeWitt (2000).

The principles decribed above apply to terrestrial, aerial or satellite stereo-imaging. A wide variety of terrestrial, airborne and spaceborne sensors that allow photogrammetric measurements, i.e. DEM extraction, exists and large archives of data are available. One of the first examples of analogue stereo-imaging from space are the Corona satellites from the late 1950s. Since then the development of high resolution stereo-imaging has advanced noticeably and today several satellite systems offer digital stereo-imaging functionality, e.g. IKONOS, SPOT and ASTER. Given that sensors have changed over time, their integration is one of the biggest challenges. Stereo-photogrammetry is one of the best tools for the supply of 3D data for use in glaciological applications. Analogue photography has been widely replaced by digital sensors but the photogrammetric principles remain the same.

[11] A vector based data representation which stores points (x,y,z) as nodes and connecting lines in a form of non-overlapping triangles.

GNSS

Global Navigation Satellite Systems (GNSS) are used to determine point elevation and velocity information down to mm level from space (Groves, 2008). GNSS systems are based on a *trilateration* process. The position of a point is calculated by measuring the distances between the unknown point and at least three known points (geometry of triangles). There are several GNSS systems available, e.g. the Global Positioning System (GPS) which is operated by the United States, the Galileo system of the European Union, and the GLONASS system which is operated by Russia. The widely-used GPS constellation consists of 24 satellites which transmit a carrier signals in the L band (L1 and L2) of the electromagnetic spectrum. The signal code[12] contains the transmission time, the orbit information and the satellite status. The receiver computes the distance to the satellite (sender) by measuring the time it took the signal to travel between the two. The time needs to be measured very precisely (within nanoseconds; Allan and Weiss, 1980). This time difference is measured by syncronising[13] a code that is identical in the satellite and the receiver. All GNSS signals are influenced (delayed) by the atmosphere, especially the ionosphere. Additional error sources are clock errors, imprecise orbits, or multi-path errors. Consumer-grade (satnav, handheld systems) receivers, which use the C/A-code, are accurate to the m level. This is because the more accurate P-code is encrypted and not available for the public.

However, for many applications higher accuracy is needed, e.g. for ground control point measurement, velocity or tidal measurements of ice sheets and glaciers. To achieve this differential GPS (DGPS) can be applied. DGPS deploys a second GPS receiver over a known position (reference station) in proximity to the (moving) receiver at an unknown location. The GPS error for the reference station and secondary receiver is assumed to be similar (within < 200 km). Since the position of the reference station is known, the timing error can be corrected for the (moving) receiver to achieve the desired accuracy.

[12] The signal code (also called pseudo-random code) is subdivided in a C/A and P code depending on the complexity. The less complex C/A code is the base for civil GPS receivers, while the complex P code is used for precise point positioning. The code is modulated onto the signal using phase modulation.

[13] Synchronization is achieved by delaying one signal with respect to another until they are in syncronised.

For long-term measurements, GNSS receivers are often left in the field. This can be problematic with regards to energy supply and rough weather conditions. An overview of the accuracy of GPS in glaciological applications is given in King (2004). Khan et al. (2010) used GNSS to measure crustal uplift in Greenland and infer glacial mass loss. Although GNSS can offer very high resolution it has a major drawback in regions that are generally inaccessible such as the AP. GNSS is best used in combination with other measurements and methods. Rivera et al. (2005) combined remote sensing data, aerial photography and GNSS data to measure the glacier mass balance for a glacier in Southern Patagonia. However, there is almost no data available in the AP for the registration of airborne or spaceborne stereo-imagery.

Radar

Radar is an active remote sensing technique where short pulses of radio-wavelength beams, in the range of 1 cm to 20 m, are emitted from an antenna mounted on a satellite or an aircraft. When these beams are reflected by an object the receiver can measure the distance (range) to that object by measuring the time it took the pulse to return to the sensor. In most radar systems, the receiver and transmitter are co-located, using one antenna, with an electronic switch to change the mode of the antenna. The principle of radar is based on the relation between speed (of light), distance and time (Lillesand et al., 2004). Radar signals reflect or penetrate objects depending on the emitted wavelength and the object's physical properties. The strength of the reflected signal is very dependent on the object that is observed and the radar wavelength employed. Objects smaller than the wavelength, e.g. water vapor or the upper layer of snow, are transparent to radar beams (Pellikka and Rees, 2010). The biggest advantage of this technique is that measurements from space are less sensitive to atmospheric (cloud) conditions and, as an active technique radar can be used day and night. With shorter wavelengths, radar can be made sensitive to water vapour which makes it suitable for monitor water content of the atmosphere and weather forecasting. With suitably long wavelengths, a glacier surface can be completely penetrated and the glacier bed can be mapped, for example using ground based radar systems (Fretwell et al., 2013). With shorter wavelengths internal

Band name	Frequency range [MHz]	Wavelength range [cm]	Common use
VHF	30-300	100-1000	Ground penetrating radar
L	2000-1000	15-30	GPS
C	8000-4000	3.75-7.5	Weather radar
X	12500-8000	2.4-3.75	Earth observation, mapping

Table 2.1: Typical radar frequency bands and their application

layers of glaciers and snow can be observed (Rau and Braun, 2002). Radar systems are used ground-based, airborne or spaceborne. The wavelength is usually fixed depending on the application (Table 2.1).

The spatial resolution of a radar image is dependent on the emitted wavelength, the antenna length and the beamwidth (Lillesand et al., 2004). To get a high resolution without changing the wavelength, antennas need to be sufficiently long. In practice this can be achieved by moving a smaller antenna along-track and combining several transmit/receive cycles into one simulated larger antenna. This technique is called Synthetic Aperture Radar (SAR) and has been used in many glaciological applications (e.g. Rignot et al., 2001a, 2008; Strozzi and Mool, 2012; Rignot et al., 2011b). The imaging geometry is different to conventional airborne photogrammetry (Figure 2.7b) as a radar effectively measures distances and not angles.

By using images from different viewing angles or positions, DEMs can be extracted from radar. This is accomplished either by using overlapping images (using stereo-photogrammetry) or by using the phase information of the radar beam. The latter is known as Interferometric SAR (InSAR). This technique calculates phase shifts in the radar signals (for each corresponding pixel) from an object that is observed from two different positions in space. This is either achieved by using repeated images from one sensor or a twin-satellite arrangement. Assuming the object has not moved, a shift in the phase is observed because of the different times it takes the signals to get back to the moving sensor. The baseline between the sensor positions and the phase shifts can be calculated very precisely and, thus, allows measurements of elevations at the sub-cm level. An interferogram is the visualization of the phase differences and has a fringe pattern. These fringes represent the differences in surface height and sensor position. When the sensor signal is removed, a DEM can be generated. When the underlying

topography of a radar image is already known, differential interferometry can be applied. This allows the measurement of elevation changes and shifts (flow) over time and applies the same principles as before but includes removing the underlying topography from the signal. A wider introduction and overview can be found in Lillesand et al. (2004); Massonnet and Feigl (1998) and Pellikka and Rees (2010).

Various SAR sensors exist and they are commonly used to extract elevation information. The Space Shuttle Topography Mission (SRTM) mapped the Earth's surface, using X- and C-band radar, between 56° S and 60° N with a resolution of 90 m in 2000 (Farr et al., 2007), excluding the polar regions. In 2011 TanDEM-X (TerraSAR-X add-on for Digital Elevation Measurements) was launched into space to generate a first global DEM, using two TerraSAR-X satellites, at a resolution of up to 6 m by using SAR single-pass interferometry. The so called WorldDEM is expected to be available in 2014 (ASTRIUM, 2013). The two identical satellites operate in a so called HELIX formation, in which the satellites operate in slightly different orbits (Krieger et al., 2007). Other radar satellites that have been used in glaciological application and for DEM generation are ERS, PALSAR and RadarSat. It can be said, that SAR/InSAR is a well established technique which offers similar possibilities compared photogrammetry. However, most satellites with SAR capabilities were launched in the late 1990s which means they do not provide long-term records. Compared to DEMs from spaceborne stereo-imaging, InSAR DEMs provide similar spatial resolutions. Though, over steep terrain the use of radar can be problematic because of non-returning signals and radar shadow. One advantage of photogrammetry over radar is the use of wavelengths in the visible spectrum and the near-infrared. This is particularly useful for glacier mapping glacier and visual interpretation. The combination of DEMs and imagery derived from InSAR and stereo-photogrammetry offers a strong potential.

Altimetry/Lidar

Altimeters are active sensors sending radiation pulses at a specific wavelength and frequency, e.g. radio or light waves, and measure the time it takes the signal to return to the sensor after it is reflected from the ground. In principle this is identical to InSAR but

altimetry sensors produce individual point measurements along track, rather then continuous measurements of elevation over an area. The sensor is usually pointing directly downwards and creates a certain footprint size on the object surface. The sensor then determines the height of the sensor above the surface (range to the target) allowing the ground elevation to be estimated for the observed footprint, depending on the penetration of the surface. For this, the absolute position of the sensor needs to be known. The footprint size effectively determines the spatial resolution. The combination of multiple tracks of altimetry allows the extraction of continuous surface elevations, using interpolation. This is, however, problematic if a change in elevation has occurred between the individual measurements. On the other hand it allows change measurements to be made for repeated tracks. Examples of altimetry sensors are CryoSat and SeaSat.

CryoSat, an interferometric satellite radar altimeter, was developed by ESA to monitor the cryosphere. The first satellite was lost during launch in 2005. In 2010 CyroSat-II was successfully launched and successfully studied sea ice thickness and fluctuations at a spatial resolution of 250 m. The ESA satellites ERS-1 (1991-2000), ERS-2 (1995-2011), and Envisat (since 2002) also carry altimeters onboard. These have been successfully used in various science projects including studies of ice sheet topography and mass balance of the Antarctic continent (Remy and Parouty, 2009) at medium spatial resolution. A problem of altimetry measurements from space is the relatively large footprint which can be problematic over steep terrain as it is common in the AP (Griggs and Bamber, 2009; Shepherd et al., 2012).

Lidar sensors, also referred to laser scanners, actively transmit short pulses of electromagnetic radiation (EMR), usually in the near-infrared region, measuring the range to the observed object. They produce direct 3-dimensional point measurements (point clouds) at very high spatial resolutions. Terrestrial and airborne lidar systems exist and are widely used in earth sciences and engineering to create 3D surface models. Modern laser scanners transmit up to hundreds of thousands of pulses per second. These pulses are scanned across-track using technology such as oscillating mirrors. Modern airborne sensors can achieve accuracies up to the cm level, whereas terrestrial laser scanners can be accurate to the mm level. Because of the large number of measurements,

datasets are usually very large. Lidar campaigns over Antarctica are very rare but if flown they offer very high resolution and accurate measurements.

There are spaceborne laser altimetry systems. The Geoscience Laser Altimetry System (GLAS) onboard the NASA Ice, Cloud, and land Elevation Satellite (ICESat) operated three laser altimeters to measure ice sheet mass balance, cloud and aerosol heights, as well as the land surface topography and vegetation (Schutz et al., 2005; Abdalati et al., 2010). The ground spacing is roughly 172 m and the laser spot diameter on the ground 70 m. ICESat was launched in 2003 and operated successfully until 2009. To fill the gap in observations until ICESat-II is launched in 2016, NASA initiated an airborne program called Operation IceBridge that maps ice sheet elevations over Antarctica, the Arctic, and Greenland. IceBridge campaigns have been flown regularly since 2009 and data is collected using several sensors, including laser altimeters.

Gravimetry

Ice mass changes can also be determined by measuring the gravity field of the earth. Gravity measurements are different from other geodetic methods that generally quantify changes in elevation as described in the above sections. Under the assumption that the gravity field changes when mass is transferred away or towards a location of the earth the respective mass change can be measured as a signal in the gravity field. The NASA Gravity Recovery and Climate Experiment (GRACE), launched in 2002, consists of two satellites in a near polar orbit (~500 km) that follow each other at a distance of about 220 km. The satellites are either pulled apart or together when the gravity field beneath them changes. This difference in the distance between the sensors can be measured very precisely by using the microwave ranging system and non-gravitational forces removed through accelerometer measurements (Tapley et al., 2004). GRACE can measure the earth mass field and mass changes at spatial resolutions at about 400 km, with a repeat period of 10 to 30 days. Wouters et al. (2013) used GRACE data to measure the ice sheet mass balance in Antarctica and Greenland between 2003 to 2012. Over this period they observed a significant mass loss of 249 $\pm$ 20 Gt/yr for the Greenland ice sheet and 112 $\pm$ 23 Gt/yr over Antarctica. For the glaciers in the Gulf of Alaska, GRACE data was

successfully used to determine mass balance changes between 2003 and 2007 (Luthcke et al., 2008; Arendt et al., 2008). The relatively low resolution of 300 to 500 km, however, limits the application for measurements on a small-scale glacier level.

2.3.5 Comparison of geodetic techniques

In summary, a wide range of glacier mass balance measurement techniques exist of which all have their advantages and disadvantages (Table 2.2). The relative accuracy of each technique is crucial. If different methods are applied rigorously on the same glacier similar results of mass balance can be measured. Cox and March (2004) compared the mass balance derived from a geodetic method, using aerial imagery, and the glaciological method outlined above, using stake measurements. They found the differences to be <6 %. They note that this level of agreement may only be achieved when no systematic error is evident and the aerial imagery offers good contrast for photogrammetric processing. Cogley (2009a) noted direct measurements are nearly all annual, whereas geodetic measurements are mostly multi-annual. The differences between techniques are not completely resolved yet, mainly because of errors within each method. For that reason, it is important to assess the uncertainties (see Section 3.3) of each measurement method (Rolstad et al., 2009) and consider the potential systematic errors present in generated techniques. The comparison of DEMs derived from radar and lidar for instance is not always straight forward given potential penetration issues.

A comparison between each technique is therefore not always straightforward. For the task of long-term glacier mass balance studies in the AP, a combination of DEMs derived from stereo-photogrammetry is ideal. The key benefits are:

- There is a large number of stereo-images available for the AP, which date back as far as the 1940s
- Photogrammetry is a well-established technique that works for a variety of sensors with stereo-imaging capabilities
- The achievable spatial resolution is similar or better compared to many radar or altimetry instruments

Technique	Advantages/ Benefits	Drawbacks/ Limitations	Examples for use in Antarctica
Photo-grammetry	+ large historical archives + high coverage of the AP + well established technique + high resolution	+ image matching may fail + passive technique (day time operation)	Fox and Cziferský (2008)
SAR/InSAR	+ all-time/weather operation + surface penetration + similar to stereo-photogrammetry	+ complex processing + only for last two decades + surface penetration + radar shadow	Rignot et al. (2001b) Rignot et al. (2004) Rignot et al. (2008)
Radar altimetry	+ high spatial resolution when from airborne sensors	+ repeated measurements needed for complete coverage + high resolution relatively rare on the AP	Thomas et al. (2004) Griggs and Bamber (2009)
Laser altimetry	+ high spatial resolution	+ relatively large spacing between footprints + repeated measurements or interpolation needed for complete coverage + no long-term records	Rott et al. (2011) Shuman et al. (2011)
Lidar	+ high accuracy and spatial resolution + active technique	+ expensive and rare on the AP	Wendt et al. (2010)
Gravimetry	+ complete coverage of the AP + direct measurement of mass balance	+ low spatial resolution + only for last decade	Velicogna (2009) Velicogna and Wahr (2013)
Direct	+ long-term records	+ rare in the AP + extensive and complex over large areas + undersampling	Smith et al. (1998)

Table 2.2: Advantages and disadvantages of geodetic and direct mass balance monitoring techniques in relation to the AP

- Photogrammetry is a remote sensing technique and as such allows to map inaccessible regions
- Images are acquired in the visible and near-infrared spectrum which is useful for glacier mapping

2.4 Previous glacier change studies in the Antarctic Peninsula

In general, in-situ observations of glacier mass balance in the AP are rare and climate data is only available for discrete points with wide geographical spread. A first detailed map of the net surface mass balance by combining meteorological (gauges, stakes) and glaciological (ice core and snow pits) in-situ measurements was produced by Turner et al. (2002). At locations with sparse or no data, the mass balance was estimated from a linear relationship between orography and existing mass balance measurements elsewhere. Separate relationships were used for the eastern side, which has a more continental climate, and the western side of the AP. It was found that the largest values of mass balance are found in the northern part of the AP along the spine with over 2.5 m/yr. Very low values were measured to the north-east of Rothera station. The contributing measurements at the individual locations were taken at different times and, thus, do not necessarily represent the mean.

An example where temperature records and ice surface elevation have been mapped in conjunction is the ice ramp at Rothera Point. Here a single line along the ramp has been mapped using optical tacheometry and GPS over recent years. Between 1989 and 1997 a mean surface lowering rate of ~0.32 m w.e./yr has been observed (Smith et al., 1998). The rate of surface lowering showed correspondence with the number of positive degree days that have been calculated from temperature records. The observed negative mass balance at the Rothera ice ramp is mostly related to climatic changes and not ice flow (Smith et al., 1998). However, the ice ramp is only a small ice body and not necessarily an indicator for all glaciers in the region.

There are several studies that use remote sensing to cover larger areas. However, these mostly map the spatial extent of glaciers and ice shelves rather than volumetric changes

of the grounded ice. Cook et al. (2005) mapped glacier frontal changes for 244 glaciers in the AP using historical and modern remote sensing imagery. It was found that 87 % of the observed glaciers have retreated in the period between 1940 to 2004 and that the retreat first started in the northern parts and then migrated further south. Until the 1950s more glaciers advanced than retreated. After that time, retreat became the dominant signal and was greatest in the period after 2000. This is in general agreement with climatic observations. Rau et al. (2004) mapped glacier frontal position for six regions across the AP between 1986 and 2002 using ASTER and Landsat TM imagery. They found that the glaciers along James Ross Island (north-eastern AP) and the Graham Coast (south-western AP) retreated most. Glaciers with floating tongues showed the highest frontal retreat. Glaciers in the north-western AP, along the Danco Coast, showed relative stability in the frontal positions. This stability was explained by increased snow accumulation that counter-balanced eventual losses. A comprehensive study of the glaciers in the northern AP was made by Davies et al. (2011). They observed 194 glaciers on Trinity Peninsula, Vega Island and James Ross Island between 1988 and 2009 using ASTER, SPOT and Landsat imagery. It was found that 90 % of these glacier receded between 1988 and 2001. After 2001 the glacier retreat reduced and slowed down with some glaciers going back into dynamic equilibrium. Additionally they classified the glaciers and mapped the drainage basins and glacier hypsometry. There is, however, less knowledge about the elevation change of these glaciers.

One study that mapped changes in glacier extent as well as volume was presented by Fox and Czifersky (2008). They used historical aerial photos from different sources and modern GPS controlled aerial stereo-photography to measure the volume change between 1947 and 2005 for parts of Moider glacier located on Pourqoui Pas Island (located roughly 30 km south-east of Rothera station, see Figure 2.1). As reference, digital aerial imagery from a 2005 BAS campaign with known interior and exterior orientation parameters was used. From this an orientated image block with accuracies better than 0.5 m in X, Y and Z was produced. For the historical photos the exterior and interior orientation parameters were incomplete. To orientate the historic image blocks additional tie points, that could be identified in the historic and modern photo sets, were

added to the reference block. The reference block was then re-adjusted using these additional tie points and keeping the external orientation parameters fixed to derive secondary control points with known accuracies. These secondary control points were then used to orientate the historical imagery. Accuracies within 2 m in X, Y and Z have been achieved for the historical data. A comparison between the multi-epoch images and extracted DEMs showed significant retreat and surface lowering at the front of Moider Glacier over 48 years. The loss of ice was greatest in recent years. This study showed the enormous potential of archive imagery in combination with modern imagery. In addition to the measurement of volumetric changes the study showed where potential problems in the data integration are found.

The orientation of the historical photographs is especially problematic without sufficient reference information. Archive photos are often subject to film degradation and distortions. Significant variations in snow cover were observed between the different photos which should be noted as it can introduce uncertainties into the measurement of surface elevations and especially glacier extent.

Cook and Vaughan (2010) present a comprehensive overview of the areal changes of the AP ice shelves to date, which shows that since the 1960s the total ice-shelf area reduced by more than 28,000 km^2 . That is a loss of about 18 % compared to the original extent. The largest changes where observed between the 1970s and 1980s. Of twelve ice-shelves in the AP, four have totally disintegrated (Jones, Wordie, Prince Gustav, Larsen A) and three showed significant retreat (Larsen B, Müller, Wilkens) since the 1940s. It was proposed that the thermal limit for ice shelf viability is bounded by the -9 ºC isotherm (Cook and Vaughan, 2010; Figure 2.8). The ice shelf disintegration has followed the southern migration of the thermal boundaries.

Hence, much is known about the areal changes of glaciers and ice shelves but the underlying causes for these changes are still not fully understood. There is strong evidence that the ice shelf retreat is mainly attributed to atmospheric warming (Mercer, 1978; Skvarca et al., 1999; Scambos et al., 2000; Cook and Vaughan, 2010) but this might not be the exclusive driver, particularly with regard to ocean temperatures and dynamics.

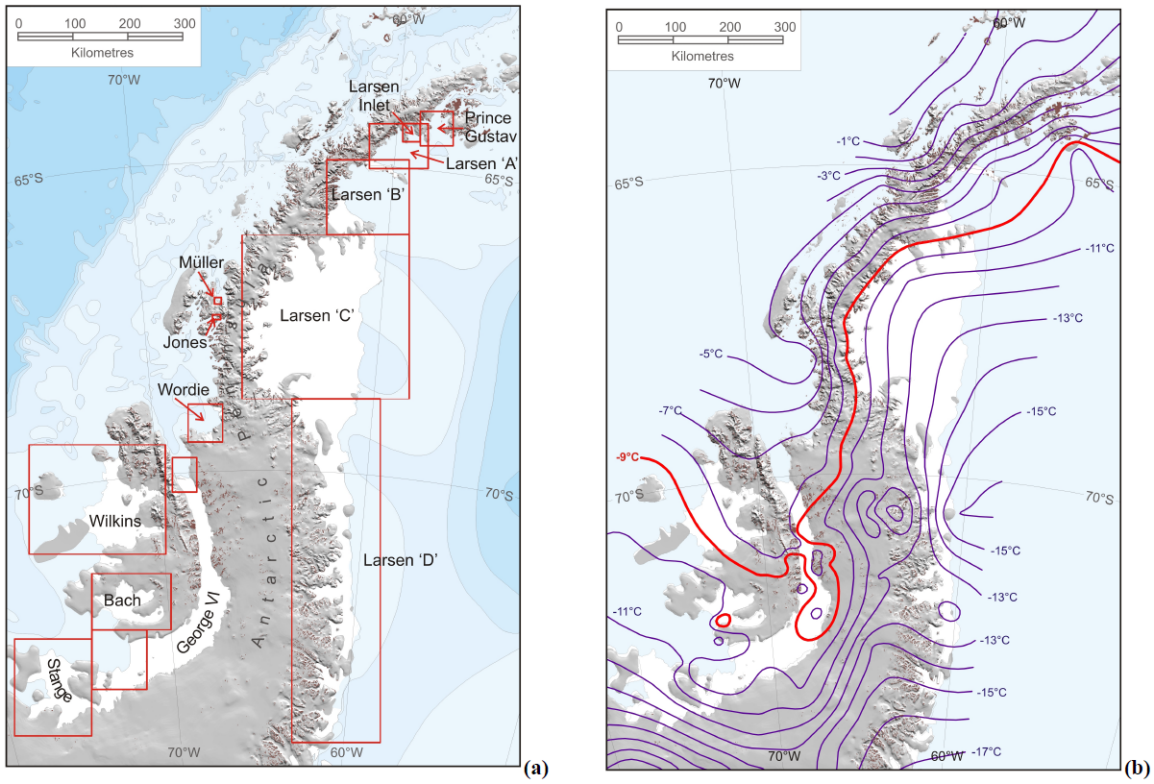

Figure 2.8: Ice shelf locations (a) and isotherms (b) in the AP (Figure 1 from Cook and Vaughan, 2010). The red line in (b) is highlighting the -9 ºC isotherm which is believed to be a boundary for ice sheet stability.

Using ERS satellite radar altimetry data and stake measurements, it was shown by Shepherd et al. (2003) that the Larsen C Ice Shelf has lowered by up to 0.27 m between 1992 and 2001. This lowering was assumed to be caused by atmospheric and oceanic warming in the Wendell Sea that led to increased surface and basal melting. As shown by Holland et al. (2011), firn densification is another likely explanation for the observed surface lowering, especially under warming and longer melt conditions. The thinning made large portions of the ice-shelf more exposed to crevasse fractures and therefore potentially unstable. The Larsen B ice shelf lost substantial parts in 1995 and 2002. Scambos et al. (2000) studied the break-up of several ice shelves of the AP, using optical and radar imagery in combination with stake measurements, and observed increased ice flow speeds and surface ponding before break-up events. The surface melting causes crevasse propagation as meltwater penetrates into the ice shelf. Pritchard et al. (2012) reveal that the ice-shelf thinning around Antarctica, including ice shelves of the AP, can be partially explained by increased basal melt. Warm water is transported beneath the ice-shelves through changing wind patterns and ocean upwelling. They also found a

positive feedback between dynamic thinning of grounded, fast-flowing tributary glaciers and ocean-driven ice-shelf thinning.

Although the loss of large ice shelves has an effect on the sea-level its impact is relatively small (90 % of the ice is under water). However, the thinning or loss of the restraining ice shelf triggers a speed-up in glacier flow (Dupont and Alley, 2005). After the Larsen B Ice Shelf partly disintegrated, increased flow of the adjacent glaciers was observed. The glacier acceleration stretches the ice and causes thinning. Rignot et al. (2004) analyzed the acceleration and thinning of glaciers behind the Larsen Ice Shelf following the collapse of Larsen B by using InSAR from ERS and RadarSat imagery. It was found that the glaciers (Crane, Jorum, Hektoria, Green, and Evans glaciers) that lost the buttressing ice shelf showed increased flow while the ones further south (Flask, Leppard glaciers) did not as they were still buttressed by the remnant parts of the Larsen B Ice Shelf. The flow acceleration resulted in an increased total mass loss of 27 km^3 /yr. Surface lowering of several tens of meters was observed for the accelerated glaciers. The ice loss was measured with the dynamic mass balance method by using an outflow and upstream gate. Rott et al. (2011) and Shuman et al. (2011) found significant lower mass loss rates (less than 11 Gt/yr) for the Larsen B embayment compared to the results of Rignot et al. (2004). Despite this observation, it is important to note that six years after the breakup of Larsen B glaciers glacier thinning and acceleration is still ongoing (Berthier et al., 2012). Similar observations were made by Scambos et al. (2004) who used Landsat 7 ETM imagery and ICESat profiles to measure speed and elevation changes for the same glaciers that were studied by Rignot et al. (2004). Hektoria Glacier showed surface lowering of up to 38 m in a six month period one year after the break up.

This increased flow rate after ice sheet breakup has been observed for various other locations in the Antarctic Peninsula. The ice discharge of glaciers, e.g. Airy Glacier and Fleming Glacier, flowing into the Wordie Ice Shelf, located in the west Antarctic Peninsula, is over 80 % higher than snow accumulation within the region causing a substantial loss of ice (Rignot et al., 2005). Coherent with the acceleration, thinning rates of up to 4 m/yr on Fleming Glacier were observed (Wendt et al., 2010). If increased regional melting due to warming affects the viability of ice-shelves it will likewise affect

glaciers. When surface melt water reaches the glacier bed via crevasses it can reduce the basal stress and induce a speed up of the glacier (Zwally et al., 2002). Glasser et al. (2011) used optical ASTER and ERS radar data to map the changes of Röhss Glacier (located on James Ross Island; Figure 2.1), a glacier that was buttressed by the Prince Gustav ice shelf. After a collapse of this ice shelf in 1995 the glacier retreated very fast, increased its flow speed and showed thinning of up to 150 m between 2001 and 2009.

When the ice-shelf is removed, tributary glaciers transit to tidewater glaciers and increased calving is observed until the glaciers eventually become land-terminating (Glasser et al., 2011). Accelerating flow speed of glaciers leads to increased mass contribution towards the ocean. If not compensated by snow accumulation the mass balance will be negative and an increase in sea-level is the result.

Pritchard and Vaughan (2007) studied over 300, fast-flowing, highly crevassed, tidewater glaciers on the western AP, between 64° S and 70° S, and observed a widespread acceleration of glaciers between 1992 and 2005. They used SAR feature tracking and measured an average increase in flow speed of 12 %. The observed acceleration was not explained by increased precipitation (accumulation) or increased runoff from melting. Thinning of the glacier terminus at low altitudes is considered to be the likely cause but validation is missing. If this theory holds, a clear signal of surface lowering at the glacier terminus can be expected. Frontal thinning reduces the pressure on the glacier base and induces faster flow. The grounded ice eventually becomes afloat and the glacier begins to retreat. Similar observations have been made for glaciers in Greenland and Antarctica (Rignot and Kanagaratnam, 2006; Luckman et al., 2006; Thomas et al., 2011). However, as previously mentioned there are only few observations for surface elevation changes in the AP and existing records often do not date back before 2000. Comprehensive large-scale mass balance studies of the AP only exist for recent years.

The study of Pritchard et al. (2009) allowed the first larger scale view of elevation change in the AP. They used repeated laser altimetry from ICESat observations and showed strong dynamic thinning of tributary glaciers located behind collapsed ice-shelves. Thinning of over 10 m/yr (over the period 2003 to 2007) was observed for glaciers feeding into the southern part of the Larsen Ice Shelf (e.g. Clifford Glacier),

which is in agreement with other studies, e.g. Rignot et al. (2004). For slow-flowing ice caps and higher altitudes along the Peninsula's divide, thickening of up to 1 m/yr was observed. There is strong evidence that most of the glacier thinning in the AP is a result of dynamic glacier changes, meaning it is related to ice-shelf collapses and glacier acceleration. Changes in precipitation, atmospheric temperature and oceanographic conditions are also affecting the AP glaciers and contribute to an overall negative mass balance. However, they are assumed to be less influential. Ice-shelf collapse and ocean warming are seen as the main causes for the observed thinning, and climate warming is not necessarily required (Pritchard et al., 2009).

Using InSAR data and regional climate modeling, Rignot et al. (2008) estimated an annual AP ice mass loss of 25 $\pm$ Gt/yr in 1996 and 60 $\pm$ 46 Gt/yr for 2006. Note that this value relies on upscaling since only a few glaciers were sampled in the AP. Nonetheless, this is an increase of 140 %. The majority of losses are attributed to outlet glaciers along the small channels of the AP. The likely cause is an acceleration of these glaciers, and has also been observed by Pritchard and Vaughan (2007). The observed loss cannot be explained by a change in snowfall since a noticeable increase in snowfall for recent years was observed, especially in the western AP (van den Broeke et al., 2006). A later study of Rignot et al. (2011c) uses GRACE measurements and states the mass loss from AP glacier and ice caps (GIC) is 25 Gt/yr. Similar findings are given by Ivins et al. (2011) who also used GRACE data, GPS records and GIA corrections. They determined a present day loss rate of 41.5 $\pm$ 9 Gt/yr for Graham Land. Shepherd et al. (2012) used a combination of satellite altimetry, interferometry, and gravimetry. They calculate a negative ice-sheet mass balance for the AP of 20 $\pm$ 14 Gt/yr between 1992 and 2011. This change accounts for roughly 25 % of all mass losses from Antarctic regions that currently exhibit negative mass balance, although the AP occupies just 4 % of the continental area. King et al. (2012) estimate a mass loss of 34 Gt/yr for the AP over the period 2002 to 2010, using GRACE data and improved GIA models.

It becomes obvious that existing mass balance studies only present results for recent years and that the spatial resolution is relatively low which explains the variations in their estimates (Table 2.3). There is much evidence for an overall negative mass balance.

A recent paper from Velicogna and Wahr (2013) reports an accelerated mass loss for Antarctica with a dominance over West Antarctica and the AP. However, it should be noted that, increased accumulation can be reconstructed at higher elevations in the northern and western AP resulting in local ice mass gain (Nield et al., 2012). Such changes can be captured by GRACE as well, despite the low resolution. Nonetheless, complete mass balance estimates on an individual glacier level are rare.

2.4.1 Sea-level estimates

It is predicted that over the coming decades the thermal expansion of the global ocean, which causes changes in the water density, will contribute more than half towards sea-level rise and the contribution from melting ice will increase as well (Meier et al., 2007; IPCC, 2007; Leclercq et al., 2011). According to recent (climate) models it is believed that mountain glaciers and ice shelves will contribute up to 0.124 m to sea-level rise with the largest contribution from glaciers in Arctic Canada, Alaska and Antarctica (Radic and Hock, 2011). Excluding these glaciers can lead to considerable uncertainties in sea-level rise estimates (Van de Wal and Wild, 2001). The overall sea-level is projected to rise between 0.5 m up to 1.4 m until 2100, compared to the level in 1990 (Rahmstorf, 2007). The glaciers of the AP are primarily classified as mountain glacier (MG) or small ice caps (IC). As such they are often not included, or simply ignored, in global or Antarctic mass balance and sea-level estimates (Dyurgerov and Meier, 2000; Church et al., 2001; Zwally et al., 2005; Kaser et al., 2006; Shepherd and Wingham, 2007). In the last four IPCC reports the Antarctic Peninsula mass balance was not directly assessed (Lemke et al., 2007). This is obviously unsatisfactory and leads to uncertainties in global sea-level projections. The lack of data for the AP glaciers also meant that they were not included into inventories of mountain glaciers as compiled by Dyurgerov (2002).

In 1992, Drewry and Morris estimated a 1 mm sea-level rise from the Antarctic Peninsula assuming a 2 °C warming of the mean temperature over 40 years. Vaughan (2006) estimate the contribution to sea-level rise from the Antarctic Peninsula to be around 0.16 mm/yr in 2050. For the year 2000 a total surface melt of 54 $\pm$ 26 Gt/yr and

Author	MB [Gt/yr]	SLE [mm]	Method	Note
Vaughan (2006)	-54.0 ± 26	0.15	Modelling	incl. GIC
Pritchard and Vaughan (2007)	-57.6 ± 22	0.16	SAR	incl. GIC
Rignot et al. (2008)	-60.0 ± 46	0.17	InSAR	incl. GIC
Hock et al. (2009)	-79.2 ± 58	0.22	Modelling	incl. MG/IC
Ivins et al. (2011)	-41.5 ± 9	0.12	GRACE	incl. GIC
Rignot et al. (2011c)	-42.0 ± 24	0.12	GRACE	excl. GIC
Shepherd et al. (2012)	-20.0 ± 14	0.06	Combined	incl. GIC

Table 2.3: Mass balance (MB) and sea-level (SLE) estimates for the Antarctic Peninsula. The reference periods stated in the literature vary. Note: 1 mm eustatic sea-level rise is equal to 360 Gt of ice loss.

a runoff of 2.9 to 20 Gt/yr was determined (Vaughan, 2006). Hock et al. (2009) estimated the contribution of Antarctic mountain glaciers and ice sheets to be 0.22 $\pm$ 0.16 mm/yr and this contribution is expected to come almost entirely from the AP. To put these values in perspective, the contribution of Alaskan glacier, which are seen as the "largest glaciological contributor" to sea-level rise, is estimated as 0.27 $\pm$ 0.10 mm/yr over the past decade. Now, the area of Alaskan glaciers (90,000 km^2), which are of similar types, is smaller than the Antarctic Peninsula's ice sheet area (120,000 km^2) which highlights the potential of the AP glaciers as another significant contributor. In contrast, Shepherd and Wingham (2007) concluded that the AP contribution to sea-level rise is "negligible", but based on the above this seems arguable. In a recent paper of Shepherd et al. (2012) it is noted that the spatial sampling of mass fluctuations of the AP ice-sheet is currently inadequate and that spatially more comprehensive observations and longer temporal sampling of the AP region is needed.

2.5 Summary

It can be said that the efforts in mapping the AP have expanded over the last 15 years. Primarily, this is due to the fact that the region is changing rapidly and it has gained wide attention from scientists and the media. Not only is it important to map the changes, as they have a direct impact on sea-level, but also to understand them. The AP as an example of rapid climate change can reveal information for regions elsewhere that may experience similar changes in the future. Secondly, advanced remote sensing techniques and new sensors have improved the knowledge of Antarctica as a whole. Several decades ago the use of satellite information of polar regions was more experimental rather than

applied. Especially the use of radar, which allows year-long day and night measurements, has become frequent in polar remote sensing. With growing archives and the emergence of new sensors the demand for data integration has increased.

From what was reviewed to date it can be concluded that the AP air and sea temperatures are increasing. The extent of glaciers, ice shelves and sea-ice is reducing. These changes follow a north-south pattern that is influenced by the topography. While changes in the last ten years have been studied reasonably well, long-term records are missing and needed. Such long-term time-series studies have become greate attention recently but results are still missing. To draw conclusions about long-term climatic changes the usual time period is about 30 years which to some extend is the time of available records of climatic and remote sensing data for the AP. It was shown that areal changes in glacier and ice sheet extent have been mapped reasonably well over the last 50 years. Meteorological records cover similar periods and the understanding of the climate variability across the AP has significantly improved. The viability of ice shelves and their interaction with the climate has been widely assessed. Particular attention is dedicated to studies using radar sensors that assess glacier velocities and ice mass changes for the recent years. The use of stereo-photogrammetry and archive photography to estimate glacier mass balance in the AP is underexplored within the literature.

Fox and Czifersky (2008) showed the huge potential offered by unexplored archive datasets that allow the extraction of topographic information. As such they are applicable for geodetic mass balance calculation. Therefore, the work presented here aims to provide extended long-term measurements of glacier mass balance changes across the AP using available archive and modern stereo-photography. This is not a trivial task for several reasons:

1. Analogue archive photography needs to be converted to digital format to enable the use of modern digital photogrammetric workstations. This is achieved by scanning, but introduces a potential source of error, especially if non-photogrammetric scanners are used. If original paper prints were stored under improper conditions they may have degraded and likewise, where original roll film survives, film flatness can not be guaranteed over time. This has an impact on the

image quality and introduces distortions. In addition, calibration data of historic cameras and flight campaigns might be lost over time, e.g. when the operator or owner of the data has changed. Thus, the interior orientation is not straightforward.

2. Over time, sensors and measurement techniques have changed. While modern platforms carry GPS and IMU instruments to measure the exterior orientation of the sensor, this information is not available for historical datasets. Hence, the reproduction of the absolute orientation at the time of image acquisition is more complex and makes the co-registration of datasets more difficult. This is particularly the case, when GCPs are not available. Even if the interior and exterior orientation can be reproduced individually it is likely that a discrepancy in the relative orientation between multi-temporal, multi-resolution and multi-source datasets will occur. The absolute orientation of multi-source datasets to a common reference frames is rarely exact, unless ground control data is available. Translational or rotational offsets between DEMs will have a significant influence on the derived volume changes. Again, correction is needed.

3. The original imaging purpose might be different to the application today. It is not uncommon that new techniques for old datasets are developed and reprocessing is applied. Some datasets are used for the first time several decades after they were collected. The amount of available satellite information is growing day-to-day and often datasets have not been fully explored simply because there is 'too much' data, e.g. the BAS or USGS Antarctic Single Frame archive. A user needs to carefully select the data that holds the highest amount of information. To some extent this also applies to historic data. Therefore, analysis of the data quality and availability is essential. In polar environments images often lack contrast due to snow cover and less distinct features. Another major problem is cloud cover in images. The extraction of corresponding images points is not always perfect and consideration should be given to this before selecting suitable imagery.

The above points need to be addressed before any meaningful glacier change measurement can be made. The following chapter will address these issues in detail and

provide an introduction to the datasets and methods that will be used to achieve this. The potential benefits of this work are:

1. An exploration of potential archive and modern imagery that is suitable for DEM extraction and therefore geodetic mass balance calculations.
2. An investigation and analysis of the individual accuracy and quality of these datasets.
3. The development and improvement of DEM co-registration in areas with steep topography, especially in glaciated regions.
4. Quantification of long-term glacier mass balance of the AP and comparison with climate data.

Chapter 3. Datasets and Methods

The previous chapter established that a combination of historic and modern DEMs is most suitable to resolve the existing gap of long-term glacier mass balance records for the AP. This implies a combination of different sensors because long-term observations with just one sensor are rare and often difficult to achieve. The reason for that, is the short lifespan of satellites and the development of new, more advanced, remote sensing techniques. In general this is beneficial. When new sensors are employed, changes in instruments mean that different resolutions, uncertainties and biases that exist between measurement types need to be considered. Thus, an integration of multi-source data is not trivial.

Before any measurement of change can be made, it is important to understand the data thoroughly. The assessment and removal of errors is a major part of this. The geodetic method, in particular DEM differencing, is highly dependent on the accuracy and resolution of the input DEMs. This chapter presents and explains 1) the data that is used in this study, 2) the processing steps, and 3) the methods that are applied to combine and validate these datasets. At the end of this chapter a method for the reliable measurement of historic glacier volume change in the AP is established and explained.

3.1 Datasets

Various high-resolution sensors (ASTER, Envisat, Landsat, or SPOT) cover the AP, especially with data of recent years, but not all have the desired specifications or quality to derive topographic information. Here, primarily ASTER satellite stereo-imagery and USGS/BAS aerial stereo-photography will be used to estimate multi-decadal glacier volume change. ASTER data has been chosen for this study because the scale-stability

of the DEM product offers a solution for the registration of DEMs extracted from aerial imagery without the use of ground control (Miller et al., 2009) and there is sufficient data coverage since 2000. Furthermore, ASTER data is available at no cost for educational users or participants of the GLIMS project and has been used widely in the glaciological community (Section 3.1.1). Historic information of the AP is less well represented. A major source for historic imagery of the AP are the BAS/USGS archives (Section 3.1.2). This archive imagery is freely available and covers several decades, dating back to the 1920s. In addition to the topographic information, atmospheric and oceanic temperature data is used to investigate links between glaciers and the climate. For the validation of the ASTER DEM high resolution GPS controlled aerial imagery is used.

3.1.1 ASTER

The ASTER instrument on-board NASA's TERRA (formerly EOS AM-1) satellite was launched in late 1999, with first data becoming available in 2000. The satellite has a circular, sun-synchronous, nearly polar orbit at an altitude of 705 km with an orbital inclination of 98.3°. ASTER has 4 telescopes, three for nadir-viewing and one backward-viewing that enables stereo-imaging. The spatial resolution of the telescopes ranges from 15 m, 30 m, and 90 m. The spectral bands cover the visible, near-infrared (VNIR, 3 bands, nadir and backwards), the short wavelength-infrared (SWIR, 6 bands) and the mid-infrared (VIR, 5 bands) (Figure 3.1). ASTER can observe the earth surface under cloud free conditions between 82° N and 82° S with a repeat cycle of approximately 16 days (Welch et al., 1998). Using the along-track nadir-viewing (band 3N) and backward-viewing (band 3B, 27.6° off-nadir) image within the near-infrared (0.76 - 0.86 μm), digital elevation models can be produced (Figure 3.1) with a base-to-height (B/H) ratio of 0.6. The stereo-viewing capability is an advantage over other satellite systems and allows direct ortho-image generation without the need of external DEMs. The swath width is approximately 60 km. Neighbouring orbits are separated by roughly 172 km on the ground and converge nearer to the poles. An ASTER scene covers approximately 60 km x 60 km. The data has been used in various studies and applications including geology, glaciology, land cover mapping or soil

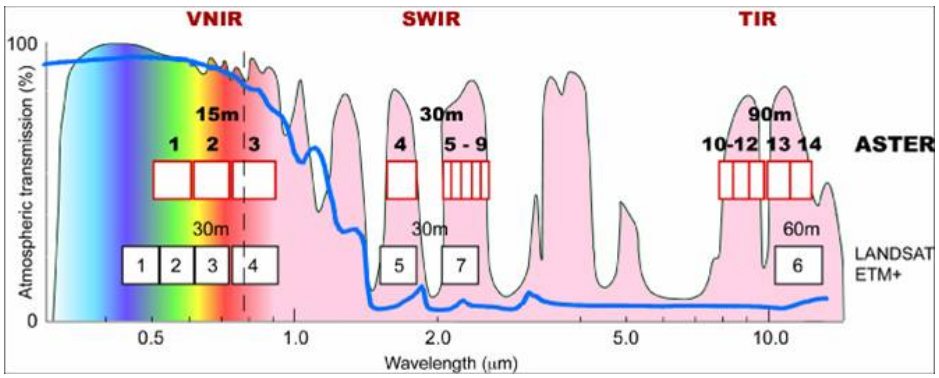

Figure 3.1: Electromagnetic spectrum and ASTER bands. Source: JPL (2013).

science (Kääb et al., 2002; Kamp et al., 2003; Stevens et al., 2004; Nimomiya et al., 2005; Kato and Yamaguchi, 2005; Kääb, 2007; Bolch et al., 2007; Toutin, 2008).

ASTER in glaciological studies

For glaciological studies ASTER is a favorable source of data because it allows mapping in the visible, the near-infrared and the thermal spectrum. This multi-spectral information is useful for the classification of snow, ice or debris as well as the thermal properties. In combination with the simultaneously collected terrain information additional information about surface roughness and topography is provided. With the near polar coverage most glaciers in the world can be studied at a resolution of up to 15 m. The revisit cycle is short (16 days under ideal conditions) which allows the detection of change over relatively short time periods. Ice surface velocities can be extracted from multi-temporal imagery using feature tracking. Differencing of DEMs allows the measurement of elevation change. In theory, these are simple approaches that can be applied easily assuming error-free data. Often ASTER is used in combination with data from other sensors, in particular radar. It is beyond the scope of this thesis to give a full overview of ASTER studies within the field of glaciology but it can be said that ASTER has contributed largely to the understanding of glacier and ice sheets and their respective change (Kääb et al., 2002; Kamp et al., 2003; Kääb, 2005, 2007; Stearns and Hamilton, 2007; Bolch et al., 2007; Howat et al., 2007; Toutin, 2008; Miller et al., 2009; Shuman et al., 2011; Davies et al., 2011; Glasser et al., 2011).

Products and DEM generation

ASTER data is available as standard (lower level) or semi-standard products (higher level). The lowest product level (Level 1A) is the reconstructed, unprocessed instrument data which is distributed together with the radiometric and geometric coefficients (RCC) for further processing by the user. Level 1B contains radiometrically calibrated and geometrically co-registered data for the acquired channels of the three different telescopes (VNIR, SWIR, TIR) of Level-1A data. Higher level products (Level 2 and 3) can be ordered on request via the NASA Land Processes Distributed Active Archive Center (LP DAAC). These include atmospherically corrected images (Level 2), orthographic images (Level 3) and the DEM (Level 3) products. A full overview on the available data products can be found in the ASTER Reference Guide (ERSDAC, 2003) or on the ASTER webpage (JPL, 2013). Available ASTER scenes can be searched and browsed online using *ASTER GDS*, *NASA Reverb* (formerly *WIST*; NASA, 2013) or *GloVis*. Data is usually delivered in HDF or GeoTiff format together with a file containing the metadata. Most standard photogrammetric/remote sensing packages such *ENVI*, *PCI Geomatica* or *Erdas* allow the automated or semi-automated processing of ASTER data.

In this study the DEM product is of main interest. ASTER DEMs, including the on-request product from LP DAAC, are generated using a stereo cross-correlation (least-squares matching) approach that extracts the parallax information for each pixel in the image. The mathematical concept for digital image correlation can be found in Ackermann (1984) or Ehlers and Welch (1987). The relative ground height is measured from the parallax difference of corresponding points within the stereo pair. It is crucial that the corresponding image pair is registered well relative to each other to ensure corresponding pixels are compared. The data transformation coefficients between map and image coordinates are applied using a sensor model and the ephemeris and attitude information from the ASTER metadata (Fujisada et al., 2005). An overview of parameters that are needed to register along-track stereo images is found in Dowman and Neto (1994) or Poli et al. (2004). After the image correlation step all pixels are georectified.

At the LP DAAC the DEM is produced with standard PCI photogrammtric software on a scene-by-scene basis. Other commercial software packages that offer ASTER DEM generation are ENVI or SILCAST. The rectification and image registration is usually done simultaneously. A full description on the ASTER DEM generation can be found in Fujisada (1998); Lang and Welch (1999); Fujisada et al. (2005). When ordered via the LP DAAC a customer can submit ground-control (GCPs) data in order the get an *absolute* DEM. Without the distribution of GCPs the user will receive a *relative* DEM. In an absolute DEM the elevation values refer to the absolute vertical datum (i.e. the mean sea-level) whereas in a relative DEM the elevation value refers to the lowest elevation pixel. An absolute DEM can also been produced without GCPs in the actual the scene, when ground control exists within a block of scenes. In the absence of ground control, the absolute position of a relative ASTER DEM is approximated using the satellite orbit information. In this case the $RMSE_{xyz}$ values for relative DEMs will be higher compared to the products with ground control (see Section 3.1.1) due to potential translational and/or rotational shifts of the DEM from truth. The LP DAAC DEM generation process includes an 'editing' step. In most image correlation procedures some pixels will fail or produce incorrect results, meaning that they will have a wrong elevation value associated with them. Using standard filters, such as median or sigma filters, the relative DEM accuracy can be improved (Giles and Franklin, 1996). These types of filters are used at LP DAAC on the ASTER DEM product to improve quality but this reduces the end-user control (see Section 3.3.1) over the DEM generation. The user generated DEM production is described in Section 3.2.1 of this chapter. The ASTER data used for this study were provided at no cost via LP DAAC (with privileged user status).

With a resolution of up to 15 m, ASTER is one of the best sources for elevation data with a near-global coverage. Thus, in 2009 a global ASTER DEM (GDEM) was compiled. The elevation information in this dataset is derived from multiple overlapping ASTER scenes to achieve global cloud free coverage (METI/NASA, 2009). However, the quality is relatively poor (large variations in elevation over actual smooth terrain), due to apparent spikes in smooth terrain, but more important this product is not suited for (short-term) glacier change assessment as it represents averaged elevation values.

Product Name	# of GCPs (minimum)	GCP ($RMSE_{xyz}$) Accuracy	DEM ($RMSE_{xyz}$) Accuracy
Relative DEM	0	N/A	10 - 30 m
Absolute DEM	1	15 - 30 m	15 - 50 m
Absolute DEM	4	5 - 15 m	7 - 30 m

Table 3.1: Accuracy of standard LP DAAC ASTER DEM products (30 m X-Y posting, 1 m smallest Z increment) (Lang and Welch, 1999)

Although in 2011 a second version has been released the ASTER GDEM was found to be not suitable for this study.

ASTER DEM accuracy

Applying a simple geometry-based photogrammetric rule on the image correlation error it is possible to estimate the ASTER DEM accuracy. Consider $\Delta h = \frac{H \Delta p}{B}$ where H/B is the inverse of the base-height ratio (in the case of ASTER 1.0/0.6 or 1.67), and Δp is the difference in parallax (xy displacement). Assuming a realistic correlation error Δp of 0.5 to 1.0 pixels (7 - 15 m) the respective Δh errors ($RMSE_z$) would be in the range of ± 12 m to ± 26 m. Note, that this only accounts for the image correlation error and does not include geometric or atmospheric errors.

The measured standard ASTER DEM accuracies are shown in Table 3.1. The lowest $RMSE_{xyz}$ for the ASTER DEM is ± 7 m in the ideal case which corresponds to half a pixel. Studies by Li (1998) and Tokunaga et al. (1996) have estimated $RMSE_z$ values of ± 12.5 m, which is similar to the results of Cuartero et al. (2004). Fujisada et al. (2005) assessed the ASTER DEM performance and compared the results against reference databases including the USGS National Elevation Dataset (NED). They state a vertical DEM accuracy of 20 m (95 % confidence) for DEMs generated from Level 1A without ground control. The planar accuracy was given to be better than 50 m. For rapid mapping purposes the sensor can be rotated by up to $\pm 24°$ from nadir in the across-track direction, but increased geolocation errors can be expected for large cross-track pointing angles above $\pm 9°$ (Fujisada et al., 2005). Eckert et al. (2005) showed that the accuracy decreases in terrain with steep topography with reported RMS errors of 15 m to 20 m for hilly terrain and and 30 m in mountainous terrain. The main source of error was found to

be the positional inaccuracy of ASTER caused by incomplete correction of nutation[1] (Fujisada et al., 2005). Another problem are shadows in the imagery that can decrease the image matching success and introduce errors. Similar results can be found in Hirano et al. (2003), ERSDAC (2004), Bolch et al. (2005) or Toutin (2008). Because ASTER is a similar sensor to SPOT some authors have used SPOT-based ASTER simulations and stated RMSE values between ±13 m (XY) and ±26 m (Z) (Dowman and Neto, 1994). In general, the ASTER DEM accuracy (considering DEM and instrument errors) can be assumed to be between 7 and 50 m, both, vertically and horizontally.

Although the ASTER DEM accuracy has been widely assessed in the literature, there is still a discrepancy between the theoretical possible accuracy and the accuracy in real world applications. Inaccurate positional and elevation values can translate to very large errors when differencing DEMs. Several papers note offsets between individual ASTER DEMs and relative to other datasets such as SRTM (Kääb et al., 2002; Vignon et al., 2003; Bolch and Kamp, 2006; Racoviteanu et al., 2007; Miller et al., 2009, 2012). Another factor is the existence of potential elevation-dependent biases (see Section 3.3.2). When using multi-temporal DEMs the major limitation is the relative accuracy between DEMs. Less effort has been made so far to reduce those errors and to reveal the full potential (accuracy). Ideally users want to achieve the highest possible accuracy. Especially for glacier change assessment it is important to co-register DEMs precisely to avoid an over- or underestimation of mass balance changes.

3.1.2 Aerial archive imagery

The availability of historical datasets (here the term historic is referred to data that is older than 20 years) of the AP is limited. The exploration of the Antarctic continent and its glaciers is relatively young compared to other regions, e.g. the Alps. Before the satellite era existing aerial photography was mainly flown for rapid mapping purposes and the exploration of the Antarctic continent but not for the purpose of glacier monitoring. The first aerial images of the region date back to the 1920s. At this time it was not known that Antarctica would become one of the most important regions in terms

[1] Variations in the Earth's rotational axis.

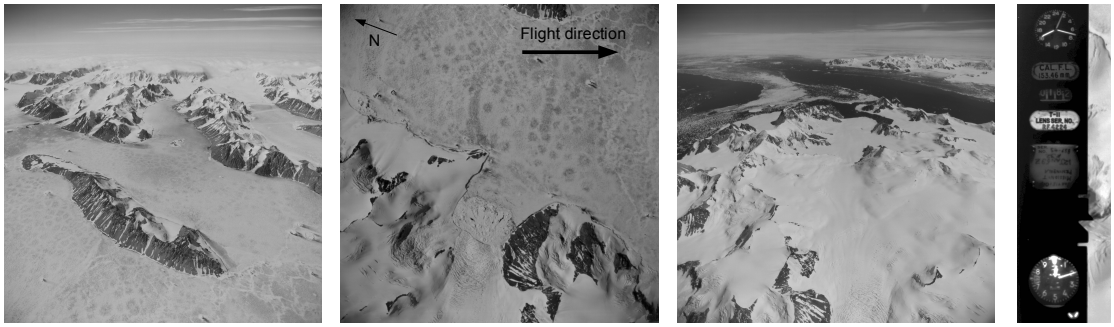

Figure 3.2: Typical trimetrogon (TMA) photography of Antarctica

of environmental change. To date several mapping campaigns have been flown over the Antarctic Peninsula, however, mainly to fill gaps for unmapped areas. Existing imagery was often acquired from different countries and not necessarily in international collaborations which makes the data availability more complicated. Overlapping flight strips of areas with different time stamps are rare. Most of the photography exists in analogue form and is stored in archives. Digital aerial sensors were introduced only recently and high resolution GPS controlled imagery is sparse. Alongside satellite imagery an increased effort is made in mapping the AP more frequently by aerial photography. Here, two major sources for historic and modern aerial photography of Antarctica are explored, the BAS and USGS archives.

USGS Data

The USGS EROS Data Centre has a collection of over 330,000 single frame records of Antarctica from 1946-present. The archive contains aerial black-and-white, natural colour and colour infrared images from the United States Antarctic Resource Center (USARC) and the British Antarctic Survey. The ground scale of the images ranges from 1:1,000 to 1:64,000. Most of these archive images were acquired by the U.S. Navy with a trimetrogon sensor configuration. This configuration is highly suited for rapid topographic mapping and consists of one nadir looking photograph and two oblique looking photographs that are taken simultaneously (Figure 3.2). To enable the use with modern digital photogrammetric workstations and to preserve information for future

Figure 3.3: The Phoenix V scanning system (Smith and Longhenry, 2008)

generations these single frames were scanned at different resolutions by the Earth Resources and Observation and Science (EROS) Center.

For the scanning a BetterLight scanning back with a Kodak 10,400 pixel tri-linear array sensor mounted on a view camera with a Schneider Macro-Digitar 120 mm lens was used. This scanning system has been developed by EROS and is called Phoenix-V (Figure 3.3). The frames were scanned in high resolution at 25 micron (1000 dpi). In post-processing, distortions caused by the BetterLight scanner, were removed and the final products were stored in TIFF format. Lower resolution (400 dpi) scans were made with a Kodak PRO SLR camera on a similar system. However, the medium resolution scans were not corrected for error and thus are not suitable for photogrammetric processing. Here the 1000 dpi scans are used. Data is freely available via EarthExplorer (USGS, 2013) or the Polar Geospatial Center (PGC, 2013b). The original image size is approximately 9x9 inch. The TIFF file size of each scanned frame is about 45 Mb. After scanning the original acetate film rolls were shipped to the U.S. National Archives for permanent cold storage to suspend any further decay due to the affects of vinegar syndrome (Smith and Longhenry, 2008; Smith, personal communication).

Metadata information of the original imagery is available but limited. Each of the frames contains information about the focal length, lens type and acquisition date. However, full camera calibration protocols and exact flight information are often missing or incomplete. Documentation on available camera and flight strip information can be

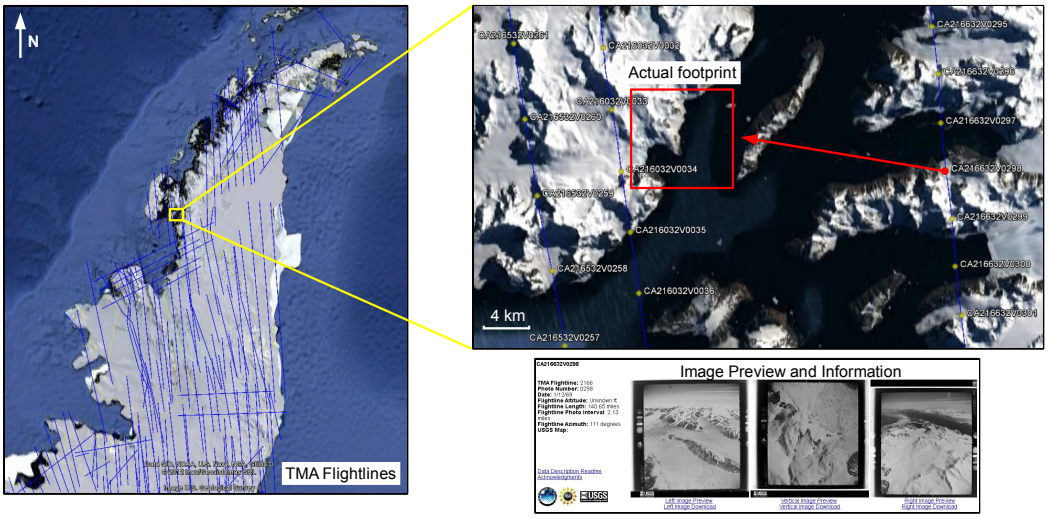

Figure 3.4: TMA flightlines and camera centers. Note the offset between stored camera centers and the actual image footprint.

found at the PGC online (PGC, 2013a). PGC provides a KML (.kmz) file containing the individual flightlines and camera centers together with the data link and meta information. This is useful for quick browsing of the imagery. Notice that there is a significant offset between the positions provided in the KML file by PGC and the actual image footprints (Figure 3.4). This makes the identification of the actual ground location difficult especially if one wants to search for specific locations and for comparison with existing data.

Given the complete coverage of ASTER data for the AP, the selection of suitable study sites is more tied to the availability of historical imagery. To identify suitable sites all flight strips (273 strips for the AP region) and image footprints were visually analyzed for image pairs that are suitable for photogrammetric processing and DEM extraction. Images were selected using the following criteria:

- Stable terrain with high detail and little snow cover
- Glacier(s) can be identified, if possible with distinct surface features e.g. crevasses
- High image contrast and sufficient image brightness
- Low cloud cover and little shadowing
- Along-track overlap between images at least 60 %

Suitable stereo-imagery was selected for 12 sites (see Section 5.1, Figure 5.1) of which most are located in the western AP. A minimum of three overlapping images was

selected per site allowing for feasible DEM extraction. Each image covers visible stable terrain (i.e., rock outcrops) and at least one glacier section for which the surface elevation change was estimated. Where possible, coverage of the glacier front was desired to allow for measurements of glacier length change. A systematic selection was not possible since the selection is constrained by the data quality and availability. In total 55 images (between three to six images per site) with longitudinal overlap in the direction of flight were selected. The selected frames are summarized in Table 3.2. Many flight strips are not suitable for DEM extraction because they cover large parts of ice fields or inland ice in the vertical imagery with very low image contrast making it difficult to find corresponding points. Particularly the image strips of the eastern AP are unsuited. Other images cover large parts of water bodies and sea ice. This can be useful for other studies, e.g. measurement of sea ice, but it is not of interest for the work here. There is no lateral overlap between the image frames and full systematic stereo-coverage of larger glacier systems is not available due to the flight pattern which was aimed at topographic mapping of the entire region but not for individual glacier monitoring. Most of the USGS imagery is not orientated along the flow of glaciers. The gaps between the strips (see Section 3.4) are relatively large. The data processing of the selected imagery is described in Section 3.2.2. For all historic image frames selected at least one overlapping pair of ASTER or modern stereo-photography was available from which reference DEMs were derived.

Flightline	Frames	Flight Date	Interv. [km]	Azimuth [°]	Camera	Lens	c [mm]	H [m]	Scale
CA2152	V0368-V0371	27/12/1968	3.51	292	T-11	DS2294	154.430	5813	1:37643
CA2147	V0011-V0014	24/12/1968	2.80	115	T-11	DS2294	154.430	5690	1:36851
CA2137	V0053-V0057	23/12/1968	2.35	115	T-11	DS2294	154.430	5769	1:37361
CA2138	V0209-V0212	23/12/1968	3.36	293	T-11	DS2294	154.430	7282	1:47158
CA2149	V0140-V0143	27/12/1968	2.86	112	T-11	DS2294	154.430	5163	1:33438
CA2141	V0040-V0045	23/12/1968	2.95	116	T-11	DS2294	154.430	5459	1:35353
CA2153	V0465-V0470	27/12/1968	2.54	145	T-11	DS2294	154.430	5677	1:36764
CA2140	V0363-V0366	23/12/1968	2.55	294	T-11	DS2294	154.430	5584	1:36163
CA2166	V0298-V0300	12/01/1969	3.43	111	T-11	RF4224	153.460	5584	1:37464
CA1813	V0081-V0083	16/11/1966	3.23	111	KC-1	585	151.982	6029	1:39045
CA1813	V0094-V0097	16/11/1966	3.23	111	KC-1	585	151.982	5998	1:38843
CA1823	V0015-V0017	26/11/1966	3.06	0	KC-1	585	151.982	5606	1:36305

Table 3.2: Flightline and image information for USGS archive data. c is the focal length. H is the estimated flight height over ground.

Camera	Lens	CFL [mm]	Cal. Date	AWAR	Tang Dist	Lens Distortion
T-11 (54-655)	DS2294	154.430	22/11/1955	26.0	0.008	Known
T-11 (54-658)	RF4224	153.450	05/10/1955	26.1	0.006	Known
KC1	585	151.982	N/A	N/A	N/A	Unknown

Table 3.3: Camera information and calibration for historical USGS datasets (Spriggs, 1966). Note that for some image frames full camera calibration information was not available. CFL=Calibrated Focal Length, AWAR=Area-weighted average resolution.

Campaign (Date)	Photo Scale	Camera model	Lens type (FL)
RARE (1947)	1:20,000	Fairchild K17	Metrogon 6in (152 mm)
FIDASE (1957)	1:27,000	Williamson Eagle IX	Ross 6in (152 mm)
IfAG (1989)	1:70:000	Zeiss RMK	Pleogon S (85.5 mm)
BAS (1991)	1:20,000	Zeiss RMK	Pleogon (153 mm)
BAS (1995)	-	Zeiss RMK	-
BAS (2005)	1:30,000	Zeiss RMK	Pleogon

Table 3.4: Characteristics of aerial photography provided by BAS

BAS Data

Alongside the USGS data, BAS provided additional datasets for three locations (Moider Glacier, Nemo Glacier, and Corrie Glacier in Figure 5.1). All images were scanned at 20 microns using a photogrammetric-standard scanner. In addition to all aerial datasets BAS provided at least one overlapping ASTER scene. For Moider Glacier, on *Pourquoi Pas Island*, AP, aerial photography was available for five different epochs. The data was collected from different campaigns: the Ronne Antarctic Research Expedition (RARE) 1947, the Falkland Islands and Dependencies Aerial Survey Expedition (FIDASE) 1957, the Institut für Angewandte Geodäsie (IfAG) 1989, BAS 1991, and BAS 2005. Four datasets had full camera calibration. For the RARE 1947 dataset only the focal length was known. The most accurate dataset was flown in January 2005 by BAS in combination with a GPS ground survey and covers the entire Moider Glacier basin and another glacier basin, Nemo Glacier, on the eastern side of Pourquoi Pas Island. The data for this study site was provided fully processed (image files and photogrammetric project file with interior, exterior and absolute orientation) and could be used directly for further processing, such as DEM extraction. For 2005 an ortho-image and high-resolution DEM was provided. The $RMSE_{xyz}$ for provided block adjustments is better than 2 m for all five epochs. Full details about the data can be found in Fox and Czifersky (2008). All photographs are pan-chromatic, except the 2005 imagery.

For *Ryder Bay*, located west of Rothera station, an ortho mosaic and a 5 m resolution DEM was provided together with the corresponding photogrammetric project file and original imagery. This dataset was derived from the same 2005 BAS campaign as described above and could be used without any further processing. For the same area aerial imagery from 1989 was provided. Full camera calibration was available. However,

ground control for the Ryder Bay area was not available. For the area around *Fossil Bluff* station, located on Alexander Island, areal imagery from 1995 was made available together with full camera calibration and orientation parameters as well as GPS ground control observations. For some epochs (1989 and 1995) the original photogrammetric project files and previously extracted were lost so that reprocessing was necessary.

3.1.3 IceBridge

For limited areas of the AP high resolution altimetry data is available from the NASA IceBridge mission. The airborne mission was launched in 2009 to fill the gaps in measurements between the ICESat-1 and upcoming ICESat-2 satellite mission (Studinger et al., 2010). The data acquisition and availability is focused on areas of rapid change e.g. the Larsen A and B embayments. Currently most of the available datasets cover small portions of the eastern and northern parts of the AP. Data for the western AP has not been available before the writing up up stage of this thesis and, thus, was not included in this research. It should be noted that this data offers strong potential for use as modern reference data and is used in many interesting research projects (e.g. Shepherd et al., 2012; Qi and Braun, 2013). Each IceBridge flight has several instruments (altimeter, radar, gravimeter) on board. Of interest is the Land, Vegetation and Ice (LVIS) sensor, a laser altimeter that can map large areas of glacier zones from high altitudes, and the Airborne Topographic Mapper (ATM), which is a lidar system. Currently this is the highest resolution data available for the AP, although the coverage is limited. Data and conversion tools are freely available from NSIDC (NSDIC, 2013).

3.1.4 Meteorological and supplementary data

Meteorological data for Antarctica is available online (SCAR, 2013b) and maintained by BAS. Long-term and dense meteorological records for the AP are rare (see Section 2.1.1). Temperature data from three stations (Rothera, Faraday and Esperanza) across the AP that have long-term temperature records were used. For these stations the positive degree days (PDD) have been calculated (see Section 6.2) for comparison with glacier change results. For the PDD calculation, detrended standard deviations for the monthly

and seasonal temperatures were provided by Dr Gareth Marshall at BAS. Oceanic temperature data was provided by Prof Michael Meredith at BAS.

Additional datasets that were used are the LandSat Imaging Mosaic of Antarctica (LIMA; USGS, 2012) and data from the Antarctic Digital Database (ADD; SCAR, 2013a) which provides land and ice shelf outlines as well as place names for the production of maps. The National Snow & Ice Data Center (NSIDC) provides a complete Antarctic DEM at resolution of 200 m, 400 m and 1 km which is derived from radar altimetry and airborne radar surveys (Liu et al., 2001). NSIDC (NSIDC, 2011) also provides datasets containing the grounding line (GL) position around Antarctica. Here the data of Scambos et al. (2007) (MOA GL) and Bindschadler et al. (2011) was used as these are more complete for the AP than the dataset derived by Rignot et al. (2011a).

The World Glacier Inventory (WGI) currently lists approximately 1000 individual glaciers for the AP (data also available via NSIDC). Glacier outlines for Antarctica are available from the GLIMS webpage (GLIMS, 2012) as part of a global glacier inventory (Arendt, 2012). However, these are incomplete for the central parts of the Antarctic Peninsula. Most of the available outlines cover the most northern part of the AP as a result of the study of Davies et al. (2011). Derived glacier outlines from the study presented were submitted to GLIMS/WGI to extend existing records.

3.2 Data (pre-)processing

The data processing was carried out on a 64bit PC with 6 GB RAM and Intel QuadCore Q9300 CPU. A range of software packages (explained in the following) was used for processing due to different data formats and processing requirements. Licenses for all software products were held by the School of Civil Engineering and Geosciences or Newcastle University. Data was stored locally.

3.2.1 Processing of satellite data

The raster satellite data, was processed in *ITT ENVI 4.6.1.* ASTER DEMs were generated from Level 1B imagery with the additional *ENVI DEM Extraction Module*

(Version 4.7) unless they were already provided as Level 3 products. The nadir image (band 3N) was used as the left, the backward image (band 3B) as the right image in the stereo-pair. The left image is used as the basis during image matching in the DEM extraction module and the nadir image contains less geometric distortions. Minimum and maximum scene elevations were estimated from the RPCs or available topographic datasets. Elevations were corrected for geoid height (EGM2008; GFZ (2010)). For each image pair a minimum of 50 tie points was automatically generated. The search window size was 81 pixels and the moving window size was 11 pixels. The generated tie points were examined individually and manually corrected or removed if necessary. In the areas of interest additional tie points were included if they improved the result. Final tie points were accepted when the resulting y-coordinate parallax was less than 0.5 pixel. For DEM extraction, which uses automatically generated epipolar[2] images, the moving window size for corresponding pixel was set to 7x7 pixels and the minimum correlation value was 0.7. Given the steep terrain, the terrain relief option was set to high and the terrain detail was set to the highest level. Background values were set to -9999. The output resolution was set to 15 m and elevations were stored in integer values. Given that no ground control data was available, DEMs are relative DEMs. Additionally, for each scene an ortho-image was produced from the extracted DEM and the VNIR bands. Results were projected into UTM/WGS84 and stored in GeoTiff format. No filtering to the DEM product was applied. For conversion of the DEM raster into xyz point format GDAL[3] was used. Point files were clipped in *Microstation TerraScan*. The processing of the ASTER data is relatively straight forward compared to the archive imagery. The reason for that is, the calibration and metadata is more complete and professional remote sensing software allows almost automated processing with sufficient user control. SPOT SPIRIT DEMs were provided as geo-referenced raster files by E. Berthier.

[2]Images with known stereo-orientation

[3]The Geospatial Data Abstraction Library (GDAL) is a translator library for raster geospatial data formats. See GDAL (2010) for more detail.

3.2.2 Processing of aerial photography

For the photogrammetric processing (interior, exterior, and absolute orientation) of the aerial imagery *SOCET SET 5.5.0* was used. For the automated DEM extraction the SOCET SET add-on *NGATE* was used. Individual frames and image blocks for each site were processed using the multi-sensor triangulation (MST) module of SocetSet. The MST module allows automated triangulation and point measurement as well as bundle-adjustment. BAS provided scanned image frames together with photogrammetric project files for five epochs of Moider Glacier. This made input into SOCET SET and respective DEM extraction relatively straight forward. For the BAS frames camera calibration, flight information and partially ground control data was available.

The USGS data was selected as described previously (Section 3.1.2). For each identified area of interest between three and six image frames were downloaded depending on the size of the covered glacier. The image frames have a standard size of 9 inch (~22.9 cm). All images were checked for metadata information i.e. acquisition date, camera calibration, and flight information. For all USGS frames an acquisition date and camera focal length was found. Original full camera calibration protocols from the manufactures were unavailable for the selected USGS frames. The only available calibration information can be found in Spriggs (1966) a report on the calibration of military cameras. It provided the focal length and radial distortion parameters (Table 3.3). The measurement error for the calibrated focal length is specified with 0.100 mm and 0.020 mm for the distortion error. Figure 3.5 shows the typical radial lens distortion for two of the USGS camera lenses. Hothmer (1958) states height displacements for a typical Metrogon lens, as used in the Fairchild T-11 camera, of up to 1 % of the flight height if the radial lens distortions remains uncorrected. Given an average flight height of 20,000 ft (~6000 m) this would lead to errors of up to 6 m within the USGS data. To correct for unknown lens distortion parameters, i.e. for the KC-1 camera lens, a generic distortion curve, derived from many other lenses of the same type, was applied (Sewell, 1954). It was found by Sewell, who studied 276 Metrogon lenses, that the calibration curve for 74 % of the lenses varied by less than 15 µm around the average curve of all lenses. The overall difference was found to be less than 50 µm. Given a maximum

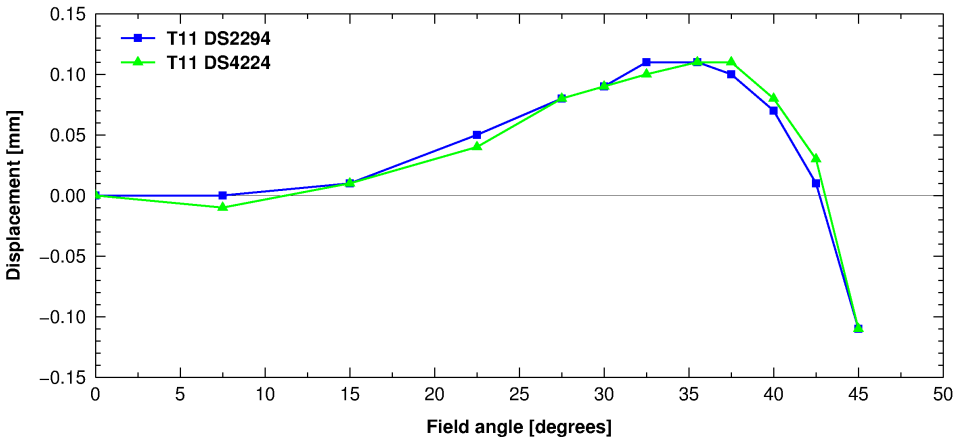

Figure 3.5: Radial distortion for two T11 camera lenses used by USGS

distortion of up to 100 µm for historical Metrogon lenses, the application of a generic curve is sensible if direct measurements are missing. For comparison, modern lenses only show radial distortions of up to 5 µm.

Information about the fiducial marks was not available which made the interior orientation not trivial. To calculate unknown calibration parameters, such as lens distortion, self-calibrating bundle adjustment (SCBA) can be used. However, this is very difficult in practice (Chandler and Cooper, 1989). Here, a new camera coordinate system was introduced with the known focal length and lens distortion parameters for each image strip to solve for the interior orientation of the USGS photographs. The USGS frames contain four observable fiducial marks in the middle of each image side. The image coordinates for each fiducial mark were measured in mm using *Adobe PhotoShop CS2* and the centre of the image was determined as the intersection between lines of opposing fiducial marks. The image centre (principle point) is assumed to be located at (0,0) and the calculated intersection point gave the respective offsets to reduce the fiducial mark coordinates. The final fiducial marks were then calculated as the average of the reduced fiducial marks. The described lack of calibration information is not uncommon in studies that include archive imagery. The work-around as described here was successfully adopted in other studies (Miller, 2007; Dornbusch et al., 2008; Fox and Czifersky, 2008). In the absence of radial distortion parameters a generalized distortion curve was applied after Sewell (1954).

The height over ground for the USGS image strips had to be estimated as no information was available. For this, the image distance d and ground distance D between two distinctive features was measured in the scanned archive image and a georectified LIMA image respectively. Together with the focal length c the height over ground H was calculated assuming $\frac{c}{H} = \frac{d}{D}$ (Kraus, 2007). Given a scanning resolution of 1000 dpi and an average flight height of approximately 5800 m the estimated ground sampling distance (GSD) is around 1 m. The measurement of fiducial marks for the interior orientation was done manually and accepted when the RMS value was better than 0.5. For the exterior orientation at least 25 tie points per image pair were measured automatically. The resulting tie points were manually examined and adjusted or deleted if necessary. Additional points at varying elevations were added to strengthen the orientation solution. Distinctive features such as mountain ridges, rock outcrops or features on stable sea-ice were utilised.

To initiate the absolute orientation of the historic image blocks a minimum of six 'artificial ground control' points were extracted, at the location of distinct surface features, from the ASTER ortho-image and DEM or were available from the modern stereo-imagery DEMs. At first, a suitable point in the orthorectified ASTER image was selected. Then the historical image was checked for point correspondence. A control point was accepted and selected when the ASTER DEM did not show blunders within the area of selection. The control points were regularly distributed over the image block and at measured at different height levels to minimize wrong orientation. Because of the high snow cover or shadowing in steep terrain it is not trivial to find suitable and stable points that can be identified for each image and epoch (James et al., 2006). The strip adjustment was accepted when the RMS residual for each image tie points was less than 1.0 and when the RMS for the control points was within the range of the ASTER DEM accuracy, i.e. less than 50 m without GCPs. After the successful absolute orientation (Figure 3.6) DEMs were generated as TINs, with an irregular distribution of points. Extraction of points on a grid basis was not applied because systematic point sampling on a regular grid is inefficient over smooth areas, such as snow covered glacier parts with low image contrast and can result in oversampling (Fox and Nuttall, 1997). Points with

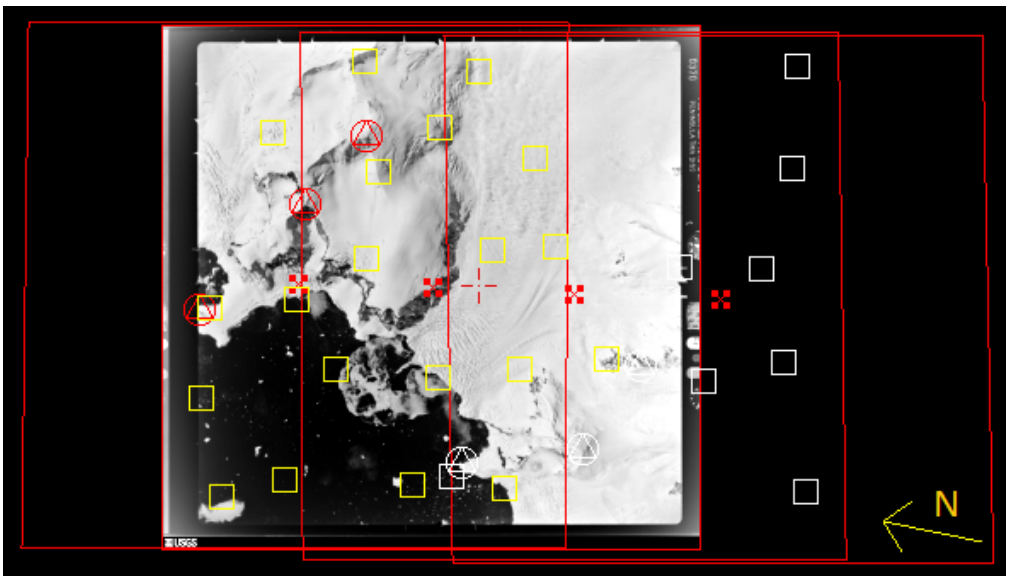

Figure 3.6: Bundle block adjustment of USGS archive imagery (1968) over Leonardo Glacier in SocetSet. Squares represent tie points, circles with triangles represent ground control points. Image footprints are shown in red together with the image centres.

low correlation values from the extraction in SOCET SET were excluded from the DEM. The extracted DEM was manually checked and edited for gross errors using a contour overlay and the figure of merit of the point extraction. The spatial coverage of each glacier is incomplete due to the combination of limited coverage of the historical data and a lack of surface features at increasing distance from the glacier front. Most of the selected glaciers are heavily crevassed at their fronts which makes these areas more suitable for photogrammetric point extraction. It is rare to have glaciers with an equally dense point measurement over the entire glacier surface. This is a notable limitation for glacier-wide mass balance assessment. After DEM extraction points were stored in an xyz file and a ortho-image was generated. Coordinates were projected into the Universal Transverse Mercator (UTM) system with WGS84 reference ellipsoid.

3.3 Accuracy and error assessment

After DEM generation the fit between corresponding DEMs was assessed. Results for the DEM error assessment and DEM differencing are presented in the following chapter. Here the theoretical background is described. In theory and under the assumption of no existing surface change or error, the elevation difference dh at all locations for two surfaces S_1 and S_2 is zero ($dh = h_{S_1} - h_{s_2} = 0$) , that is, the two surfaces are identical

$S_1 = S_2$. This is, however, unlikely. The nature of measurements (and known variables) is that they will contain some form of error. Errors in DEMs can occur in both vertical (Z) and horizontal (XY) coordinates. The accuracy analysis is often focused on the vertical error because planimetric error will produce elevation error (Fisher and Tate, 2006). The measurement of real change is only reliable to the extent at which elevation differences over stable, or non-changing, terrain can be assumed to be free of significant error and around zero. Therefore, the aim is 1) to get an estimate of existing errors and 2) to remove errors within and between datasets. The detection of errors and their underlying cause (Section 3.3.1) is not always straight forward. Errors may be random[4] or systematic[5]. They all have in common that they reduce the accuracy[6] and precision[7] of measurements and that they introduce uncertainties.

A first way to check for error is to calculate the **mean** elevation difference:

$$\mu = \bar{x} = \frac{1}{n}\sum_{i=1}^{n} x_i \tag{3.1}$$

where x_i represents a single measurement or, in this case, an elevation difference at a certain location. For a high accuracy the mean is expected to be zero or at least close to zero depending on the precision of measurements which will vary for different sensors. In the case of ASTER elevations are measured within the meter range whereas for example with Lidar measurements are are made up to the mm level. This should be considered when comparing statistics for datasets. The mean is a good first estimate for any systematic bias. If systematic errors are removed the remaining (random) errors are assumed to be normal (Gaussian) distributed around a zero mean.

There are generally two ways of describing uncertainty. One is the **standard deviation of a sample**, given by:

[4]Errors that are always present in the measurement. Random errors are unpredictable and usually small.
[5]Errors that follow some physical law. Systematic errors (also referred as bias) can be predicted, modeled and eventually corrected.
[6]Measure of the absolute closeness of an observed quantity to its true value.
[7]Degree of consistency (reproducibility and repeatability) of repeated measurements.

$$\sigma = \sqrt{\frac{1}{n-1}\sum_{i=1}^{n}(x_i - \bar{x})^2} \tag{3.2}$$

which is simply the square root of the sample variance. The other is the **standard deviation of the mean**, also called the standard error:

$$SE = \sigma_{\bar{x}} = \frac{\sigma}{\sqrt{n}} \tag{3.3}$$

which is an estimate of the standard deviation of the sample mean based on the population mean. The term standard error is somewhat ambiguous. It is generally useful to construct confidence intervals (Streiner, 1996; Ghilani, 2010). Confidence intervals indicate the boundaries within which the 'true' value lies and are a measure of accuracy. The upper and lower limits are usually calculated for plus and minus two times the standard error, which represents 95 % of the data:

$$95\% \text{ Limits} = \bar{x} \pm (SE \cdot 1.96)$$

Another statistical measure is the **root mean square error** (RMSE) which is widely used and suggested as a standard for DEM accuracy assessment (Li, 1988; National Digital Elevation Program (NDEP), 2004; Aguilar et al., 2007; Maune et al., 2007; Höhle and Höhle, 2009):

$$RMSE = \sqrt{\frac{1}{n}\sum_{i=1}^{n}(x_{ref} - x_{check})^2} \tag{3.4}$$

The RMSE is a measure of the differences between predicted or estimated values and observed values. It is based on residuals rather than errors. An error is the difference between any individual observed quantity and its true value; $e_i = y_i - \mu$. A residual is the difference between any individual measured quantity and the most probable value for

that quantity; $v_i = \bar{y} - y_i$. In the case of an unbiased estimator the RMSE is identical to the square root of the variance, also known as the standard deviation or standard error. Together, the mean, standard deviation and RMSE form a useful statistical accuracy measure of DEMs against the reference data. The reference data might be individual control points or an entire overlapping DEM with thousands of points. In addition, the sample **minimum** and **maximum** values should be stated to complete the statistical description of the data.

Before calculating the overall statistics and accuracy it is often useful to remove gross errors (also referred as mistakes or outliers). Such outliers, which might be elevation spikes or falsely measured points, can have a significant influence on the accuracy measure . The '3-sigma-rule', which removes values that are larger than $\pm 3 \cdot \sigma$, is generally a good way to remove outliers as it keeps 99.7 % of the data and often shows a significant improvement in the data quality (Aguilar and Mills, 2008; Vaze et al., 2010). A similar way to remove outliers is to apply the threshold at $\pm 3 \cdot \text{RMSE}$ (Höhle and Höhle, 2009), which was used here.

3.3.1 Error sources in (photogrammetric) DEMs

Ideally, errors are detected and removed at the time of DEM generation itself. Thus, next to the quantification of errors, knowledge about the sources of error is equally important. It can be differentiated between errors that are related to the data source itself and errors that result from processing or interpolating information derived from this data (Fisher and Tate, 2006). In DEM studies, the chosen form of terrain representation also influences the occurrence of errors.

In classic photogrammetry lens distortion or film degradation are typical errors related to the data source. Other examples might be missing calibration data or physical errors of the sensor. If uncorrected, they introduce systematic errors into the conceptional model that is used to measure real world coordinates from the data source, for example into the collinearity equation. Systematic errors can be avoided or corrected with sufficient knowledge about the sensor and technique that is applied to collect the data. However, most data, from which DEMs are generated, requires several processing steps after

collection, especially data that does not directly provide elevation information. This can produce additional or new errors. In stereo-photogrammetry, which is almost entirely performed digitally nowadays, errors may be the result of low image contrast or shadows which limit the precise identification of target or tie points in an image. Two or more overlapping images are generally not identical and will show some form of difference in the pixel value due to shadow, different illumination or cloud cover. Especially over features that lack contrast, e.g. snow or water, neighboring pixel values are often similar. This problem can be partly corrected by applying image stretching to increase contrast. Most modern digital photogrammetric software uses some form of hierarchical stereo-image correlation[8] to derive surface elevations in a (semi-)automated manner. If the correlation threshold for accepting a parallax measurement is set very low the resulting measurement might be of low certainty or wrong. Very high thresholds result in more accurate measurements but often reduce the number of points that are extracted. Image classification, e.g. of clouds or water bodies, can help to locate areas that are potentially erroneous. With a sufficient number and distribution of tie-points the success rate may be further improved.

Whether a passive or active data source is used to generate a DEM, the relative accuracy is of highest importance because it shows how well the actual terrain is represented. It is typically that with increased terrain slope and roughness the elevation accuracy decreases because of an uncertainty in the horizontal coordinates. When elevations are measured from aerial stereo images the accuracy depends mainly on the flying height, focal length of the camera, surface slope and the accuracy of images measurements (Kraus, 2007). Thus, the priority is to minimize error that will affect the accuracy of each measurement relative to each other within the DEM. The absolute orientation of a DEM is generally established by using adequate and well-distributed ground control points or another DEM with known reference. If such information is missing or wrong, the absolute accuracy will be reduced. In this study, ultimately, elevation differences are

[8]The pixel values within a defined reference window, e.g. 3x3 pixel with a central pixel, are compared (correlated) with the pixel values inside a moving search window until the correlation is above a certain threshold and the pixels are found to be corresponding. The search is often performed hierarchically, that is, the image resolution is stepwise increased to allow faster search. In theory the corresponding pixels are found along the epipolar line, a line that is on the plane which is formed by the two perspective centres and the object point.

computed. It is therefore important, that elevations that represent the same relative location on the ground are compared. This underpins the importance of DEM co-registration before any elevation change is assessed.

3.3.2 Geostatistics

DEMs are often the result of second-level processing or have been further processed before use e.g. filtering or re-projection. If the original transformation equations or acquisition parameters are unknown, physical error modeling becomes difficult. In this case, statistical modeling of errors is applied and can be used globally for different types of elevation datasets (Nuth and Kääb, 2010). So far only simple elevation differences have been examined. The calculation of statistics purely based on elevation differences does not provide information about the spatial distribution of errors. In addition, errors are usually assumed to be independent of each other when global statistics are calculated. It is, however, possible that the accuracy varies spatially and that existing errors are correlated within space or with specific terrain characteristics such as slope, aspect or elevation. In this case, an analysis of the spatial distribution and dependency of errors is useful and adds additional value to the accuracy assessment. Geostatistics is a specific field of statistics that deals with spatial datasets and utilizes statistical measures that describe the distribution of natural variables in space (and time). Geostatistical analysis is used in various applications including geology, glaciology, hydrology or soil science (Webster and Oliver, 2007) and allows to search for anomalies, to predict data at unknown locations, e.g. in kriging, or to analyse uncertainties. The latter is of specific interest here.

Elevation dependent bias

In more complex cases the elevation differences between DEMs show correlation within the spatial domain. This introduces biases that are more complex and that can have a significant effect on the accuracy. Large-scale biases between DEMs, e.g. constant elevation offsets, can be removed relatively well but stochastic, small-scale, differences are more difficult to detect. One example is an elevation dependent bias. Such a bias has

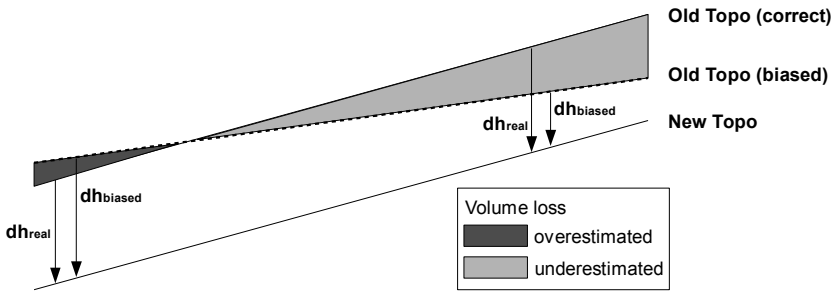

Figure 3.7: Effect of over- or undererstimation of glacier elevation change due to elevation-dependent bias. This example is based on the case that constant lowering at all altitudes has occurred over time. (modified after Berthier et al. (2006))

been reported within the SRTM data set by Berthier et al. (2006) and differences over ice-free areas of up to 10 m/1000 m were found, with an underestimation at higher elevations. Similar biases, up to 20 m/1000 m, have been found in DEMs derived from SPOT5 and ASTER (Berthier et al., 2004, 2007; Racoviteanu et al., 2007; Kääb, 2008; Nuth and Kääb, 2011). This can result in the over- or underestimation of glacier change, which can then lead to false assumptions about the change ((Berthier et al., 2010), see Figure 3.7).

An elevation dependent bias may originate from inaccurate satellite parameters (sensor model), failure in the image matching process or an uneven distribution of ground control points (Toutin, 2002; Berthier et al., 2004, 2007; Nuth and Kääb, 2010, 2011). For ASTER the steep north-facing slopes often show elevation errors as they are missed by the back-looking sensor (Kääb et al., 2002). Together this can lead to an incorrect scaling of the z-component during DEM extraction (Nuth and Kääb, 2011) from ASTER data. The origin of bias in the SRTM data is assumed to be a combination of different radar penetration depths and the spatial resolution of the SRTM DEM product (Berthier et al., 2006; Paul, 2008). The characteristics of ice and snow have an influence on the penetration depth of the C-band radar signal from the SRTM sensor. Over dry, cold firn the radar signal can penetrate up to 10 m into the snow and therefore the measured surface elevation value becomes biased (Rignot et al., 2001a). The resolution-dependent component is related to the fact that elevations of steep ridges/mountain crests, which are more frequent at higher altitude, are underestimated at coarser resolution. In reverse, an overestimation at lower altitude can be found where steep slopes are more related to

gorges or crevasses (Paul, 2008). Therefore, the comparison of DEMs with different spatial resolution should be taken into consideration when checking for biases (Gardelle et al., 2012). However, as noted by Möller and Schneider (2010) the effect of steep slopes is less pronounced over glaciated terrain because a glacier surface usually exhibits less steep slopes. Thus, it is difficult to apply a correction of an elevation-dependent bias that accounts for both the glaciated and non-glaciated terrain. If an existing bias over ice-free areas differs from any bias over glaciated areas artificial errors would be introduced over the glacier surface when corrected globally. Often corrections are based upon measurements over ice-free terrain.

Whether an elevation-dependent bias is apparent or not, it should be considered and estimated before the calculation of elevation changes. However, some studies do not account for this (Rignot et al., 2003; Muskett et al., 2009; Sund et al., 2009). In most studies that search for vertical bias (Racoviteanu et al., 2007; Berthier et al., 2007; Kääb, 2008; Nuth and Kääb, 2010; Berthier et al., 2010; Pieczonka et al., 2011), a polynomial function is fitted into the vertical differences over non-glaciated terrain. This polynomial is then applied to all elevations to remove or minimise the bias. In all cases, an exact DEM co-registration is required to ensure that the same location on the ground is compared. To check for elevation-dependent bias it is useful to plot the vertical differences against elevation. If such a bias exists corrections can either be applied by fitting a polynomial or linear function or ideally it can be removed within the DEM co-registration process. A direct correction within the co-registration process would offer increased flexibility for future use with a range of ASTER, photogrammetric and other DEM surfaces. Section 3.4.2 addresses this aspect.

Spatial distribution of errors and uncertainty

In Section 3.3 a simplistic formula for quantifying the uncertainty was given. However, if elevation differences between DEMs are correlated with each other, the uncertainty of measurements degrades, especially when they are integrated over an area. When using the standard error (Equation 3.3), to express uncertainty, simply dividing the standard deviation by the number of samples would underestimate the error when spatial

auto-correlation exists (Nuth et al., 2007). This is because measurements cannot be seen as independent in such a case, that is, there is significant variation in the variance[9] in space. Some authors assume the elevation errors to be uncorrelated (Thibert et al., 2008) while other studies assume total correlation (Cox and March, 2004; Cogley and Jung-Rothenhäusler, 2004). It is therefore important to check for existing correlations and, if necessary, to adjust the uncertainty estimate. The uncertainties are often estimated over stable bedrock areas. Such areas may not represent the same surface properties as found over glaciated terrain especially if the stable terrain is steep. Spatial auto-correlation may occur at different scales and depends on various parameters, such as recording geometry, slope and terrain roughness, or surface-type properties (Thibert et al., 2008; Rolstad et al., 2009). Rolstad et al. (2009) found three correlation scales in photogrammetrical data at a few hundred meters, at a few kilometers and at tens of kilometers. The shortest scale is assumed to be related to the digital photogrammetrical-matching in various terrain types. The intermediate scale is presumably related to weak relative orientation of the stereo blocks. Errors in the absolute orientation are likely to be expressed in largest scale correlations.

Spatial auto-correlation is usually measured by calculating a variogram (or semi-variogram), a function that describes the degree of spatial dependence of a spatial random field, e.g. elevation as a function of location. The concept is based on the first principle in geography, which says that neighbors are equal or similar. The typical graphical representation of a variogram (Figure 3.8) shows the (semi-)variance in relation to the spatial distance (so called lag distance) between measurements across realizations of the field. If no spatial dependence in a stationary random field exists the variogram is constant everywhere, except at the origin where it is always zero. It is distinguished between an empirical and theoretical variogram. The latter is a usually estimated by fitting a model (e.g. spherical, exponential, Gaussian) into the empirical variogram, which is derived from the available data itself. While the empirical variogram does not necessarily has be to be valid and positive the theoretical variogram is. The theoretical (modeled) variogram allows a better generic description of the data and

[9]Measure of how far a set of numbers is spread out. Unit σ^2. Co-variance is a measure of how much two variables change together.

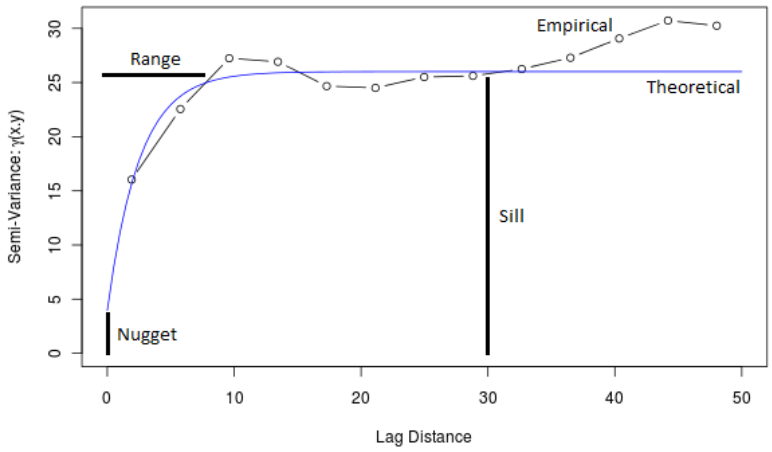

Figure 3.8: A semi-variogram (binned) showing spatial auto-correlation between values of a random field. Nugget, range and sill are descriptive parameters derived from the theoretical variogram that is modeled from the respective empirical variogram.

interpolation of values at unknown locations, similar to regression analysis. The model can be described with three parameters: nugget[10], sill[11] and range[12]. The sill parameter allows an estimate of the variance in the data. The range gives information about the distance over which measurements are assumed to be correlated or uncorrelated. For a more complete introduction the reader may refer to Cressie (1993) or Webster and Oliver (2007). The variogram is also used in kriging to assign weights to known values from which values at unknown locations may be interpolated. Various software packages, such as *ArcGIS* or *R*, allow to calculate semi-variograms and variogram model fitting. Here the *geoR* package of *R* was used.

To calculate a robust uncertainty estimate, the method of Rolstad et al. (2009) was applied because it takes spatial auto-correlation and averaging of elevation differences into account and can be adopted for various surface types, if needed. Furthermore, it can give information on the cause of error by investigating the scale of correlations. The variogram of elevation differences over stable terrain is derived at maximum correlation distances of 1 km and 5 km to check for different scale effects. Large scale effects over tens of kilometers are not assessed here because such large distances are not covered by the data. Here the uncertainties are estimated over stable terrain only because the

[10] Variance on scales less than the sampling distance, that is, relates to co-location or effect below the minimum distance between points.
[11] Limit of the (semi-)variance towards infinite lag distances.
[12] Distance at which the differences in the variogram from the sill value becomes negligible.

glaciated areas are assumed to show large surface changes that have substantial spatial autocorrelation of geophysical origin. The standard errors over the glacier surface are assumed to be lower than those over steep bedrock. Using the theoretical variogram parameters, the variance of the elevation difference $\sigma^2_{\Delta z}$ is calculated with:

$$\sigma^2_{\Delta z} = c_0 + c_1$$

where c_0 is the nugget and c_1 the sill. The uncertainty of the spatially averaged elevation difference for an area is then calculated with:

$$\sigma_A = \sqrt{\sigma^2_{\Delta z} \frac{1}{5} \frac{A_{cor}}{A}} \tag{3.5}$$

where A_{cor} is the correlation area, defined as $A_{cor} = \pi a_1^2$. a_1 is the correlation range parameter as derived from the theoretical variogram. A is the area over which the differences are measured. The uncertainty estimate from Equation (3.5) is assumed to be valid when the area over which elevation differences are estimated is larger than the determined correlation range (see Rolstad et al. (2009) for more detail).

3.4 Surface matching

For an accurate determination of surface elevation change, an accurate fit between corresponding DEMs is essential. This requires that only elevations at corresponding locations are compared. Otherwise errors, e.g. shifts or rotational offsets, between elevation datasets will bias the results. The lack of ground control, in the Antarctic Peninsula, is limiting the possibility for an accurate absolute orientation of each dataset. For most DEMs that are derived from satellite data or GPS controlled areal imagery, the absolute orientation on the ground can be approximated from the satellite orbits or GPS positions of the aircraft. This approximation can differ for each dataset and result in offsets between DEMs. Offsets may also originate from other causes, e.g. different

datums or biases in the data. The fact that multi-source, multi-temporal and multi-resolution datasets are used makes this problem complex. As previously mentioned, the relative fit between DEMs is most important because absolute errors in rotation or translation have no bearing on volume change measurements. This is not to say that the absolute orientation is less important but it can be seen as a secondary problem in this case. Therefore, if the relative fit between DEMs, as assessed by the statistical methods described above, is found to be of poor quality (high RMSE values), improvement is needed. This can be achieved by DEM co-registration, which is commonly referred to as surface matching. The aim is to transform corresponding datasets into one common reference frame so that accurate measurements are possible and errors are minimized. These techniques do not rely on ground control points as they use all surface points to achieve co-registration. Here, the term surface is used in analogy to DEM.

3.4.1 Previous work on DEM matching

Various surface matching techniques do exist and a useful overview can be found in Grün and Akca (2005). Most surface matching techniques have in common, that they aim to minimize differences between corresponding datasets in a classical iterative least-squares fashion. Thereby, differences are seen as residuals with a mean of zero at the best fit position. In general, one DEM has a relatively good absolute orientation (e.g. due to higher resolution or ground control) and is chosen as *reference surface*. In most cases, this will be the DEM with the best known accuracy and resolution. The surface that is co-registered is referred to as the *matching surface*. Depending on the surface representation, two different problems need to be addressed for DEM co-registration. First, a relationship between surface features (*correspondence problem*) must be established and secondly a set of transformation parameters (*transformation problem*) must be found so that the differences between the two surface descriptions are minimized (Schenk et al., 2000). There are differences in the available techniques and their best use depends on the application and the type of surfaces that are co-registered. Here the focus is on DEM matching.

Many approaches in DEM matching are based on the principle of least-squares image correlation which was developed by Förstner (1982) and Gruen (1985). An image can be described as a 2.5D surface with a regular (gridded) distribution of grey values, where the values are a function of location. In image matching grey level differences are minimized to find the best fit, or match, between an image patch and a reference image. While the reference image is held fixed, the matching image patch is moved, or transformed, across the reference image until a match is found. This is for example used to track features between images or to extract features from stereo-imagery. Without a sufficient signal the solution may converge slowly or towards a wrong solution (Gruen, 1985).

Ebner and Strunz (1988), as well as Rosenholm and Torlegard (1988), were the first who adopted the image correlation principle for the use of DEMs as control information. Similar approaches, based on gridded data, were developed by Karras and Petsa (1993); Pilgrim (1996); Mitchell and Chadwick (1999); Zhang and Cen (2008). In a DEM elevations are also a function of location, i.e. $z = f(x,y)$. Thus, in analogy to image matching, DEM matching aims to minimize (vertical) surface separations, along the z-axis, at corresponding points across the surface. DEM matching, or co-registration, is achieved by iteratively applying a defined coordinate transformation, e.g. a seven-parameter 3D conformal transformation (three translations, three rotations, and one scale), to the matching surface until convergence is achieved, that is, the differences to the reference surface approach a global minimum. Local derivatives, which are gradients of the surface as explained latter, are used to direct the solution to a global minimum. In order to derive surface gradients a continuous surface representation or interpolation is required.

Maas (2000) presented a surface matching technique that is based on a irregular distribution of points, which is for example found in laser scanning data. It estimates a translation vector with three parameters, also minimizing the differences along the z-axis, from the data points in a triangular irregular network (TIN) structure. This three-parameter transformation can, for example, be used to correct for positional and vertical shifts between corresponding airborne laser scanning strips. Similar approaches

were presented by Postolov et al. (1999); Habib and Schenk (1999); Martin et al. (2005); Kraus et al. (2006).

Nuth and Kääb (2010) presented a technique that achieves DEM co-registration by applying a three step correction. First, translational offsets are corrected by calculating a shift vector which is derived from differences in slope and aspect. This technique works well where the offsets can be corrected by simple shifts between the surfaces but it does not account for rotational offsets. Secondly, remaining differences are corrected by fitting a polynomial into the elevation differences, e.g. to correct for elevation dependent bias. Finally, biases that may result from satellite specific errors are corrected, again using polynomials.

Akca (2004) developed an approach that minimizes the Euclidean distances between two or more fully 3D surface patches, using a seven-parameter 3D conformal transformation. It allows the matching of multi-scale, real 3D surfaces of arbitrary orientation and is based on the same principles of least-squares correlation. It has been shown that this approach is well suited for the co-registration of multi-quality and multi-resolution DEMs (Akca, 2010). The minimization of the Euclidean distance as opposed to the vertical distance is an important difference to the approaches described previously. Schenk et al. (2000) compared both minimization approaches and found that with increasing slope angles the Euclidean distance approach performs better. This is explained by fact that the Euclidean distance is independent of the slope angle, because it minimizes differences along the surface normal. Minimization along the z-axis produces larger differences with increasing slope. This can have an effect on the convergence behavior, especially for angles larger than 50° (Schenk et al., 2000). This is relevant for studies with steep topography as it is typically found in the Antarctic Peninsula.

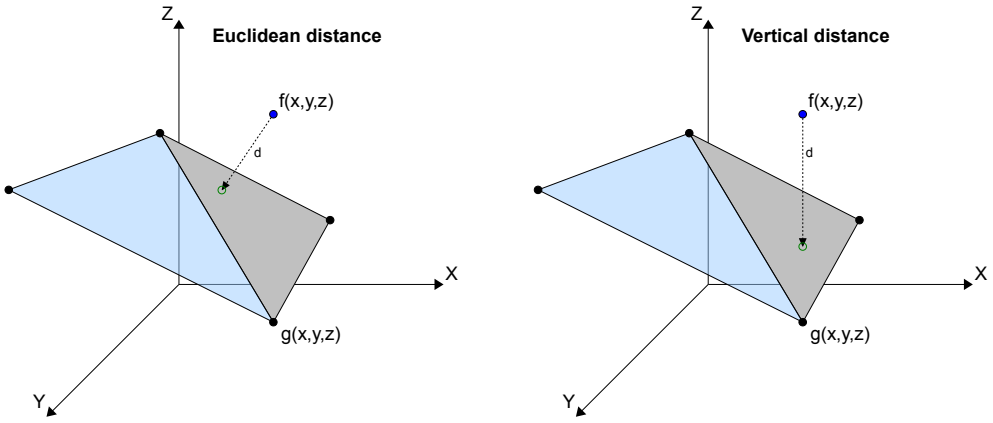

Figure 3.9: Euclidean and vertical distance between a point and a plane. The reference surface g(x,y,z) is represented as a TIN, that forms planes. This TIN is then used as the basis to calculate (interpolate) corresponding point pairs between the matching surface f(x,y,z) and the reference surface.

Another popular surface matching technique is the Iterative Closest Point (ICP) algorithm, developed by Besl and McKay (1992). The algorithm is aimed to find pairs of nearest points within 3D point clouds. The solution, usually a six-parameter rigid transformation, is achieved by iterative minimization of the Euclidean distances between existing corresponding points. Many variants of this algorithm exist, e.g. the point-to-tangent plane technique from Chen and Medioni (1992). It is often applied in computer vision but other examples can be found in object reconstruction and medicine (e.g. Johnson and Hebert, 1998; Chetverikov et al., 2005). It is well suited for fully three-dimensional surfaces and has the advantage of being insensitive to the viewpoint direction and the relative initial orientations of the surfaces can be random. However, this approach is not always ideally suited for surveying applications where datasets are often only 2.5D, like DEMs. Furthermore, ICP algorithms are unsuited for cases where datasets contain regions of outliers or are subsets of the other, meaning parts of separate surfaces may not directly correspond to each other (Besl and McKay, 1992; Zhang, 1994; Li et al., 2001). This situation is likely to occur in the study presented here as surface change is expected. It is also unsuited for matching of multi-scale surface patches (Akca, 2004) and less efficient for regular gridded data formats, which are common in DEM studies (Zhang and Cen, 2008). Therefore, the ICP algorithm is not further considered in this work.

To solve for offsets between DEMs in this study, an in-house iterative robust least squares (IRLS) matching approach is used. It allows to match, both, irregular and regular 2.5D datasets and has been developed at Newcastle University by Buckley (2003) and Miller (2007). It is is based on the early works on DEM matching of Ebner and Strunz (1988); Rosenholm and Torlegard (1988); Pilgrim (1996). The matching approach estimates a seven-parameter 3D conformal transformation by iteratively minimizing the z-differences between points of the matching surface and a TIN structure of the reference surface. Robust estimation is achieved by using a weighting function, based on a maximum-likelihood operator, which is embedded in the software in order to down-weight points which display large residuals. This robust matching strategy allows to deal efficiently with possible terrain changes (Pilgrim, 1996; Grün and Akca, 2005; Miller, 2007; Zhang and Cen, 2008), because local discrepancies between surfaces will influence the estimation of the transformation parameters, and where the effects are significant, conventional least squares approaches may fail to converge, or may converge to an erroneous solution (Li et al., 2001). For more details on robust matching the reader may refer to Pilgrim (1996) or Hoaglin et al. (2000). The algorithm has been proven to work successfully in studies of coastal erosion (Mills et al., 2005; Miller et al., 2008) and glacier dynamics (Miller et al., 2009).

However, as previously noted for terrain with steep slopes the minimization of the Euclidean distance may yield better results. Steep terrain is typical for the Antarctic Peninsula. Thus, the available algorithm of Buckley (2003) and Miller (2007) was enhanced to allow for minimization of, both, the vertical (Ebner and Strunz, 1988) and Euclidean distance (Akca, 2004). In addition, it has been extended to account for directional scales, i.e. elevation dependent bias, if required. In the following the theoretical background and development is outlined. For a full overview on the theory behind surface matching the reader may refer to Ebner and Strunz (1988); Rosenholm and Torlegard (1988); Karras and Petsa (1993); Pilgrim (1996); Mitchell and Chadwick (1999); Grün and Akca (2005); Miller (2007).

3.4.2 Theory of least squares surface matching

Suppose we have two sets of, randomly or regularly distributed, points $S_1(x,y,z)$ and $S_2(x,y,z)$ which describe the same surface in euclidean space R^3, at different times or from different data sources. These two surfaces are identical if following functional model is fulfilled:

$$S_1(x,y,z) = S_2(x,y,z) \tag{3.6}$$

Equation (3.6) states that for each point of surface S_2, which will be referred as the matching surface, a corresponding point in the reference surface S_1 exists. In reality this case is unlikely due to stochastic or systematic discrepancies between the two surfaces. Thus, an error term (assuming normal distribution of errors) is added to the functional model, so that:

$$S_1(x,y,z) = S_2(x,y,z) + v(x,y,z) \tag{3.7}$$

Equation (3.7) are observation equations, which relate the observations $S_1(x,y,z)$ to the parameters of $S_2(x,y,z)$. To relate one surface to another in euclidean space a seven-parameter 3D conformal transformation is used (Kraus, 2007; Ghilani, 2010):

$$\begin{bmatrix} x \\ y \\ z \end{bmatrix} = sR^T \begin{bmatrix} x_0 \\ y_0 \\ z_0 \end{bmatrix} + \begin{bmatrix} T_x \\ T_y \\ T_z \end{bmatrix} \qquad \text{with} \qquad R = \begin{bmatrix} r_{11} & r_{12} & r_{13} \\ r_{21} & r_{22} & r_{23} \\ r_{31} & r_{32} & r_{33} \end{bmatrix} \tag{3.8}$$

where the terms of the rotation matrix R are defined with:

$$
\begin{aligned}
r_{11} &= cos\,\phi \cdot cos\,\kappa \\
r_{12} &= sin\,\omega \cdot sin\,\phi \cdot cos\,\kappa + cos\,\omega \cdot sin\,\kappa \\
r_{13} &= -cos\,\omega \cdot sin\,\phi \cdot cos\,\kappa + sin\,\omega \cdot sin\,\kappa \\
r_{21} &= -cos\,\phi \cdot sin\,\kappa \\
r_{22} &= -sin\,\omega \cdot sin\,\phi \cdot sin\,\kappa + cos\,\omega \cdot cos\,\kappa \\
r_{23} &= cos\,\omega \cdot sin\,\phi \cdot sin\,\kappa + sin\,\omega \cdot cos\,\kappa \\
r_{31} &= sin\,\phi \\
r_{32} &= -sin\,\omega \cdot cos\,\phi \\
r_{33} &= cos\,\omega \cdot cos\,\phi
\end{aligned}
\tag{3.9}
$$

This transformation accounts for translations T_x, T_y, T_z, rotations ω, ϕ, κ (around the X, Y and Z axes respectively) and one global scale s. Other types of transformation with more or fewer parameters could be used (see Section 3.4.2). To register the matching surface S_2 to the reference surface S_1, we want to find a solution for the transformation parameters $Tx, Ty, Tz, \omega, \phi, \kappa, s$ so that the differences d between the surfaces become zero or minimal. This minimization problem is expressed as:

$$
\sum_{i=1}^{m} d_i^2 \rightarrow min \tag{3.10}
$$

where d^2 represents the squared differences between the surfaces.

Here, a point-to-plane approach is used to address the correspondence problem because a point-to-point correspondence is not directly defined when the data has a discrete or irregular structure. That is, a location with an elevation in one DEM may not have an elevation available in another DEM. Here, the reference surface is converted into a continuous surface description by generating a TIN structure (Figure 3.9) from the observed points using Delaunay triangulation. This TIN structure describes the surface in triangular planes and can be seen as a scalar field, meaning, it is possible to associate a value to each point in space, even if no direct measurement is available. This is an advantage over the earlier described ICP method which is constrained by the total number of surface points. A plane in euclidean space (R^3) is defined as:

$$S_1(x,y,z) = Ax + By + Cz + d \qquad \text{where} \qquad \vec{n} = \begin{pmatrix} A \\ B \\ C \end{pmatrix} \tag{3.11}$$

Where $\vec{n}$ is the normal vector to the plane. The correspondence problem is to identify the triangle (plane) in the reference surface that corresponds with a point in the matching surface (Schenk et al., 2000). Here two different mathematical models are used to establish the correspondence and transformation parameters between the two surface representations. The first approach minimizes the vertical surface differences (distance along the z-axis) and the second approach the Euclidean distance (distance along the surface normal). The point in the reference surface, that fulfills the mathematical model, is derived by linear interpolation on the corresponding plane. The plane equation is derived from the three points that form the corresponding triangle. The idea behind using two different approaches is to find which offers the best results for our application. As discussed previously the Euclidean approach is assumed to be superior but the vertical approach has also been proven to work successfully in similar applications. By including both approaches into the matching software (see Section 3.4.3) the surface matching options become more flexible. Figure 3.9 illustrates the two minimization approaches.

Minimization of Euclidean distance

To minimize the distance d from a point in $S_2(x_{\Delta x}, y_{\Delta y}, z_{\Delta z})$ to a point on a plane in $S_1(x,y,z)$ we calculate the distance along the surface normal $\vec{n}$ of the plane:

$$d = \frac{|\vec{n} \cdot w|}{|\vec{n}|} \quad \text{with} \quad w = \begin{pmatrix} x_{\triangle x} - x \\ y_{\triangle y} - y \\ z_{\triangle z} - z \end{pmatrix} \tag{3.12}$$

where d is a component of w along n. This can be written as:

$$d = \frac{|Ax_{\Delta x} + By_{\Delta y} + Cz_{\Delta z} - Ax + By - Cz|}{\sqrt{A^2 + B^2 + C^2}} \tag{3.13}$$

Dropping the absolute value signs and substituting Equation (3.11) into Equation (3.13) we get:

$$d = \frac{Ax_{\Delta x} + By_{\Delta y} + Cz_{\Delta z} + D}{\sqrt{A^2 + B^2 + C^2}} \tag{3.14}$$

Now $x_{\Delta x}, y_{\Delta y}, z_{\Delta z}$ are actually functions of the transformation parameters $p_i \in \{T_x, T_y, T_z, \omega, \phi, \kappa, s\}$. To solve via least squares estimation we need to linearize Equation (3.14) and Equation (3.8) since the problem contains non-linear unknowns. Using Taylor expansion, and ignoring the second and higher order terms, we get:

$$\frac{\delta d}{\delta p_i} = \frac{\delta d}{\delta x}\frac{\delta x}{\delta p_i} + \frac{\delta d}{\delta y}\frac{\delta y}{\delta p_i} + \frac{\delta d}{\delta z}\frac{\delta z}{\delta p_i} = \nabla x \cdot \mathrm{d}x + \nabla y \cdot \mathrm{d}y + \nabla z \cdot \mathrm{d}z \tag{3.15}$$

where ∇ simply represents the surface gradient (for the euclidean case) in each direction of x, y, z:

$$\nabla x = \frac{A}{\sqrt{A^2 + B^2 + C^2}} \qquad \nabla y = \frac{B}{\sqrt{A^2 + B^2 + C^2}} \qquad \nabla z = \frac{C}{\sqrt{A^2 + B^2 + C^2}} \tag{3.16}$$

Differentiation of Equation (3.8) gives:

$$\begin{aligned} dx &= dT_x + a_{10}ds + a_{11}d\omega + a_{12}d\phi + a_{13}d\kappa \\ dx &= dT_x + a_{20}ds + a_{21}d\omega + a_{22}d\phi + a_{23}d\kappa \\ dx &= dT_x + a_{30}ds + a_{31}d\omega + a_{32}d\phi + a_{33}d\kappa \end{aligned} \tag{3.17}$$

where the a_{ji} are the coefficient terms:

$$
\begin{aligned}
a_{10} &= r_{11}x_0 + r_{21}y_0 + r_{31}Z_0 \\
a_{20} &= r_{12}x_0 + r_{22}y_0 + r_{32}Z_0 \\
a_{30} &= r_{13}x_0 + r_{23}y_0 + r_{33}Z_0 \\
a_{11} &= 0 \\
a_{12} &= s(-sin\,\phi\,cos\,\kappa\,x_0 + sin\,\phi\,sin\,\kappa\,y_0 + cos\,\phi\,z_0) \\
a_{13} &= s(r_{21}x_0 - r_{11}y_0) \\
a_{21} &= s(-r_{13}x_0 - r_{23}y_0 - r_{33}z_0) \\
a_{22} &= s(-sin\,\omega\,cos\,\phi\,cos\,\kappa\,x_0 - sin\,\omega\,cos\,\phi\,sin\,\kappa\,y_0 + sin\,\omega\,sin\,\phi\,z_0) \\
a_{23} &= s(r_{22}x_0 - r_{12}Y_0) \\
a_{31} &= s(r_{12}x_0 + r_{22}Y_0 + r_{32}z_0) \\
a_{32} &= s(-cos\,\omega\,cos\,\phi\,cos\,\kappa\,x_0 + cos\,\omega\,cos\,\phi\,sin\,\kappa\,y_0 - cos\,\omega\,sin\,\phi\,z_0) \\
a_{33} &= s(r_{23}x_0 - r_{13}y_0)
\end{aligned}
\tag{3.18}
$$

Now we can form the observation equations that are suitable to solve Equation (3.7) via least squares estimation. Substituting Equation (3.17) into Equation (3.15) and using the notation from Equation (3.18) we get:

$$
\begin{aligned}
d + v(x,y,z) = \quad & \nabla x \cdot \mathrm{d}T_x + \nabla y \cdot \mathrm{d}T_y + \nabla z \cdot \mathrm{d}T_z \\
& + (\nabla x \cdot a_{10} + \nabla y \cdot a_{20} + \nabla z \cdot a_{30})\mathrm{d}s \\
& + (\nabla x \cdot a_{11} + \nabla y \cdot a_{21} + \nabla z \cdot a_{31})\mathrm{d}\omega \\
& + (\nabla x \cdot a_{12} + \nabla y \cdot a_{22} + \nabla z \cdot a_{32})\mathrm{d}\phi \\
& + (\nabla x \cdot a_{13} + \nabla y \cdot a_{23} + \nabla z \cdot a_{33})\mathrm{d}\kappa
\end{aligned}
\tag{3.19}
$$

which can be written in matrix notation as:

$$
Ax = l + v \tag{3.20}
$$

where A is the matrix of coefficients obtained from Equation (3.19) and x the vector of parameter correction. The vector l contains the observations (surface differences) and v is a residual vector. Equation (3.20) is then solved using iterative least squares adjustment. In each iteration the approximation of the transformation parameters is

applied to the matching surface until convergence between the reference and matching surface is achieved. The convergence criteria are defined by combined monitoring of changes in the reference standard deviation and changes in the corrections of the estimated parameters. If the changes are found to be insignificant the solution is accepted. These criteria can be adopted depending on the expected accuracy of the data. It can be seen from Equation (3.17), that the observations equations are highly dependent on surface gradients. This highlights that without sufficient surface gradients in the data the solution may not converge to a correct solution because the parameters are not well enough constrained. Note, that for optimization reasons the coordinate systems should shifted to the centre of the DEM position in space to avoid large x and y values when projected coordinates, e.g. UTM, are used (Pilgrim, 1996; Buckley, 2003).

Minimization of the vertical distance

The vertical distance minimization is a simplified case because it can be seen as 2.5D problem which compares elevations as a function of location. As previously mentioned it derives from image matching where corresponding pixels at the same location are compared. Thus the surface representation simplifies to:

$$z = f(x,y) = Ax + By + C \tag{3.21}$$

which also is a plane and can simply be derived from the TIN structure. To minimize the difference in the vertical component between two points in $S_2(x_{\Delta x}, y_{\Delta y}, z_{\Delta z})$ and on a corresponding plane in $S_1(x,y,z)$ we simple write:

$$d = z_{\Delta z} - z$$

Since z is a function of x,y we can also write:

$$d = z_{\Delta z} - (Ax + By + C) \tag{3.22}$$

Again, to solve via least squares we linearize Equation (3.22) and Equation (3.8), ignoring second and higher order terms, so that:

$$\frac{\delta d}{\delta p_i} = \frac{\delta z}{\delta p_i} - \frac{\delta d}{\delta x}\frac{\delta x}{\delta p_i} - \frac{\delta d}{\delta y}\frac{\delta y}{\delta p_i} = -\nabla x \cdot \mathrm{d}x - \nabla y \cdot \mathrm{d}y + 1 \cdot \mathrm{d}z \tag{3.23}$$

where ∇ are surface gradients (for the vertical case) in each direction of x, y, z:

$$\nabla x = -A \qquad \nabla y = -B \qquad \nabla z = 1 \tag{3.24}$$

Substituting Equation (3.17) into Equation (3.23) and using the notation from Equation (3.18) we can form the observation equations and get:

$$\begin{aligned} d + v(x,y,z) = \; & -\nabla x \cdot \mathrm{d}T_x - \nabla y \cdot \mathrm{d}T_y + 1 \cdot \mathrm{d}T_z \\ & + (-\nabla x \cdot a_{10} - \nabla x \cdot a_{20} + a_{30})\mathrm{d}s \\ & + (-\nabla x \cdot a_{11} - \nabla x \cdot a_{21} + a_{31})\mathrm{d}\omega \\ & + (-\nabla x \cdot a_{12} - \nabla x \cdot a_{22} + a_{32})\mathrm{d}\phi \\ & + (-\nabla x \cdot a_{13} - \nabla x \cdot a_{23} + a_{33})\mathrm{d}\kappa \end{aligned} \tag{3.25}$$

This can be again written in the matrix form $Ax = l + v$ and be used to solve Equation (3.7) via least squares estimation.

Extension with additional scale parameters

The common seven-parameter Helmert transformation (Equation 3.8) has only one global scale factor. While a global scale retains similarity of a surface it does not account for directional-dependent scales. An elevation dependent bias (see Section 3.3.2) causes directional offset and false scaling in the vertical axis of the surface. If such a bias is found in the data it needs to be addresses and, in the best case, removed. An elevation dependent bias can be complex and often polynomials are used to correct for it (Nuth and Kääb, 2010). It is mostly corrected after DEM co-registration, which is acceptable in most cases. However, by introducing an independent scale factor for the z-axis such a bias can be corrected directly in the matching process. Here, this is achieved by

implementing an optional eight-parameter affine transformation with a common scale in the *xy*-plane and one scale parameter for the *z*-axis:

$$\begin{bmatrix} x \\ y \\ z \end{bmatrix} = \begin{bmatrix} s_{xy} & 0 & 0 \\ 0 & s_{xy} & 0 \\ 0 & 0 & s_z \end{bmatrix} R^T \begin{bmatrix} x_0 \\ y_0 \\ z_0 \end{bmatrix} + \begin{bmatrix} T_x \\ T_y \\ T_z \end{bmatrix} \quad \text{with} \quad R = \begin{bmatrix} r_{11} & r_{12} & r_{13} \\ r_{21} & r_{22} & r_{23} \\ r_{31} & r_{32} & r_{33} \end{bmatrix} \tag{3.26}$$

The extension of the model with additional scale parameters should only be used if a significant bias is found. A two step process is proposed. In the first step, a potential elevation dependent bias is assessed by applying matching with the additional scale parameters. Then the significance is assessed by checking the differences in the individual scale parameters and the elevation differences with relation to elevation. If the bias is found to be insignificant (i.e. less than 1 m/1000 m) or non-existent, a re-estimation with just one global scale is performed in a second step. Otherwise the first matching solution is used. For most cases the standard Helmert transformation is recommended as similarity is guaranteed. It is possible to introduce independent scales for each direction so that the transformation becomes a nine-parameter 3D affine transformation (Palancz et al., 2007) or to use fewer parameters, for example to solve for translational offsets only. Note, that depending on the complexity of the transformation the observations equations change slightly (not all shown here). For the eight parameter transformation (Euclidean distance case) the observations equations would change to:

$$\begin{aligned} d + v(x,y,z) = \; & \nabla x \cdot \mathrm{d}T_x + \nabla y \cdot \mathrm{d}T_y + \nabla z \cdot \mathrm{d}T_z \\ & + (\nabla x \cdot a_{10} + \nabla y \cdot a_{20})\mathrm{d}s_{xy} \\ & + (\nabla z \cdot a_{30})\mathrm{d}s_z \\ & + (\nabla x \cdot a_{11} + \nabla y \cdot a_{21} + \nabla z \cdot a_{31})\mathrm{d}\omega \\ & + (\nabla x \cdot a_{12} + \nabla y \cdot a_{22} + \nabla z \cdot a_{32})\mathrm{d}\phi \\ & + (\nabla x \cdot a_{13} + \nabla y \cdot a_{23} + \nabla z \cdot a_{33})\mathrm{d}\kappa \end{aligned} \tag{3.27}$$

Robust estimation

In ordinary least squares certain assumptions about the data are made and these are assumed to be true for all observations, e.g. normality or independence. In such a case all observations may be weighted equally. This concept works in the case of surface matching when no or only minor differences between the surfaces of the same object exist. This is, however, not guaranteed when matching surfaces that partially include large differences or contain other forms of outliers. As mentioned before, DEM extraction from stereo-imagery is not free of error and noise which can result in blunders over regions that lack in contrast. Another issue is that in our case datasets are match that are not from the same sensor and where acquired at different epochs. Such differences or outliers can influence the least squares adjustment and may lead to weak or erroneous solutions (Pilgrim, 1996; Li et al., 2001).

Although, in our case the actual surface differences are of interest for mapping glacier surface elevation change, they are not beneficial for the surface co-registration itself. It is assumed that $S_1(x,y,z) = S_2(x,y,z)$. When all observations are weighted equally large outliers will influence the matching solution. To overcome this issue one option would be to remove all erroneous observations prior to the matching. This is, however, impractical because these "critical" observations are usually unknown. A better solution is to deal with outliers directly within the matching strategy. Such solutions are known as robust estimators and have been used in a range of fields. There are several robust estimation methods described in the literature (e.g. Rousseeuw and Leroy (1988); Draper and Smith (1998); Hoaglin et al. (2000)). It is beyond the scope of this thesis to describe them in detail. The reader may refer to Miller (2007) for information on the exact method implemented here. What robust estimators have in common is that they apply a weighting function to the residuals from which a weight is calculated for each observation, meaning that observations are not weighted equally. Equation (3.10) can then also be expressed as:

$$\sum_{i=1}^{m} w_i d_i^2 \rightarrow min \tag{3.28}$$

where w are the weights, and d, the least squares residuals. The resulting matrix notation for the weighted least squares is expressed as:

$$Ax = l + v, \quad W \tag{3.29}$$

where W is the associated weigth matrix and A,x,l and v are defined as in Equation (3.20) and solved analogical.

In an iterative reweighted least squares (IRLS) approach these weights are updated during each iteration. This results in faster convergence and stronger, more robust, solutions. An additional advantage is that possible outliers can be included in the matching and that less reliable observations will be down-weighted accordingly. Miller (2007) incorporated such a robust estimator, in particular a Tukey's biweight M-Estimator (also known as Maximum Likelihood Estimator), into the here described surface matching approach. It was shown that the robust estimator works efficiently with multi-temporal DEMs and has since been successfully applied in the context of coastal erosion studies (Miller et al., 2008) and glacier change assessment (Miller et al., 2009). Thus, the existing M-estimator from the precursor surface matching software has been adopted. The implemented biweight function is defined as:

$$w_b(u) = \begin{cases} (1-u^2)^2 & |u| \leq 1 \\ 0 & |u| > 1 \end{cases} \tag{3.30}$$

Where u are the standardised least squares residuals and w_b represents the weights, ranging from 0 to 1. The residuals are standardised and adjusted by calculating so called leverages (observations that can be treated as outliers) using the diagonal elements of the 'hat matrix' Hwhich can also be computed using SVD (Hoaglin and Welsch, 1978). For more details refer to Miller (2007).

3.4.3 Implementation and development

In the previous section the theoretical background of the in-house surface matching algorithm was outlined and two theoretical improvements (Euclidean distance matching,

parameter extension) were made. The algorithm of Buckley (2003) and Miller (2007) was originally implemented in a software called *3DSurf* and coded by them in *Visual Basic 6.0* in a *Windows* environment. *3DSurf* is able to handle irregular distributed point datasets and has been proven to work successfully in medium to small scale coastal and glaciological studies (Mills et al., 2003; Miller et al., 2008, 2009). However, despite its applicability, the *3DSurf* software has some specific drawbacks that limit its use for large scale assessment of glacier volume change in the Antarctic Peninsula. Before the theoretical improvements were included, existing limitations were identified and, where possible, improved or removed.

Requirements

The *3DSurf* software does not directly perform the Delaunay triangulation of the reference surface, which is needed to describe a continuous surface and to interpolate surface points. Till now, the triangulation had to be calculated using *Triangle* (a freely available Delaunay triangulation algorithm developed at Carnegie Mellon University, USA, by Shewchuk (1996)) and then a file containing the triangulation structure was imported into the *3DSurf* software. This is an additional pre-processing step which could be removed. The run-time of the software is relatively slow because every point in the matching surface is compared with each triangle in the triangulated reference surface. The currently implemented point-in-polygon search checks firstly whether a point on the matching surface falls within the convex hull of the reference surface, and secondly into which triangle of the reference surface the point falls (Miller, 2007). This is a very time consuming task and computationally inefficient. Once the correct triangle is found, the corresponding point on the reference surface is interpolated.

However, the point-in-triangle search becomes problematic when Euclidean distance matching is introduced. The minimization of the Euclidean distance is assumed to be advantageous over the vertical distance approach in steep terrain (see Section 3.4.4), as it often occurs in the AP. In this case a point on the matching surface may not directly correspond to the triangle into which it falls in a 2-dimensional space, as illustrated in

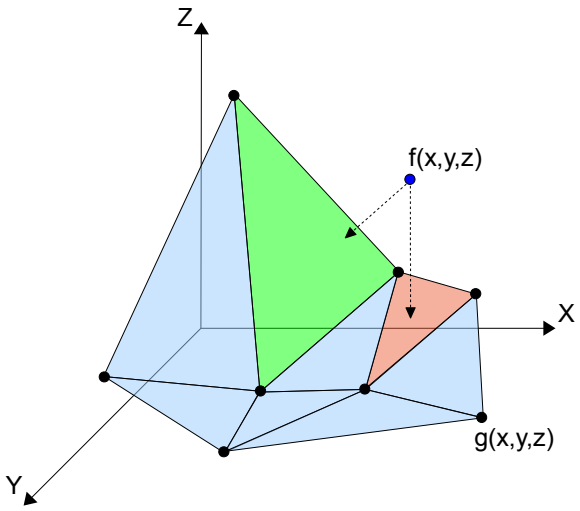

Figure 3.10: Problem of finding the corresponding triangle in the reference surface. In the case of a 2-dimensional point-in-triangle search, the wrong triangle may be selected when the Euclidean distance is minimized.

Figure 3.10. Thus, an efficient 3-dimensional search is needed when Euclidean distance matching is to be included.

Due to the slow processing and long run-time the number of points is another limiting factor, especially when large datasets are used. The more points are included in the matching, the longer the code has to run ($O(n \log n)$ where n is the number of points). For instance, matching a surface with 50,000 points to a similar reference surface takes up to 16 h with *3DSurf*. This is a particular problem of surface matching algorithms. For example for the ICP algorithm Besl and McKay (1992) report that finding the point correspondences consumes 95% of the run-time.

The *3DSurf* software would benefit from a functionality that allows batch processing, meaning that multiple datasets can be matched to the same reference surface without the need for 'external' triangulation or user input for each individual match. This is particularly useful if a user has data from more then two time steps or wants to perform matching with different settings. Also, the software does not automatically compute surface differences between the input surfaces which is required later to assess change. The software is tied to the *Microsoft Windows* environment due to coding in *Visual Basic*.

Therefore, in order to improve the performance and functionality of *3DSurf*, in the context of large datasets, the following improvements were required:

- Calculation of Delaunay triangulation within the software.
- Ability to handle large datasets with more than 1,000,000 points.
- Improved run-time and optimized spatial (3D) search of corresponding points.
- Batch processing for matching of surfaces.
- Improved functionality and platform independent, easy-to-use, interface.

Recoding and computational acceleration

To realize the above mentioned improvements a complete recoding of the surface matching software was decided. The improved version was called *SMT (Surface Matching Tool)* and has been coded in C++, a cross-platform programming language. While a complete recoding is very work intensive it also has various advantages which will become evident in the following. The realization of the the *3DSurf* software in Visual Basic constrains its use to the Windows environment. By using a platform independent language, such as C++, the software can be run on both Linux and Windows environments. Another advantage of C++ over Visual Basic is, that various well established open-source libraries exist in C++ that enable faster performance and computation. In particular, parts of the *Computational Geometry Algorithms Library* (CGAL, 2013) were implemented to perform spatial computation and the *BOOST* (BOOST, 2013), *BLAS* (BLAS, 2013) and *LAPACK (LAPACK, 2013)* libraries have been implemented to perform large matrix computations, such as the singular value decomposition (SVD) to solve the least-squares problem. SVD is particular useful for large matrices (Golub and Reinsch, 1970; Arun et al., 1987). The actual differences in the code for Euclidean and vertical distance matching are minimal.

The Delaunay triangulation process (see Boissonnat et al., 2002; Hert and Seel, 2012) has been directly implemented within the *SMT* software and is now automatically performed within the matching strategy. To enable faster spatial computation of corresponding points and distances queries between the matching surface and reference surface, an AABB tree is calculated for the reference surface (see Alliez et al., 2012b). An AABB tree (Figure 3.11) takes a geometric data structure, i.e. a 3D point cloud, and

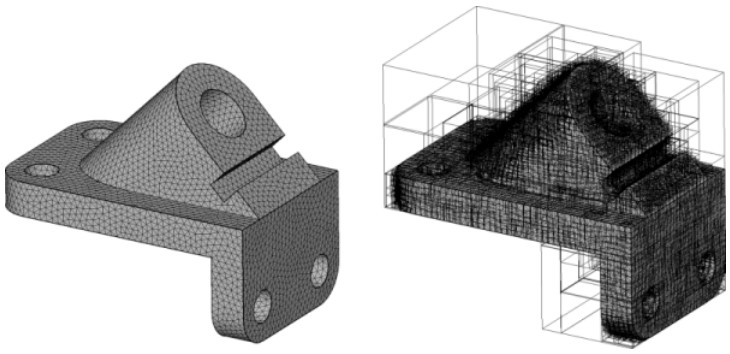

Figure 3.11: AABB tree. Left: surface triangle mesh of a mechanical part. Right: AABB tree constructed.(Alliez et al., 2012b)

converts it into primitives. From these primitives a hierarchy of axis-aligned bounding boxes (AABBs) is constructed. Based on this hierarchy, faster intersection and distance queries are possible. Similar partitioning methods, such as octrees, are commonly applied in 3D studies (e.g. Barber et al., 2008 or Grün and Akca, 2005).

Another possibility to improve performance is to reduce the number of points, that are included in the matching, by using surface simplification techniques (Garland and Heckbert, 1997). However, this can be a risk, in particular when surface gradients are lost. Surface simplification was not directly implemented into the matching strategy. Instead, the software includes an optional tool that allows a grid based simplification of (regular or irregular) point clouds (Alliez et al., 2012a). The user defines a particular grid size and then from each grid cell one arbitrary point is chosen. This reduces the number of points in cells that contain many points. For best use, the size of the cells should be set relatively small. The simplified points can then be used in the matching.

The user interface (Figure 3.12) was developed in *Qt*. The interface, as built, offers the user the chance to directly select the number of requested parameters for the matching. The user can perform matching based on three parameters (translations only), six parameters (translations and rotations), seven parameters (translations, rotations and global scale), eight parameters (translations, rotations, one planar scale and one vertical scale), or nine parameters (translations, rotations and separate directional scales). Note that the planimetric x-y scaling (eight parameters) is actually indicated by ‘sx’ whilst ‘sz’ represents the z parameter. The user has the possibility to change the convergence and weighting settings. If needed, batch processing can be enabled. For this, only one

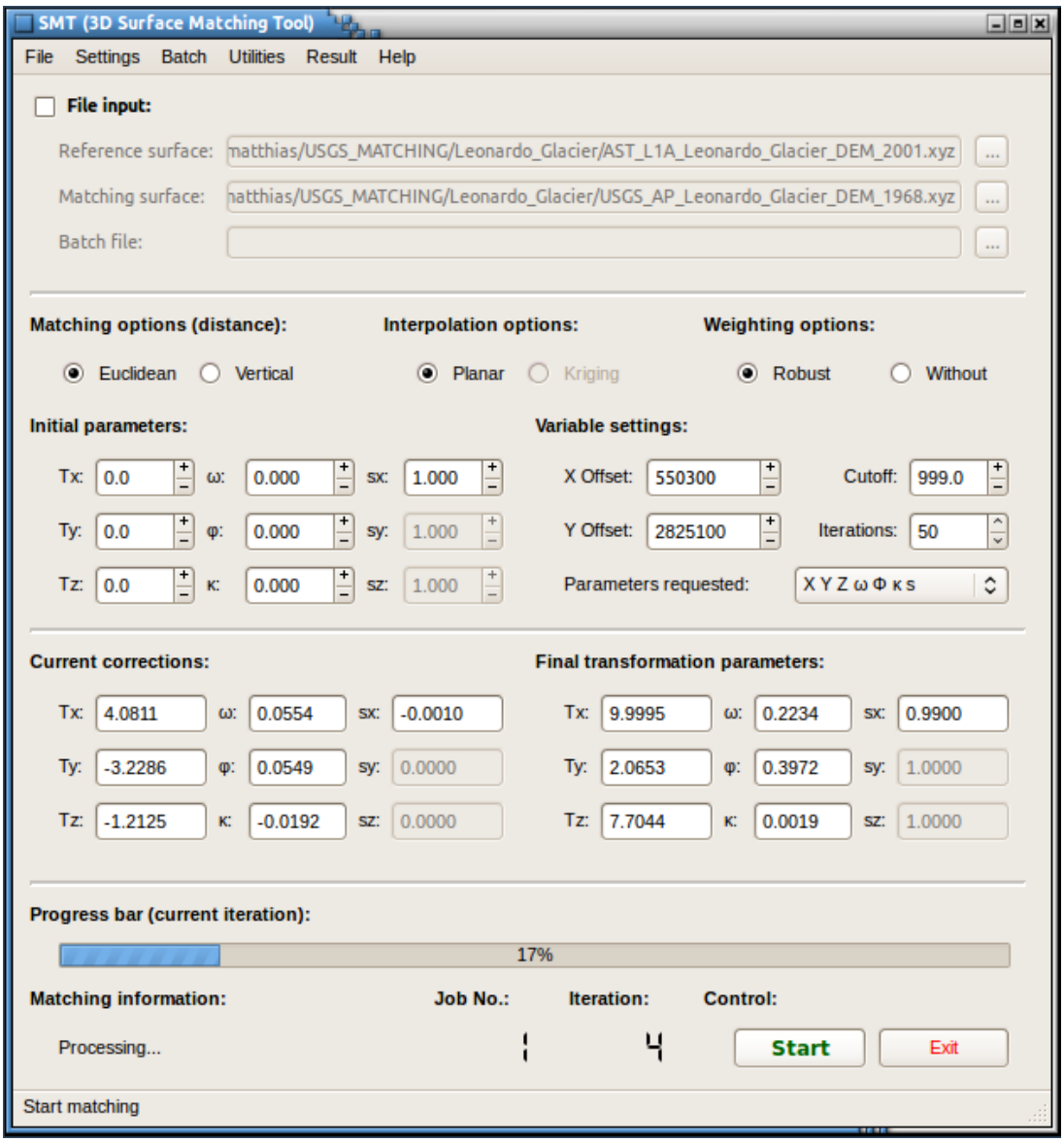

Figure 3.12: The *SMT* user interface.

batch file is needed that contains matching settings, i.e. the convergence parameters, and path to the point datasets. This allows to run several matching jobs after each other without further input of the user. The vertical differences between the matching and reference surface are calculated previous to the matching and afterward when convergence is achieved. This allows comparison of the pre- and post match differences. In addition, a file is generated which contains the surface correspondences (points that formed the observations) and additional information to the reference surface plane such as slope and aspect.

Code	Data	Points	Iter.	Time [s]	T_x	T_y	T_z	ω	ϕ	κ	s
VB	Artificial	2500	2	22	-0.500	-0.500	-0.5000	0.000	0.000	0.000	1.000
	Lidar #1	8786	18	4763	57.604	42.087	16.771	0.238	0.052	0.212	0.994
	Lidar #2	31545	19	5859	-30.527	30.002	33.496	0.017	-0.018	-0.036	1.002
C++	Artificial	2500	2	1	-0.500	-0.500	-0.500	0.000	0.0000	0.000	1.000
	Lidar #1	8785	20	37	57.189	41.698	16.784	0.237	0.052	0.214	0.995
	Lidar #2	31257	7	81	-28.313	31.158	34.225	0.017	-0.022	-0.025	1.002

Table 3.5: Comparison of successful matching results and performance for different datasets between VB6 (*3DSurf*) and C++ (*SMT*) coding. The individual transformation parameters show the solution of the match. For the real world datasets the solutions are slightly different due differences between the matching and reference surface. Software and parameter settings (vertical matching) were the same. Iter. = Number of iterations.

3.4.4 Software performance and validation

The original *3DSurf* algorithm of Buckley (2003) and Miller (2007) was extensively tested in their works using artificial and topographic datasets. Here, additional tests were performed with the *SMT* software for validation purposes and to compare performance. Three different tests were performed:

1. Test of performance and comparison of solutions between *3DSurf* and *SMT* software.
2. Comparison of vertical and euclidean case matching in different terrain types.
3. Test of matching with additional scale parameter.

The performance of the *3DSurf* and *SMT* software was evaluated using an artificial template surface with 2500 points (identical to the template used by Miller (2007)) and two topographic datasets of around 10000 and 40000 points. The topographic datasets are small patches of ASTER elevation data that were used in a study by Miller et al. (2009). The artificial surface was shifted by half a unit in each direction and then matched back to itself. In both versions the correct transformation was found from the matching solution (Table 3.5). More complex configuration were tested, analogous to Miller (2007), with similar results (not shown here). The uncontrolled ASTER data was matched to a reference Lidar surface of around 50,000 points. In both versions successful matching was achieved (Table 3.5). Minor differences in the solutions are explained by real differences between the ASTER and lidar data that influence the convergence behavior and the solution of the match.

Figure 3.13 illustrates that the recoded (C++) version has significantly faster run-time (up to 100 times faster) compared to the older version (Figure 3.13). This is mainly attributed to the faster correspondence search within the triangulation and the AABB tree data structure. This means much larger datasets may be matched in less time. Surfaces with up to 2 million points were successfully matched. The number of points is mostly limited by the random-access memory (RAM) of the computer because large matrices have to be stored and inverted within the least squares procedure. This first test showed that the *SMT* software is stable and delivers robust results with improved performance.

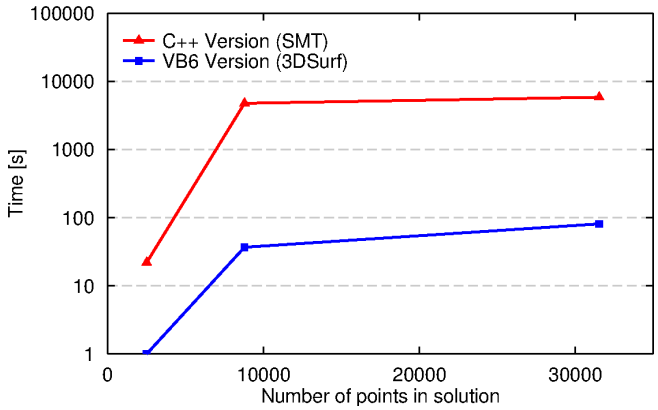

Figure 3.13: Comparison of processing time between VB6 (*3DSurf*) and C++ (*SMT*) coding. Y-axis is a log scale.

The influence of surface slope on vertical and Euclidean case matching was tested by using artificial template surfaces (6500 points) with different relief gradients (Figure 3.14). Each template surface (representing either flat, hilly, steep, very steep terrain) was shifted by 3.5 units and rotated around each axis by two degrees. The scale was held fixed. The transformed surface was then matched back to the original position. Results (Table 3.6) show that matching was achieved in all terrain types. The Euclidean matching performs slightly better as indicated by smaller standard deviations of the remaining differences and faster convergences of the algorithm in hilly to very steep terrain. The difference in the number of iterations for the flat terrain case is likely explained by insufficient relief gradients and thus slower convergence, although in both cases a similar solution was achieved. As mentioned earlier, the differences (distance between corresponding points) in steep terrain will be smaller for the Euclidean case so that the reference standard deviation changes will be smaller as well. Another explanation is that the Euclidean distance is more likely to represent the 'true'

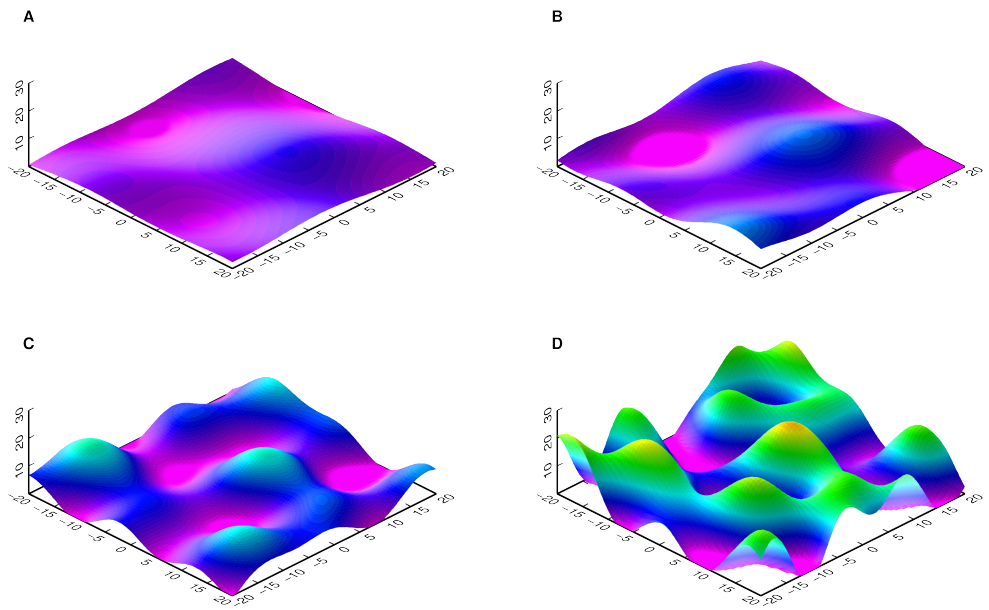

Figure 3.14: Template surfaces with different slope gradients: flat (A), hilly (B), steep (C), and very steep (D). Distance units are dimensionless.

Vertical	Iter.	$\sigma_{\Delta z}$	T_x	T_y	T_z	ω	ϕ	κ	s
Flat	18	0.0001	-3.5048	-3.4996	-3.4958	-2.0698	-1.9281	-2.0691	1.0000
Hilly	9	0.0002	-3.5044	-3.4994	-3.4960	-2.0698	-1.9278	-2.0698	1.0000
Steep	10	0.0005	-3.5036	-3.4997	-3.4957	-2.0692	-1.9275	-2.0696	1.0000
Very steep	7	0.0005	-3.5040	-3.4999	-3.4961	-2.0700	-1.9280	-2.0702	1.0000
Euclidean									
Flat	11	0.0002	-3.5034	-3.4991	-3.4956	-2.0695	-1.9279	-2.0686	1.0000
Hilly	6	0.0002	-3.5037	-3.5003	-3.4956	-2.0693	-1.9275	-2.0706	1.0000
Steep	8	0.0004	-3.5038	-3.4992	-3.4953	-2.0690	-1.9291	-2.0691	1.0000
Very steep	7	0.0002	-3.5040	-3.4956	-3.4956	-2.0697	-1.9279	-2.0700	1.0000

Table 3.6: Comparison of performance of vertical and euclidean distance case in varying terrain gradients

corresponding point in the reference surface and therefore the observations will be better and lead to a better solution. Accurate matching relies on the presence of surface gradients - that is two perfectly flat surfaces cannot be matched uniquely and hence the solution will not converge. As the matching depends on gradients the Euclidean distance algorithm is assumed to perform better because the vertical difference algorithm tends to underestimate gradients in steep terrain. However, this was not clearly observable in these test. The results do indicate that the Euclidean distance algorithm is better as it needs less iterations to achieve convergence although the computation per iteration is slightly more time consuming (up to 10 %) because of the 3D search rather than 2.5D.

In Section 3.3.2 a possible bias in the vertical direction of ASTER DEMs was discussed. By using an additional transformation parameter for an independent scale of the z-axis (see Section 3.4.2) such a bias can be removed if it is of linear form. More complex

biases, e.g. polynomial, can potentially be reduced although they are not coded in *SMT* at present.. To test the correct implementation, a linear and polynomial bias was added to the z-component of the template surface. Using an eight-parameter transformation which accounts for linear scaling in the vertical direction these biases were successfully reduced in the polynomial case and removed in the linear case (Figure 3.15).

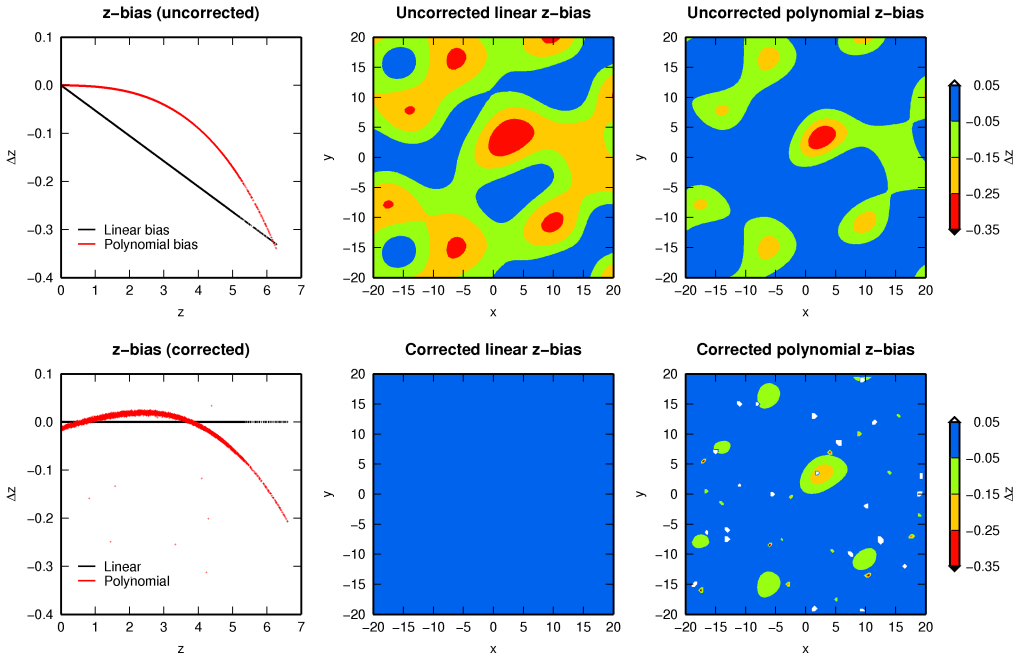

Figure 3.15: Removal of bias in the vertical axis using independent z-scaling within the matching strategy.

3.5 Summary

This chapter has established the basis for a monitoring technique of long-term glacier mass balance of the AP that utilizes DEMs derived from airborne (USGS/BAS) and spaceborne (ASTER) stereo-imaging. The underlying surface matching software has been recoded and further improved for the application of matching multi-temporal and multi-resolution DEM in areas with steep topography. There are commercial software solutions (e.g. LS3D from 4DiXplorer AG) that perform similar DEM co-registration but these are rare and expensive. Thus, they were not assessed further here and assumend to not add substantial benefits. The advantage of the here described and developed matching software is that full control over the settings and input/output is possible. Currently, the algorithm deals with point datasets, i.e. xyz ASCII files. This means

surface elevations from raster files need to be converted first into ASCII files in order to be used within the matching strategy. A direct import of raster DEMs and their respective matching would be beneficial but is currently not implemented. In the following chapter the matching will be validated and tested in a real world study before it is applied in a wider study across the AP. Limitations exist due to insufficient coverage of the historical imagery. This limits the potential for a region wide mass balance assessment. However, the potential to fill gaps in the existing archives is large and can contribute further to a better understanding of recent and past ice mass balance changes in the AP.

Chapter 4. Applicability of surface matching in glaciated rugged terrain

In the preceding chapters a monitoring strategy for long-term glacier mass balance assessment in the Antarctic Peninsula was outlined, using historic and modern DEMs. The proposed surface matching algorithm allows these DEMs to be rigorously combined without the need for ground control information. Before the DEM matching and glacier change assessment was applied in a wider study, an applicability study was made for which the results are presented in this chapter. The aim of this study was to find the most sensible surface matching strategy and to evaluate the accuracy of DEMs derived from ASTER data and the USGS/BAS archive imagery, especially with respect areas of steep topography. A number of different configurations were established, investigating matching of the entire DEM surface and also focusing on smaller individual regions. After establishing an optimal approach, the final phase of the test involved assessing the accuracy of the ASTER DEM in the context of different terrain types, including flat glacier surfaces, steep, rocky mountain slopes and icefalls (frozen waterfalls). This was expected to deliver valuable information on the reliability of the matching approach under different terrain types, allowing uncertainty estimates to be attached to glacial change measurements derived more widely across the AP. Three main aspects were evaluated through the test, which can be summarised as follows:

1. Assessment of ASTER DEM quality and investigating potential elevation bias;
2. Development of an optimal surface matching strategy, adopting an experimental approach;
3. Evaluation of ASTER DEM quality in relation to terrain type.

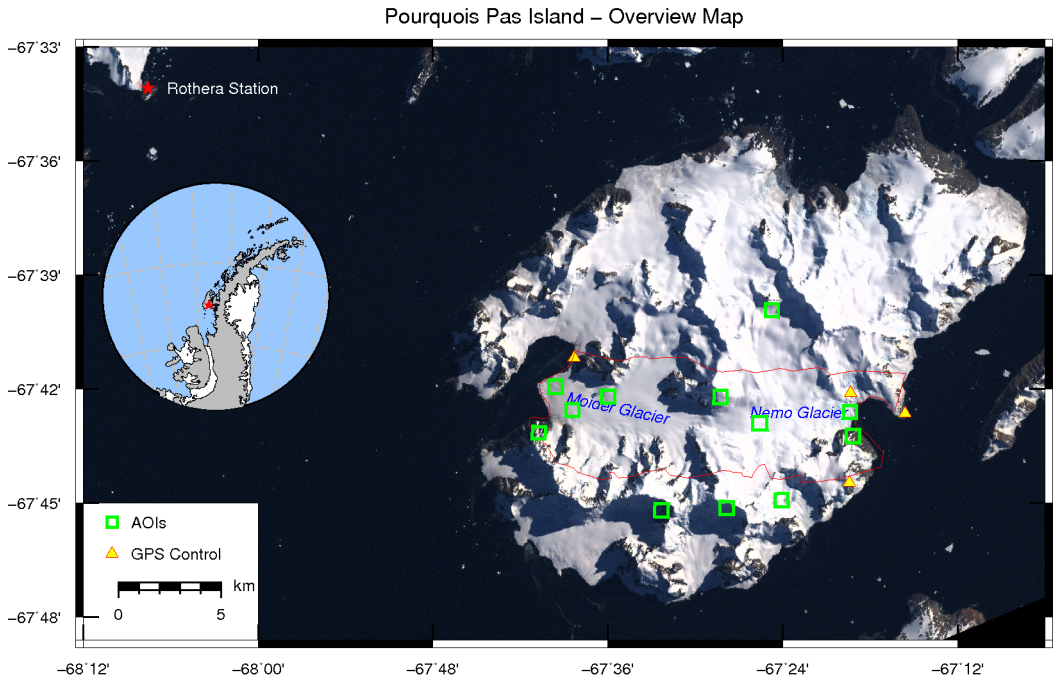

Figure 4.1: Pourquoi Pas Island overview map, with inset highlighting location within Antarctic Peninsula

4.1 Test site and datasets

Through collaboration with the BAS the applicability study was applied to a test site located on the western Antarctic Peninsula at Pourquoi Pas Island, which lies on the western Antarctic Peninsula at 67° 40' S, 67° 30' W (Figure 4.1). Pourquoi Pas Island is composed of glaciated, mountainous terrain, characteristic of that found more widely across the Antarctic Peninsula. The test site straddles two glaciers systems, extending over an area of 86 km², and provides a variety of terrain types over which to investigate the approach. Moider Glacier flows in a westerly direction, whilst Nemo Glacier flows to the east. Figure 4.1 also indicates the close proximity of the test site to the BAS research station at Rothera.

To test the accuracy of the ASTER elevation data, a DEM with a spatial resolution of 30 m was available from ASTER imagery acquired on the 30th December 2004. Previous investigation of the datasets under consideration here, indicates that the RMSEz of the December 2004 ASTER DEM ranges from 5 – 160 m depending on the terrain type (Cziferszky et al., 2010). Clearly, errors of this magnitude would bias or obscure genuine terrain change which may exist between DEMs acquired at different periods in time (referred to here as multi-temporal DEMs). What is not clear from the work of

Cziferszky et al. (2010), is whether any systematic offsets exist in the ASTER DEM. Some of the larger RMSE values will be due to gross errors, caused by difficulties in the DEM extraction process in areas of shadow or very steep terrain. However, the ASTER DEM may also contain systematic error, which must be removed before multi-temporal analysis can be undertaken. Conventionally, this is achieved through the use of GCPs. However, as noted previously, this is not feasible for polar environments due to the remote, inaccessible and inhospitable terrain.

In addition to the ASTER DEM, a high-accuracy DEM, derived from aerial photography captured at the same time as the ASTER data, was available for the Pourquoi Pas Island test site through collaboration with BAS. This provided a strong basis for the validation exercise, as any systematic offsets between the datasets will be due to registration deficiencies rather than terrain change. The aerial photography was collected by BAS on the 20th January 2005, only three weeks after the ASTER acquisition, thus minimising any surface differences due to snow/ice melt/accumulation. The BAS data was flown with GPS positioning of camera centres, thus eliminating the requirement for ground control points. The imagery offers a spatial resolution of 0.6 m and an absolute positional accuracy of better than 0.5 m_{xyz}, as validated and reported by Fox and Cziferszky (2008). A DEM at a spatial resolution of 2 m was extracted for this project and refined through manual editing in *BAE Systems SocetSet v5.5.0* digital photogrammetric workstation. BAS also provided access to thirteen 500 m x 500 m areas of interest (AOI) which had been sub-sampled through manual measurement of the photogrammetric DEM. Figure 4.1 illustrates the distribution of these AOI across the test area. Each AOI is individually homogeneous in terms of terrain type, but in combination the AOI offer a range of slope gradients, slope aspects and land-cover types, as indicated in Table 4.1. This helped to facilitate assessment of the registration solutions under a range of typical surface conditions. It should be noted, that AOI 1 was not used in this study, as it was located outside the coverage of photogrammetric dataset. BAS also provided coordinates for four check points, with distribution as indicated in Figure 4.1. The check points were measured through GPS field survey and provide an independent source of validation for assessing the quality of the results for the ASTER DEM matching.

Class	AOI ID	Terrain Type	Aspect	Height Range	Surface Texture
I	3	glacier tongue	west	low (49 m)	high
I	4	glacier	west	low (37 m)	high
I	5	glacier	west	low (92 m)	medium
I	9	glacier	east	low (31 m)	low
II	7	icefall	south	moderate (347 m)	high
II	10	glacier	south	moderate (137 m)	low
II	11	icefall	east	moderate (392 m)	high
II	12	glacier tonque	east	moderate (166 m)	high
III	1	rock/ice face (shadow)	west	high (606 m)	high
III	2	rock/ice face	north	high (617 m)	high
III	6	rock/ice face (shadow)	south	high (537 m)	high
III	8	rock/ice face	south	high (732 m)	high
III	13	rock/ice face (shadow)	north	high (652 m)	high

Table 4.1: AOI characteristics at Pourqoui Pas Island. AOIs with similar height range were grouped into terrain classes to allow comparison of results with respect to terrain type.

4.2 Evaluation strategy

Least squares surface matching minimises DEM offsets in a global manner, providing the 'best fit' for the matching area as a whole. However, previous experience has shown that over large areas (e.g. tens of km²), this may provide a sub-optimal solution at a more localised scale. Furthermore, some studies have explored the use of patch-based matching (e.g. Grün and Akca, 2005) in order to introduce computational efficiency by matching on the basis of multiple well-distributed surface patches, as opposed to the DEM surface in its entirety. A patch is a small subset of points from a larger surface. This approach may be valid in the context of this research, where the glacier systems extend over tens of km², and where extended areas may be unreliable due to poor correlation (lower than 0.5) in the DEM generation process, as already discussed. This test therefore focused on evaluating this aspect. Initially, matching was performed on a very local scale, utilising the individual 500 m² AOI. This was then extended to multi-patch matching, whereby multiple AOI are aggregated to form a single matching surface, before finally implementing matching over the entire study area. This leads to a number of matching strategies, which are presented in Table 4.2, and explained in greater detail below.

Under Strategy A, the matching and reference surfaces are comprised of small regions (500 m x 500 m), covering the respective AOI only. The reference surface was configured to cover a slightly extended region in all directions, on the assumption that

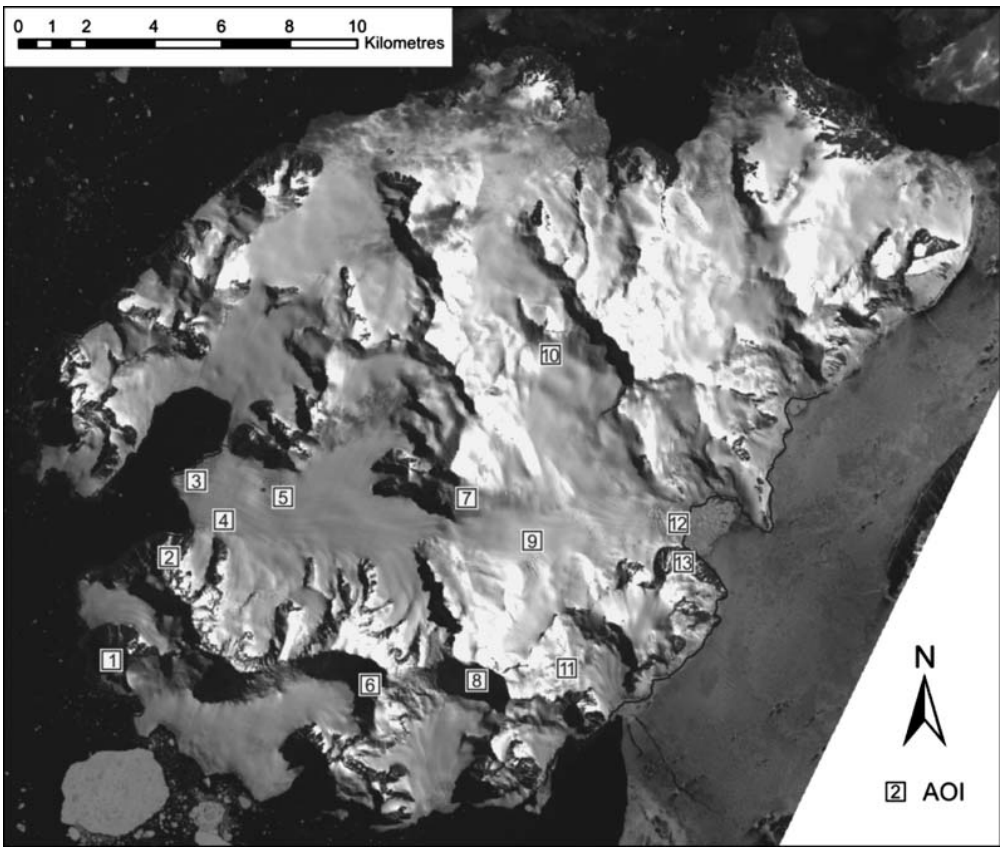

Figure 4.2: AOI distribution across test site. Each AOI represents an area of 500 x 500 for which the elevation values of the photogrammetric DEM to the ASTER DEM were compared. (Figure 2 from Cziferszky et al., 2010)

Strategy	Reference DEM	Matching DEM
A1	BAS AOI 2	ASTER AOI 2
A2	BAS AOI 3	ASTER AOI 3
A3	BAS AOI 4	ASTER AOI 4
A4	BAS AOI 5	ASTER AOI 5
A5	BAS AOI 6	ASTER AOI 6
A6	BAS AOI 7	ASTER AOI 7
A7	BAS AOI 8	ASTER AOI 8
A8	BAS AOI 9	ASTER AOI 9
A9	BAS AOI 10	ASTER AOI 10
A10	BAS AOI 11	ASTER AOI 11
A11	BAS AOI 12	ASTER AOI 12
A12	BAS AOI 13	ASTER AOI 13
B1	BAS all points*	ASTER AOI {2,3,4,5}
B2	BAS all points*	ASTER AOI {7,9,12,13}
B3	BAS all points*	ASTER AOI {2,3,4,5,7,9,12,13}
C	BAS all points*	ASTER all points

Table 4.2: Surface matching strategies. Strategy A is based on matching of individual patches, strategy B is based on matching groups of patches, and strategy C uses all points. (*overlapping points from BAS DEM with 10 m spatial resolution)

offsets already existed between the surfaces prior to matching, and hence the algorithm may require points which had initially fallen outside the ASTER AOI location.

Strategy B provides a step up from the local matching scale of strategy A and examines the patch-based matching approach. The AOI are distributed across the test site, as shown in Figure 4.2. It is evident that whilst some AOI are relatively isolated (e.g. 6, 10), others are clustered more closely. This provided an opportunity to explore the patch-based matching approach over a range of scales. Three separate multi-patch schemes were devised. B1 and B2 consider Moider (western) and Nemo (eastern) glaciers separately (Figure 4.1), with the matching surface composed of the points falling within the AOI {2, 3, 4, 5} for B1, and {7, 9, 12, 13} for B2. The algorithm considers the individual points which are input as the matching surface file, and therefore is unaffected by the fact that large gaps exist across the surface between these points. In contrast, the reference surface is triangulated to form a surface mesh, which is then used to evaluate the overlapping points from the matching surface. Consequently, for B1 and B2 the BAS photogrammetric DEM, clipped to the area surrounding the relevant AOI, was used as the reference surface. This was sampled to a spatial resolution of 10 m, as this is still significantly better than the 30 m ASTER points used in the matching surfaces, and will offer faster execution of the code. Previous testing has indicated that under this type of scenario (low resolution matching surface), there would be no significant advantage to applying the BAS DEM at the highest resolution of 2 m. Finally, match B3 extended this approach over the entire glacier system, encompassing the AOI patches from B1 and B2. This should provide some indication of the sensitivity of this approach to the scale of the region under consideration.

The final approach, Strategy C, explored matching performance under the more conventional scenario whereby the surfaces were matched in their entirety, across the entire region of interest. Again, the 10 m version of the BAS photogrammetric DEM was applied, in order to increase speed of execution. In all of the above cases, the quality of the matching solution was assessed through inspection of the output matching statistics (number of iterations, final transformation parameters, etc).

In addition, the vertical distances between the surfaces were calculated based on the matching residuals. This is the distance between the ASTER points and the intersecting surface patch (triangle) from the reference BAS DEM. This then enabled determination of the mean elevation offset and an $RMSE_z$ value, where the photogrammetric elevations are taken as the 'correct' values. The two DEMs will contain differences due to random error and possible gross errors (e.g. spikes). In addition, differences will exist due to the disparate spatial resolution of the two datasets. As the DEMs are only separated by a period of three weeks, discrepancies due to terrain change should be minimal. Therefore it can be expected that differences in the results obtained from the three matching strategies will be principally due to the different approaches, with some manifestation of the DEM differences (random error, spikes, etc).

4.2.1 Evaluating Performance with Respect to Terrain Type

In order to facilitate the broader application of the approach, it is important to assess the quality of the results in the context of the different terrain classes (flat, moderate, steep) as outlined in Table 4.1. This test also validates the methodology in comparison to a well-controlled reference DEM, with additional assessment in comparison to check points. This should allow conclusions to be drawn with respect to the performance of the algorithm in an absolute sense. However, the post-match differences between the photogrammetric and ASTER surfaces should be similar even in circumstances where the reference surface is less well-controlled, i.e. in the case where the ASTER DEM forms the reference surface for registration of archival aerial photogrammetric DEMs. Thus, evaluating the performance of the algorithm with respect to different terrain types as a part of this project should provide valuable information on the reliability of the approach, allowing uncertainties to be more accurately quantified with respect to broader application across the Antarctic Peninsula. This was achieved by assessing final post-match surface differences with respect to the different terrain categories.

An initial match was performed using the standard 7 parameter transformation, in order to register the ASTER DEM to the BAS photogrammetric DEM. Following this, the vertical distances between the ASTER and reference DEM, before and after matching,

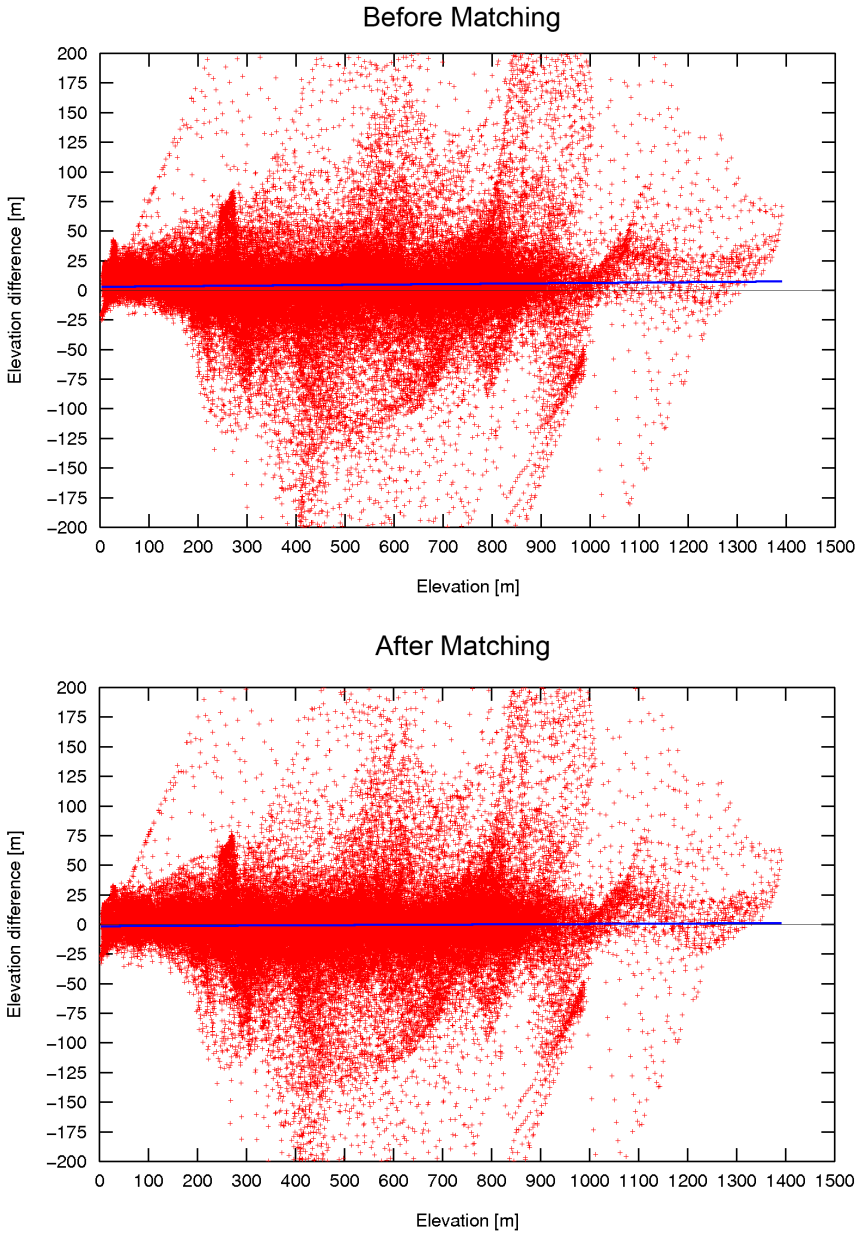

Figure 4.3: Elevation differences with respect to elevation before (top) and after (bottom) matching, with linear trend fit (blue line). An elevation dependent bias is evident if there is positive or negative trend in the line fit.

were plotted on a point-by-point basis against terrain elevation (Figure 4.3, top). This reveals that a small systematic elevation offset appears to exist between the surfaces prior to matching. Although a small correlation with elevation does appear to exist, this is most likely due to the previously discussed deterioration in DEM quality over steep slopes, leading to increased errors in the ASTER DEM at high elevation. Any small planimetric offsets, or differences in the spatial resolution of overlapping DEMs, will be exacerbated over steep terrain. Nuth and Kääb (2011) suggest that the bias in the ASTER DEM may in some cases be non-linear (as already discussed in Section 3.3.2), and can be approximated to a polynomial function. However, extensive analysis of multiple ASTER DEMs, carried out during this research has returned inconclusive results. Although some indications of elevation-dependent offsets were encountered, these were found to approximate to a linear distribution, and furthermore, were likely not related to the sensor geometry or GCP distribution. Therefore, for the DEM data examined, it seems more likely that any elevation-related effects are due to this phenomenon rather than the type of sensor dependent aspect reported by Nuth and Kääb (2011). Following application of the matching algorithm, this offset has been successfully eliminated (Figure 4.3, bottom), indicating that for the ASTER DEM used in this project, application of a single scale parameter is sufficient. To confirm this, an eight parameter transformation was applied to the datasets, recovering separate scales for x-y and z. However, no significant deviation from unity was detected in plan or elevation, and on this basis, it was decided that the research should be implemented using a single scale factor.

4.3 Determining an Optimal Matching Strategy

The surface matching registration technique was implemented following the three strategies outlined in Table 4.2 and producing a total of sixteen sets of results. The results were assessed on a strategy-by-strategy basis as follows.

4.3.1 Strategy A

The final transformation parameters and post-match statistics for strategy A are presented in Table 4.3 and Table 4.4. Solutions were obtained for A2, A4, A10, A11 and A12, whilst the other seven configurations failed to converge. Examination of the pre-match surface differences as shown in Table 4.4 indicates that the seven failures contained relatively large surface differences, as highlighted through the pre-match RMSE, minimum and maximum difference values. This would indicate that within these AOI, the ASTER DEM may be relatively weak, containing some error points or insufficient spatial gradients. It is likely that across these specific AOI, the 500 m x 500 m extent is simply not large enough to contribute enough reliable points from which the matching could establish a solution. In the five cases where the matching converged, initial inspection suggests that good solutions have been achieved, as evidenced through significant improvements in the mean and RMSE surface differences. However, the scale factors of 0.8453 and 0.8872, recovered for A4 and A10 respectively, show a significant and unlikely departure from unity. This suggests that whilst the post-match differences may indicate an acceptable result for these configurations, in fact, the algorithm has most likely converged to an erroneous solution. Based on these concerns and the fact that strategy A has failed for more than 50 % of cases, it can be concluded that the approach is not particularly successful, and is highly sensitive to the quality of the DEM within the localised AOI.

4.3.2 Strategy B

The transformation solutions and difference results for strategy B are shown in Table 4.5 and Table 4.6. In this case, all three matches have successfully converged, and inspection of the transformation parameters suggests that acceptable solutions have been achieved. There is little notable difference between the results obtained through the more restricted patches of B1 (western area) and B2 (eastern area), and that obtained by combining all of these patches (B3) to bridge the broader glacier system. Inspection of the matching differences confirmed that significant improvements have been achieved over the

pre-match alignment of the DEMs. For example, in the case of B2, the mean elevation difference has been improved from 8.87 m (pre-match) to -0.26 m (post-match), indicating that a significant systematic offset has been removed. Although the RMSE and s values are still relatively high following the matching, this is likely due to the presence of outlier points. Under strategy A, the mean elevation offsets for the successful matches all fell under 0.15 m, whilst the RMSE was within 20 m. As can be seen from Table 4.6, the results of the patch-based matching approaches are poorer than this. This can be attributed to the fact that whilst the software finds the best global alignment for the matching patches, this will not necessarily provide the optimal registration for an individual patch (AOI). However, clearly strategy B is more reliable in terms of achieving successful convergence than strategy A.

4.3.3 Strategy C

Under the final matching strategy, C, the entire ASTER DEM was matched to the 10 m BAS photogrammetric DEM, producing the results detailed in Table 4.7 and Table 4.8. This delivered a small improvement in the RMSE and standard deviation, but the mean elevation offset has slightly deteriorated overall. There are clearly large disparities between the surfaces in places, as evidenced previously under strategies A and B through the large minimum and maximum values. Under strategy C, which includes all surface points, the extremes of difference are in the order of 500-600 m both before and after matching.

In comparing the three matching strategies, it seemed that strategy A should be discarded, as the AOI are too limited in size to guarantee a successful match. Further exploration of strategies B and C was required before any final conclusions could be drawn. It is evident that the ASTER and photogrammetric surfaces contain significant disparities in places. Therefore in order to directly compare the results of the two strategies, the differences were analysed only for the AOI. This also enabled analysis of differences in relation to surface type.

Strategy	Iter.	T_x [m]	T_y [m]	T_z [m]	ω [°]	ϕ [°]	κ [°]	s
				Transformation Solution				
A1				No convergence				
A2	6	-6.05	-6.29	10.79	-0.029	0.5576	0.454	0.9588
A3				Noconvergence				
A4	34	-21.1	4.71	22.75	0.113	-0.8787	-1.5755	0.8453
A5				No convergence				
A6				No convergence				
A7				No convergence				
A8				No convergence				
A9				No convergence				
A10	21	26.67	-41.75	43.32	0.9307	3.4265	-2.8959	0.8872
A11	20	24.5	-12.8	1.95	-0.0779	-0.2831	-2.7664	0.9618
A12	22	3.16	-6.95	45.86	1.3682	2.5681	4.2156	0.9167

Table 4.3: Strategy A transformation solutions

Strategy	Pre-Match Differences [m]					Post-Match Differences [m]				
	Mean	σ	RMSE	Min.	Max.	Mean	σ	RMSE	Min.	Max.
A1	33.68	79.45	86.26	-110.49	324.27					
A2	9.18	5.23	10.56	-12.36	27.27	-0.05	4.69	4.69	-18.44	17.09
A3	0.32	15.15	15.15	-67.26	52.53					
A4	2.1	5.27	5.67	-22.51	21.04	-0.13	4.46	4.46	-31.24	15.19
A5	-112.76	117.77	163.02	-426.65	91.55					
A6	25.37	23.93	34.87	-97.48	81.24					
A7	3.68	55.46	55.56	-193.78	137.3					
A8	-4.55	38.21	38.46	-100.53	93.94					
A9	9.69	41.05	42.16	-143.84	177.99					
A10	29.55	19.97	35.66	-39.44	109.56	0.13	15.39	15.39	-190.15	65.05
A11	4.7	6.42	7.95	-12.12	30.79	0.13	5.2	5.2	-19.96	22.05
A12	9.95	18.61	21.1	-90.06	96.08	0.12	18.6	18.6	-87.45	95.04

Table 4.4: Strategy A matching statistics

	Transformation Solution							
Strategy	Iter.	T_x [m]	T_y [m]	T_z [m]	ω [°]	ϕ [°]	κ [°]	s
B1	11	27.1	-1.63	5.99	0.2066	0.1633	0.8946	0.9872
B2	13	71	-29.25	1.83	0.0622	-0.0129	0.3519	0.9837
B3	19	58.95	-13.84	2.52	0.4062	0.0257	0.0458	0.9979

Table 4.5: Strategy B transformation solutions

	Pre-Match Differences [m]					Post-Match Differences [m]				
Strategy	Mean	σ	RMSE	Min.	Max.	Mean	σ	RMSE	Min.	Max.
B1	11.37	38.63	40.27	-110.49	324.27	3.05	28.07	28.23	-142.65	224.41
B2	8.87	28.28	29.64	-104.23	105.42	-0.26	24.14	24.14	-138.71	103.38
B3	10.08	33.72	35.19	-110.49	324.27	1.31	26.75	26.79	-143.33	215.59

Table 4.6: Strategy B matching statistics

	Transformation Solution							
Strategy	Iter.	T_x [m]	T_y [m]	T_z [m]	ω [°]	ϕ [°]	κ [°]	s
C	8	62.40	-22.93	2.36	0.0655	0.0068	-0.0488	1.0002

Table 4.7: Strategy C transformation solutions

	Pre-Match Differences [m]					Post-Match Differences [m]				
Strategy	Mean	σ	RMSE	Min.	Max.	Mean	σ	RMSE	Min.	Max.
C	1.16	54.72	54.73	-594.22	472.60	-1.48	50.02	50.04	-579.56	497.96

Table 4.8: Strategy C matching statistics

4.4 Performance in Relation to Terrain Type

4.4.1 Patch-Based vs. Global Matching

The surface differences for strategies B and C were evaluated for individual AOI. In considering the results for Strategy B1 (Table 4.9), it can be seen that whilst the post-match differences for AOI 3 and 5 show significant improvement, the results for AOI 2 and 4 are less dramatic. AOI 4 appeared to exhibit a small deterioration in the mean offset, from 1.45 m (pre-match) to -2.03 m (post-match). There is no clear explanation for this, as AOI 4 falls within terrain class I, and is described as relatively flat, with high surface texture, indicating that the ASTER DEM should be reliable for this area. Inspection of Table 4.9 reveals particularly poor results for AOI 2. Although a distinct improvement in the registration solution was achieved for AOI 2, the post-match differences remain several orders of magnitude greater than for the other AOI, with high post-match RMSE, and large extreme values, ranging from -142.65 m to 224.41 m. AOI 2 falls within terrain class III and is described as a rock/ice face, with a large elevation range (617 m). This likely indicates that large disparities may exist between the ASTER and photogrammetric surfaces due to the effects of the steep slopes in exacerbating differences in the spatial resolutions of the DEMs. Such effects would not be so evident over the flatter glacier surfaces covered by AOI 3, 4 and 5.

It is likely that the effect of these discrepancies in AOI 2 has reduced the quality of the overall solution. In order to explore this assumption, strategy B1 was repeated, but with AOI 2 omitted. The results are shown in Table 4.10. This revealed a stronger overall solution, with the mean post-match surface offset reduced from 3.05 m (Table 4.9) to -0.75 m. The post-match RMSE was reduced from 28.23 m to 9.57 m through the removal of AOI 2. The results for the remaining AOI (3, 4, 5) based on this new solution are similar to those obtained initially, although there is a small overall deterioration. This is likely due to the fact that the matching is now based on fewer points, and hence may not offer the same redundancy.

Similar analysis was also performed for strategy B2, with results as shown in Table 4.11. In this case, all AOI show a clear improvement in the mean elevation offset after the

matching, achieving similar magnitudes to those obtained through B1. In the case of AOI 9, 12 and 13, the mean offset was reduced to less than 0.20 m. AOI 7 did not quite attain this level of agreement, although there is still a significant improvement from the pre-match mean offset of 23.28 m to -1.20 m.

The results for strategy B3 are detailed in Table 4.12. Again, AOI 2 exhibits particularly high offsets post-match, which lends further credence to the assumption that the ASTER DEM is particularly poor over this region. For the remaining AOI, the post-match mean offsets do not attain quite the same level of agreement as through strategy B1 and B2, but nevertheless, still display significant improvement in most cases, indicating that a successful registration solution has been achieved. In a small number of cases (AOI 4, 9) strategy B3 results in a small deterioration in elevation offset. For AOI 4, this observation is consistent with the outcomes of B1. It is likely that these results arise from the algorithm determining the best 'global' fit for the eight patches, which will return strong solutions for the majority, but potentially poorer solutions in a small number of cases.

In comparing the results of B1/B2 and B3 – i.e. localised patch-based matching versus a more global patch-based matching, Table 4.9, Table 4.10, Table 4.11 and Table 4.12 reveal that for the individual AOI, a stronger solution is clearly achieved through the localised patch-based approach of B1/B2. Under B1/B2, it has been possible to reduce the mean offset to less than one metre for the majority of AOI.

The next step was to compare the individual patch-based results for strategy B to those returned through strategy C, where matching was performed across the entire DEM datasets. The results for the individual AOI for strategy C are shown in Table 4.13. The results appear to be rather variable, with some areas showing improvement (e.g. AOI 7, 10, 11 and 13), whilst others have significantly deteriorated (e.g. AOI 5, and 8). This is likely because instead of focusing only on the AOI, strategy C considers all points in the ASTER DEM and attempts to find the best overall fit to the photogrammetric DEM.

The results presented in this section allow some conclusions to be drawn regarding optimal matching approach and scale. It would seem that patch-based matching over restricted extents offers an acceptable solution for the AOI. In the case of the Pourquoi Pas Island study site, strategy B1 covered part of the western glacier (Moider), whilst B2

encompassed the eastern-flowing glacier (Nemo). This would suggest that matching could be successfully applied on a glacier-by-glacier basis in order to obtain the optimal solution for a specific region of interest. Further, Section 3.2.2 has highlighted the difficulties in extracting a continuous DEM from archival aerial photography, due to low image texture across glaciated terrain, and difficulties caused by shadows in mountain regions. The patch-based matching approach is well-suited to this scenario, as there are only limited regions of the DEM which can be considered stable (unchanged over time) and reliable in terms of DEM quality.

	Pre-Match Differences [m]					Post-Match Differences [m]				
AOI	Mean	σ	RMSE	Min.	Max.	Mean	σ	RMSE	Min.	Max.
Comb.	11.37	38.63	40.27	-110.49	324.27	3.05	28.07	28.23	-142.65	224.41
2	33.52	73.54	80.8	-110.49	324.27	15.24	53.33	55.45	-142.65	224.41
3	9.89	5.42	11.27	-12.36	29.79	-0.12	5.22	5.22	-22.05	16.58
4	1.45	14.73	14.80	-66.76	53.21	-2.03	14.61	14.75	-69.70	49.00
5	2.48	5.51	6.04	-35.17	22.7	-0.09	5.80	5.80	-33.33	22.30

Table 4.9: AOI results for strategy B1

	Pre-Match Differences [m]					Post-Match Differences [m]				
AOI	Mean	σ	RMSE	Min.	Max.	Mean	σ	RMSE	Min.	Max.
Comb.	4.62	10.24	11.23	-66.76	53.21	-0.75	9.54	9.57	-71.29	49.59
3	9.89	5.42	11.28	-12.36	29.79	0.04	5.29	5.29	-21.94	19.33
4	1.46	14.73	14.8	-66.76	53.21	-2.23	14.67	14.84	-71.29	49.59
5	2.48	5.51	6.04	-35.05	22.7	-0.1	5.6	5.6	-35.61	21.82

Table 4.10: AOI results for strategy B1 with AOI 2 removed

	Pre-Match Differences [m]					Post-Match Differences [m]				
AOI	Mean	σ	RMSE	Min.	Max.	Mean	σ	RMSE	Min.	Max.
Comb.	8.87	28.28	29.64	-104.23	105.42	-0.26	24.14	24.14	-138.71	103.38
7	23.28	26.81	35.5	-100.72	100.27	-1.20	18.55	18.59	-138.71	81.50
9	-3.34	38.18	38.32	-104.23	100.4	0.16	37.31	37.31	-98.20	103.38
12	6.29	7.84	10.06	-21.37	34.79	0.10	6.61	6.60	-23.40	27.28
13	10.6	22.07	24.48	-95.64	105.42	-0.11	21.17	21.17	-106.94	87.42

Table 4.11: AOI results for strategy B2

	Pre-Match Differences [m]					Post-Match Differences [m]				
AOI	Mean	σ	RMSE	Min.	Max.	Mean	σ	RMSE	Min.	Max.
Comb.	10.08	33.72	35.19	-110.49	324.27	1.31	26.75	26.79	-143.33	215.59
2	33.53	73.54	80.8	-110.49	324.27	15.13	53.34	55.43	-143.33	215.59
3	9.89	5.42	11.28	-12.36	29.79	-0.95	5.81	5.89	-21.81	16.91
4	1.45	14.73	14.80	-66.76	53.21	-2.05	15.08	15.22	-70.90	49.02
5	2.47	5.51	6.04	-35.05	22.7	-1.06	5.44	5.54	-42.95	17.61
7	23.28	26.81	35.5	-100.86	100.27	4.47	20.44	20.92	-126.73	60.31
9	-3.34	38.18	38.32	-104.23	100.4	-3.72	38.21	38.39	-103.36	98.72
12	6.28	7.85	10.05	-21.37	33.29	-3.50	7.48	8.26	-26.28	31.08
13	10.58	22.06	24.46	-95.64	105.42	3.72	21.37	21.68	-105.45	88.83

Table 4.12: AOI results for strategy B3

	Pre-Match Differences [m]					Post-Match Differences [m]				
AOI	Mean	σ	RMSE	Min.	Max.	Mean	σ	RMSE	Min.	Max.
Comb.	1.16	54.72	54.73	-594.22	472.6	-1.48	50.02	50.04	-579.56	467.96
2	33.53	73.54	80.8	-110.49	324.27	16.34	54.76	57.13	-135.96	235.26
3	9.89	5.42	11.28	-12.36	29.79	8.94	5.78	10.64	-11.1	27.83
4	1.45	14.73	14.8	-66.76	53.21	1.02	14.99	15.02	-67.05	53.33
5	2.47	5.51	6.04	-35.05	22.7	5.14	5.67	7.65	-38.1	23.61
6	-152.94	120.53	194.66	-94.15	424.63	-92.76	91.62	130.32	-87.09	338.37
7	23.28	26.81	35.5	-100.86	100.27	6.57	20.29	21.32	-127.14	66.81
8	-6.21	59.47	59.71	-129.21	201.44	-43.89	58.55	73.11	-90.19	201.81
9	-3.34	38.18	38.32	-104.23	100.4	-8.03	38.05	38.88	-107.65	96.58
10	15.75	34.02	37.44	-135.41	140.5	-4.74	33.96	34.24	-131.68	167.57
11	29.84	18.94	35.32	-108.41	18.93	-0.27	16.34	16.32	-57.75	50.23
12	6.28	7.85	10.05	-21.37	33.29	-8.12	8.28	11.59	-32.91	27.36
13	10.58	22.06	24.46	-95.64	105.42	1.38	22.24	22.27	-105.49	89.88

Table 4.13: AOI results for strategy C

		Elevation Offsets [m]			
Check Point	GPS Elev. [m]	Δ Pre-Match	Pre-Match	Post-Match	Δ Post-Match
Nemo Cove 1	597.08	499.0	-98.08	534.40	-62.68
Nemo Cove 2	252.80	226.0	-26.80	235.00	-17.80
Nemo Cove 3	45.15	25.00	-20.15	26.10	-19.05
Dalgleish Bay	24.62	13.00	-11.62	30.90	6.28

Table 4.14: Check point analysis for strategy B2

4.4.2 Validating the matching results

By assessing the individual AOI results, it was also possible to investigate the results in relation to terrain type. As strategy B delivered the strongest performance for the AOI, this approach has been used to investigate whether there is any correlation with terrain class. Although B1 and B2 delivered the best results, these matches do not encompass all the AOI. Therefore the results from B3 were used to assess this aspect. As a preliminary step, and in order to ensure the reliability of the solution produced through B3, the absolute accuracy of the results were assessed by applying this transformation solution to the entire ASTER DEM and then comparing this surface to the GPS check points. The results of this analysis are presented in Table 4.14, where they are also compared to the original (pre-match) position of the ASTER DEM. With the exception of the first check point (Nemo Cove 1), the pre-match results generally agree with NASA design specifications for the relative ASTER DEM product, which indicate an off-the-shelf $RMSE_{xyz}$ of within $\pm$25 m (Fujisada et al., 2005). However, following matching, the overall elevation accuracy of the ASTER DEM has been further improved. With the exception of the first point (Nemo Cove 1), the remaining points all offer post-match accuracies of less than a pixel (30 m), and generally show improvement in comparison to the pre-match offsets. Nemo Cove 1 is located at a relatively high altitude (597 m) in comparison to the other check points. This implies that it may be located in the vicinity of steeper, more mountainous terrain, and therefore the quality of the ASTER DEM may be poorer in this locale.

These results are extended through visual analysis, as presented in Figure 4.4, where pre- and post-match (B3) elevation differences are plotted graphically across the central part of the study area, encompassing the main region of interest (including the glaciers). The most obvious features in both plots are the large elevation differences over the mountains

which fringe the north and south of the glacier systems. This is to be expected, and has already been explained in relation to correlation with increased DEM error. However, following the matching, some other differences can also be noted. Prior to matching, notable red regions (positive elevation difference) exist, predominantly around the eastern part of the study area (Nemo Glacier), but also around the front of Moider Glacier in the west, where it meets the ocean. As the surfaces were captured only three weeks apart, this type of offset makes little sense, and is likely a systematic error in the alignment of the ASTER DEM. This would agree with the trend indicated in Figure 4.3 (top), which reveals a small positive (~4 m/1400 m) pre-match systematic error in elevation.

Following the matching procedure, there are fewer red areas across the central region, which encompasses the glaciers. However, the areas of positive change now appear more concentrated along the southern part of the study area. The reason for this is not clear, although it may be that strategy B3 offers a sub-optimal solution in this area, as the utilised AOI patches were all more centrally located within the glaciers. The pattern of differences across the glacier surfaces is now more random and closer to zero (represented by yellow in the plot). There are notable areas of negative change (blue) located between AOI 3 and 5, near the front of Moider Glacier. An explanation for this is not immediately obvious, but one possible cause may be that this region corresponds to weak areas in the ASTER DEM where image matching has failed due to lack of image texture across the featureless ice surface. Overall however, Figure 4.4 demonstrates an improvement in the registration of the ASTER DEM following matching strategy B3, and provides an indication of how the technique can be extended in order to quantify glacier change over time.

4.4.3 Investigating correlation with terrain type

The ASTER DEM transformed under strategy B3 was used to investigate whether any correlation existed between DEM quality and terrain type (see Table 4.1). Analysis of this aspect by BAS, using the same datasets and AOI, has indicated a deterioration, particularly under class III (steep) terrain (Table 4.15), although differences between

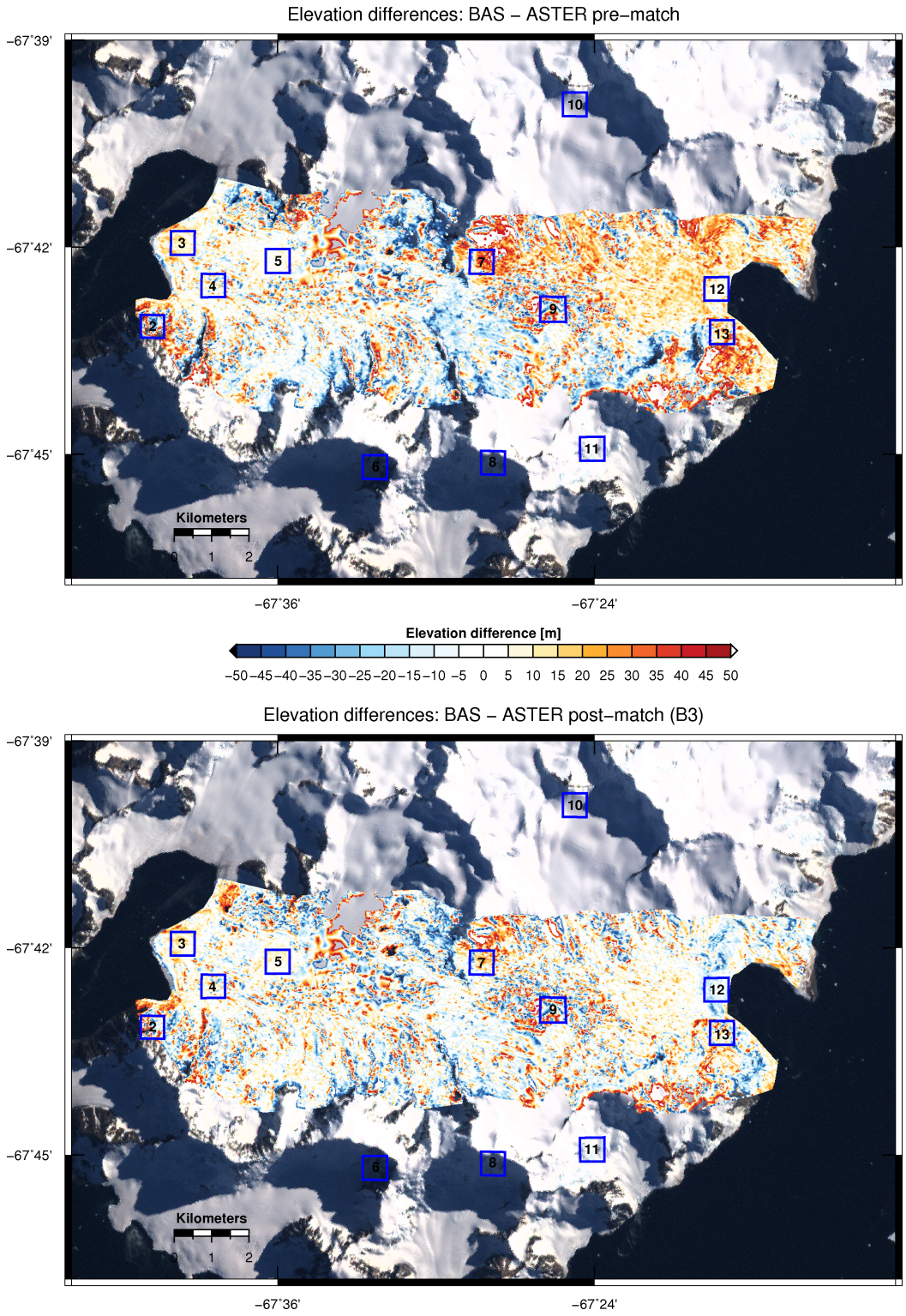

Figure 4.4: Elevation differences before matching (top) and after matching through strategy B3 (bottom). Note the improvement in the general fit before and after the matching. Remaining (large) differences are mainly associated to steeper slopes or areas with low image contrast where the DEM generation may resulted in wrong elevation values.

class I (generally flat) and II (moderate changes in height) appear to be less clear cut (Cziferszky et al., 2010). However, the study performed by BAS utilised the original datasets in their pre-match alignment. Hence it is possible that this interpretation of DEM quality in relation to terrain type may be clouded by the presence of unresolved systematic error. It is expected that the results presented here, following matching, will allow more robust conclusions to be drawn with respect to the influence of terrain. The AOI, which this time included all AOI, are organised under terrain class and presented in Table 4.15, detailing the surface differences following application of strategy B3. The results show a strong correlation between terrain type and mean surface offset. AOI 3, 4, 5 and 9, which fall within class I, generally display the best agreement. The offsets deteriorate in class II, and are slightly poorer again in class II. Although there are exceptions to this (e.g. AOI 13), there is a clear trend in relation to terrain type (see Figure 4.5).

		Post-Match Differences [m]				
Terrain Class	AOI	Mean	σ	RMSE	Min.	Max.
I	3	-0.95	5.81	5.89	-21.81	16.91
I	4	-2.05	15.08	15.22	-70.9	49.02
I	5	-1.06	5.44	5.54	-42.95	17.61
I	9	-3.72	38.21	38.39	-103.36	98.72
II	7	4.47	20.44	20.92	-126.73	60.31
II	10	26.86	34.18	43.44	-131.58	183.49
II	11	-34.07	17.27	38.19	-98.6	16.01
II	12	-3.5	7.48	8.26	-26.28	31.08
III	2	15.13	53.34	55.43	-143.33	215.59
III	6	41.51	90.21	99.23	-132.5	317.14
III	8	-26.77	64.9	70.12	-144.25	136.76
III	13	3.72	21.37	21.68	-105.45	88.83

Table 4.15: AOI offset by terrain class after surface matching

The results are also displayed graphically for the three terrain classes in Figure 4.6. This clearly indicates the strong agreement within class I and the progressive deterioration of mean offset under class II and then class III terrain types. These results agree logically with the terrain types found within the three classes. Class I relates to relatively flat glacier surfaces, with low elevation change across the AOI. Within class I, AOI 9 is recorded as offering low surface texture (Table 4.1), and this may explain the slightly poorer result for this AOI. Class I terrain would be expected to return the strongest results, and provides a valuable indication of the reliability of the matching technique.

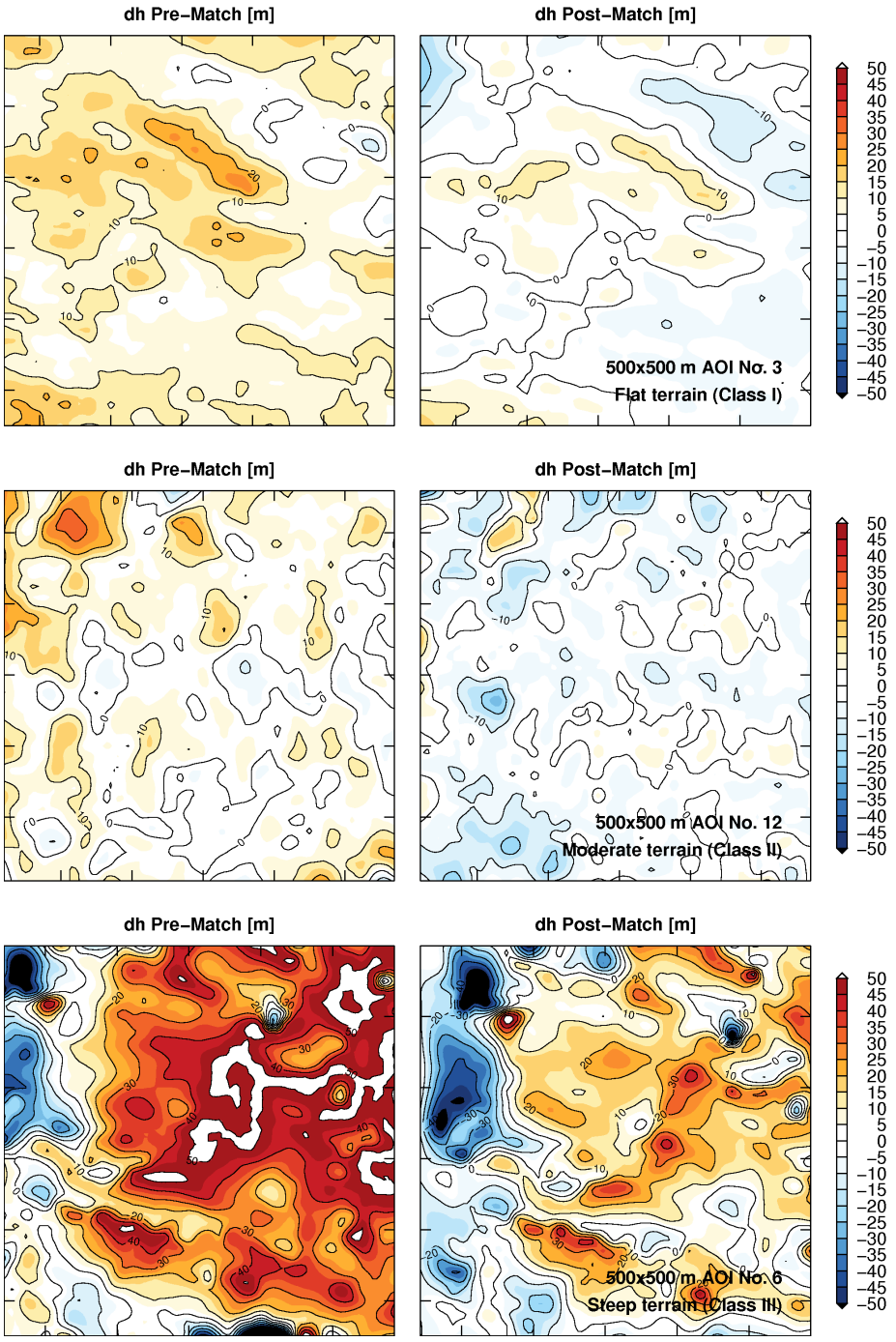

Figure 4.5: Isopachyte map of elevation differences before (left) and after (right) surface matching (strategy B3) for representative AOIs of each terrain class. AOI 3 represents flat terrain (top). AOI 13 represents moderate terrain (middle). AOI 6 represents steep terrain (bottom). Note that in all cases the matching has improved the fit between the DEMs. Lowest accuracies were observed over steep terrain while flat and moderate terrain exhibit a good fit after the matching. Remaining variations are likely to be attributed to erroneous elevation points. Each AOI covers an area of roughly 500 x 500 m.

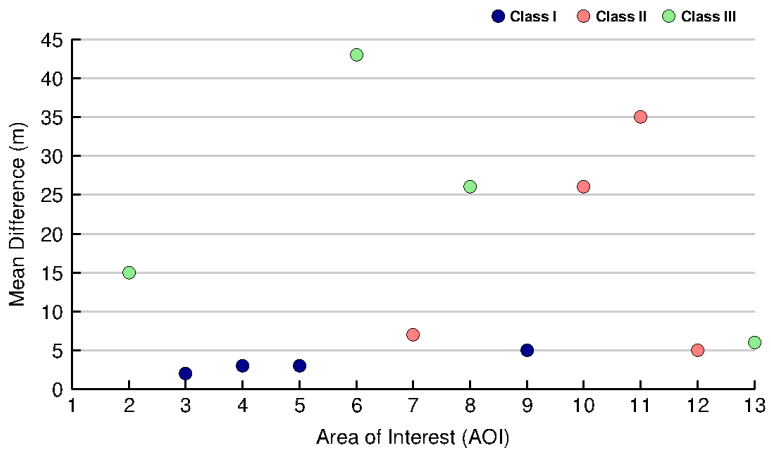

Figure 4.6: Mean elevation difference for the AOI, organised under terrain class (I=flat, II=moderate,III=steep).

Most parts of the glacier front will fall within this terrain class and thus can be associated with more reliable measurements here after the matching.

Class II generally encompasses slightly steeper terrain, with moderate elevation range across the AOI (Table 4.1). This type of steeper terrain will exacerbate any minor offsets between the surfaces, and this is likely to explain the generally poorer results. Figure 4.6 and Table 4.16 highlight that poorest results are returned for class III overall, although within this class AOI 13 can be considered an exception. Class III terrain covers the AOI with the greatest elevation range (up to 723 m). Additionally, these AOI also include rock faces and shadow areas, which are likely to result in weak correlation through the DEM extraction process, possibly resulting in gross errors within the ASTER DEM. This analysis provides valuable insight into the correlation between terrain type and DEM quality. Furthermore, the results allow performance to be assessed specifically for those AOI covering only glacier surfaces, and therefore not influenced by the detrimental effects of the steeper, mountainous terrain (Figure 4.5). The individual AOI results can be summarised by terrain class, as detailed in Table 4.16 where the mean absolute values over the four AOI per class are reported. This clearly reveals the progressive deterioration in the ASTER-photogrammetric DEM agreement as the terrain becomes increasingly rugged, and the quality of the ASTER DEM likely decreases.

	DEM Differences [m]		
Terrain Class	Mean	σ	RMSE
I	1.94	16.14	16.26
II	17.23	19.84	27.70
III	21.78	57.46	61.62

Table 4.16: Mean differences by terrain class

4.5 Summary

The primary outcome of this applicability study has been the identification of an optimal registration approach for assessment of glacial change in the Antarctic Peninsula. The following can be highlighted as the main findings:

1. Least squares surface matching has been shown to provide a cost-effective registration solution and a reliable alternative to the use of GCPs;
2. A patch-based matching approach, limited to individual glacier scale, was found to offer the strongest solution;
3. The ASTER DEM is likely to be less reliable over steep terrain and shadow regions;
4. The matching approach can be expected to offer a mean relative agreement between DEMs of around 2 m over glacier surfaces.

In elaborating on these findings, the test has shown that the surface matching approach is capable of eliminating systematic error associated with the ASTER DEM. Over the glacier AOI, the localised patch-based matching approach consistently aligned the ASTER surface to within a mean value of ± 0.20 m of the BAS photogrammetric DEM. However, in carrying this finding forward, it must be borne in mind that this agreement will be sensitive to the spatial resolution of the DEMs under consideration. Figure 4.4 and Figure 4.6 effectively illustrate the overall improvement in the alignment of the ASTER DEM following the application of the matching technique.

Overall, this evidence confirms the value of surface matching for registration of satellite-derived DEMs, facilitating subsequent assessment of multi-temporal glacier change, including mass balance fluctuations. This test has established surface matching as a reliable mechanism for registration of multi-temporal DEMs, and has demonstrated

this in the context of ASTER DEM data for the Antarctic Peninsula. The results clearly demonstrated that surface matching is able to enhance the accuracy of ASTER elevation data, achieving accuracies with a similar level of magnitude as could be expected through the use of ground control. Furthermore, this test suggests that DEMs extracted from archival BAS/USGS imagery may be aligned to modern ASTER DEMs through a patch-based matching approach. The patch-based approach delivered significantly better performance for the selected areas of interest than the two alternative approaches, providing strong evidence to support the broader application of this strategy at other glacier sites across the Antarctic Peninsula. Following validation of these results through comparison to GPS check points, ASTER DEM quality was explored with respect to terrain type. This revealed strongest agreement between the ASTER and reference DEMs over relatively flat glacier surfaces, with significant errors occurring over steep terrain and in regions of shadow. This applicability study supports the broader application, and alongside more extensive error analysis, will allow quantification of uncertainty in the change measurements.

Chapter 5. Multi-decadal glacier change from historical & modern DEMs

The previous two chapters formed the foundation for a wider study of multi-decadal glacier change assessment across the Antarctic Peninsula, for which the results are presented here. A particular focus is made on the measurement of glacier surface elevation change and the uncertainties associated with these measurements. The findings from Chapter 4 were used as the basis for the matching strategy.

5.1 Study sites

From the available datasets historic and modern DEMs were produced, in combination with ortho-imagery, at 12 locations across the AP (Figure 5.1). Location names were selected based on the observed glaciers from the GLIMS archive or, in case no glacier name was available, on the basis of a larger glacier nearby. Approximate location coordinates (Table 5.4) correspond to a position at the glacier front of the observed glacier. Note that Moider Glacier and Nemo Glacier were sites on which the applicability study (Chapter 4) was performed. The data selection process and DEM generation was described in greater detail in Chapter 3.

The restricted availability of the historical data (see Section 3.1.2) did not allow the entire glacier to be covered. The selected historical imagery covers roughly 20 %, on average, of each glacier that was observed (Table 5.4), mostly the glacier front. This part of a glacier is generally located at lower altitudes and often associated with a negative mass balance due to increased temperatures and ablation. With respect to sea-level rise, negative mass balance changes are of particular interest. In the northern part of the AP,

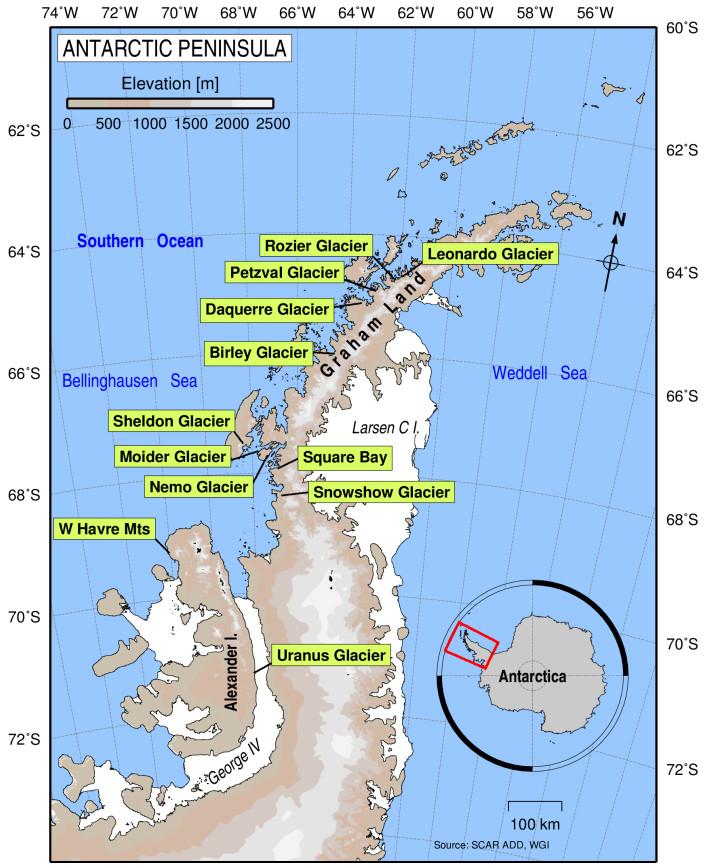

Figure 5.1: Overview of study sites with historic (USGS/BAS) and modern stereo-imagery overlap.

where most of the observed glaciers are located, a third of the area is lying within 200 m of sea-level and summer temperatures are frequently above 0° C which causes substantial surface melt (Pritchard and Vaughan, 2007). It is important to keep in mind, that the complete coverage of individual glacier basins was not possible and, thus, results may be biased towards a negative mass balance. Ideally, both, the entire accumulation and ablation zones need to be covered to study glacier wide mass balance. Due to the partial coverage, the term mass balance is here referred to as *specific surface mass balance*. As such it might be difficult to compare it to glaciers elsewhere that have glacier-wide mass balance records. This needs to be taken into account when assumption about regional trends are made (see Section 6.3). Nonetheless, the available data allows a first glimpse of historic glacier change across the AP, in particular the western AP. For two locations (Moider Glacier and Nemo Glacier) multi-epoch data was available. All other glacier change observations are based on one historical and one modern reference dataset.

Table 5.1 shows the longitudinal and latitudinal coordinates of the observed glaciers and their classification based on their geographic location. The position corresponds to a point on the lower part of the glacier near the front. The glacier classification, except for W Havre Glacier and Uranus Glacier, was taken from the World Glacier Inventory (WGI; WGMS and NSDIC, 2012) and is based on observation from Rau et al. (2004). The observed glaciers in this study are all classified as outlet or valley glaciers with marine terminus. Although located in close proximity to steep and mountainous terrain, they are not classified as mountain glaciers, presumably due to their relatively large size. The exact classification or separation of the AP glaciers is not clear within the literature. Dyurgerov and Meier (2005) include them in the Antarctic ice sheet while Leclercq et al. (2011) exclude them from the main ice sheet. This ambiguity leaves room for uncertainties in estimates from glacier inventories. All glaciers extend over more than 5 km in length. Their flow is constrained by the terrain. From the glaciers studied here, most are located along the coast of the western AP and drain into the Bellinghausen Sea. Uranus Glacier, located on Alexander Island, drains into the George VI Ice Shelf. The longitudinal glacier profiles vary between relatively even, e.g. Moider Glacier or Snowshoe Glacier, to more complex profiles, e.g. Square Bay Glacier or Leonardo Glacier, where the glaciers flow over a series of marked steps. Steps in elevation are often associated with crevasses due to increased glacier surface stress. At the glacier front, all observed glaciers show crevasses. It should be noted, that this was a data selection criteria and can not be assumed for all glaciers elsewhere on the AP. Due to the complex mountainous terrain of the AP, most glaciers are formed by two or more individual glacier basins (compound basin form). From the here observed glaciers, only Rozier and Daguerre Glacier are formed in a single basin, although the actual basin shape is complex. Also shown in Table 5.1 is the main orientation of each glacier front with respect to the direction of glacier flow. The orientation in the higher elevation zone can be different compared to the lower parts, especially for glaciers with a large and complex basin form. Information about the equilibrium line altitude was not available. Moider Glacier and Nemo Glacier are connected via a terrain saddle on Pourquoi Pas Island (roughly 30 km south-east of Rothera Station) but they flow in opposite

Glacier	Lat[°]	Lon[°]	Class. [Type, Basin, Profile]	Orient.
Leonardo	-64.690	-61.930	Outlet, Compound, Cascading	W
Rozier	-64.744	-62.171	Outlet, Simple, Interrupted	NW
Petzval	-64.945	-62.910	Outlet, Compound, Cascading	N
Daguerre	-65.101	-63.565	Valley, Simple, Regular	N
Birley*	-65.934	-64.452	Valley, Compound, Regular	W
Sheldon*	-67.510	-68.337	Outlet, Simple, Cascading	SE
Moider*	-67.700	-67.724	Valley, Compound, Regular	W
Nemo	-67.712	-67.330	Valley, Compound, Regular	E
Square Bay†	-67.925	-66.882	Valley, Compound, Cascading	N
Snowshoe	-68.310	-66.721	Valley, Compound, Regular	W
W Havre Mts†	-69.244	-72.055	Outlet, Compound, Cascading	SW
Uranus*	-71.370	-68.300	Outlet, Compound, Regular	E

Table 5.1: Glacier classification and location. Note: *BAS data for historical imagery; †no name given in WGI WGMS and NSDIC, 2012.

directions. All other glacier basins are not connected with each other. None of the observed glaciers had floating extensions at the acquisition time of the most recent imagery. The recent glacier fronts are in close agreement with the MOA grounding line positions (Scambos et al., 2007).

5.1.1 Glacier area mapping

Data on glacier area and length for the observed glaciers were not available prior to this study. Semi-automated or manual glacier mapping is challenging because a clear delineation of glacier boundaries in the AP is difficult. Much of the terrain is snow covered and ice masses are connected. The differentiation of stable terrain is not always trivial. It is possible that snow covered stable terrain may be falsely mapped as glacier or snow. Figure 5.2 illustrates the ambiguity in glacier area and length mapping. According to the WGI database, Remus Glacier and Snowshoe Glacier are two individual glaciers but there is a clear connection in the upper part which is contradictory to the GLIMS guidelines (Raup and Khalsa, 2010) that defines "all tributaries and connected feeders that contribute ice to the main glacier" as one glacier.

Semi-automated mapping was tested using the band ratio of the ASTER bands B3 (visible) and B4 (near-infrared). Given the spectral signature of snow it allows for semi-automated detection of snow and glacier outline delineation (Paul and Kääb, 2005; Rastner et al., 2012). However, results were unsatisfactory and not considered further for

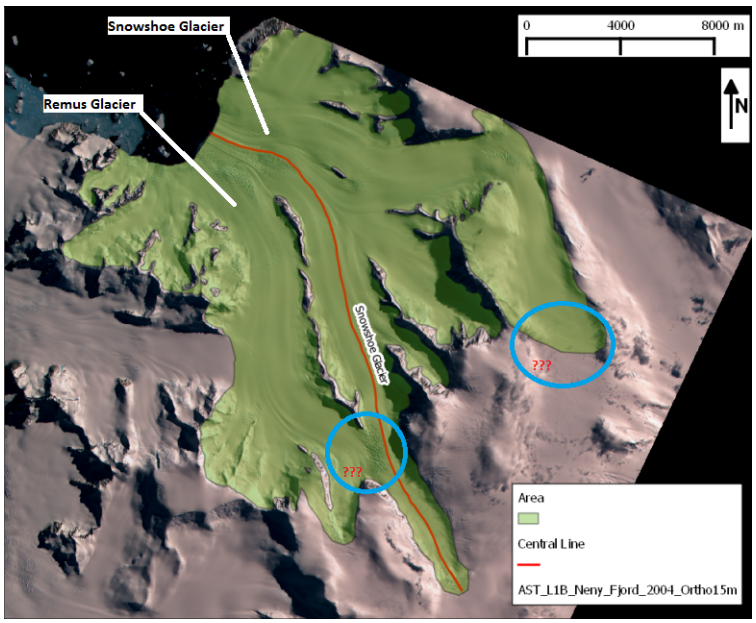

Figure 5.2: Ambiguity of glacier boundary delineation (indicated by blue circles) in the AP. Example shows an image of Remus Glacier and Snowshoe Glacier. In this study, the site has been mapped as one glacier.

glacier area mapping in the AP. Most of the ice is covered by snow and a clear delineation was not possible. Instead, the terrain and glacier area was mapped manually from the ortho-rectified ASTER imagery using *ArcGIS 10*. The terrain was classified into stable, e.g. nunataks or mountain ridges, and potentially unstable terrain, e.g. glacier surface and snow covered areas. In most cases the stable terrain is not connected and discontinuous across the area. Clearly identifiable stable terrain is formed by mountain ridges or exposed rock outcrops. This local characteristic can actually support the patch-wise matching approach. In any case, large areas of continuous stable terrain provide the best stability and redundancy for the matching. Glaciers were mapped in accordance to the GLIMS guidelines (Raup and Khalsa, 2010). Results were stored as polygon shapefiles and then used to clip the DEM points. Measurements of total glacier area and length were made but are somewhat uncertain ($\pm$20 % is not unrealistic) due to the partial coverage of the imagery and the previously discussed issues. Manual glacier delineation was also used by Davies et al. (2011) to map glaciers in the northern AP. They also found the manual mapping advantageous over semi-automated approaches in the AP.

5.2 DEM co-registration

Before the glacier elevation change was assessed, surface elevation differences were computed and the fit between corresponding DEMs, i.e. historic DEM minus ASTER DEM, was evaluated. Depending on the reference dataset, the RMS_{xyz}values from the absolute orientation of the historical DEMs were within $\pm$30 m when initiated by ASTER and $\pm$10 m for the modern aerial imagery. Despite the successful extraction and absolute orientation of DEMs, the initial fit between the historic and the modern DEMs was found to be unsatisfactory for a precise measurement of glacier elevation change. Mean DEM offsets over stable terrain ranged from -45 to 69 m in plan to -11 to 50 m in elevation. This is because it was only possible to extract a minimal number of artificial GCPs from the present-day ASTER imagery. The accuracy of the extracted points was relatively low in comparison to what could be achieved through field survey with modern GPS. Consequently, the absolute orientation of the archival imagery using these points resulted in only an approximate alignment of the datasets. To overcome this limitation and to correct for remaining offsets between corresponding DEMs, robust surface matching was performed. The matching algorithm was described in Section 3.4. Chapter 4 showed that DEM matching on an individual glacier basis using a patch-based approach offers the best matching strategy. Both of these conditions are given here because the overlapping areas are within the scale of individual glaciers and due to the non-uniform (patch-wise) distribution of stable terrain.

Matching was performed over stable terrain only. Ice and snow covered terrain is likely subject to surface change and could otherwise influence the matching solution. Most of the clearly identifiable stable terrain is associated with steep slopes (Figure 5.5) because flatter areas are more likely covered by snow or ice and where therefore excluded from the matching. However, Section 4.4.3 showed that steep terrain is more prone to errors. Therefore, the sea surface was also assumed to be stable because it provides an additional reference surface and allows for any rotational offset between DEMs to be determined. Differences in ocean elevation between scenes (due to tides and atmospheric effects) were assumed to be within the expected accuracy range of the ASTER data ($\pm$7.5 m at best). In all cases the Euclidean surface differences were minimized and

robust estimation was used to account for remaining differences or outliers over stable terrain. Points with low correlation values from the DEM extraction in *SOCET SET* were excluded from the historical DEM. Erroneous areas in the ASTER DEM were manually masked. Differences of more than 50 m were directly excluded from the least squares estimation by using a threshold check. Remaining errors in the DEMs, e.g falsely included non-stable surface points, were down-weighted through robust estimation. The matching solution was accepted when the rotational corrections were less than 0.01°, the corrections in the translations were less than 0.1 m and the reference standard deviation change of the differences to the previous iteration was less than 0.0001. A maximum of 50 iterations was allowed. If a solution took more than 50 iterations it is less likely to be of good quality (Miller, 2007). Before the matching, coordinates (UTM/WGS84) were shifted to the centre of the reference DEM patch to avoid large x and y coordinates (see Section 3.4.2). After successful matching over stable terrain, the estimated seven parameter conformal transformation parameters were applied to all points (over stable and glaciated terrain) of the historical surface. The centre offset was added again after the match to the corrected coordinates. The vertical differences between the matching and reference surface were calculated before and after the match to check for accuracy and improvements. After DEM co-registration, surface elevation change (see Section 5.3.2) was computed by subtracting the earlier DEM from the later with computed summation over the DEM extent. The workflow is summarised in Figure 5.3.

5.2.1 Surface matching results

The surface matching was successful in all cases. This underpins that the applied matching strategy is suitable for DEM co-registration of DEMs derived from USGS aerial imagery and ASTER data. An improved fit and accuracy for the historical DEMs was achieved which enabled a more accurate measurement of surface elevation changes. Successful matching was achieved after 11 iterations, on average. Table 5.2 shows the summarized statistics of the elevation differences over stable terrain before and after the matching. The mean and parameter uncertainties show significant improvement after the matching. The elevation difference means after the matching are around zero and in all

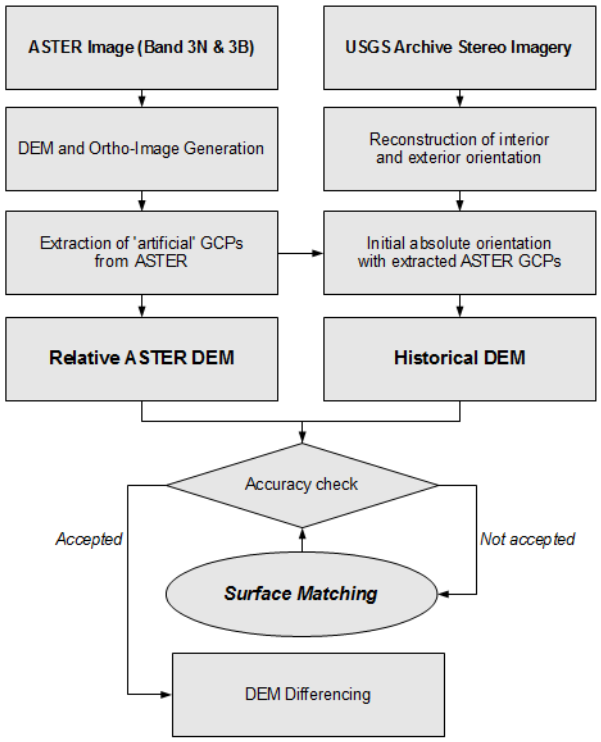

Figure 5.3: Workflow of DEM production and assessment using ASTER imagery and historical archive stereo-photography without ground control.

cases within the accuracy that can be expected. The post-matching RMS of DEM differences over stable, generally rough, terrain was ~25 m, but this overstates the error over the generally flatter glacier surfaces (see Section 4.4.3).

The best fit was achieved for Sheldon Glacier, Moider Glacier and Nemo Glacier sites with RMS values better than than 15 m over stable terrain. Here a high resolution DEM from BAS aerial photography and direct ground control data was available. In cases where ASTER DEMs provided the reference surfaces the uncertainties show more variation with values of up 40 m. The mean difference over stable terrain was within ±2 m on average, equivalent to an uncertainty in rate of 0.05 m/yr over a typical 40-year span between DEMs. Highest uncertainties were found in areas where the stable terrain is almost entirely represented by steep topography and where shadowing or low image contrast resulted in errors in the ASTER DEM, an issue that was already discussed in Section 4.4.2. The mean values after the matching express an improvement of the fit by 76 %, on average. The relatively large minimum and maximum values are associated with blunders in the DEMs that were not masked well enough. As these were down-weighted or removed in the matching, they have no influence on the solution.

Location	Pre-Match					Post-Match				
	$\bar{x}$	σ	*RMSE*	*min*	*max*	$\bar{x}$	σ	*RMSE*	*min*	*max*
Leonardo	11.21	46.86	47.44	-191.36	191.82	0.58	24.87	28.63	-166.00	147.26
Rozier	12.22	56.68	57.16	-165.64	171.00	4.22	39.12	39.68	-169.05	170.77
Petzval	-12.92	69.65	70.24	-193.71	193.83	1.26	36.59	38.55	-192.41	193.54
Daguerre	-10.17	53.82	53.89	-175.79	176.37	-2.44	39.88	41.90	-176.34	175.79
Birley	49.06	86.32	97.73	-231.56	292.36	-0.65	40.00	43.26	-220.24	293.46
Sheldon	9.98	18.75	20.88	-63.56	63.60	0.36	11.55	14.57	-63.56	63.62
Moider	-3.19	10.90	11.18	-45.57	43.97	-1.80	10.53	10.51	-44.13	42.46
Nemo	-15.98	10.99	19.21	-56.54	55.57	-1.71	8.67	10.02	-54.05	56.34
Square Bay	1.35	41.21	40.70	-122.07	121.46	-0.97	19.78	23.29	-119.14	121.66
Snowshoe	1.90	30.54	30.27	-94.51	92.94	0.84	22.51	24.19	-94.33	93.98
W Havre	-8.58	73.79	73.15	-214.87	215.19	2.99	33.66	37.32	-192.25	213.81
Uranus	-176.45	146.24	229.17	-522.82	359.56	-0.22	16.65	19.44	-148.08	131.44
	-11.80	53.81	62.59	-173.17	164.81	0.21	25.32	27.61	-136.63	142.01

Table 5.2: Level difference statistics over stable terrain. Observations above $\pm 3 \cdot$RMSE were removed.

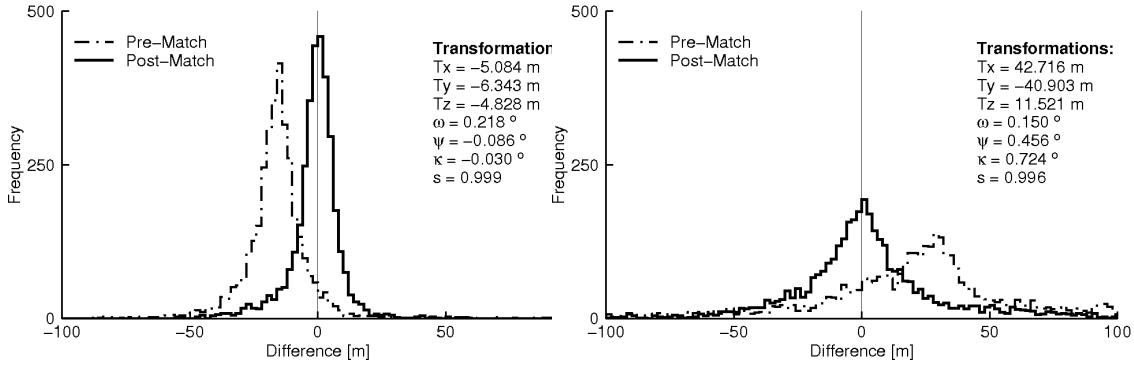

Figure 5.4: Histogram of level differences over stable terrain before and after surface matching for Nemo Glacier (left, USGS 1969 to BAS 2005) and Leonardo Glacier (right, USGS 1968 to ASTER 2010).

Figure 5.4 shows two representative examples of computed surface level differences before and after the matching. It can be seen that with higher resolution and GPS controlled reference data (BAS DEM from 2005; Figure 5.4, left) better accuracies can be achieved and that the extracted historical USGS DEMs are generally suitable for elevation change measurements. The post-match differences over stable terrain show a normal distribution with means around zero. The greater uncertainty and lower spatial resolution of the ASTER data is reflected in a wider spread in the differences and the lower spatial resolution. Additionally shown in Figure 5.4 are the transformation parameters that were obtained from the matching solution. The scale parameters are relatively stable around unity while translations and rotations can vary substantially. Shifts of more than 50 m or rotations of more than half a degree were not unusual given the lack of ground control data. Without the matching these would bias the elevation change estimates. It is important to note that a simple translation estimation would not remove the rotational biases.

After the matching potential elevation and slope dependent biases were assessed, to check the findings from the test at Pourqoui Pas Island (see Section 4.2.1). Again, no evidence of an elevation dependent bias in the ASTER data was found. An ASTER jitter[1] as reported by Nuth and Kääb (2010) was not observed. Thus, matching with the optional eight parameter transformation was not necessary. Nonetheless, a test with this option was performed and showed that the scales in the xy direction and the z direction were very similar and around 1.0. Figure 5.5 shows that no significant correlation

[1]High frequency changes (e.g. in rotation) in the satellite position that can cause image distortion.

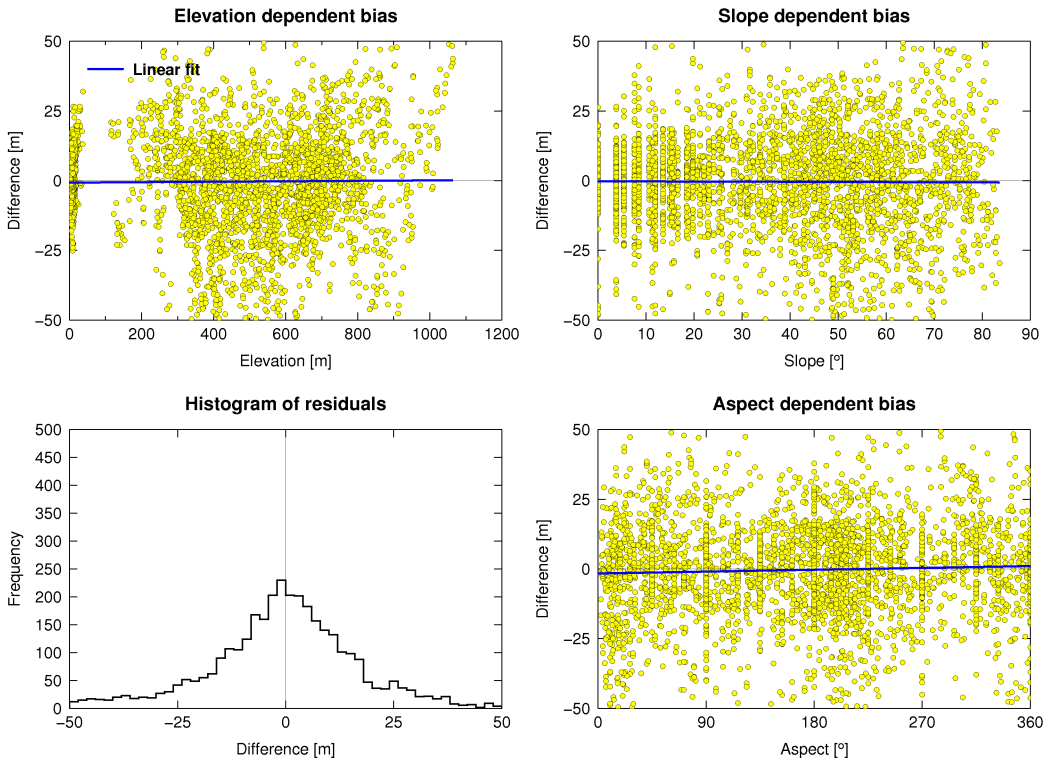

Figure 5.5: Check for bias in elevation differences with respect to elevation, slope and aspect at the Leonardo Glacier study site.

between elevation, slope and aspect with respect to the elevation differences is evident. Similar observations were found for all other study sites. However, complete ASTER scenes were not assessed and such biases might only be obvious over larger areas. In the BAS and USGS datasets no systematic bias was found. This provides confidence in the quality of the data and the matching.

Uncertainties in the elevation differences were assigned by calculating the semivariograms using the geostastistical analysis described in Section 3.3.2. Semivariograms (Figure 5.6) were calculated for lag distances of 1 km and 5 km. Larger lag distances were not assessed because the spatial extent of the data was only within the range of a few kilometers. Binning was carried out at 25 m intervals for scales less than 1 km, and at 200 m over the 5 km scale. The resulting parameters of the theoretical variograms are summarised in Table 5.3 together with the derived uncertainty estimate. Visual interpretation of the variograms showed that spatial correlation is evident in ranges of up to 200 m. This scale is assumed to be correlated to the image matching procedure (not to be confused with the surface matching) within the photogrammetrical software for the identification of conjugate points in the stereo model for elevation

Location	Nugget [m]	Sill [m]	Range [m]	σ_A
Leonardo	0.00	808.48	60.77	2.34
Rozier	10.80	2896.81	193.23	5.44
Petzval	0.00	2455.38	127.40	5.00
Daguerre	0.00	3110.15	173.90	5.65
Birley	0.00	1771.37	136.71	3.92
Sheldon	0.00	212.82	115.21	1.41
Moider	0.00	130.81	104.07	1.75
Nemo	0.00	80.01	19.83	1.20
Square Bay	26.30	585.40	101.74	2.68
Snowshoe	0.00	588.60	61.61	2.11
W Havre Mts	0.00	1608.48	119.67	3.86
Uranus	0.00	331.83	62.11	1.87

Table 5.3: Theoretical semivariogram parameters (1 km lag distance) and spatially averaged uncertainty σ_A over stable terrain points. This uncertainty was used for the glacier change assessment. The range parameter is an indicator for spatial autocorrelation. Lower values indicate less correlation and uncertainty.

measurements (Rolstad et al., 2009). The image matching is typically performed with search windows of the size of 7x7 or 15x15 pixels, which corresponds to a ground distance of a few hundred meters. In case of a spatial resolution of 15 m for the ASTER data, 105 to 225 m (7x15 and 15x15). Evidence of spatial correlation over intermediate (km size) scales, which are assumed to be related to weak a relative orientation of the stereo pairs, was not found (Rolstad et al., 2009). This confirms that the relative orientation of the DEMs has been successfully solved by the matching. Thus, over distances greater than 200 m the elevation differences were assumed to be spatially uncorrelated. Variances smaller than the sampling distance (nugget parameter) were found to be negligible. The relatively large nugget value of 26.30 at the Square Bay site may be due to sampling errors in the ASTER DEM, since the stable terrain at this site shows very high relief gradients. The sill parameter reflects the (semi-)variance in the data. It is slightly larger than the values which were obtained without geostatistical analysis, presumably due to the discussed spatial correlations. The uncertainties were also used to assign uncertainties to the glacier elevation changes (Table 5.4). It was assumed that the uncertainties over the glacier surface are actually less or equal to the uncertainties that were obtained over stable, generally more steep, terrain and hence these represent a conservative uncertainty estimate.

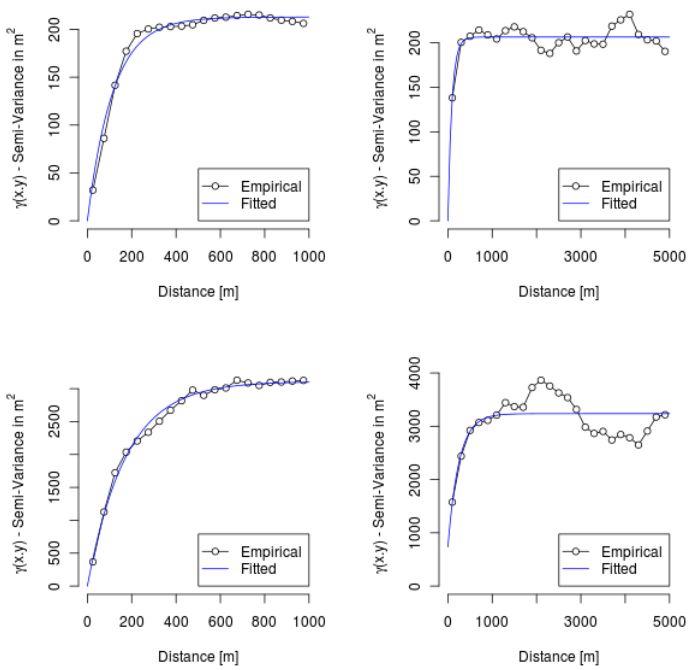

Figure 5.6: Semivariograms for elevation differences (at 1 km and 5 km lag distance) over stable terrain for Sheldon Glacier (top) and Daguerre Glacier (bottom).

5.3 Glacier change assessment

5.3.1 Glacier length change

Due to the incomplete coverage of the historical data, changes in the overall glacier extent could not be mapped. This is a major drawback at many interesting sites in the AP, especially where glaciers have a large basin. However, the glacier fronts are often covered, partially because they are more narrow than the upper glacier parts. This allowed the mapping of frontal changes in comparison with the modern data. Alongside the mapping of areal glacier extent (as described earlier), frontal glacier length changes are a good indicator for the response of a glacier to environmental changes, e.g. regional or global warming (for example Cook et al., 2005; Oerlemans, 2005; Paul, 2010; Leclercq and Oerlemans, 2012).

The glacier fronts were mapped in the historical and modern ortho-image using *ArcGIS 9.3* and results were stored as shapefiles. Frontal length changes were only mapped for glaciers that terminate in open water. In analogy to Cook et al. (2005), the length change was surveyed by drawing a minimum of five lines perpendicular to the direction of flow

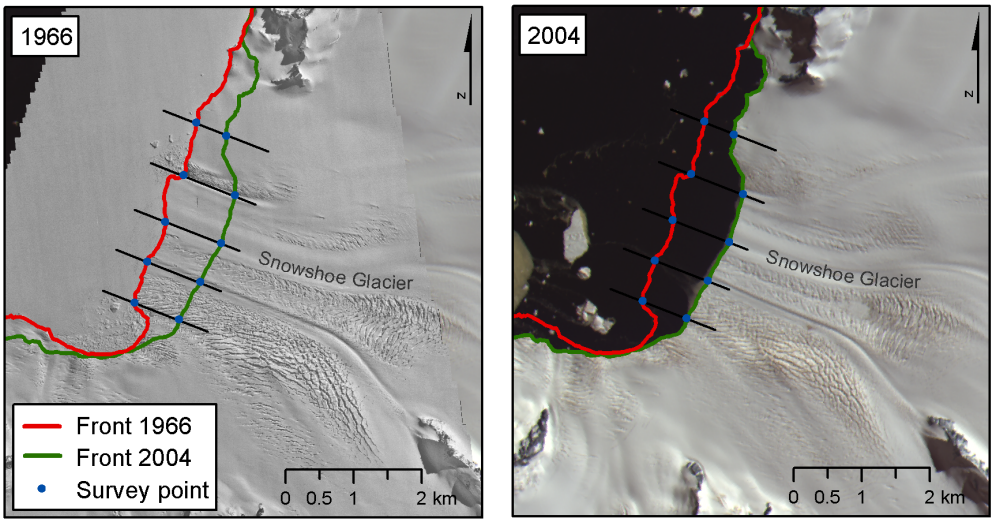

Figure 5.7: Measurement of glacier length change of Snowshoe Glacier, AP (68.38° S, 66.73° W). A minimum of five measurements per glacier were made to account for variations in the length change along the glacier front.

of the glacier and measuring intersection points between the glacier fronts and the lines of flow. Lines were separated in approximate equal intervals. Averaging the differences between corresponding intersection points gave the respective glacier length change (Figure 5.7). Single measurements per glacier are not recommended because the pattern of glacier retreat or advance can be complex. Parts of a glacier may have advanced while other parts have retreated or the retreat is different along the glacier front. Results of these measurements can be found in Table 5.4. Glacier fronts are generally stable (e.g. Petzval and Leonardo glaciers) or display retreat of up to 1 km (Table 5.4). Moider Glacier (Figure 5.8), for which five epochs of data were available, is a representative example of the general trend of glacier retreat in the AP. Only one smaller glacier, located in proximity to Leonardo glacier, showed advance (Figure 5.11).

5.3.2 Surface elevation change

The extracted glacier surface elevation changes are shown in Figure 5.11 and summarised in Table 5.4. For all glaciers, net surface lowering was observed near the glacier fronts (Figure 5.11, Table 5.4), with an average total lowering of 20-30 m and a maximum of up to ∼50 m over the multi-decadal periods. Figure 5.9 shows an exemplary cross-section along the front of Leonardo Glacier showing the negative change in surface elevation. For glaciers where sufficient spatial coverage of

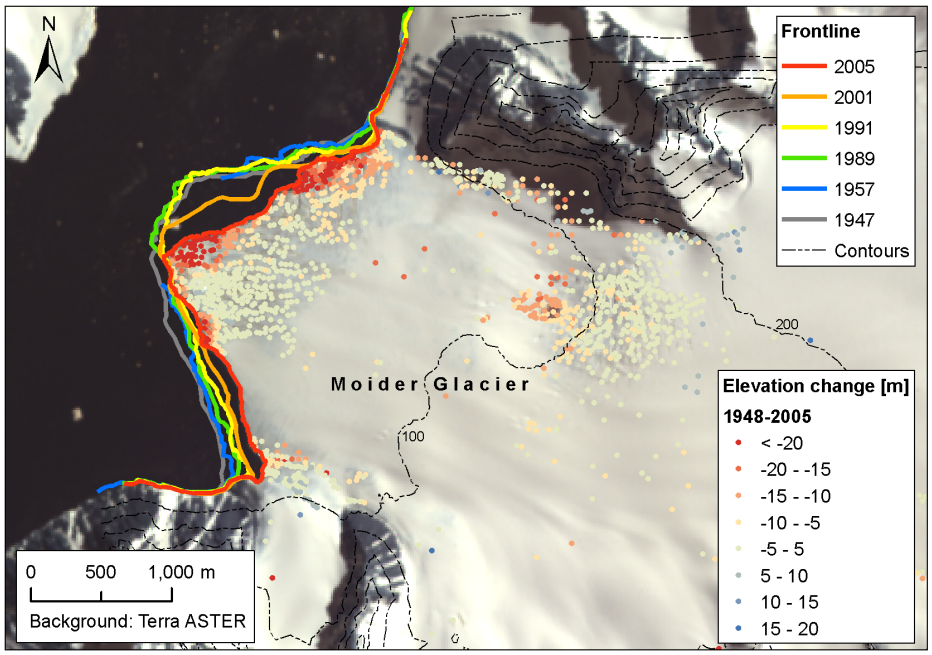

Figure 5.8: Glacier length change of Moider Glacier

observations was available, the lowering decays to zero within a few km or less of the ice front (e.g. Nemo and Sheldon glaciers) and is bounded to regions lower than ∼400 m elevation (Table 5.4). Figure 5.10 shows a plot of the elevation change rate dh/dt in relation to elevation. The measurements for this plot were obtained along the glacier centrelines. The signal of Sheldon glacier shows a rather strong variation over elevation in comparison with the other glaciers. In combination with the large retreat of the glacier this may not be unusual. However, the time difference in the observations for Sheldon Glacier was only 15 years whereas the other glaciers were observed over a period 37 years in average. The low elevation change rate for Uranus Glacier is explained by its southern location (71°). Some glaciers show elevation increases of up to ∼20 m at higher elevations (e.g. Sheldon and Petzval glaciers). There is some localised variation in these patterns, as is evident on the small glacier adjacent to Leonardo Glacier where glacier advance and thickening of up to 30 m is evident (Figure 5.11), but for larger glaciers the general pattern of surface lowering and frontal retreat appears robust. Seasonal variations of snow cover between images are within the level of accuracy that can be achieved from the ASTER DEMs.

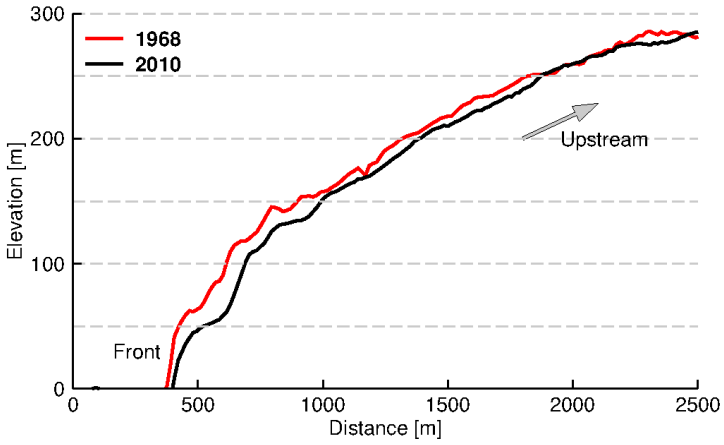

Figure 5.9: Multi-epoch elevation profiles along the front of Leonardo Glacier

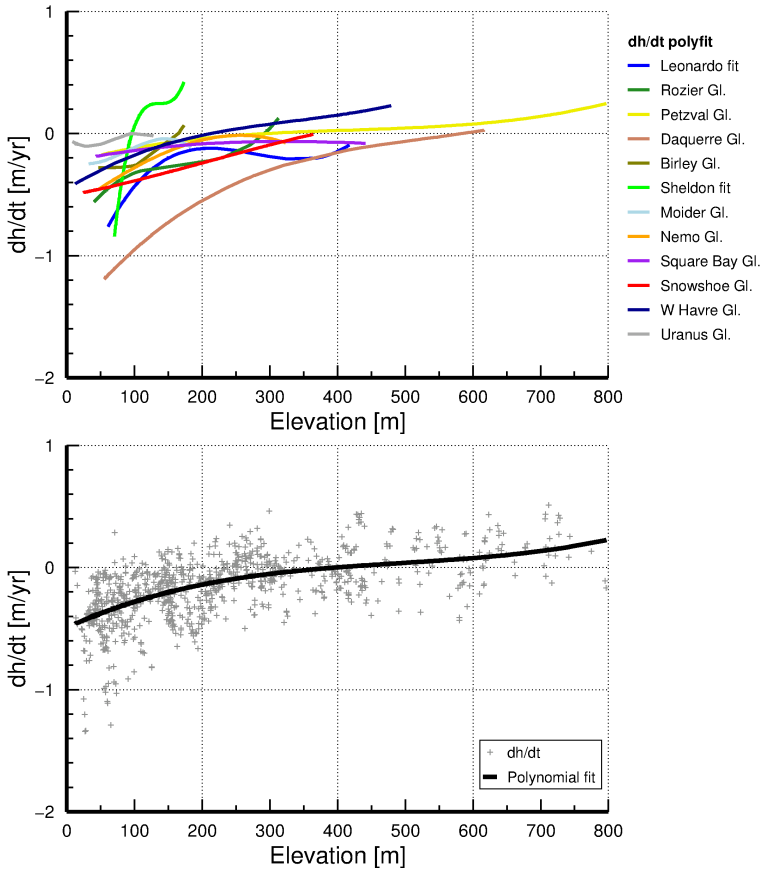

Figure 5.10: Elevation change rate dh/dt over elevation for individuals glaciers and combined (excl. Sheldon glacier). Note that the lowering decays to zero at around 400 m of elevation.

Mean lowering rates (Table 5.4) for the glacier fronts were computed using points sampled within a representative 1 km^2 area of each glacier within the lowest first km. The rate is expressed in water equivalent elevation change rates with the assumption that the majority of the lowering occurs at the density of ice (917 kg/m^3). The sampling is limited by the lack of surface detail and coverage of the whole glacier surface. Uncertainties for each lowering rate were assigned using the spatially averaged uncertainties from the matching (Table 5.3) over the time span. For the Rothera ice ramp a surface lowering of 0.28 ± 0.09 m/yr (1989-2005) was measured, which is in agreement with in-situ measurements of 0.32 m/yr (1989-1997) from Smith et al. (1998). This comparison provides both a partial validation of the measurement accuracy and suggests that the lowering of the ice ramp has continued at a similar average rate since 1997. The average frontal lowering rate measured for all observed glaciers was 0.28 ± 0.03 m/yr over an average period of 37 years (1970-2007). Examining the spatial distribution of lowering rates (Figure 5.12) reveals a pattern of increased rates of lowering in the northern Peninsula, with correspondingly lower rates further south. The latter is highlighted by the insignificant 0.04 ± 0.13 m/yr lowering at Uranus Glacier. Petzval Glacier exhibits a relatively low negative change rate compared to the other observed glaciers in the north-western AP. This may be explained due to mass transport from the upper part of the glacier, which shows increased elevations, and an average advancing at the front of around 1.1 m/yr over the observed period. Sheldon Glacier appears to be an exception to the north-south pattern, but the time period of data for this glacier covers only 1989 to 2005. One possible interpretation is it stands apart from nearby glaciers because lowering rates have increased recently (see Section 6.1).

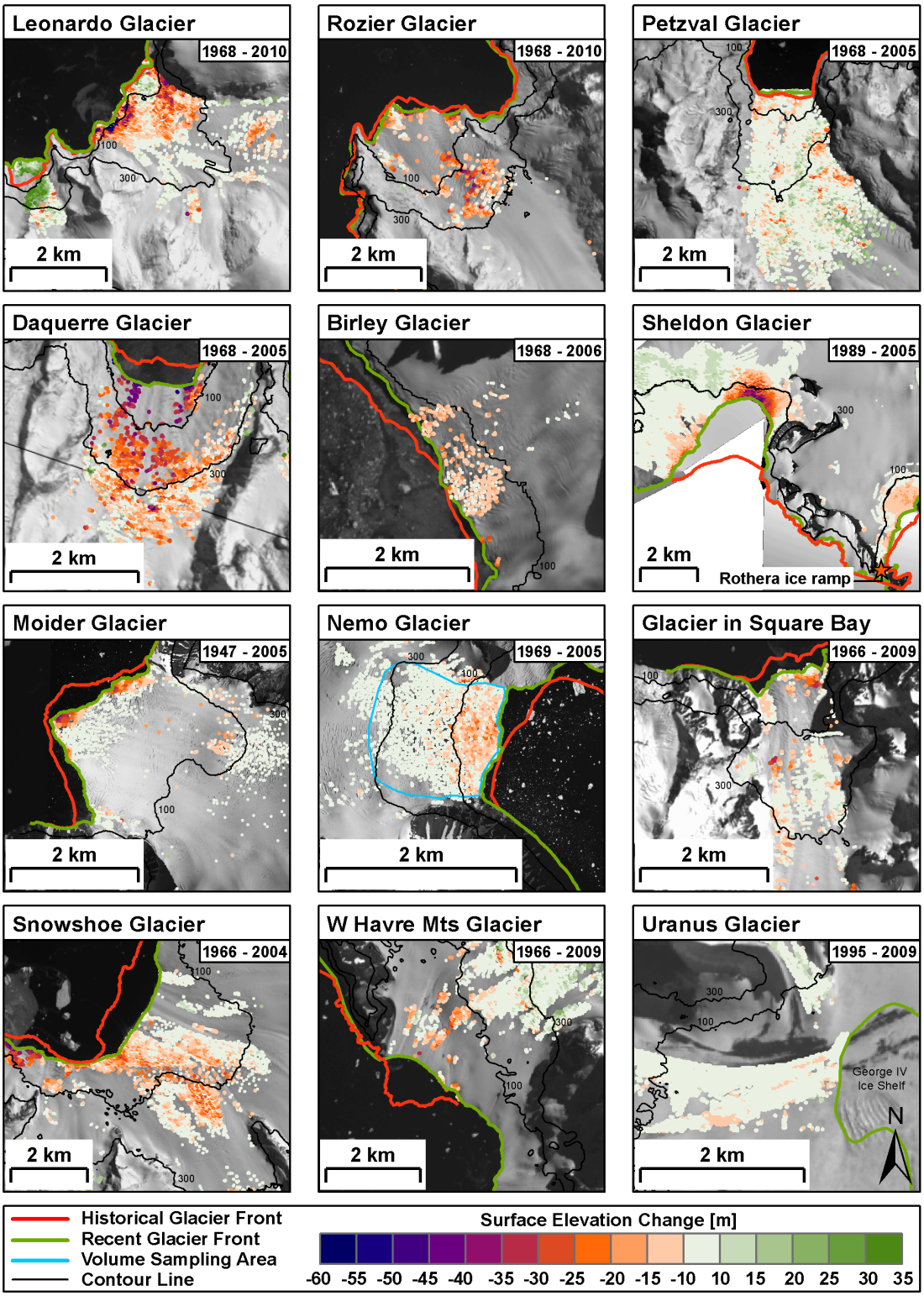

Figure 5.11: Overview of glacier surface elevation changes in the western AP. 100 m and 300 m contours lines are shown to illustrate the elevation range of the surface lowering. Zero-mean elevation changes over stable terrain are not shown for clarity.

Glacier	Lat [°S]	Long [°W]	Year Historical	Year Recent	Span [y]	LC[a] [m][m/yr]	FEC[a] [m/yr w.e.]	Elev dh_0[b][m]	Dist dh_0[b][m]	Total Area [km²]	Coverage [%]
Leonardo	64.70	61.93	1968	2010	42	49 (-1.2)	-0.29 ± 0.06	550	4300	51.3	13
Rozier	64.75	62.17	1968	2010	42	-81 (-2.0)	-0.40 ± 0.13	n/a	n/a	21.1	21
Petzval	64.94	62.91	1968	2005	37	42 (1.1)	-0.10 ± 0.14	600	4000	46.3	20
Daguerre	65.10	63.56	1968	2005	37	-311 (8.4)	-0.42 ± 0.15	600	2700	17.2	25
Birley	65.93	64.45	1968	2006	38	-130 (-3.4)	-0.32 ± 0.10	n/a	n/a	17.3	33
Sheldon[c]	67.51	68.34	1989	2005	16	-967 (-60.4)	-0.57 ± 0.09	150	1200	191.8	19
Moider[c]	67.70	67.63	1947	2005	58	-299 (-5.2)	-0.12 ± 0.03	200	4000	54.3	17
Nemo[c]	67.71	67.33	1969	2005	36	-165 (-4.6)	-0.24 ± 0.03	300	1700	45.5	7
Square Bay	67.93	66.88	1966	2009	43	-207 (-4.8)	-0.29 ± 0.06	500	4100	22.3	23
Snowshoe	68.31	66.71	1966	2004	38	-682 (-17.9)	-0.28 ± 0.06	400	4800	233.9	24
W Havre Mts	69.24	72.05	1966	2009	43	-662 (-15.4)	-0.22 ± 0.09	450	2300	72.2	20
Uranus[c]	71.37	68.30	1995	2009	14	n/a	-0.04 ± 0.13	n/a	n/a	n/a	n/a
Mean			1970	2007	37	-310 (-11.3)	-0.28 ± 0.03	417	3233	70.3	20

Table 5.4: [a]LC = Frontal length change; FEC = Frontal elevation change rate.
[b]Elev=Elevation of zero lowering; Dist=Distance to zero lowering from glacier front; n/a = Measurement not applicable due to limited data coverage or indefinite signal of lowering. Measurements were made along longitudinal profiles for glaciers where a distinct decay in the lowering signal was observable. Note: Full glacier extent is not covered by historical imagery.
[c]BAS datasets for historical data.

5.3.3 Volume change and mass balance

DEM differencing allowed the measurement of volumetric changes for parts of the observed glaciers. A glacier wide surface mass balance could not be assessed, due to the already discussed reasons. Areas with sufficiently dense measurements of elevation differences are mainly located over the frontal parts of the observed glaciers (Figure 5.11). This is explained by the higher surface texture in these areas which resulted in more observations. The historical DEMs were stored as TINs leaving out areas with low correlation in the image matching. The ASTER elevations were computed on a raster basis (for each pixel) which leaves room for erroneous elevation values over the same areas with low contrast, e.g. the accumulation zone. In order to get a specific surface mass balance, one could either compute a volume over smaller areas with sufficiently dense measurements or use interpolation to close gaps between areas with sparse or no measurements.

Given the rather small number of 12 observed glaciers and the fact that predominantly frontal parts are covered, the computation of surface mass balance for each glacier was found to be not beneficial. In particular, the lack of observations at higher elevations (accumulation zone) would lead to biased results. Pritchard and Vaughan (2007) also observed increased accumulation of snow which might outbalance the observed loss. The overestimation of mass loss and undersampling at higher elevations has to be kept in mind when making conclusions with respect to mass balance changes, in particular with respect to climate signals (see Chapter 6). Here the change in glacier extent and glacier-wide mass balance could not be mapped.

Nonetheless, for the two glaciers (Moider and Nemo) where multi-epoch data was available, volume change measurements at the front were derived. The multi-epoch data allows changes over shorter time-spans to be analysed in contrast to the rather long spans for the other glaciers. For Moider glacier results from Cziferszky et al. (2010) were used.

Figure 5.13 shows the area (roughly 1.5 km²) that was assessed for Nemo Glacier. The volume change was calculated using *ArcGIS 9.3*. First, the area of interest was outlined and clipped. Then the cut/fill option of the Spatial Analysis Tool was used. Again, an ice

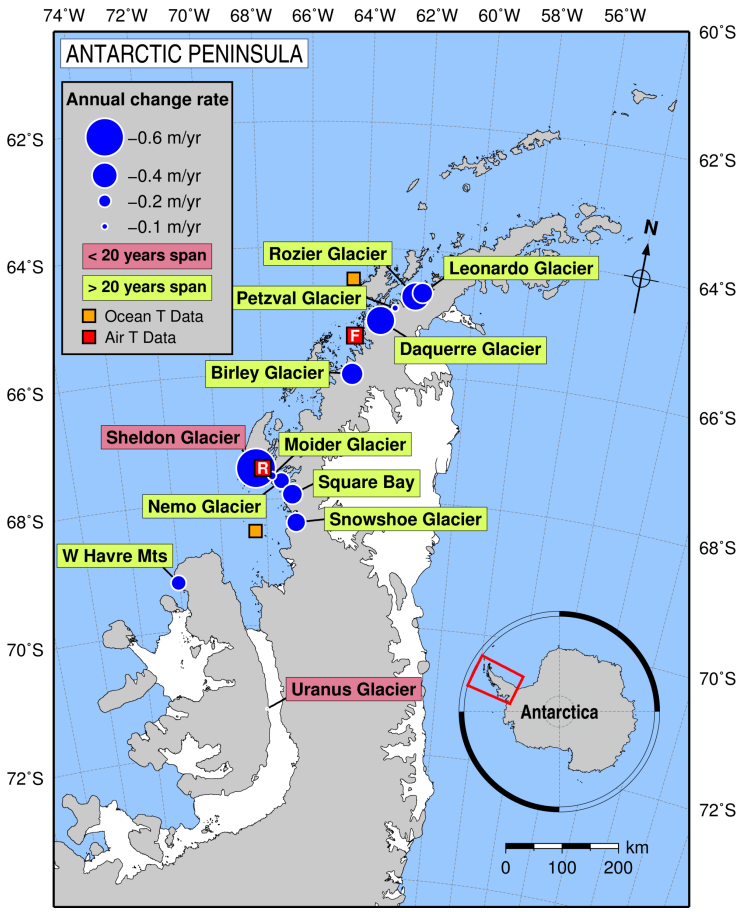

Figure 5.12: Annual mean surface lowering in the western AP

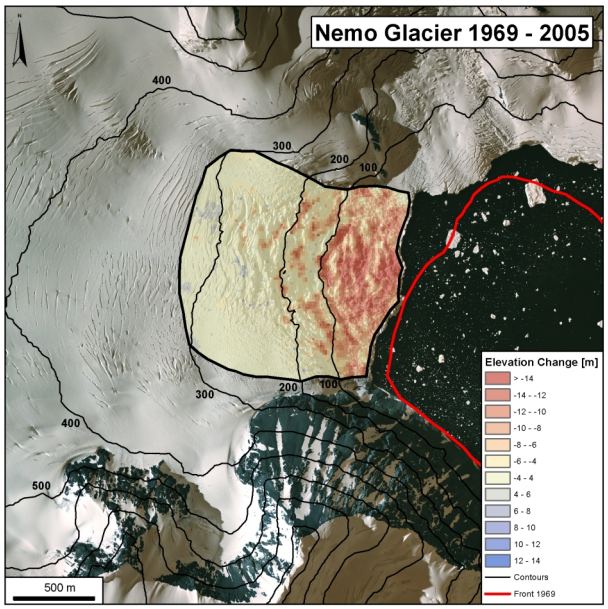

Figure 5.13: Glacier surface lowering at the front of Nemo Glacier. The thick black line shows the area for which the volume change was calculated (see Figure 6.1a).

density of 0.917 kg/m³ was assumed. The resulting measurements for the multi-epoch data are shown in Figure 6.1a. The relatively small area for Nemo Glacier is explained by the limited coverage and sparse measurement further upstream.

5.4 Summary

This chapter has demonstrated that multi-decadal glacier surface elevation change of the AP can be assessed using a combination of historic aerial stereo-photography and ASTER data. In limited cases modern aerial imagery was available and served as the basis for reference DEMs. It was shown, that that the improved surface matching software (Section 3.4.3) and proposed matching strategy (Section 4.3) was able to efficiently co-register multi-source DEMs, without the need for ground control. This has significantly improved the accuracies at which the surface change can be assessed. The general observation is a surface lowering at the front of 12 glaciers in the western AP with a mean lowering rate of 0.28 ± 0.03 m/yr, over an average period of 37 years (1970-2007). At higher elevations, of around 400 m, the lowering decays to zero or elevation increases are observed. This is presumably explained by accumulation. In the next chapter these results are analysed and discussed in combination with temperature observations. If the lowering is related to climatic changes a clear link between the two should be observable. Furthermore, the spatial and temporal pattern of change across the AP region will be discussed.

Chapter 6. Analysis and Discussion

In Chapter 2 the current state of observations of mass balance changes in the AP was discussed and a research gap of long-term records was identified. To close this gap, a combination of DEMs derived from aerial archive stereo-photography and modern stereo-imagery from spaceborne ASTER and airborne sensors was proposed (Section 2.3.5). In order to align these DEMs without the need of ground control observations, an improved robust surface matching approach was applied (Section 3.4). This enabled the observation of multi-decadal glacier surface changes for 12 glaciers across the western AP (Section 5.3). The general finding was a frontal surface lowering in combination with retreat over the past four decades. This lowering is assumed to be partially balanced by observed higher elevation accumulation. A potential increase in the lowering rates since the early 1990s was noticed. This chapter analyses these results and will discuss them in relation to climate observations.

6.1 Historical glacier change in the AP

The results thus far suggest that the majority of the marginal glaciers in the AP have been subject to thinning over the last ~4 decades. The average frontal lowering rate for the observed glaciers was 0.28 ± 0.03 m/yr over an average period of 37 years (1970-2007). However, this needs to be examined with caution for several reasons:

- The glaciers studied here are located along the western margins of the AP between 64° and 72° S.
- The average period between time stamps is 37 years and ranges from 14 to 58 years.

- Redundant measurements are rare and most measurements are based on only two epochs.
- The area of the observed glaciers ranges from 17 km² to 233 km² with only roughly 20 % covered by the historic data.
- The observations are bounded to the frontal, generally lower, portions of the glaciers.
- The local topography varies for each glacier.

Despite these rather weak constraints, similarities in the observations can be found. The frontal lowering is broadly linked with observations of frontal retreat. This excludes glaciers where the front coincides with the grounding line position (e.g. Rozier Glacier and Leonardo Glacier). The parts of glaciers that show advance a corresponding surface thickening is observed (e.g. at Leonardo Glacier and the smaller glacier nearby). At some glaciers (e.g. Leonardo Glacier, Sheldon Glacier, and Moider Glacier) the surface lowering is unequally distributed over the glacier front. This is probably explained by spatial variations in the local glacier bed topography. Areas with higher surface lowering are often linked with steeper slopes. The terrain under the glacier bed is not known here but heavily crevassed areas usually correspond to changes in surface slope due to increased shear stress. Increased shear stress results in increased velocities, which serves the discharge of ice masses (Benn and Evans, 1998). Additionally, the areas where this can be observed are situated below 400 m in elevation and influenced by surface melting (see Section 6.2).

Uranus Glacier which is located furthest south at ~71°S exhibits a very small surface change rate of -0.04 $\pm$ 0.13 m/yr over the period of 1995 to 2009. The glacier is flowing into the buttressing George IV ice shelf which lies on the eastern part of Alexander Island (Figure 5.1). The effects of climate change are less strong in that area and temperatures are well below zero degrees (Figure 2.8). Hence, it can be concluded that the glacier lowering in that area has been relatively low over recent decades. However, there are observations of ice shelf thinning in that region due to basal melting which could have an impact in the future (Pritchard et al., 2012; see also Section 6.4). On the other end of the spectrum is Sheldon Glacier were the highest lowering rate with 0.57 $\pm$ 0.09 m/yr over

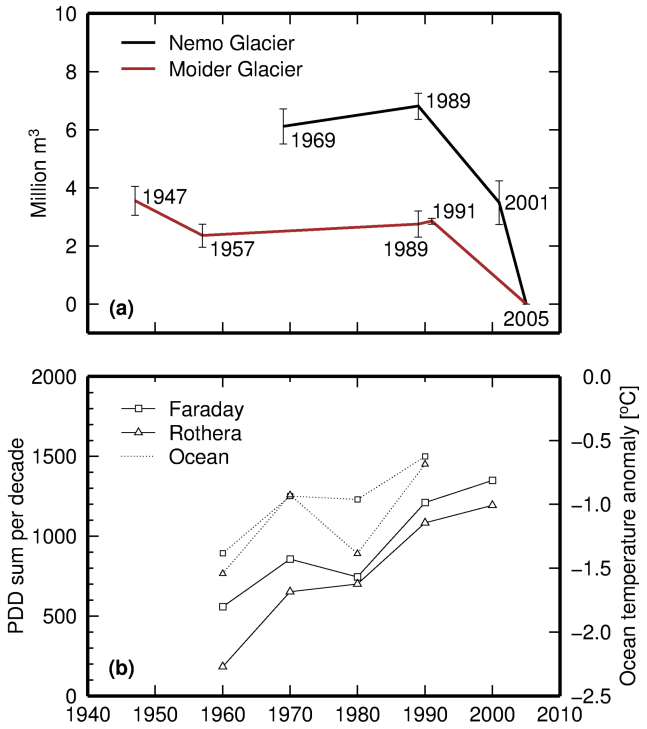

Figure 6.1: Multi-decadal surface volume change of frontal areas relative to 2005 (a). Change in positive degree days (PDD) and ocean temperature (b). Temperature data was averaged on a decadal scale, data points represent the mid-decade point. The ocean temperature represent the average column temperature between 0 and 100 m depth at locations in proximity to the air temperature data.

the period 1989 to 2005 was observed and a large portion of its floating extension was lost (967 m in average). Sheldon Glacier is located at ~67° S and is more affected by open water and warmer atmospheric temperatures in the summer month. Consequently, any change in the oceanic and atmospheric temperatures will be much more direct at this location. For Sheldon Glacier the time span is relatively short with 16 years. All the other glaciers, except the already discussed Uranus Glacier, have much longer time spans and exhibit less strong lowering at the front. This suggests that the lowering was not constant over time or is spatially varied. Otherwise, a much higher surface lowering (at least doubled) would be needed to get similar rates for the last two decades at the other glaciers. However, this was not observed. Nonetheless, these results may be used to determine a point in time at which the glacier lowering began to be significant.

Moider and Nemo glaciers, located in proximity to Sheldon Glacier (Figure 5.12), provided an opportunity to examine any temporal variability more closely, since elevation data was available on more than two epochs. For an area with sufficient point density along the front of Nemo Glacier the volumetric change on a decadal timescale

(Figure 6.1a) relative to 2005 was calculated. Also plotted are data for Moider Glacier as given in Fox and Czifersky (2008). The multi-decadal trend is negative and shows dramatically increased rates of lowering since 1989. The mean elevation change rate of Nemo Glacier has changed significantly in the last two decades from being almost zero at +0.03 m/yr (1969-1989) to -0.44 m/yr (1989-2005), which is a significant lowering. The latter is in relative agreement with the rates for Sheldon Glacier for a similar time period. Despite being based on a small sample size, together, these results suggest a strong increase in glacier lowering since the early 1990s.

6.2 Relation to atmospheric and ocean temperature observations

All of the glaciers observed here can be classified marine terminating and hence are potentially subject to both atmospheric and oceanic warming. For this reason, the number of atmospheric positive degree days (PDD; Braithwaite, 1984) at the nearby research stations Rothera and Faraday (the latter is also known as Vernadsky station; Figure 5.12) since 1955 was calculated (Figure 6.1b). Temperature data were averaged by decade around the mid-decade points, to make the data more comparable to the derived volume change observations. Almost 60 % of the PDDs since 1955 have occurred during the two decades following 1985, with a particularly notable increase in the decade centred on 1990, spanning the time when increased lowering at Nemo and Moider glaciers was observed. Increased lowering is centred on the period following 1989, so a five-year delay in their response to increased temperatures is evident, perhaps due to initial refreezing of surface melt. Furthermore, PDDs increase northwards, corresponding to the higher rates of lowering we observe there. This strong atmospheric PDD trend implicates surface melting as a dominant source for the surface lowering. Given a temperature lapse rate of -0.0082°C/m for the western Peninsula (Morris and Vaughan, 2003), total PDD in this region reduces by 60 % at 100 m elevation and 98 % at 400 m elevation. This is in agreement with the reduction in surface lowering to zero at around 400 m (Figure 5.10). However, some glaciers exhibit quite complex spatial patterns of lowering (e.g. Leonardo and Snowshoe glaciers) as would be expected given

that there is not a linear relationship between PDD and surface melt due to, for example, glacier aspect, shadow and cloudiness.

Also plotted on Figure 6.1b are upper 100 m oceanic temperature anomalies (Meredith and King, 2005), represented as the average column temperature between 0 and 100 m depth, for the two cells located closest to our glaciers (see locations in Figure 5.12). The ocean temperatures show a distinct warming as noted by Meredith and King (2005) although, unfortunately, the data do not span the full period of the elevation data and do not clearly show a signal which could be related to faster rates of lowering at our more northerly glaciers. Further data are required to allow a complete partitioning of the respective roles of atmosphere and ocean in the observed glacier lowering.

Pritchard and Vaughan (2007) observed western Antarctic Peninsula glaciers accelerated by 12 % on average from 1992 to 2005. They found no direct relationship to PDDs and suggested that the thinning of glacier fronts was bringing them nearer to floating, reducing their effective basal pressure resulting in faster sliding. The observations made here confirm that there is widespread glacier front thinning in the western Antarctic Peninsula. Based on a thinning-retreat relation Pritchard and Vaughan (2007) calculated that a thinning rate of 5 m/yr could cause the observed acceleration. However, the here observed surface lowering is more than an order of magnitude smaller. This either suggests that there is another mechanism controlling acceleration rates, or that a much lower rate of thinning could explain their observed accelerations; increased lowering since the 1990s cannot explain the difference. From Figure 5.8 it can be seen that the front of Moider Glacier was relatively stable until 1991. After that the retreat was larger and faster. This supports the theory of increased lowering since the 1990s as observed in the lowering rates of Moider Glacier, Nemo Glacier, and Sheldon Glacier.

As mentioned in Section 2.2.1, many variables determine the relationship between glacier mass balance and changes in atmospheric and oceanic temperatures. While changes in temperature or precipitation can be significant over the course of a year the mass balance of a glacier may not change. Given that the mean temperature of the AP is generally below zero (see Figure 2.8) it would seem contradictory to measure surface lowering. Increased accumulation (in the form of snow) under these temperatures would

also cause more mass input and potentially a lowering of the ELA. However, the observations show a negative mass balance at the front of the glaciers. Changes in atmospheric temperature towards positive degrees and increased melting potential can cause substantial ablation. If the time period at which ablation takes place increases over time (e.g. during the Antarctic summer) the mass balance can change towards a negative direction. Accumulation at higher elevations can also cause increased pressure on a glacier and cause a speed up in glacier flow, especially when the buttressing ice shelves have been removed, and lead to dynamic mass output. If the ELA on the western AP is close to sea level (Hjort et al., 1997) then the lowering is observed in the accumulation zone. This could be explained by decreased accumulation (which is not known) over time and increased summer melting. Another explanation could be that the ELA has moved to higher elevations (at around 400 m). There are observations of an upward shift of the dry-snow[1] line in the eastern AP between 1992 and 1998 (Rau and Braun, 2002). This means that more areas are potentially affected by melt. If this also holds for the western AP it would be in agreement with the observations and PDD calculation earlier on. Increased oceanic and atmospheric temperatures could explain an upward shift of the ELA and increased accumulation at higher elevations with lowering at the lower portions of the glaciers.

The temperature data also shows a period of stable and partially decreased temperatures around 1980 (Figure 6.1b). Unfortunately, there were no stereo-photographs in the archives from that period that would have allowed to investigate this signal in more depth. Other sensors may cover that period but this has not been followed further. If the frontal lowering and retreat is linked to the the oceanic and atmospheric forces, the response of the glaciers should be mirrored when the temperatures decrease, possibly with some delay. First, because a cooler atmosphere will hold less water, which gives less accumulation of snow, and secondly fewer days (PDDs) with melting conditions. Thus, smaller lowering rates or potentially thickening would be expected. As a matter of fact, Cook et al., 2005 observed lower retreat rates for glaciers located between 64° and

[1] Snow that is not affected by melt.

70° S over the period 1985 to 1989. The period between 1970 and 1989 currently remains largely unsampled.

6.3 Regional glacier change

In this study only 1.2 % of the approximately 1000 glaciers in the Antarctic Peninsula were examined and only at the glacier fronts (~20 % coverage of each glacier). Most of these glaciers are located along the western AP margins. Thus, it is not directly possible to draw conclusions from these observations for the entire AP. It is evident that the studied glaciers have seen substantial surface lowering along their frontal zones. Assuming that the glacier lowering is due to a contribution of atmospheric and oceanic melting, it can be assumed that the majority of glaciers on the western Antarctic Peninsula, approximately 400, have lowered at their fronts over recent decades. The same is expected for the northern and eastern parts of the AP where similar observations for the last two decades were made (e.g. Scambos et al., 2004; Zwally and Giovinetto, 2011).

On the other hand, the observed spatial and temporal variation in the lowering rates suggests that the pattern of surface change is not a simple one and that a regional upscaling is not straight forward. The small sample size and incomplete coverage of each glacier cannot be seen as representative for the entire AP with its complexity. Accumulation has generally increased in the AP over the period of the observations (see Pritchard and Vaughan, 2007) and hence reduced mass input cannot be the reason for the observed lowering. Indeed, elevation increase was observed here at some higher altitude locations within a few km of the glacier fronts, raising the potential that the observed surface lowering over relatively small regions may be at least partially compensated by increased higher elevation accumulation over much larger regions. Similar observations were made by Nield et al. (2012). Given glacier thinning is likely linked to acceleration and possible calving, its greatest impact on sea-level may not be direct.

6.3.1 Projection across AP

Despite the small number of observed glaciers, it is worth exploring how the results may be used for regional upscaling. Using multiple linear regression it is possible to get an estimate of the observed changes for other locations within the region. This was tested using multiple linear regression inside *Matlab*. The aim was to find a relationship between the lowering rates and specific parameters that can describe the observed pattern of change for individual glaciers elsewhere on the AP. Two regression models were tested and applied to all elevation change observations over the glacier surfaces. In the first model (Equation 6.1) a third order polynomial was used which describes the surface elevation change $\Delta z/\Delta t$ in dependence on the elevation value E. In the second model (Equation 6.2) a spatial and terrain component was added and the surface elevation change $\Delta z/\Delta t$ was assumed to be dependent on latitude ϕ and longitude λ, elevation E, slope α and aspect i. Higher order polynomials and other parameter combinations were also tested but did not result in further improvement or findings.

$$\frac{\Delta z}{\Delta t} = aE^3 + bE^2 + cE + d \tag{6.1}$$

$$\frac{\Delta z}{\Delta t} = a\lambda^3 + b\lambda^2 + c\lambda + d\phi^3 + e\phi^2 + f\phi + gE^3 + hE^2 + iE + k\alpha + l \tag{6.2}$$

Figure 6.2 shows the result for the model that included location and elevation. This model (Equation 6.2) explained 16 % of the data variance. For the other model the value was around 10 %. This is to low to be of use for regional extrapolation. The unaccounted variance in the data is most likely related to the noise in the data or inter-annual effects that were not accounted for. Two dates of observation over several decades are too less. Yearly measurements would be desirable. Another fact is that, the observations made here are bounded to the western AP and one station at the eastern bound of Alexander Island. The challenge is to account for more glacier types across the entire AP (e.g. length, area, hypsometry) and there dynamics (e.g. speed of flow, thinning rate).

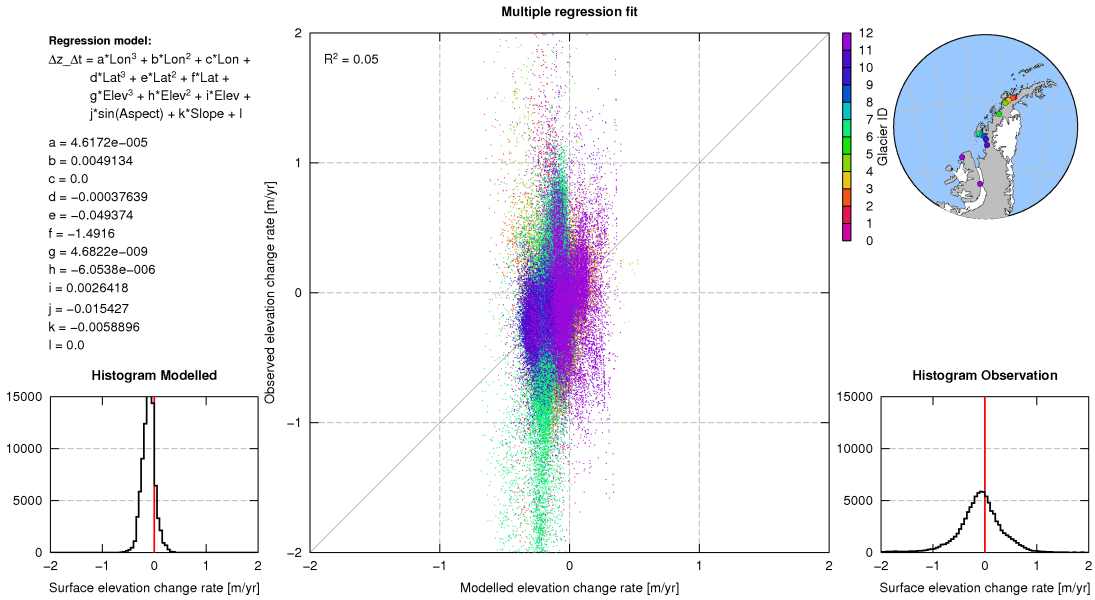

Figure 6.2: Regional upscaling using multiple linear regression.

Although, regional upscaling was unsatisfactory at this stage, the observations still hold valuable information as discussed earlier.

In a more simplistic approach, correlation coefficients on the observed variables of Table 5.4 were calculated (see Table 6.1). They show that there is a weak positive correlation between the frontal length change (LC) and the frontal elevation change rate (FEC) of 0.54. The retreat is explained by basal and surface melting which causes surface lowering. The weak correlation may also be explained by calving for which a surface lowering is not implicitly required or the fact that most of the glaciers have lost there floating extensions. There is a weak negative correlation of -0.24 between the latitudinal location of the glacier and the frontal length change. At first this seems unexpected because temperatures decrease polewards and smaller retreat would be expected. However, as noted by Cook et al. (2005), there was a period of high retreat for regions below 66° S whereas the more northern glaciers have already retreated. As discussed above, the time span for most of the observed glaciers is too large to show a clear link with atmospheric forcings. Interestingly, there is a relatively low correlation of 0.41 between the latitudinal location and the frontal lowering (Table 5.4). It would be expected to be a much higher correlation because of the observed temperature changes (Figure 6.1). Over recent decades the link is more clear. Individual variations (location, topography, area, aspect, etc.) and the low number of observed glaciers currently limits

Variable 1	Variable 2	r	r^2
LC	FEC	0.54	0.30
Latitude	FEC	0.41	0.17
Latitude	LC	-0.24	0.06
Longitude	FEC	0.17	0.03

Table 6.1: Correlation coefficients of observed variables. LC = Frontal length change; FEC = Frontal elevation change rate; Elev=Elevation of zero lowering; Dist=Distance to zero lowering from glacier front.

the use for regional upscaling. It is estimated that a number of around 50 glaciers across the AP is needed to account for local and temporal variations as well as outliers. Especially the climatic differences between the western and eastern AP, and their change over time, will result in different patterns of glacier change. Thus, it is desirable to get one or two time stamps per decade to increase the temporal resolution. Currently it is difficult to allow clear statements about the onset of increased thinning and at which point the thinning actually began to be significant (overall negative mass balance). Assuming a representative sample size of 50 glaciers across the AP with observations from 1950 to 2010 and two time stamps per decade, 6000 DEMs (ideally with full coverage of each glacier) would need to be extracted and matched. This is a very work intensive task. Nonetheless, a workflow for this is presented in this work.

6.4 Summary and future prediction of mass balance

Given the multi-decadal trend of negative ice mass balance in the AP, the findings of this research and from others (e.g. Cook et al., 2005; Cook and Vaughan, 2010; Pritchard and Vaughan, 2007), it is very likely that this negative trend will continue for several years. Although measurements have shown increased accumulation at higher elevation (e.g. this study, Nield et al., 2012) it remains in question whether this will outbalance the losses. The overall temperature trend for the AP shows a clear signal of warming (Figure 2.3, see Section 2.1.1), which is displayed in increased precipitation and accumulation of snow. Likewise, increased atmospheric and oceanic temperatures lead to more PDDs resulting in greater surface and basal melting of the glaciers and ice shelves, especially in the lower parts. Recalling that a third of the AP area lies within 200 m of sea-level and summer temperatures climb frequently above 0 °C. The AP is the only Antarctic region

that experiences such a substantial summer melt (Pritchard and Vaughan, 2007). The marginal marine-terminating glaciers of the AP are likely to be more sensitive to changes in climatic variables than the larger continental ice sheets as it has been observed for similar regions in the Arctic (DeWoul and Hock, 2005). Additionally, the retreat and break-up of large ice shelves off the coast removes the buttress for many glaciers which leads to a speed-up in the glacier flow (Dupont and Alley, 2005) and calving. In reverse there is a feedback between dynamic thinning of grounded, fast-flowing tributary glaciers and ocean-driven ice-shelf thinning as observed by Pritchard et al. (2012). The result is again increased mass loss. The frontal melting observed here removes further basal stress and can reinforce the speed of glacier flow. This ice mass transport towards the ocean may be amplified by increased pressure from the accumulation zone (Benn and Evans, 1998) because here increased mass input is observed. Currently, the net contribution of the western Antarctic Peninsula to recent sea-level change will remain ambiguous until more spatially and temporally comprehensive measurements are made. The findings presented here can help to achieve this goal.

Chapter 7. Conclusions

7.1 Revisit of aims and objectives

The aim of this research was to investigate multi-decadal glacier volume change in the Antarctic Peninsula from aerial archive stereo-imagery and modern satellite stereo-imagery. To achieve this aim the following objectives were addressed:

- *Objective One*: to provide an improved surface matching algorithm that is able to handle large datasets efficiently.

The first objective has been achieved by reviewing and recoding the existing surface matching software from Buckley (2003) and Miller (2007) from VB.NET into C++ code. The implementation and validation was described in Section 3.4. The recoding increased the performance by the factor 100 and enabled the use of datasets with several million points. The new code is designed to be platform-independent and utilises public libraries only. Furthermore, the underlying matching algorithm has been extended to enable the co-registration of surfaces with directional scales, e.g. linear elevation bias.

- *Objective Two*: to investigate the accuracy and reliability of surface matching for glacier volume change studies in areas with steep topography.

In Chapter 4 it was demonstrated that the enhanced surface matching software is capable of performing robust co-registration of DEMs derived from aerial imagery and ASTER data in areas of steep topography. It was proved that ASTER elevation data can serve as modern reference data, for areas where no higher resolution data is available. In this context three different matching strategies were compared and it was found that a patch based approach, using points over stable terrain only, is most suitable when individual glacier are assessed. This approach showed the best accuracies for assessment on an

individual glacier scale. The achievable accuracies are within ± 2 m and no ground control data is required. Highest accuracies were observed over flat terrain with decreased accuracies over steep terrain. Since the glacier surface is usually more flat than generally steep stable terrain, uncertainties were computed using semivariograms which account for spatial autocorrelation. In Section 5.2 the matching of was successfully applied in a wider study across the AP.

- *Objective Three*: to investigate the useability of DEMs derived from archive stereo-imagery and modern ASTER data for glacier change studies.

Despite the absence of ground control data it was possible to extract DEMs from the historic TMA aerial photography of Antarctica (Section 3.1.2). While the USGS and BAS archives contain a large number of images not all image strips are suitable for DEM extraction. A lack of contrast or strong cloud cover does limit the success rate for automated aerotriangulation and DEM extraction. Where suitable contrast and a mix of stable and glaciated terrain with extinct surface features exists, DEM extraction was possible. The absolute orientation of the historic DEMs can be approximated using artificial ground control from the modern reference data. However, ground control data from field measurements is often unavailable in the AP and, thus, it is not guaranteed that an ASTER DEM has the correct absolute orientation either. Fortunately, this is not too critical to glacier change assessment because the calculation of surface elevation change is reliant on a good relative orientation between the multi-epoch data rather than the absolute position or rotation in space. It was shown that ASTER elevations are suitable for glacier change studies and it was demonstrated that these can be successfully combined with high quality DEMs that were extracted from archive stereo-imagery (Chapter 5). The historic TMA data has strong potential because it contains information with high spatial resolution on the state of glaciers long before satellite observations were available.

- *Objective Four*: to apply the developed approach to study multi-decadal glacier mass change in the Antarctic Peninsula and to extend the number of records for the region.

It was discussed in Section 3.1.2 that the coverage of the historical imagery limits a region-wide assessment of ice mass changes. The modern reference data covers the AP completely from the early 1990s with relative high spatial resolution (see Section 2.4). The extraction of mass balance records before that time will possibly stay limited to individual glaciers or smaller regions of the AP. Nonetheless, the successful extraction and co-registration of historical and modern DEMs for 12 glaciers illustrates that the method is suitable for enabling long-term glacier volume change assessment in the AP (Chapter 5). The relatively low number of observations, of which most glaciers are located along the coast of the western AP, currently constraints a wider glacier mass balance assessment of the AP. It was shown that despite this fact a strong potential exists and a foundation for further research was laid out. More records, of the roughly 1000 glaciers, are needed, especially for the eastern and central parts of the Peninsula.

- *Objective Five*: to analyse past and predict future changes of glaciers in the Antarctic Peninsula with respect to climate and glaciology data.

The final objective was addressed in Chapter 6. The measurements that were obtained in Section 5.3 are in agreement with existing and recent observations of negative ice mass balance in the AP. The retreat of floating tongues and glaciers (Cook et al., 2005; Cook and Vaughan, 2010) is mirrored in a signal of frontal lowering for all of the observed glaciers. Analysis of the upper ocean and atmospheric temperatures (Meredith and King, 2005) over the same period are in relation to the observed changes in glacier volume. There are some exceptions to this pattern but overall trend is clear and likely to continue. There is still uncertainty whether this negative trend will be outbalanced to some extend by accumulation at higher elevations due to increased snowfall.

In summary it can be said that all objectives were achieved. The result is the first multi-decadal glacier volume change map of the western AP (Figure 5.12). Limitations remain with respect to the spatial and temporal coverage of the data for the AP. The prediction of future changes remains somewhat uncertain although a general trend was found and supports other studies.

7.2 Research outcome

This research has successfully demonstrated the impacts of regional climate warming to the glaciers in the AP. Using archival aerial stereo-photography combined with ASTER DEMs, this work presents the first multi-decadal glacier volume change map of the western AP. This was achieved by utilising a robust surface matching technique which enabled the precise co-registration elevation datasets without the need for ground control data. This is particularly important for the AP, since almost no ground control is available and the region is generally difficult to assess. Existing observation of recent negative glacier mass balance were extended by multi-decadal observations for 12 glaciers. It was found that the trend of negative mass balance is evident for a number of decades with a mean lowering rate of 0.28 ± 0.03 m/yr at glacier fronts. The lowering generally confined to within 1 km of the front, and below 400 m of elevation. Glacier frontal lowering exhibits a latitudinal pattern in accordance with higher surface temperatures in the north. A glacier wide mass balance assessment was not possible due to limited coverage of the historical data. However, the overall trend of negative ice mass balance of the AP appears robust and is likely to continue. Two glaciers which have multi-epoch coverage show significantly larger-than-average lowering since about 1990, in close correspondence with an increase in positive degree days in the decade centred on 1990. The frontal surface lowering of the glaciers in this study is partially balanced by increased accumulation at higher elevations. Thus, the contribution to sea-level change is smaller than the frontal lowering would suggest, but feedbacks in terms of ice dynamics mean it is likely that it cannot be ignored. The spatial and temporal variation in the lowering rates suggests that the pattern of surface change is not a simple one and that a regional upscaling is not straight forward. The 12 observed glaciers represent just 1 % of the Peninsula glaciers, and only two of them have more than two epochs of data.

While geodetic mass balance methods such as gravimetry or spaceborne altimetry can produced large scale maps of ice mass balance of the AP they are prone to errors in areas with steep topography. Such surface characteristics are typically for the margins of the AP and higher spatial resolution is required to assess the changes of glaciers in these areas. The use of stereo-photogrammetry is sufficient to provide these measurements and

to complement other mass balance studies. The particular advantage is the long-term availability of historical stereo-photography. Although, it should be noted that, the coverage is far from complete. The best approach for assessing ice mass balance in the AP, or elsewhere, is to rigorously combine historic stereo-imagery with DEMs derived from modern sensors and to feed the results into improved climate and ice models. Clearly, further spatial and temporal coverage is required, and indeed such additional archives of the kind exploited here do exist.

The **key findings** of this thesis can be summarised as follows:

- Historical TMA photography of Antarctica is suitable for DEM extraction and glacier change assessment
- ASTER DEMs are applicable to serve as modern reference data
- IRLS matching enabled the rigorous co-registration of uncontrolled historic and modern DEMs in areas with steep topography
- Successful assessment of multi-decadal glacier volume change in the western Antarctic Peninsula
- Mean surface lowering of 0.28 ± 0.03 m/yr at glacier fronts over recent decades were measured, with higher lowering rates in the north-western parts of the AP
- A post-1990 increase in lowering is observed, in agreement with increased temperatures
- More spatially and temporal comprehensive data is needed to assess the mass balance of the entire AP

The relevant results were successfully published in scientific journals, including one peer-reviewed publication in Geophysical Research Letters (Kunz et al., 2012). The underlying surface matching approach has also contributed to the ESA Climate Change Initiative (CCI). In this context various algorithms for creation of glacier area, elevation change and velocity products were evaluated and compared (Paul et al., 2013).

7.3 Beneficiaries and future work

The glaciological and climate science communities will benefit from this work because it gives a better picture of multi-decadal elevation changes of glaciers along the margins of the western AP. The frontal lowering rates may be put into ice mass balance models and can be used to validate and adjust these models. Assuming the observation of increased post-1990 lowering is valid, this signal should be observable at other locations as well. Results of this research were shown to be in agreement with other studies and findings. One statement from the last IPCC Assessment Report (IPCC, 2007, p. 364), that declares that "the balance of the Antarctic Peninsula was not assessed", may now be replaced with novel results from this research and other interesting projects over recent years.

In the context of geomatics practitioners, surface matching provides a flexible, automated and robust registration approach which could be applied to a range of scenarios. The technique is directly relevant to projects where it is necessary to align a number of DEM datasets prior to performing subsequent analysis. For example, in the case of flood modelling, it is essential to ensure that any systematic errors between datasets have been eliminated prior to undertaking analysis. However, although DEMs may be delivered from a data provider in a particular coordinate system, it is often the case that systematic offsets still exist. Surface matching avoids the expense of undertaking a labour intensive field survey to collect GCPs, and instead provides a completely software-based solution which normally takes only a matter of minutes to execute. Furthermore, as already explained, the technique simultaneously delivers change information on a DEM point-by-point basis, enabling instant mapping of elevation change. This provides a valuable and low-cost resource for landslide monitoring, analysis of mining subsidence, coastal change, and even automated detection of urban development/change.

The following work packages are suggested to contribute to a further development and extension of this research in a wider context:

- Implementation of a 3D triangulation to enable the matching of fully three-dimensional surfaces.

The studied elevation datasets represent 2.5-dimensional surfaces and the matching performed well. However, in theory, the current code does not allow more than one z value per location (xy) (see Section 3.4.3). The triangulation would fail in such a case. This situation is not uncommon in cases where terrestrial laser scans are combined with airborne or spaceborne datasets. A typical example are overhanging cliffs or complex objects such as crevasses. Extending the software with this functionally can open the door to many additional applications inside and outside of glaciology.

- Allocation of the surface matching tool (SMT) to the scientific community.

The matching software used here is currently only utilised at Newcastle University and could be made available to other researchers around the world. The need for efficient and low-cost co-registration of elevation datasets is high, especially in fast-response monitoring situations. Examples are landslides or coastal erosion. Frameworks could be developed that allow researchers to share and combine their datasets in one place, e.g. web-based servers, using an (semi-)automated surface matching and analysis tool. Most data from modern sensors is processed using some form of automation. However, the integration of multi-source data could be pushed further and the required tools do exist, as presented in this research.

- Application of the method to a large scale study across the entire AP.

As discussed in the previous section, this work has formed the foundation for a wider extension of this research. The potential and usability of the historical TMA imagery for DEM extraction and precise co-registration with modern reference data has been successfully demonstrated, without the need of ground control. The applied surface matching approach has unlocked the time-capsule of long-term glacier mass balance studies in the AP. The here studied imagery only represent a small portion of the archives. Further investigation of the image archives is currently ongoing and this research will continue in a NERC funded research project, entitled "*The spatial and temporal distribution of 20th century Antarctic Peninsula glacier mass change and its drivers*" between Newcastle University and the British Antarctic Survey (NERC Grant Ref: NE/K005340/1). The proposal for the project partly relied on the work established in this thesis and will rely on the here made code developments. The time period

between 1970 and 1989 remains of specific interest because the changes from this period are currently not sufficiently explored, presumably because of a shortage in available data. In the prospect of high resolution data from missions such as IceBrigde and TanDEM-X, the potential of combining this data with historical aerial stereo-photography and ASTER data is large and could further extend the time series. TanDEM-X will offer a 6 m DEM with global coverage. Although, the coverage in areas of steep terrain is not yet known. A particular interesting source of unexploited data are the oblique images of the trimetrogon photography. Originally they were used for rapid mapping purposes. They could add another source of information. Although DEM extraction from oblique images is far from straight forward the information contained in the images could help solving the problem of non overlapping lateral flight strips. This can help to map the full glacier and not only parts of a glacier. Glacier-wide mass balance mapping would increase the representativeness of the data. Glacier outline mapping could be another application because the GLIMS archive is far from complete for the AP. The glaciological community could benefit from a better understanding of the impacts of atmospheric and oceanic changes across on the AP when the presented technique as applied to the full range of historic data. The results could then be used as starting or validation values for numerical ice-sheet models. The closing of the remaining gap of records for the AP and elsewhere in Antarctica is in view.

References

Abdalati, W., Zwally, H. J., Bindschadler, R., Csatho, B., Farrell, S. N., Fricker, H. A., Harding, D., Kwok, R., Lefsky, M., Markus, T., Marshak, A., Neumann, T., Palm, S., Schutz, B., Smith, B., Spinhirne, J., and Webb, C. (2010). The ICESat-2 Laser Altimetry Mission. *Proceedings of the IEEE*, 98:735–751.

Ackermann, F. (1984). Digital Image Correlation: Performance and potential application in photogrammetry. *Photogrammetric Record*, 11(64):429–439.

Aguilar, F. J., Aguilar, M. A., and Agüera, F. (2007). Accuracy assessment of digital elevation models using a non-parametric approach. *International Journal of Geographical Information Science*, 21(6):667–686.

Aguilar, F. J. and Mills, J. P. (2008). Accuracy assessment of Lidar-derived digital elevation models. *The Photogrammetric Record*, 23(122):148–169.

Akca, D. (2004). A new algorithm for 3D surface matching. *International Archives of the Photogrammetry, Remote Sensing and Spatial Information Sciences*, XXXV(B7):960–965.

Akca, D. (2010). Co-registration of Surfaces by 3D Least Squares Matching. *Photogrammetric Engineering & Remote Sensing*, 76(3):307–318.

Allan, D. W. and Weiss, M. A. (1980). Accurate time and frequency transfer during common-view of a GPS satellite. In *Annual Frequency Control Symposium, 34th, Philadelphia, PA, May 28-30, 1980, Proceedings.*, pages 334–346. Electronic Industries Association.

Alliez, P., Saboret, L., and Salman, N. (2012a). Point set processing. In *CGAL User and Reference Manual*. CGAL Editorial Board, 4.0 edition.

Alliez, P., Tayeb, S., and Wormser, C. (2012b). 3D fast intersection and distance computation (aabb tree). In *CGAL User and Reference Manual*. CGAL Editorial Board, 4.0 edition.

Angelis, H. D. and Skvarca, P. (2003). Glacier surge after ice shelf collapse. *Science*, 299:1560–1562.

Arendt, A. A. (2012). Randolph glacier inventory: A dataset of global glacier outlines, version: 1.0. Technical report, GLIMS Technical Report.

Arendt, A. A., Luthcke, S. B., Larsen, C. F., Abdalati, W., Krabill, W. B., and Beedle, M. J. (2008). Validation of high-resolution GRACE mascon estimates of glacier mass in the St Elias Mountains, Alaska, USA, using aircraft laser altimetry. *Journal of Glaciology*, 54(188):778–787.

Arun, K., Huang, T., and Blostein, S. (1987). Least-Squares Fitting of Two 3-D Point Sets. *IEEE Transactions on Pattern Analysis and Machine Intelligence*, 9(5):698–700.

ASTRIUM (2013). WorldDEM. http://www.astrium-geo.com/worlddem/. Accessed: 23.08.2013.

Barber, D. M., Mills, J. P., and Holland, D. (2008). Change detection for topographic mapping using threedimensional data structures. *International Archive of Photogrammetry, Remote Sensing and Spatial Information Sciences*, 37(B4):1177–1182.

Barrand, N. E., Hindmarsh, R. C. A., Arthern, R. J., Williams, C. R., Mouginot, J., Scheuchl, B., Rignot, E., Ligtenberg, S. R. M., Van den Broeke, M. R., Edwards, T. L., Cook, A. J., and Simonsen, S. B. (2013). Computing the volume response of the antarctic peninsula ice sheet to warming scenarios to 2200. *Journal of Glaciology*, 59(215):397–409.

Benn, D. G. and Evans, D. J. A. (1998). *Glaciers and Glaciation*. London: Hodder Education.

Berthier, E., Arnaud, Y., Baratoux, D., Vincent, C., and Rémy, F. (2004). Recent rapid thinning of the "Mer de Glace" glacier derived from satellite optical images. *Geophysical Research Letters*, 31:L17401.

Berthier, E., Arnaud, Y., Kumar, R., Ahmad, S., Wagnon, P., and Chevallier, P. (2007). Remote Sensing estimates of glacier mass balance in the Himachal pradesh (western himalaya, india). *Remote Sensing of the Environment*, 108:327–338.

Berthier, E., Arnaud, Y., Vincent, C., and Rémy, F. (2006). Biases of SRTM in high-mountain areas: Implications for the monitoring of glacier volume changes. *Geophys. Res. Lett.*, 33(8):L08502–.

Berthier, E., Scambos, T. A., and Shuman, C. A. (2012). Mass loss of Larsen B tributary glaciers (antarctic peninsula) unabated since 2002. *Geophys. Res. Lett.*, 39:L13501.

Berthier, E., Schiefer, E., Clarke, G. K. C., Menounos, B., and Remy, F. (2010). Contribution of Alaskan glaciers to sea-level rise derived from satellite imagery. *Nature Geosci*, 3(2):92–95.

Besl, P. J. and McKay, N. D. (1992). A Method for Registration of 3-D Shapes. *IEEE Transactions on Pattern Analysis and Machine Intelligence*, 14(2):239–256.

Bindhoff, N. L., Willebrand, J., Artale, V., Cazenave, A., Gregory, J., Gulev, S., Hanawa, K., LeQuere, C., Levitus, S., Nojiri, Y., Shum, C. K., Talley, L. D., and Unnikrishnan, A. (2007). *Climate Change 2007: The Physical Science Basis. Contribution of Working Group I to the Fourth Assessment Report of the Intergovernmental Panel on Climate Change*, chapter Observations: Oceanic Climate Change and Sea Level, pages 385–432. Cambridge University Press, Cambridge, United Kingdom and New York, NY, USA.

Bindschadler, R., Choi, H., Wichlacz, A., Bingham, R., Bohlander, J., Brunt, K., Corr, H., Drews, R., Fricker, H., Hall, M., ans J Kohler, R. H., Padman, L., Rack, W., Rotschky, G., Urbini, S., Vornberger, P., and Young, N. (2011). Getting around Antarctica: new high-resolution mappings of the grounded and freely-floating boundaries of the antarctic ice sheet created for the international polar year. *The Cryosphere*, 5:569–588.

BLAS (2013). BLAS (Basic Linear Algebra Subprograms). http://www.netlib.org/blas/. Accessed: 23.08.2013.

Boissonnat, J. D., Devillers, O., Pion, S., Teiilaud, M., and Yvinec, M. (2002). Triangulations in CGAL. *Computational Geometry*, 22(5-19):1–18.

Bolch, T., Buchroithner, M. F., Kunert, A., and Kamp, U. (2007). Automated Delineation of Debris-Covered Glaciers Based on ASTER Data. In *27th EARSel Symposium "Geoinformation in Europe"*, pages 403–410.

Bolch, T. and Kamp, U. (2006). Glacier Mapping in High Mountains Using DEMs, Landsat and ASTER Data. *Grazer Schriften der Geographie und Raumforschung*, 41:37–48.

Bolch, T., Kamp, U., and Olsenholler, J. (2005). Using ASTER and SRTM DEMs for studying geomorphology and glaciation in high mountain areas. In Oluic, M., editor, *Proceedings of the 24th Symposium of the European Association of Remote Sensing Laboratories, Dubrovnik, Croatia, 25 - 27 May 2004*.

BOOST (2013). Boost C++ Libraries. http://www.boost.org. Accessed: 23.08.2013.

Braithwaite, R. J. (1984). Calculation of degree-days for glacier-climate research. *Zeitschrift für Gletscherkunde und Glazialgeologie*, 20:1–8.

Braithwaite, R. J. (2002). Glacier mass balance: the first 50 years of international monitoring. *Progress in Physical Geography*, 26(1):76–95.

Buckley, S. (2003). *A geomatics data fusion technique for change monitoring*. Phd thesis, University of Newcastle upon Tyne.

CGAL (2013). Computational Geometry Algorithms Library. http://www.cgal.org. Accessed: 23.08.2013.

Chandler, J. H. and Cooper, M. A. R. (1989). The extraction of positional data from historical photographs and their application to geomorphology. *The Photogrammetric Record*, 13(73):69–78.

Chen, Y. and Medioni, G. (1992). Object modelling by registration of multiple range images. *Image and Vision Computing*, 10(3):145–155.

Chetverikov, D., Stepanov, D., and Krsek, P. (2005). Robust Euclidean alignment of 3D point sets: the trimmed iterative closest point algorithm. *Image and Vision Computing*, 23(3):299–309.

Church, J. A., Gregory, J. M., Huybrechts, P., Kuhn, M., Lambeck, K., Nhuan, M. T., Qin, D., and Woodworth, P. L. (2001). *Climate Change 2001: The Scientific Basis: Contribution of Working Group I to the Third Assessment Report of the Intergovernmental Panel on Climate Change*, chapter Changes in Sea Level, pages 638–689. Cambridge University Press, Cambridge, United Kingdom and New York, NY, USA.

Church, J. A., White, N. J., Konikow, L. F., Domingues, C. M., Cogley, J. G., Rignot, E., Gregory, J. M., van de Broeke, M. R., Monaghan, A. J., and Velicogna, I. (2011). Revisiting the Earth's sea-level and energy budgets from 1961 to 2008. *Geophys. Res. Lett.*, 38:L18601.

Cogley, J. G. (2009a). Geodetic and direct mass-balance measurements: comparison and joint analysis. *Annals of Glaciology*, 50(50):96–100.

Cogley, J. G. (2009b). A more complete version of the World Glacier Inventory. *Annals of Glaciology*, 50(53):32–38.

Cogley, J. G., Hock, R., Rasmussen, L. A., Arendt, A. A., Bauder, A., Braithwaite, R. J., Jansson, P., Kaser, G., Möller, M., Nicholson, L., and Zemp, M. (2011). Glossary of Glacier Mass Balance and Related Terms. Technical report, IHP-VII Technical Documents in Hydrology No. 86, IACS Contribution No. 2, UNESCO-IHP, Paris.

Cogley, J. G. and Jung-Rothenhäusler (2004). Uncertainty in digital elevation models of axel heiberg island, arctic canada. *Arctic, Antarctic, and Alpine Research*, 36(2):249–260.

Cook, A. J., Fox, A. J., Vaughan, D. G., and Ferrigno, J. G. (2005). Retreating Glacier Fronts on the Antarctic Peninsula over the Past half-century. *Science*, 308:541–544.

Cook, A. J. and Vaughan, D. G. (2010). Overview of areal changes of the ice shelves on the Antarctic Peninsula over the past 50 years. *The Cryosphere*, 4:77–98.

Cox, L. H. and March, R. S. (2004). Comparison of geodetic and glaciological mass-balance techniques, gulkana glacier, alaska, u.s.a. *Journal of Glaciology*, 50(170):363–370.

Cressie, N. A. C. (1993). *Statistics for spatial data*. John Wiley & Sons.

Cuartero, A., Felicisimo, A., and Ariza, F. (2004). Accuracy of DEM generation from Terra-ASTER stereo data. *International Archive of Photogrammetry, Remote Sensing and Spatial Information Sciences*, XXXV(B2):559–564.

Cziferszky, A., Fleming, A. H., and Fox, A. (2010). An assessment of ASTER elevation data over glaciated terrain on Pourquois Pas Island, Antarctic Peninsula. *Geological Society, London, Special Publications*, 345:23–32.

Davies, B. J., Carrivick, J. L., Glasser, N. F., Hambrey, M. J., and Smellie, J. L. (2011). A new glacier inventory for 2009 reveals spatial and temporal variability in glacier response to atmospheric warming in the northern antarctic peninsula, 1988-2009. *The Cryosphere Discussions*, 5:3541–3594.

DeWoul, M. and Hock, R. (2005). Static mass-balance sensitivity of Arctic glaciers and ice caps using a degree-day approach. *Annals of Glaciology*, 42:217–224.

Dornbusch, U., Moses, C., Robinson, D. A., and Williams, R. (2008). Soft copy photogrammetry to measure shore platform erosion on decadel timescales. *J Coast Conserv*, 11:193–200.

Dowman, I. and Neto, F. (1994). The accuracy of along track stereoscopic data for mapping: Results from simulations and jers ops. *International Archive of Photogrammetry, Remote Sensing and Spatial Information Sciences*, 30(4):216–221.

Draper, N. R. and Smith, H. (1998). *Applied Regression Analysis*. second ed. John Wiley & Sons, New York.

Drewry, D. J. and Morris, E. M. (1992). The Response of Large Ice Sheets to Climatic Change. *Phil. Trans. R. Soc. Lond. B*, 338:235–242.

Dupont, T. K. and Alley, R. B. (2005). Assessment of the importance of ice-shelf buttressing to ice-sheet flow. *Geophys. Res. Lett.*, 32:L04503.

Dyurgerov, M. (2002). Glacier Mass Balance and Regime: Data of Measurements and Analysis. Technical report, University of Colorado, Institute of Arctic and Alpine Research, Occasional Paper 55.

Dyurgerov, M. (2011). Reanalysis of Glacier Changes: From the IGY to the IPY, 1960-2008. *Data of Glaciological Studies*, 108:116pp.

Dyurgerov, M. B. (2003). Mountain and subpolar glaciers show an increase in sensitivity to climate warming and intensification of the water cycle. *Journal of Hydrology*, 282:164–176. doi:10.1016/S002-1694(03)00254-3.

Dyurgerov, M. B. and Meier, M. F. (2000). Twentieth century climate change: Evidence from small glaciers. *PNAS*, 97(4):1406–1411.

Dyurgerov, M. B. and Meier, M. F. (2005). Glaciers and the Changing Earth System: A 2004 Snapshot. Occasional paper 58, Institute of Arctic and Alpine Research, University of Colorado, Boulder, CO, USA.

Ebner, H. and Strunz, G. (1988). Combined point determination using digital terrain models as control information. *International Archive of Photogrammetry, Remote Sensing and Spatial Information Sciences*, 27(B11/3):578–587.

Eckert, S., Kellenberger, T., and Itten, K. (2005). Accuracy assessment of automatically derived digital elevation models from ASTER data in mountainous terrain. *International Journal of Remote Sensing*, 26(9):1943–1957.

Ehlers, M. and Welch, R. (1987). Stereo correlation of Landsat TM images. *Photogrammetric Engineering & Remote Sensing*, 53(9):1231–1237.

ERSDAC (2003). *ASTER Reference Guide Version 1.0*. Earth Remote Sensing Data Analysis Center.

ERSDAC (2004). *ASTER User's Guide, Part III (3D Ortho Product), Version 1.1*. Earth Remote Sensing Data Analysis Center.

Farr, T. G., Rosen, P. A., Caro, E., Crippen, R., Duren, R., Hensley, S., Kobrick, M., Paller, M., Rodriguez, E., Roth, L., Seal, D., Shaffer, S., Shimada, J., Umland, J., Werner, M., Oskin, M., Burbank, D., and Alsdorf, D. (2007). The Shuttle Radar Topography Mission. *Reviews of Geophysics*, 45(2):RG2004.

Fisher, P. F. and Tate, N. J. (2006). Causes and consequences of error in digital elevation models. *Progress in Physical Geography*, 30(4):647–489.

Fox, A. and Czifersky, A. (2008). Unlocking the time capsule of historical aerial photography to measure changes in antarctic peninsula glaciers. *Photogrammetric Record*, 23(151)(151):51–68.

Fox, A. J. and Nuttall, A. M. (1997). Photogrammetry as a research tool for glaciology. *Photogrammetric Record*, 15(89)(89):725–737.

Fretwell, P., Pritchard, H. D., Vaughan, D. G., Bamber, J. L., Barrand, N. E., Bell, R., Bianchi, C., Bingham, R. G., Blankenship, D. D., Casassa, G., Catania, G., Callens, D., Conway, H., Cook, A. J., Corr, H. F. J., Damaske, D., Damm, V., Ferraccioli, F., Forsberg, R., Fujita, S., Gim, Y., Gogineni, P., Griggs, J. A., Hindmarsh, R. C. A., Holmlund, P., Holt, J. W., Jacobel, R. W., Jenkins, A., Jokat, W., Jordan, T., King, E. C., Kohler, J., Krabill, W., Riger-Kusk, M., Langley, K. A., Leitchenkov, G., Leuschen, C., Luyendyk, B. P., Matsuoka, K., Mouginot, J., Nitsche, F. O., Nogi, Y., Nost, O. A., Popov, S. V., Rignot, E., Rippin, D. M., Rivera, A., Roberts, J., Ross, N., Siegert, M. J., Smith, A. M., Steinhage, D., Studinger, M., Sun, B., Tinto, B. K., Welch, B. C., Wilson, D., Young, D. A., Xiangbin, C., and Zirizzotti, A. (2013). Bedmap2: improved ice bed, surface and thickness datasets for antarctica. *The Cryosphere*, 7(1):375–393.

Förstner, W. (1982). On the geometric precision of digital correlation. In *Proceeding of the ISPRS Symposium Mathematical Models, Accuracy Aspects and Quality Control*, volume 24 of *International Archives of Photogrammetry*, pages 176–189.

Fryer, J. G., Mitchell, H. L., and Chandler, J. H. (2007). *Applications of 3D Measurements from images*. Whittles Publishing.

Fujisada, H. (1998). ASTER Level-1 Data Processing Algorithm. *IEEE Transactions on Geosciences and Remote Sensing*, 36(4):1101–1112.

Fujisada, H., Bailey, G. B., Kelly, G. K., Hara, S., and Abrams, M. J. (2005). ASTER DEM Performance. *IEEE Transactions on Geosciences and Remote Sensing*, 43(12):2707–2714.

Gardelle, J., Berthier, E., and Arnaud, Y. (2012). Impact of resolution and radar penetration on glacier elevation changes computed from dem differencing. *Journal of Glaciology*, 58:419–422.

Gardner, A. S., Moholdt, G., Wouters, B., Wolken, G. J., Burgess, D. O., Sharp, M. J., Cogley, J. G., Braun, C., and Labine, C. (2011). Sharply increased mass loss from glaciers and ice caps in the Canadian Arctic Archipelago. *Nature*, 473(7347):357–360.

Garland, M. and Heckbert, P. S. (1997). Surface Simplification Using Quadric Error Metrics. In *Computer Graphics (SIGGRAPH '97 Proceedings)*, pages 209–216.

GDAL (2010). GDAL - Geospatial Data Abstraction Library. http://www.gdal.org. Accessed: 25.04.2010.

GFZ (2010). International Centre for Global Earth Models (ICGEM). http://icgem.gfz-potsdam.de/ICGEM/ICGEM.html. Accessed: 15.04.2010.

Ghilani, C. D. (2010). *Adjustment computations: spatial data analysis*. John Wiley & Sons, 5th edition.

Giles, P. T. and Franklin, S. E. (1996). Comparison of Derivative Topographic Surfaces of a DEM Generated from stereoscopic spot images with field measurements. *Photogrammetric Engineering & Remote Sensing*, 62(10):1165–1171.

Glasser, N. F., Scambos, T. A., Bohlander, J., Truffer, M., Pettit, E., and Davies, B. J. (2011). From ice-shelf tributary to tidewater glacier: continued rapid recession, acceleration and thinning of rošhss glacier following the 1995 collapse of the prince gustav ice shelf, antarctic peninsula. *Journal of Glaciology*, 57(203)(203):397–406.

GLIMS (2012). Randolph Glacier Inventory 3.0. http://www.glims.org/RGI/randolph.html. Accessed: 25.06.2012.

GLIMS (2013). Glims: Global Land Ice Measurements from Space. http://www.glims.org. Accessed: 23.08.2013.

Golub, G. and Reinsch, C. (1970). Singular value decomposition and least squares solutions. *Numerische Mathematik*, 14(5):403–420.

Griggs, J. A. and Bamber, J. L. (2009). A new 1 km digital elevation model of antarctica derived from combined radar and laser data - part 2: Validation and error estimates. *The Cryosphere*, 3:113–123.

Grün, A. and Akca, D. (2005). Least squares 3D surface and curve matching. *ISPRS Journal of Photogrammetry & Remote Sensing*, 59:151–174. doi:10.1016/j.isprs.jprs.2005.02.006.

Groves, P. D. (2008). *Principles of GNSS, Inertial, and Multisensor Integrated Navigation Systems: Second Edition*. Artech House, Inc.

Gruen, A. W. (1985). Adaptive least squares correlation: a powerful image matching technique. *S Afr J of Photogrammetry, Remote Sensing and Cartography*, 14:13 p.

Habib, A. and Schenk, T. (1999). A new approach for matching surfaces from laser scanners and optical scanners. *IAPRS*, 32:55–61.

Hansen, J., Sato, M., Ruedy, R., Lo, K., Lea, D., and Medina-Elizade, M. (2006). Global temperature change. *PNAS*, 103(39):14288–14293.

Harrison, C. G. A., Barron, E. J., and Hay, W. W. (1979). Mesozoic evolution of the Antarctic Peninsula and the southern Andes. *Geology*, 7(8):374–378.

Heipke, C. (1997). Automation of interior, relative, and absolute orientation. *ISPRS Journal of Photogrammetry & Remote Sensing*, 52:1–19.

Hert, S. and Seel, M. (2012). dD convex hulls and Delaunay triangulations. In *CGAL User and Reference Manual*. CGAL Editorial Board, 4.0 edition.

Höhle, J. and Höhle, M. (2009). Accuracy assessment of digital elevation models by means of robust statistical methods. *ISPRS Journal of Photogrammetry & Remote Sensing*, 64:398–406.

Hirano, A., Welch, R., and Lang, H. (2003). Mapping from ASTER stereo image data: DEM validation and accuracy assessment. *ISPRS Journal of Photogrammetry & Remote Sensing*, 57:356–370.

Hjort, C., Ingolfsson, O., Möller, P., and M, L. J. (1997). Holocene glacial history and sea-level changes on James Ross Island, Antarctic Peninsula. *Journal of Quarternary Science*, 12(4):259–273.

Hoaglin, D. C., Mosteller, F., and Tukey, J. W. (2000). *Understanding Robust and Exploratory Data Analysis*. John Wiley & Sons.

Hoaglin, D. C. and Welsch, R. E. (1978). The Hat matrix in regression and ANOVA. *The American Statistician*, 32(1):17–22.

Hock, R. (2005). Glacier melt: a review of processes and their modelling. *Progress in Physical Geography*, 29(3):362–391.

Hock, R., de Woul, M., Radic, V., and Dyurgerov, M. (2009). Mountain glaciers and ice caps around Antarctica make a large sea-level rise contribution. *Geophysical Research Letters*, 36:L07501,.

Holland, P. R., Corr, H. F. J., Pritchard, H. D., Vaughan, D. G., Arthern, R. J., Jenkins, A., and Tedesco, M. (2011). The air content of Larsen Ice Shelf. *Geophys. Res. Lett.*, 38:L10503.

Holmlund, P. (1987). Mass Balance of Storglaciären during the 20th Century. *Geografiska Annaler. Series A, Physical Geography*, 69(3/4):439–447.

Hothmer, J. (1958). Possibilities and limitations for elemination of distortion in aerial photographs. *The Photogrammetric Record*, 2(12):426–445.

Howat, I. M., Joughin, I., and Scambos, T. A. (2007). Rapid Changes in Ice Discharge from Greenland Outlet Glaciers. *Science*, 315:1559–1561.

Ingolfsson, O., Hjort, C., Björck, S., and Smith, R. I. L. (1992). Late Pleistocene and Holocene glacial history of James Ross Island, Antarctic Peninsula. *Boreas*, 21:209–222.

IPCC (2007). *Climate Change 2007: The Physical Science Basis. Contribution of Working Group I to the Fourth Assessment Report of the Intergovernmental Panel on Climate Change*. Cambridge University Press, Cambridge, United Kingdom and New York, NY, USA.

Ivins, E. R., Raymond, C. A., and James, T. S. (2000). The influence of 5000 year-old and younger glacial mass variability on present-day crustal rebound in the Antarctic Peninsula. *Earth Planets Space*, 52:1023–1029.

Ivins, E. R., Watkins, M. M., Yuan, D. N., Dietrich, R., Casassa, G., and Rülke, A. (2011). On-land ice loss and glacial isostatic adjustment at the Drake Passage: 2003-2009. *Journal of Geophysical Research*, 116:B02403.

James, T. J., Murray, T., Barrand, N. E., and Barr, S. L. (2006). Extracting photogrammetric ground control from LiDAR DEMs for change detection. *The Photogrammetric Record*, 21(116):312–328.

Johnson, A. E. and Hebert, M. (1998). Surface matching for object recognition in complex three-dimensional scences. *Image and Vision Computing*, 16:635–651.

JPL (2013). Advanced spaceborne thermal emission and reflection radiometer. http://asterweb.jpl.nasa.gov. Accessed: 23.08.2013.

Kamp, U., Bolch, T., and Olsenholler, J. (2003). DEM generation from ASTER satellite data for geomorphometric analysis of cerro sillajhuay, chile/bolivia. In *Proceedings Annual Meeting Imaging and Geospatial Information Society (ASPRS)*. Anchorage, U.S.A.

Karras, G. E. and Petsa, E. (1993). DEM matching and detection of deformation in close-range photogrammetry without control. *Photogrammetric Engineering & Remote Sensing*, 59(9):1419–1424.

Kaser, G., Cogley, J. G., Dyurgerov, M. B., Meier, M. F., and Ohmura, A. (2006). Mass balance of glaciers and ice caps: Consensus estimates for 1961-2004. *Geophysical Research Letters*, 33:L19501.

Kaser, G., Fountain, A., and Jansson, P. (2003). A manual for monitoring the mass balance of mountain glaciers. Technical report, IHP-VI, Technical Documents in Hydrology, No. 59, UNESCO, Paris.

Kato, S. and Yamaguchi, Y. (2005). Analysis of urban heat-island effect using ASTER and ETM+ Data: Separation of anthropogenic heat discharge and natural heat radiation from sensible heat flux. *Remote Sensing of Environment*, 99(1-2):44–54.

Kääb, A. (2005). Combination of SRTM3 and repeat ASTER data for deriving alpine glacier flow velocities in the bhutan himalaya. *Remote Sensing of the Environment*, 94:463–474.

Kääb, A. (2007). Glacier volume changes using ASTER optical stereo. A test study in eastern svalbard. In *Geoscience and Remote Sensing Symposium, 2007. IGARSS 2007. IEEE International*, pages 3994–3996. IEEE International Geoscience and Remote Sensing Symposium (IGARSS), July 2007, Barcelona, Spain.

Kääb, A. (2008). Glacier Volume Changes Using ASTER Satellite Stereo and ICESat GLAS Laser Altimetry. A Test Study on Edgøeya, Eastern Svalbard. *IEEE Transactions on Geosciences and Remote Sensing*, 46(10):2823–2830.

Kääb, A., Huggel, C., Paul, F., Wessels, R., Raup, B., Kieffer, H. H., and Kargel, J. S. (2002). Glacier monitoring from ASTER imagery: accuracy and applications. In *E ARSeL-LISSIG-Workshop Observing our Cryosphere from Space*, Bern.

Khan, S. A., Liu, L., Wahr, J., Howat, I., Joughin, I., van Dam, T., and Fleming, K. (2010). GPS measurements of crustal uplift near Jakobshavn Isbræ due to glacial ice mass loss. *Journal of Geophysical Research*, 115:B09405.

King, M. (2004). Rigorous GPS data-processing strategies for glaciological applications. *Journal of Glaciology*, 50(171):601–607.

King, M. A., Bingham, R. J., Moore, P., Whitehouse, P. L., Bentley, M. J., and Milne, G. A. (2012). Lower satellite-gravimetry estimates of antarctic sea-level contribution. *Nature*, 491:586–590.

Kraus, K. (2007). *Photogrammetry: Geometry from Images and Laser Scans (2nd edition)*. de Gruyter Textbook.

Kraus, K., Ressl, C., and Roncat, A. (2006). Least-squares matching for airborne laser scanner data. In Gruendig, L. and O, A., editors, *'Fifth International Symposium Turkish-German Joint Geodetic Days 'Geodesy and Geoinformation in the Service of our Daily Life"*, pages 1–7.

Krieger, G., Moreira, A., Fiedler, H., Hajnsek, I., Werner, M., Younis, M., and Zink, M. (2007). TanDEM-X: A Satellite Formation for High-Resolution SAR Interferometry. *IEEE Transactions on Geosciences and Remote Sensing*, 45(11):3317–3341.

Kuipers-Munneke, P., Picard, G., van de Broeke, M. R., Lenaerts, J. T. M., and van Meijgaard, E. (2012). Insignificant change in Antarctic snowmelt volume since 1979. *Geophys. Res. Lett.*, 39:L01501.

Kunz, M., King, M. A., Mills, J. P., Miller, P. E., Fox, A. J., Vaughan, D. G., and Marsh, S. H. (2012). Multi-decadal glacier surface lowering in the Antarctic Peninsula. *Geophys. Res. Lett.*, 39(19):L19502–.

Lang, H. R. and Welch, R. (1999). Algorithm Theoretical Basis Document for ASTER Digital Elevation models (version 3.0). Technical report, JPL.

LAPACK (2013). Lapack - Linear Algebra PACKage. http://www.netlib.org/lapack/. Accessed: 23.08.2013.

Leclercq, P. W. and Oerlemans, J. (2012). Global and hemispheric temperature reconstruction from glacier length fluctuations. *Climate Dynamics*, 38(5-6):1065–1079.

Leclercq, P. W., Oerlemans, J., and Cogley, J. G. (2011). Estimating the Glacier Contribution to Sea-Level rise for the period 1800-2005. *Surv Geophys*, 32:519–535.

Lemke, P., Ren, J., Alley, R. B., Carrasco, J., Flato, G., Fuji, Y., Kaser, G., Mote, P., Thomas, R. H., and Zhang, T. (2007). *Climate Change 2007: The Physical Science Basis. Contribution of Working Group I to the Fourth Assessment Report of the Intergovernmental Panel on Climate Change*, chapter Observations: Changes in Snow, Ice and Frozen Ground, pages 337–383. Cambridge University Press, Cambridge, United Kingdom and New York, NY, USA.

Li, R. (1998). Potential of high-resolution satellite imagery for national mapping products. *Photogrammetric Engineering & Remote Sensing*, 64(12):1165–1170.

Li, Z. (1988). On the measure of digital terrain model accuracy. *Photogrammetric Record*, 12(72)(72):873–877.

Li, Z., Xu, Z., Cen, M., and Ding, X. (2001). Robust surface matching for automated detection of local deformations using least-median-of-squares estimator. *Photogrammetric Engineering & Remote Sensing*, 67(11):1283–1292.

Lillesand, T. M., Kiefer, R. W., and Chapmann, J. W. (2004). *Remote Sensing and Image Interpretation*. Wiley, 5th edition.

Liu, H., Jezek, K., Li, B., and Zhao, Z. (2001). *Radarsat Antarctic Mapping Project digital elevation model version 2*. Boulder, CO: National Snow and Ice Data Center. Digital media.

Lubin, D., Wittenmyer, R. A., Bromwich, D. H., and Marshall, G. J. (2008). Antarctic Peninsula mesoscale cyclone variability and climatic impacts influenced by the SAM. *Geophys. Res. Lett.*, 35:L02808.

Luckman, A., Murray, T., de Lange, R., and Hanna, E. (2006). Rapid and synchronous ice-dynamic changes in East Greenland. *Geophys. Res. Lett.*, 33:L03503.

Luthcke, S. B., Arendt, A. A., Rowlands, D. D., McCarthy, J. J., and Larsen, C. F. (2008). Recent glacier mass changes in the Gulf of Alaska region from GRACE mascon solutions. *Journal of Glaciology*, 54(188):767–777.

Lythe, M. B. and Vaughan, D. G. (2001). Bedmap: A new ice thickness and subglacial topographic model of antarctica. *J. Geophys. Res.*, 106(B6):11335–11351.

Maas, H. G. (2000). Least-Squares Matching with Airborne Laserscanning Data in a TIN structure. *International Archive of Photogrammetry, Remote Sensing and Spatial Information Sciences*, XXXIII(3A):548–555.

Marshall, G. J. (2003). Trends in the Southern Annular Mode from Observations and Reanalysis. *J. Climate*, 16:4134–4143.

Marshall, G. J., Orr, A., van Lipzig, P. M., and King, J. C. (2006). The impact of a Changing Southern Hemisphere Annular Mode on Antarctic Peninsula Summer Temperatures. *J. Climate*, 19:5388–5404.

Martin, C. F., Thomas, R. H., Krabill, W. B., and Manizade, S. S. (2005). ICESat range and mounting bias estimation over precisely-surveyed terrain. *Geophys. Res. Lett.*, 32:L21S07.

Martinson, D. G., Stammerjohn, S. E., Iannuzzi, R. A., Smith, R. C., and Vernet, M. (2008). Western Antarctic Peninsula physical oceanography and spatio-temporal variability. *Deep-Sea Research II*, 55:1964–1987.

Massonnet, D. and Feigl, K. L. (1998). Radar interferometry and its application to changes in the Earth's surface. *Reviews of Geophysics*, 36(4):441–500.

Maune, D. F., Maitra, J. B., and McKay, E. J. (2007). *Digital Elevation Model Technologies and Applications: The DEM Users Manual, 2nd Edition*, chapter Accuracy Standards, pages 65–98. ASPRS.

McGlone, J. G., Mikhail, E. M., and Bethel, J. S., editors (2004). *Manual of Photogrammetry. Fith Edition.* ASPRS.

Meier, M. F., Dyurgerov, M. B., Rick, U. K., O'Neel, S., Pfeffer, W. T., Anderson, R. S., Anderson, S. P., and Glazovsky, A. F. (2007). Glaciers dominate eustatic sea-level rise in the 21st century. *Science*, 317(5841):1064–1067.

Mercer, J. H. (1978). West Antarctic ice sheet and CO_2 greenhouse effect: a threat of disaster. *Nature*, 271:321–325.

Meredith, M. P. and King, J. C. (2005). Rapid climate change in the ocean west of the Antarctic Peninsula during the second half of the 20th century. *Geophys. Res. Lett.*, 32:L19604.

METI/NASA (2009). ASTER Global DEM Validation Summary Report. Technical report, ASTER GDEM Validation Team: METI/ERSDAC, NASA/LPDAAC, USGS/EROS.

Miller, P., Kunz, M., Mills, J., King, M., Murray, T., James, T., and Marsh, S. (2009). Assessment of Glacier Volume Change Using ASTER-Based Surface Matching of historical photography. *IEEE Transactions on Geoscience and Remote Sensing*, 47(7):1971–1979.

Miller, P., Mills, J. P., Edwards, S., Bryan, P., Marsh, S., Mitchell, H., and Hobbs, P. (2008). A robust surface matching technique for coastal geohazard assessment and management. *ISPRS Journal of Photogrammetry & Remote Sensing*, 63(5):529–542.

Miller, P. E. (2007). *A robust surface matching technique for coastal geohazard monitoring*. Phd thesis, University of Newcastle upon Tyne.

Miller, P. E., Mills, J. P., and Kunz, M. (2012). Improving the Accuracy of ASTER Elevation Data for Glacial Change Assessment in Antarctica. Technical report, RICS Research.

Mills, J. P., Buckley, S., and Mitchell, H. (2003). Synergistic Fusion of GPS and Photogrammetrically Generated Elevation models. *Photogrammetric Engineering & Remote Sensing*, 69(4):341–349.

Mills, J. P., Buckley, S., Mitchell, H., Clarke, P., and Edwards, S. (2005). A geomatics data integration technique for coastal change monitoring. *Earth Surface Processes and Landforms*, 30(6):651–664.

Mitchell, H. and Chadwick, R. G. (1999). Digital photogrammetric concepts applied to surface deformation. *Geomatica*, 53(4):405–414.

Möller, M. and Schneider, C. (2010). Volume change at gran campo nevado, patagonia, 1984-2000: a reassessment based on new findings. *Journal of Glaciology*, 56:363–365.

Montes-Hugo, M., Doney, S. C., Ducklow, H. W., Fraser, W., Martinson, D., Stammerjohn, S. E., and Shofield, O. (2009). Recent Changes in Photoplankton Communities Associated with Rapid Regional Climate Change Along the Western Antarctic Peninsula. *Science*, 323:1470–1473.

Morris, E. M. and Vaughan, D. G. (2003). Spatial and temporal variation of surface temperature on the Antarctic Peninsula and the limit of viability of ice shelves. *Antarctic Research Series*, 79:61–68.

Muskett, R. R., Lingle, C. S., Sauber, J. M., Post, A. S., Tangborn, W. V., Rabus, B. T., and Echelmeyer, K. A. (2009). Airborne and spaceborne DEM- and laser altimetry-derived surface elevation and volume changes of the bering glacier system, alaska, usa, and yukon, canada, 1972-2006. *Journal of Glaciology*, 55(190):316–326.

NASA (2013). Reverb | ECHO. http://reverb.echo.nasa.gov/reverb/. Accessed: 23.08.2013.

National Digital Elevation Program (NDEP) (2004). *Guidelines for Digital Elevation Data - Version 1.0*. National Digital Elevation Program (NDEP).

Nield, G. A., Whitehouse, P. L., King, M. A., Clarke, P. J., and Bentley, M. J. (2012). Increased ice loading in the antarctic peninsula since the 1850s and its effect on glacial isostatic adjustment. *Geophys. Res. Lett.*, 39:L17504.

Nimomiya, Y., Fu, B., and Cudahy, T. J. (2005). Detecting lithology with Advanced Spaceborne Thermal Emission and Rreflection Radiometer (ASTER) multispectral thermal infrared "radiance-at-sensor" data. *Remote Sensing of Environment*, 99:127–139.

NSDIC (2013). Operation IceBridge - IceBridge Data Portal. http://nsidc.org/icebridge/portal/. Accessed: 23.08.2013.

NSIDC (2011). Data at NSIDC. http://www.nsidc.org/data. Accessed: 08.10.2011.

Nuth, C. and Kääb, A. (2011). Co-registration and bias corrections of satellite elevation data sets for quantifying glacier thickness change. *The Cryosphere*, 5(1):271–290.

Nuth, C. and Kääb, A. (2010). What's in an elevation difference? Accuracy and corrections of satellite elevation data sets for quantification of glacier changes. *The Cryosphere Discussion*, 4(4):2013–2077.

Nuth, C., Kohler, J., Aas, H., Brandt, O., and Hagen, J. (2007). Glacier geometry and elevation changes on Svalbard (1936-90): a baseline dataset. *Annals of Glaciology*, 46:106–116.

Oerlemans, J. (2005). Extracting a Climate Signal from 169 Glacier Records. *Science*, 308:675–677.

Oerlemans, J., Anderson, B., Hubbard, A., Huybrechts, P., Johannesson, T., Knap, W. H., Schmeits, M., Stroeven, A. P., van de Wal, R. S. W., Wallinga, J., and Zou, Z. (1998). Modelling the response of glaciers to climate warming. *Climate Dynamics*, 14:267–274.

Ohmura, A., Bauder, A., Müller, H., and Kappenberger, G. (2007). Long-term change of mass balance and the role of radiation. *Annals of Glaciology*, 46(1):367–374.

Palancz, B., Lewis, R. H., Zaletnyik, P., and Awange, J. (2007). Computational Study of 3D Affine Coordinate Transformation, Part i. 3-point problem. Online.

Parkinson, C. L. (2002). Trends in the length of the Southern Ocean sea-ice season, 1979-1999. *Annals of Glaciology*, 34:435–440.

Paul, F. (2008). Calculation of glacier elevation changes with srtm: is there an elevation-dependent bias? *Journal of Glaciology*, 54:945–946.

Paul, F. (2010). The influence of changes in glacier extent and surface elevation on modeled mass balance. *The Cryosphere Discussions*, 4:737–766,.

Paul, F., Bolch, T., Kääb, A., Nagler, T., Nuth, C., Scharrer, K., Shepherd, A., Strozzi, T., Ticconi, F., Bhambri, R., Berthier, E., Bevan, S., Gourmelen, N., Heid, T., Jeong, S., Kunz, M., Lauknes, T. R., Luckmann, A., Merryman, J., Moholdt, G., Muir, A., Neelmeijer, J., Rankl, M., VanLooy, J., and Van Niel, T. (2013). The glaciers climate change initiative: Methods for creating glacier area, elevation change and velocity products. *Remote Sensing of Environment*, Climate Change Initiative Special Issue:19pp.

Paul, F. and Kääb, A. (2005). Perspectives on the production of a glacier inventory from multispectral satellite data in arctic canada: Cumberland peninsula, baffin island. *Annals of Glaciology*, 42:59–66.

Pellikka, P. and Rees, W. G. (2010). *Remote sensing of glaciers: techniques for topographic, spatial and thematic mapping of glaciers*. CRC Press - Taylor & Francis.

Pfeffer, W. T. (2003). Tidewater glaciers move at their own pace. *Nature*, 426:602.

PGC (2013a). Antarctic Air Photography. http://www.pgc.umn.edu/imagery/aerial/antarctica. Accessed: 23.08.2013.

PGC (2013b). Antarctic TMA Flightline Viewer. http://applications.pgc.umn.edu/flash/tma/. Accessed: 23.08.2013.

Pieczonka, T., Bolch, T., and Buchroithner, M. (2011). Generation and evaluation of multitemporal digital terrain models of the Mt. Everest area from different optical sensors. *ISPRS Journal of Photogrammetry and Remote Sensing*, 66:927–940.

Pilgrim, L. (1996). Robust estimation applied to surface matching. *ISPRS Journal of Photogrammetry & Remote Sensing*, 51:243–257.

Poli, D., Remondino, F., and Dolci, C. (2004). Use of satellite imagery for dem extraction, landscape modeling and gis applications. *International Archive of Photogrammetry, Remote Sensing and Spatial Information Sciences*, XXXVI(5/W1):8pp.

Post, A., O'Neel, S., Motyka, R. J., and Streveler, G. (2011). A Complex Relationship Between Calving Glaciers and Climate. *EOS, Transactions, American Geophysical Union*, 92(37):305–306.

Postolov, Y., Krupnik, A., and McIntosh, K. (1999). Registration of airborne laser data to surfaces generated by photogrammetric means. *International Archives of the Photogrammetry and Remote Sensing*, 32(III/W14):95–99.

Pritchard, H. D., Arthern, R. J., Vaughan, D. G., and Edwards, L. A. (2009). Extensive dynamic thinning on the margins of the Greenland and Antarctic ice sheets. *Nature*, 461:971–975.

Pritchard, H. D., Ligtenberg, S. R. M., Fricker, H. A., Vaughan, D. G., van den Broeke, M. R., and Padman, L. (2012). Antarctic ice-sheet loss driven by basal melting of ice shelves. *Nature*, 484:502–505.

Pritchard, H. D. and Vaughan, D. G. (2007). Widespread acceleration of tidewater glaciers on the Antarctic Peninsula. *J. Geophys. Res.*, 112:F03S29.

Qi, W. and Braun, A. (2013). Accelerated elevation change of greenland's jakobshavn glacier observed by icesat and icebridge. *IEEE Geoscience and Remote Sensing Letters*, 10(5):1133–1137.

Racoviteanu, A. E., Manley, W. F., Arnaud, Y., and Williams, M. W. (2007). Evaluating digital elevation models for glaciologic applications: An example from Nevado Coropuna, Peruvian Andes. *Global and Planetary Change*, 59(1-4):110–125.

Radić, V. and Hock, R. (2010). Regional and global volumes of glaciers derived from statistical upscaling of glacier inventory data. *J. Geophys. Res.*, 115:F01010.

Radic, V. and Hock, R. (2011). Regionally differentiated contribution of mountain glaciers and ice caps to future sea-level rise. *Nature Geoscience*, 4:1–4.

Rahmstorf, S. (2007). A semi-empirical approach to projecting future sea-level rise. *Science*, 315:368–370.

Rastner, P., Bolch, T., Mölg, N., Machguth, H., and Paul, F. (2012). The first complete glacier inventory for the whole of greenland. *The Cryosphere Discuss.*, 6:2399–2436.

Rau, F. and Braun, M. (2002). The regional distribution of the dry-snow zone on the Antarctic Peninsula north of 70°s. *Annals of Glaciology*, 34:95–100.

Rau, F., Mauz, F., de Angelis, H., Jana, R., Neto, J. A., Skvarca, P., Vogt, S., Saurer, H., and Grossmann, H. (2004). Variations of glacier frontal positions on the northern Antarctic Peninsula. *Annals of Glaciology*, 39:525–530.

Raup, B. and Khalsa, S. J. S. (2010). *GLIMS Analysis Tutorial*. GLIMS.

Raup, B., Racoviteanu, A., Khalsa, S. J. S., Helm, C., Armstrong, R., and Arnaud, Y. (2007). The GLIMS geospatial glacier database: A tool for studying glacier change. *Global and Planetary Change*, 56(1-2):101–110.

Remy, F. and Parouty, S. (2009). Antarctic ice sheet and radar altimetry: A review. *Remote Sensing*, 1:1212–1239.

Rignot, E., , Mouginot, J., and Scheuchl, B. (2011a). Antarctic grounding line mapping from differential satellite radar interferometry. *Geophys. Res. Lett.*, 38:L10504.

Rignot, E., Bamber, J. L., van de Broeke, M. R., Davis, C., Li, Y., van de Berg, W. J., and van Meijgaard, E. (2008). Recent Antarctic ice mass loss from radar interferometry and regional climate modelling. *Nature Geoscience*, 1:106–110.

Rignot, E., Casassa, G., Gogineni, P., Krabill, W., Rivera, A., and Thomas, R. (2004). Accelerated ice discharge from the Antarctic Peninsula following the collapse of Larsen B ice shelf. *Geophysical Research Letters*, 31:L18401.

Rignot, E., Casassa, G., Gogineni, S., Kanagaratnam, P., Krabill, W., Pritchard, H., Rivera, A., Thomas, R., Turner, J., and Vaughan, D. (2005). Recent ice loss from the Fleming and other glaciers, Wordie Bay, West Antarctic Peninsula. *Geophys. Res. Lett.*, 32:L07502.

Rignot, E., Echelmeyer, K., and Krabill, W. (2001a). Penetration depth of interferometric synthetic-aperture radar signals in snow and ice. *Geophys. Res. Lett.*, 28(18):3501–3504.

Rignot, E. and Kanagaratnam, P. (2006). Changes in the velocity structure of the Greenland ice sheet. *Science*, 311:986–990.

Rignot, E., Mouginot, J., and Scheuchl, B. (2001b). Ice flow of the antarctic ice sheet. *Science*, 333:1427–1430.

Rignot, E., Mouginot, J., and Scheuchl, B. (2011b). Antarctic grounding line mapping from differential satellite radar interferometry. *Geophys. Res. Lett.*, 38:L10504.

Rignot, E., Rivera, A., and Casassa, G. (2003). Contribution of the Patagonia Icefields of South America to Sea Level Rise. *Science*, 302:434–437.

Rignot, E. and Thomas, R. H. (2002). Mass Balance of Polar Ice Sheets. *Science*, 297:1502–1506.

Rignot, E., Velicogna, I., van den Broeke, M. R., Monaghan, A., and Lenaerts, J. (2011c). Acceleration of the contribution of the Greenland and Antarctic ice sheets to sea level rise. *Geophys. Res. Lett.*, 38:L05503.

Rivera, A., Casassa, G., A, J. B., and Kääb, A. (2005). Ice-elevation changes of Glaciar Chico, southern Patagonia, using aster dems, aerial photographs and gps data. *Journal of Glaciology*, 51(172):105–112.

Rolstad, C., Haug, T., and Denby, B. (2009). Spatially integrated geodetic glacier mass balance and its uncertainty based on geostatistical analysis: application to the western Svartisen ice cap, Norway. *Journal of Glaciology*, 55(192):666–680.

Rosenholm, D. and Torlegard, K. (1988). Three-dimensional absolute orientation of stereo models using digital elevation models. *Photogrammetric Engineering & Remote Sensing*, 54(10):1385–1389.

Rott, H., Müller, F., Nagler, T., and Floricioiu, D. (2011). The imbalance of glaciers after disintegration of Larsen-B ice shelf, Antarctic Peninsula. *The Cryosphere*, 5:125–134.

Rousseeuw, P. and Leroy, A. (1988). A robust scale estimator based on the shortest half. *Statistica Neerlandica*, 42(2):103–116.

Scambos, T. A., Bohlander, J. A., Shuman, C. A., and Skvarca, P. (2004). Glacier acceleration and thinning after ice shelf collapse in the Larsen B embayment, Antarctica. *Geophys. Res. Lett.*, 31:L18402.

Scambos, T. A., Haran, T. M., Fahnestock, M. A., Painter, T. H., and Bohlander, J. (2007). MODIS-based Mosaic of Antarctica (MOA) data sets: Continent-wide surface morphology and snow grain size. *Remote Sensing of Environment*, 111:242–257.

Scambos, T. A., Hulbe, C., Fahnestock, M., and Bohlander, J. (2000). The link between climate warming and the break-up of ice shelves in the Antarctic Peninsula. *Journal of Glaciology*, 46(154):516–530.

SCAR (2013a). Antarctic Digital Database Version 6.0. http://http://www.add.scar.org/. Accessed: 23.08.2013.

SCAR (2013b). Met READER. http://www.antarctica.ac.uk/met/READER. Accessed: 23.08.2013.

Schenk, T., Krupnik, A., and Postolov, Y. (2000). Comparative study of surface matching algorithms. *International Archive of Photogrammetry, Remote Sensing and Spatial Information Sciences*, XXXIII(B4):518–524.

Schutz, B. E., Zwally, H. J., Shuman, C. A., Hancock, D., and DiMarzio, J. P. (2005). Overview of the ICESat Mission. *Geophys. Res. Lett.*, 32:L21S01.

Sewell, E. D. (1954). Distortion - planigon versus metrogon. *Photogrammetric Engineering*, 20(1):761–764.

Shepherd, A., Ivins, E. R., A, G., Barletta, V. R., Bentley, M. J., Bettadpur, S., Briggs, K. H., Bromwich, D. H., Forsberg, R., Galin, N., Horwath, M., Jacobs, S., Joughin, I., King, M. A., Lenaerts, J. T. M., Li, J., Ligtenberg, S. R. M., Luckman, A., Luthcke, S. B., McMillan, M., Meister, R., Milne, G., Mouginot, J., Muir, A., Nicolas, J. P., Paden, J., Payne, A. J., Pritchard, H., Rignot, E., Rott, H., SÃžrensen, L. S., Scambos, T. A., Scheuchl, B., Schrama, E. J. O., Smith, B., Sundal, A. V., van Angelen, J. H., van de Berg, W. J., van den Broeke, M. R., Vaughan, D. G., Velicogna, I., Wahr, J., Whitehouse, P. L., Wingham, D. J., Yi, D., Young, D., and Zwally, H. J. (2012). A reconciled estimate of ice-sheet mass balance. *Science*, 338(6111):1183–1189.

Shepherd, A. and Wingham, D. (2007). Recent Sea-Level Contributions of the Antarctic and Greenland Ice Sheets. *Science*, 315:1529–1532.

Shepherd, A., Wingham, D., Payne, T., and Skvarca, P. (2003). Larsen Ice Shelf Has Progressively Thinned. *Science*, 302:856–859.

Shevenell, A. E., Ingalls, A. E., Domack, E. W., and Kelly, C. (2011). Holocene Southern Ocean surface temperature variability west of the Antarctic Peninsula. *Nature*, 470:250–254.

Shewchuk, J. (1996). Triangle: Engineering a 2D quality mesh generator and Delaunay triangulator.

Shuman, C. A., Berthier, E., and Scambos, T. A. (2011). 2001–2009 elevation and mass loss in the Larsen A and B embayment, Antarctic Peninsula. *Journal of Glaciology*, 57:737–754.

Skvarca, P., Rack, W., and Rott, H. (1999). 34 years satellite time series to monitore characteristics, extend and dynamics of Larsen B Ice Shelf, Antarctic Peninsula. *Annals of Glaciology*, 29:255–260.

Small, C. and Cohen, J. F. (2004). Continental physiography, climate, and the global distribution of human population. *Current Anthropology*, 45(2):269–277.

Smellie, J. L., Johnson, J. S., McIntosh, W. C., Esser, R., Gudmundsson, M. T., Hambrey, M. J., and van Wyk de Vries, B. (2008). Six million years of glacial history recorded in volcanic lithofacies of the James Ross Island Volcanic Group, Antarctic Peninsula. *Paleogeography, Paleoclimatology, Paleoecology*, 260:122–148.

Smith, A. M., Vaughan, D. G., Doake, C. S. M., and Johnson, A. C. (1998). Surface lowering of the ice ramp at Rothera Point, Antarctic Peninsula, in response to regional climate change. *Annals of Glaciology*, 27:113–118.

Smith, R. C., Ainley, D., Baker, K., Domack, E., Emslie, S., Fraser, B., Kennet, J., Leventer, A., Mosley-Thompson, E., Stammerjohn, S., and Vernet, M. (1999). Marine Ecosystem Sensitivity to Climate Change. *BioScience*, 49(5):393–404.

Smith, R. C. and Stammerjohn, S. E. (2001). Variations of surface air temperatures and sea-ice extent in the western Antarctic Peninsula region. *Annals of Glaciology*, 33:493–500.

Smith, T. B. and Longhenry, R. (2008). Improving Digital Access to the USGSFilm Archive. In *Pecora 17 - The Future of Land Imaging...Going Operational*. Personal communication with T B Smith, EROS Center.

Spriggs, R. M. (1966). The Calibration of Military Cartographic Cameras. Technical report, U.S. Army Engineer Geodesy, Intelligence and Mapping R. & D. Agency, Technical Note 66-2.

Stammerjohn, S. E., Martinson, D. G., Smith, R. C., and Iannuzzi, R. A. (2008). Sea ice in the western Antarctic Peninsula region: Spatio-temporal variability from ecological and climate change perspectives. *Deep-Sea Research II*, 55:2041–2058.

Stearns, L. A. and Hamilton, G. S. (2007). Rapid volume loss from two East Greenland outlet glaciers quantified using repeat stereo satellite imagery. *Geophysical Research Letters*, 34:5. doi:10.1029/2006GL028982.

Stevens, N. F., Garbeil, H., and Mouginis-Mark, P. J. (2004). NASA EOS Terra ASTER: Volcanic topographic mapping and capability. *Remote Sensing of Environment*, 90(3):405–414.

Streiner, D. L. (1996). Maintaining Standards: Differences between the Standard Deviation and Standard Error, and When to Use Each. *Can J Psychiatry*, 41(8):498–502.

Strozzi, T., W. A. K. A. J. S. and Mool, P. (2012). Glacial lake mapping with very high resolution satellite sar data. *Nat. Hazards Earth Syst. Sci.*, 12:2487–2498.

Studinger, M., Koenig, L., Martin, S., and Sonntag, J. (2010). Operation IceBridge: Using instrumented aircraft to bridge the observational gap between ICESat-1 and ICESat-2. In *Geoscience and Remote Sensing Symposium (IGARSS), 2010 IEEE International*, pages 1918–1919.

Sund, M., Eiken, T., Hagen, J. O., and Kääb, A. (2009). Svalbard surge dynamics derived from geometric changes. *Annals of Glaciology*, 50(52):50–60.

Tapley, B. D., Bettadpur, S., Watkins, M., and Reigber, C. (2004). The Gravity Recovery and Climate Experiment: Mission Overview and Early Results. *Geophys. Res. Lett.*, 31:L09607.

Tedesco, M. and Monaghan, A. (2009). An updated Antarctic melt record through 2009 and its linkages to high-latitude and tropical climate variability. *Geophysical Research Letters*, 36(18):18502–5.

Thibert, E., Blanc, R., Vincent, C., and Eckert, S. (2008). Glaciological and volumetric mass-balance measurements: error analysis over 51 years for glacier de sarennes, french alps. *Journal of Glaciology*, 54(186):522–532.

Thomas, R., Frederick, E., Li, J., Krabill, W., Manizade, S., Paden, J., Sonntag, J., Swift, R., and Yungel, J. (2011). Accelerating ice loss from the fatest Greenland and Antarctic glaciers. *Geophys. Res. Lett.*, 38:L10502.

Thomas, R., Rignot, E., Casassa, G., Kanagaratnam, P., Acuña, C., Akins, T., Brecher, H., Frederick, E., P. Gogineni, W. K., Manizade, S., Ramamoorthy, H., Rivera, A., Russell, R., Sonntag, J., Swift, R., Yungel, J., and Zwally, J. (2004). Accelerated sea-level rise from west antarctica. *Science*, 306:255–258.

Tokunaga, M., Hara, S., Miyazaki, Y., and Kaku, M. (1996). Overview of DEM product generated by using ASTER data. *International Archive of Photogrammetry, Remote Sensing and Spatial Information Sciences*, 31(B4):874–878.

Toutin, T. (2002). DEM from stereo Landsat 7 ETM + data over high relief areas. *International Journal of Remote Sensing*, 23(10):2133–2139.

Toutin, T. (2008). ASTER DEMs for geomatic and geoscientific applications: a review. *International Journal of Remote Sensing*, 29(7):1855–1875.

Turner, J., Colwell, S. R., Marshall, G. J., Lachlan-Cope, T. A., Carleton, A. M., Jones, P. D., Lagun, V., Reid, P. A., and Iagovkina, S. (2005). Antarctic climate change during the last 50 years. *Int. J. Climatol.*, 25:279–294.

Turner, J., Lachlan-Cope, T. A., Marshall, G. J., Morris, E. M., Mulvaney, R., and Winter, W. (2002). Spatial variability of Antarctic Peninsula net surface mass balance. *Journal of Geophys. Res.*, 107(D13):4137.

UNEP-WGMS (2008). Global glacier changes: facts and figures. Technical report, United Nations Environment Program (UNEP), World Glacier Monitoring Service (WGMS).

USGS (2012). Landsat Image Mosaic Of Antarctica (LIMA). http://lima.usgs.gov. Accessed: 23.08.2013.

USGS (2013). EarthExplorer. http://earthexplorer.usgs.gov. Accessed: 23.08.2013.

Van de Wal, R. S. W. and Wild, M. (2001). Modelling the response of glaciers to climate change by applying volume-area scaling in combination with a high resolution gcm. *Climate Dynamics*, 18:359–366.

van den Broeke, M., van de Berg, W. J., and van Meijgaard, E. (2006). Snowfall in coastal West Antarctica much greater than previously assumed. *Geophys. Res. Lett.*, 33:L02505.

van Lipzig, N. P. M., King, J. C., and Lachlan-Cope, T. A. (2004). Precipitation, sublimation, and snow drift in the Antarctic Peninsula region from a regional atmospheric model. *Journal of Geophysical Research*, 109:D24106.

Vaughan, D. G. (2006). Recent Trends in Melting Conditions on the Antarctic Peninsula and Their Implications for Ice-sheet Mass Balance and Sea Level. *Arctic, Antarctic, and Alpine Research*, 38(1):147–152.

Vaughan, D. G., Marshall, G. J., Connolley, W. M., Parkinson, C., Mulvaney, R., Hodgson, D. A., King, J. C., Pudsey, C. J., and Turner, J. (2003). Recent Rapid Regional Climate Warming on the Antarctic Peninsula. *Climatic Change*, 60(3):243–274.

Vaze, J., Teng, J., and Spencer, G. (2010). Impact of DEM accuracy and resolution of topographic indices. *Environmental Modelling & Software*, 25:1086–1098.

Velicogna, I. (2009). Increasing rates of ice mass loss from the Greenland and Antarctic ice sheets revealed by GRACE. *Geophys. Res. Lett.*, 36:L19503.

Velicogna, I. and Wahr, J. (2013). Time-variable gravity observations of ice sheet mass balance: Precision and limitations of the grace satellite data. *Geophys. Res. Lett.*, 40(12):3055–3063.

Vignon, F., Arnaud, Y., and Kaser, G. (2003). Quantification of glacier volume change using topographic and ASTER dems - a case study in the cordillera blanca. *Geoscience and Remote Sensing Symposium, 2003. IGARSS '03. Proceedings. 2003 IEEE International*, 4:2605 – 2607.

Webster, R. and Oliver, M. A. (2007). *Geostatistics for Environmental Scientists*. John Wiley & Sons.

Welch, R., Jordan, T., Lang, H., and Murakami, H. (1998). ASTER as a Source for Topographic Data in the Late 1990's. *IEEE Transactions on Geosciences and Remote Sensing*, 36(4):1282–1289.

Wendt, J., Rivera, A., Wendt, A., Bown, F., Zamora, R., Casassa, G., and Bravo, C. (2010). Recent ice-surface-elevation changes of fleming glacier in response to the removal of the wordie ice shelf, antarctic peninsula. *Annals of Glaciology*, 51(55):97–102.

WGMS (2011). *Glacier Mass Balance Bulletin: Bulletin No. 11 (2008-2009)*. World Glacier Monitoring Service (WGMS).

WGMS (2013). World Glacier Monitoring Service. http://www.geo.uzh.ch/microsite/wgms/. Accessed: 23.08.2013.

WGMS and NSDIC (1989, updated 2012). World Glacier Inventory. Compiled and made available by the World Glacier Monitoring Service, Zurich, Switzerland, and the National Snow and Ice Data Center, Boulder, CO, U.S.A Digital Media.

Wolf, P. and DeWitt, B. (2000). *Elements of Photogrammetry with Applications in GIS (3rd edition)*. McGraw-Hill.

Woodworth, P. L., Gehrels, W. R., and Nerem, R. S. (2011). Nineteenth and twentieth century changes in sea level. *Oceanography*, 26(2):80–93.

Wouters, B., Bamber, J. L., van den Broeke, M., Lenaerts, J. T. M., and Sasgen, I. (2013). Limits in the detecting acceleration of ice sheet mass loss due to climate variability. *Nature Geoscience*, 6:613–616.

Zhang, T. and Cen, M. (2008). Robust DEM co-registration method for terrain changes assessment using least trimmed squares estimator. *Advances in Space Research*, 41(11):1827–1835.

Zhang, Z. (1994). Iterative point matching for registration of free-form curves and surfaces. *International Journal of Computer Vision*, 13(2):119–152.

Zwally, H. J., Abdalati, W., Herring, T., Larson, K., Saba, J., and Steffen, K. (2002). Surface Melt-Induced Acceleration of Greenland Ice-Sheet Flow. *Science*, 297:218–222.

Zwally, H. J. and Giovinetto, M. B. (2011). Overview and Assessment of Antarctic Ice-Sheet Mass Balance Estimates: 1992-2009. *Surv Geophys*, 32(4-5):351–376.

Zwally, H. J., Giovinetto, M. B., Li, J., Cornejo, H. G., Beckley, M. A., Brenner, A. C., Saba, J. L., and Yi, D. (2005). Mass changes of the Greenland and Antarctic ice sheets and shelves and contribution to sea-level rise: 1992-2002. *Journal of Glaciology*, 51(175):509–527.